



University  
of Glasgow

Feder, Marnie Jean (2014) *Towards a rational design for sustainable urban drainage systems: understanding (bio)geochemical mechanisms for enhanced heavy metal immobilization in filters*. PhD thesis.

<http://theses.gla.ac.uk/5570/>

Copyright and moral rights for this thesis are retained by the author

A copy can be downloaded for personal non-commercial research or study, without prior permission or charge

This thesis cannot be reproduced or quoted extensively from without first obtaining permission in writing from the Author

The content must not be changed in any way or sold commercially in any format or medium without the formal permission of the Author

When referring to this work, full bibliographic details including the author, title, awarding institution and date of the thesis must be given



# Towards a rational design for Sustainable urban Drainage Systems - Understanding (bio)geochemical mechanisms for enhanced heavy metal immobilization in filters

Marnie Jean Feder

MSc. University of Surrey, UK

BSc. University of Colorado, USA

Submitted in fulfilment of the requirements for the  
Degree of Doctor of Philosophy

Infrastructure and Environment Research Division

School of Engineering

University of Glasgow

March 2014

## Abstract

Sustainable urban Drainage Systems (SuDS) have become an important approach for protection of natural watercourses from non-point sources of pollution. In particular, filtration based SuDS build on the concept of simple, low-cost technology that has been utilized in water treatment for over a century. While it is widely studied and acknowledged that filtration of polluted water through granular material is extremely effective, the inherent geochemical and biogeochemical mechanisms are complex and difficult to ascertain. This is especially true for SuDS filter drains as they have been less well studied. Therefore, this thesis set out to quantify heavy metal removal in gravel filter drains and investigate (bio)geochemical mechanisms responsible for metal immobilization. Determining specific mechanisms responsible for pollutant removal within SuDS provides data that can be used to enhance SuDS design and performance.

First, the impact of engineered iron-oxide coatings on heavy metal removal rates were investigated. It was determined that unamended microgabbro gravel immobilized similar quantities of heavy metals to the engineered iron oxide coated gravel. Consequently, engineered iron-oxide coatings were not recommended for future research or use in SuDS systems. Analysis of the surface of microgabbro gravel revealed the surface minerals are weathering to clays, enhancing the gravels affinity for heavy metals naturally. Comparison of microgabbro with other lithologies demonstrated microgabbro displayed enhanced removal by 3-80%. Comparison of microgabbro gravels with and without weathered surfaces demonstrated the weathered surface enhanced metal removal by 20%. From this, it is recommended weathered microgabbro gravel be used in filtration based SuDS where immobilization of incoming heavy metals typical in surface water runoff is important.

Following this, the contribution to metal immobilization due to biofilm growth in a gravel filter was examined. Through heavy metal breakthrough curves obtained from experimental flow cells with and without biofilm growth, it was determined that biofilm enhances heavy metal removal between 8-29%. Breakthrough curves were modelled with an advection diffusion equation. The model demonstrated heavy metal removal mechanisms within the column could

be described effectively by a permanent loss term. Further, the typical microbial community found within biofilms collected from an urban filter drain was determined to be composed of over 70% *cyanobacteria*. However, when inoculated into two different lithologies of gravel, the biofilm community composition changed and was influenced by gravel lithology. Dolomite gravel retained 47% *cyanobacteria* dominance while microgabbro demonstrated 54% *proteobacteria* dominance. Despite variations in biofilm composition, heavy metal removal capacity and mechanisms were broadly similar between different biofilm types.

An additional approach to determine effects of biofilm growth on porosity and flow patterns through a horizontal gravel flow cell was assessed with non-invasive magnetic resonance imaging (MRI). While a copper (Cu) tracer could be imaged within the gravel flow cell, the transport pathways were too complicated to model as the Cu does not follow a plug flow. Processing of 3D high resolution images determined the porosity of the gravel filter to be between 32-34%, in line with literature values for coarse grained dolomite gravel. Further post-processing allowed for localized biofouling to be analyzed. Highest concentration of biofilm growth in columns resulted from longer growth periods and exposure to light. Moreover, biofilms tended to grow closer to the inlet which typically offers a higher nutrient dose and in pore space regions close to the light source (both of which would be representative of the surface of a filter drain). Thus, MRI analysis of biofouling has important implications for filter drain design and efficiency through assessment of pore space blockage.

Finally, the possibility of enhancing heavy metal removal in sand (another filter material common in SuDS) with nano zero-valent iron (nZVI) particles was considered. Metal breakthrough curves for column experiments indicate that use of 10% nZVI enhanced sand improved metal immobilization between 12-30% and successfully removed > 98% Cu and Pb. It is therefore believed that nZVI enhanced sand is a promising avenue of future research for areas prone to high heavy metal loads.

# Table of Contents

Abstract .....	ii
List of Figures .....	viii
List of Tables .....	xi
Acknowledgements .....	xiv
Author's Declaration .....	xvii
Definitions/Abbreviations .....	xviii
1 Introduction .....	1
1.1 Background .....	1
1.2 Sustainable urban drainage systems .....	2
1.2.1 Types of SuDS .....	3
1.2.2. SuDS Performance .....	4
1.3 Runoff and heavy metal pollution .....	6
1.4 Filtration .....	11
1.5 Geochemical and Biogeochemical removal mechanisms .....	12
1.6 Regulation and guidelines .....	15
1.7 Thesis Overview .....	19
1.7.1 Aims .....	19
1.7.2 Thesis Outline .....	20
1.8 REFERENCES .....	21
2 Treatment of heavy metals by iron oxide coated and natural gravel media in Sustainable urban Drainage Systems .....	26
ABSTRACT .....	26
2.1 INTRODUCTION .....	27
2.1.1 Gravel lithology .....	27
2.1.2 Amendments to gravel .....	28
2.1.3 Motivation .....	29
2.2 MATERIALS AND METHODS .....	29
2.2.1 Uncoated filter drain gravel .....	29
2.2.2 Amended filter drain gravel .....	30
2.2.3 Further refinement with uncoated gravel .....	30
2.2.4 Batch and column experimental setup .....	31
2.2.5 Instrumentation .....	33
2.3 RESULTS .....	34

2.3.1 Uncoated filter drain gravel vs. amended filter drain gravel.....	34
2.3.2 Further refinement with uncoated gravel .....	37
2.3.3. PHREEQC modelling .....	43
2.4 DISCUSSION .....	45
2.4.1 Iron oxide coated gravel .....	45
2.4.2 Gravel lithology and heavy metal removal .....	46
2.5 CONCLUSIONS .....	53
2.6 REFERENCES .....	53
3 Influence of biofilms on heavy metal immobilization in Sustainable urban Drainage Systems .....	55
ABSTRACT .....	55
3.1 INTRODUCTION.....	56
3.1.1 Biofilms .....	56
3.1.2 Bacteria-metal and Biofilm-metal interactions .....	57
3.1.2.1 Biosorption.....	58
3.1.2.2 Biomineralization .....	59
3.1.2.3 Bioaccumulation .....	60
3.1.2.4 Biotransformation .....	60
3.1.3. Motivation .....	61
3.2 MATERIALS AND METHODS.....	61
3.2.1 Biofilm growth .....	61
3.2.2 Breakthrough experiments.....	63
3.2.3 Instrumentation .....	66
3.2.4 Breakthrough curve analysis and modelling .....	66
3.2.5 DNA extraction and clone library construction .....	67
3.3 RESULTS AND ANALYSIS.....	68
3.3.1 Breakthrough curve analysis.....	68
3.3.2 Breakthrough curve modelling .....	73
3.3.3 Clone library .....	78
3.4 DISCUSSION .....	83
3.4.1 Breakthrough curve analysis.....	83
3.4.2 Breakthrough curve modelling .....	85
3.4.3 Biofilm enhancement of metal-immobilization .....	87
3.4.4 Clone library .....	89
3.5 CONCLUSION .....	91

3.6 REFERENCES .....	92
4 Utilizing MRI to image biofilm growth and pollutant transport within gravel bed systems.....	96
ABSTRACT .....	96
4.1 INTRODUCTION.....	97
4.1.1 MRI Principles .....	97
4.1.2 MRI for use in contaminant hydrogeology .....	100
4.1.3 Motivation .....	103
4.2 MATERIALS AND METHODS.....	104
4.2.1 Experimental overview .....	104
4.2.2 Flow cell .....	105
4.2.3 Experimental materials.....	106
4.2.4 Biofilm growth .....	107
4.2.5 Flow system (Cu transport imaging) .....	108
4.2.6 MRI parameters and image acquisition.....	109
4.2.7 Image processing - clean versus biofilm scans .....	112
4.2.8 Image processing - Cu transport scans .....	117
4.3 RESULTS AND ANALYSIS.....	118
4.3.1 Clean and Biofilm image analysis .....	118
4.3.1.1 Bulk porosity data .....	118
4.3.1.2 Bulk bio-physical data.....	121
4.3.1.3 Local bio-physical data .....	127
4.3.2 Flow image analysis.....	133
4.4 DISCUSSION.....	134
4.4.1 Porosity analysis.....	134
4.4.2 Biofilm imaging with MRI.....	135
4.4.3 Biofilm growth .....	139
4.4.4 Data Uncertainty .....	141
4.5 CONCLUSION .....	145
4.6 REFERENCES .....	146
5 Nanoparticle enhanced sand for optimized heavy metal removal .....	150
ABSTRACT .....	150
5.1 - INTRODUCTION.....	150
5.1.1 Environmental nanotechnology .....	150
5.1.2 Zero valent iron (nZVI) nanoparticles .....	151

5.1.3 Slow Sand Filtration.....	152
5.1.4 Motivation .....	154
5.2 MATERIALS AND METHODS.....	154
5.2.1 Enhancing sand with nanoparticles.....	154
5.2.2 Experimental setup.....	156
5.2.3 Instrumentation .....	158
5.2.4 Breakthrough curve analysis.....	159
5.2.5 Modelling .....	159
5.3 RESULTS AND ANALYSIS.....	159
5.3.1 nZVI and nanoclay - Single metal experimental breakthrough curves	159
5.3.2 nZVI and nanoclay - Multiple metal experimental breakthrough curves .....	162
5.4 DISCUSSION.....	165
5.4.1 PHREEQC analysis .....	170
5.4.2 Standard electron potential analysis .....	175
5.5 CONCLUSION .....	178
5.6 REFERENCES.....	179
6 Conclusions and Future Recommendations.....	182
6.1 Summary of conclusions.....	182
6.2 Future recommendations.....	187
Appendix A - Literature review of metal concentrations found in runoff studies and used in experimentation .....	193
Appendix B - Chapter 2 Analytical and Experimental Error Analysis.....	195
Appendix C - Example of PHREEQC Input and Output.....	196
Appendix D - Advection Diffusion Matlab Code .....	198
Appendix E - Comparison of conductivity measurements to Na flame photometer analysis.....	201
Appendix F - Clone library breakdown, sequencing and classification .....	203
Appendix G - Class breakdown of <i>Proteobacteria</i> .....	206
Appendix H - Phylogenic tree of bacteria identified in gravel growth columns....	207
Appendix I - Specifications of experimental gravel filter .....	208
Appendix J - MRI Concentric ROI for BLL, BDL, BLS & BDS .....	209
Papers.....	212

## List of Figures

<b>Figure 1.1.</b> The SuDS triangle .....	3
<b>Figure 1.2.</b> Schematic of a filter drain and photo of a filter drain.....	5
<b>Figure 1.3.</b> Schematic of a horizontal gravel filter .....	12
<b>Figure 2.1.</b> Rinsed microgabbro .....	29
<b>Figure 2.2.</b> Iron oxide coated gravel.....	30
<b>Figure 2.3.</b> Rock samples for comparison to microgabbro.....	31
<b>Figure 2.4.</b> Pond outflow and parallel filter drain.....	32
<b>Figure 2.5.</b> Batch experiment setup and column experiment setup .....	33
<b>Figure 2.6.</b> RMG vs. IOCG percentage removal of Cu, Pb and Zn.....	35
<b>Figure 2.7.</b> Flow through column experiments. ....	36
<b>Figure 2.8.</b> SEM image of the surface of IOCG and RMG .....	37
<b>Figure 2.9.</b> MGD vs. UMG vs. RMG vs. SMG percentage removal of Cu.....	38
<b>Figure 2.10.</b> MGD vs. UMG vs. RMG vs. SMG percentage removal of Pb. ....	39
<b>Figure 2.11.</b> MGD vs. UMG vs. RMG vs. SMG percentage removal of Zn. ....	39
<b>Figure 2.12.</b> SEM image of a cross section of the surface of UMG and SMG.....	40
<b>Figure 2.13.</b> RMG, DG, RQG, GQG, MLG and SG percentage removal of Cu .....	41
<b>Figure 2.14.</b> RMG, DG, RQG, GQG, MLG and SG percentage removal of Pb .....	42
<b>Figure 2.15.</b> RMG, DG, RQG, GQG, MLG and SG percentage removal of Zn .....	42
<b>Figure 2.16.</b> EDS elemental analysis for cross sectional surface of UMG.....	49
<b>Figure 3.1.</b> Biofilm formation.....	56
<b>Figure 3.2.</b> Summary of microbe-metal interactions .....	57
<b>Figure 3.3.</b> Growth chamber after 10 months growth, Recirculating pond water after 10 months growth, SuDS filter drain gravel ~40mm grain size.....	62
<b>Figure 3.4.</b> Schematic of flow cell .....	62
<b>Figure 3.5.</b> Experimental column setup with recirculating influent after 2 months .....	3
<b>Figure 3.6.</b> Biofilm growth columns after 8 months of growth .....	64
<b>Figure 3.7.</b> Comparison of conservative DI tracer breakthrough curves between four Bio growth columns.....	69
<b>Figure 3.8.</b> Comparison of conservative DI tracer breakthrough curves between four Blank columns. ....	69
<b>Figure 3.9.</b> Comparison of DI water and Cu breakthrough between the microgabbro Bio and Blank experiments.....	71

<b>Figure 3.10.</b> Comparison of DI, Cu, Pb and Zn breakthrough between the microgabbro Bio and Blank experiments.....	71
<b>Figure 3.11.</b> Comparison of DI, Cu, Pb and Zn breakthrough between the dolomite Bio and Blank experiments .....	72
<b>Figure 3.12.</b> Comparison of DI and Cu breakthrough between the dolomite Bio and Blank experiments .....	72
<b>Figure 3.13</b> Predicted advection diffusion curve compared to observed results for the Na conservative tracer .....	75
<b>Figure 3.14</b> Predicted advection diffusion curve compared to observed results for the Cu, Pb or Zn non-conservative tracers .....	77
<b>Figure 3.15.</b> <i>k</i> loss term determined from model correlating to percentage of metals retained in experimental columns. ....	78
<b>Figure 3.16.</b> Sample of biofilm used for clone library analysis and to inoculate Bio columns.....	78
<b>Figure 3.17.</b> Graph of representative phyla of bacteria for initial filter drain biofilm growth. ....	79
<b>Figure 3.18.</b> Graph of representative phyla of bacteria for microgabbro and dolomite experimental column biofilm growth. ....	80
<b>Figure 3.19.</b> Dolomite and microgabbro columns after 4 months growth, influent/recirculated water feed for dolomite and microgabbro .....	81
<b>Figure 3.20.</b> Biofilm growth near the top, biofilm growth near the bottom and biofilm growth on the mesh diffuser plate in the microgabbro column.....	82
<b>Figure 3.21.</b> Biofilm growth in the dolomite column, biofilm growth around individual dolomite grains and biofilm growth on the mesh diffuser plate in the dolomite column.....	82
<b>Figure 3.22.</b> Biofilm collected from BioGabbroCu, BioGabbroMix, BioDolMix, and BioDolCu .....	83
<b>Figure 4.1.</b> Zeeman splitting.....	97
<b>Figure 4.2.</b> Spin up and spin down alignment, excess spin alignment along direction of magnetic field and net magnetization .....	98
<b>Figure 4.3.</b> Longitudinal relaxation following an excitation pulse .....	99
<b>Figure 4.4.</b> Transverse relaxation following an excitation pulse .....	99
<b>Figure 4.5.</b> Excitation by RF pulse .....	100
<b>Figure 4.6.</b> Photo and schematic of the experimental gravel filter.....	106

<b>Figure 4.7.</b> Original biofilm growth column and biofilm sample inoculated into pond water for MRI columns .....	107
<b>Figure 4.8.</b> Column in ‘dark’ conditions and ‘light’ conditions .....	108
<b>Figure 4.9.</b> Setup of peristaltic pump outside MRI room, setup of inlet tubing, column within MRI bore, and outlet tubing and view of column within bore ...	109
<b>Figure 4.10.</b> Orthogonal directions of x, y and z .....	110
<b>Figure 4.11.</b> Example of horizontal Z slice .....	111
<b>Figure 4.12.</b> Photo of the gravel filter column, schematic of the 8 horizontal slices for each flow scan obtained and resulting MRI image of once slice .....	112
<b>Figure 4.13.</b> Example of vertical slices in grayscale and colour .....	114
<b>Figure 4.14.</b> 3D visualization of useable ROI of experimental gravel filter .....	114
<b>Figure 4.15.</b> Middle slice of 3D scan thresholded in ImageJ. ....	115
<b>Figure 4.16.</b> Middle slice of a clean thresholded stack divided by 2 and middle slice of a biofilm thresholded stack divided by 4.....	116
<b>Figure 4.17.</b> Resulting image from adding Clean ÷ 2 with Bio ÷ 4.....	117
<b>Figure 4.18.</b> BioLightLong column after 6 months growth indicating phototrophic biofilm growth .....	120
<b>Figure 4.19.</b> Differentiating image between Clean and Bio scans.....	121
<b>Figure 4.20.</b> Example of local movement of grain and distinct area of green without blue compensation .....	122
<b>Figure 4.21.</b> Original high resolution images of slice 76 of BioLightLong, Clean, Bio and Bio subtracted from Clean .....	125
<b>Figure 4.22.</b> Photo of the right and left side of BioLightLong column after 6 months growth period. ....	126
<b>Figure 4.23</b> Slice 76 and Slice 135 of BLL, BDL, BLS and BDS .....	128
<b>Figure 4.24.</b> Illustration of concentric ROI of 0-1, 1-2, 2-3, 3-4 and 4-5 grain diameter .....	129
<b>Figure 4.25.</b> Localized ROI shown on slice 106 of BLL .....	131
<b>Figure 4.26.</b> Localized ROI throughout slices 94 - 112 of BLL.....	132
<b>Figure 4.27.</b> Bruker Paravision Cu transport experimental results.....	134
<b>Figure 4.28.</b> Photo of the BioDarkLong column after 6 months growth period.	140
<b>Figure 4.29.</b> Biofilm growth after 2 months, biofilm colonization after 6 months, orange colour of inoculated pond water after 6 months growth .....	141
<b>Figure 4.30.</b> Photo of BioLightShort compared to BioDarkLong after growth period showing colour change of the dolomite in BioDarkLong.....	141

<b>Figure 4.31.</b> Example of how image resolution effects porosity measurements during segmentation of water and gravel fractions. ....	144
<b>Figure 5.1.</b> Schematic showing mechanisms responsible for immobilization of contaminants by nZVI. ....	152
<b>Figure 5.2.</b> TEM image of the surface of Nanofer STAR. ....	155
<b>Figure 5.3.</b> Schematic of flow cell. ....	157
<b>Figure 5.4.</b> Experimental setup of sand filter columns. ....	158
<b>Figure 5.5.</b> Cu breakthrough curve in a single element solution .....	160
<b>Figure 5.6.</b> Pb breakthrough curve in a single element solution .....	161
<b>Figure 5.7.</b> Zn breakthrough curve in a single element solution .....	162
<b>Figure 5.8.</b> Cu breakthrough curve in a multi-element solution.....	163
<b>Figure 5.9.</b> Pb breakthrough curve in a multi-element solution.....	164
<b>Figure 5.10.</b> Zn breakthrough curve in a multi-element solution. ....	165
<b>Figure 5.11.</b> Summary of percentage of Cu, Pb and Zn removed within the sand columns for single metal .....	166
<b>Figure 5.12.</b> Summary of percentage of Cu, Pb and Zn removed within the sand columns for mixed systems .....	166
<b>Figure 5.13.</b> Maximum breakthrough concentration of Cu, Pb and Zn in single metal solutions .....	168
<b>Figure 5.14.</b> Maximum breakthrough concentration of Cu, Pb and Zn in multi-metal solutions .....	168
<b>Figure 5.15.</b> Percentage of enhanced Cu, Pb and Zn removal as compared to unamended sand.....	169
<b>Figure 5.16.</b> Percentage of enhanced Cu, Pb and Zn removal as compared to unamended sand.....	169
<b>Figure 5.17.</b> Impact of pH on dissolved copper speciation .....	172
<b>Figure 5.18.</b> Impact of pH on dissolved lead speciation .....	172
<b>Figure 5.19.</b> Impact of pH on dissolved zinc speciation .....	173
<b>Figure 5.20.</b> Schematic explaining different removal mechanisms involved between nZVI and different metal species. ....	176

## List of Tables

Table 1.1. Range of pollutant removal percentages for SuDS.....	5
Table 1.2. Typical diffuse pollutants found in runoff and their possible sources	7
Table 1.3. Typical metals found in runoff, prevalence throughout a monitoring program and possible sources of metal pollutants .....	8
Table 1.4. Summary of filter drain and trench performance.....	17
Table 1.5. Type B filter drain material grading and geometric requirements...	18
Table 2.1. Percentage removal of heavy metals by RMG and IOCG .....	35
Table 2.2. Percentage removal of heavy metals by RMG, UMG, SMG and MGD..	38
Table 2.3. Percentage removal of heavy metals by RMG, DG, RQG, GQG, MLG, and SG.....	41
Table 2.4. Gravel samples, pH range of solutions during batch experiments, saturation indices (SI) for metal hydroxides and dominant dissolved species....	44
Table 2.5. Summary of elements present within a section of UMG surface as determined by EDS analysis.....	50
Table 3.1. Experimental conditions of columns.....	65
Table 3.2. Percentage of metals retained within the columns between the Bio and Blank experiments..	70
Table 3.3. Advection diffusion model results for dispersal coefficient ( $D$ ), loss term ( $k$ ) in (mg/l)/h and goodness of fit (RMSE).....	74
Table 4.1. List of MRI experiments.....	104
Table 4.2. Summary of porosity of experimental columns as determined by ImageJ. ....	119
Table 4.3. Percentage area of pixel analysis illustrating differences between the Clean and Bio scans .....	123
Table 4.4. Percentage of pore space blockage by biofilm for Slices 76 versus 135 of each experiment .....	127
Table 4.5. Results of concentric ROI for BLL, BDL, BLS and BDS for % pore blockage by biofilm for the entire stack, slice 76 and slice 135 .....	130
Table 4.6 Calculated percentage of blockage by biofilm for localized ROI throughout slices 94 - 112 of BLL .....	132
Table 5.1. Summary of data for effluent water for preliminary nanoclay experiment..	155
Table 5.2. Porosity and total volume of pore space of each column. ....	157

<b>Table 5.3.</b> Percentage of Cu, Pb and Zn retained within the single and multiple metal experimental columns. ....	160
<b>Table 5.4.</b> PHREEQC results for single and multi-elemental solutions for five experimental columns. ....	171
<b>Table 5.5.</b> Possible removal mechanisms for Cu, Pb and Zn according to PHREEQC and standard electrode potentials ( $E^0$ ).....	177

## Acknowledgements

It is difficult to reflect and put into words the incredible experience this PhD has allowed me. From moving halfway across the world with my best friend, partner in crime and other half, Jay, and loyal doggy companion, Gunther, to finally submitting this hard fought thesis has been a wild and amazing journey that I can definitely say has changed me for the better and one that I will never forget.

Arriving in a city I had never been definitely had me second guessing our grand plan to live and study abroad; the bureaucratic system did not make it easy for an American in Scotland. But thanks to the incredible support system of friends and colleagues I trudged on through those first few trying weeks and was eventually able to settle in and enjoy Scottish life. This experience would not have been the same without the many friends to which I am fortunate to have found along the way. Most importantly, Elisa and Seb, who I am grateful to know, that even though we are now a continent away, will be lifelong friends for sure. Not only did Elisa navigate me through the ups and downs of PhD life, we share countless experiences as travel buddies, 'roomies' and nights on the Glaswegian town. I am also grateful to Graeme and Kirsten for all the fun times and for our vent sessions on our walks into Uni as well as Sarah and Martin for not only partaking in, but organizing all of the fun times and being there for me when times got tough. Also to Doug, Melanie and Ross for making this process a little more tolerable, I will sure miss our mornings at Artisan and evenings at the Basement and Rebecca and Dom on the Geochem side of things for making travel to conferences and South Africa so fun and memorable. Finally, to James for all of your assistance in this SuDS journey we took together and the good times as well (polish vodka?). While my wifey, Sarah is not a new friend, I must also thank her for her support, care packages and fun visits throughout this process. Thanks to all of our friends who doggy-sat and loved Gunther so much while also allowing us to fully experience and enjoy this European life: Elisa, Seb, James, Graeme, Kirsten, Ross and Jay.

This PhD would not have been possible without the encouragement, guidance and support of my supervisors. While my PhD turned out to be quite the whirlwind of supervision, I am grateful to Vernon Phoenix for stepping up from

‘Supervisor # 4’ to my primary supervisor. Thank you for having the faith in me and my research and joining me on the evolution of my PhD to an outcome I am proud of. I am also appreciative of Caetano Dorea for your friendship, guidance, assistance and one for the roads throughout and Heather Haynes for your help and sincere encouragement when I needed it most. Finally, thanks to Ian Pulford for your support in all things Chemistry.

In addition to my supervisors, I was incredibly fortunate to have the assistance of many extremely talented people with regards to experimental support. Thank you to Bill Sloan for assistance with, and creation of, the Matlab code. My MRI work would not be possible without Jim Mullen’s excellent assistance (no bubbles!) and William Holmes’ extensive knowledge. This is also true throughout my widespread network of multidisciplinary laboratories; thank you Michael Beglan for your immensely helpful assistance in the Chemistry lab, especially AAS analysis, Julie Russell and Anne McGarrity for your help in the Environmental Engineering Lab, especially with assembly of my clone library, all of the Engineering Technicians but in particular Timothy Montgomery for technical support, especially construction of the Perspex chambers, and Ian Scouller for transporting me to the MRI weekly, field support and friendly chats throughout, Peter Chung for SEM analysis and Abdulrahman Al Harthi for surface area analysis.

I am extremely appreciative of the Lord Kelvin Adam Smith Scholarship for funding this research and allowing me to disseminate the results at well regarded international conferences around the world.

Also, I am of course very grateful to my family, who have supported my every move, even this dream of studying in Scotland, which brought me exceptionally far from them for so many years. I will never forget driving up from London via Liverpool and arriving in Glasgow with my mom by my side and experiencing the first instances of Scottish life together, I don’t know if I would have made it through the first week without her love and assistance! Of course I am grateful to Bud (my dad) for your unfaltering encouragement and the optimistic outlook you have instilled in me. Also thanks to my sister Dionah, Grandma Jean, Grandpa Don, Grandpa Lyle and Sage (the dog) for your love and support. Finally, I am incredibly appreciative of John and Cathy for their support and

belief in us to make this dream a reality and for joining us on some incredible journeys along the way.

And last but certainly not least, I dedicate this thesis to the two that joined me on this crazy journey, Jay and Gunther. Your unfaltering love and support is truly what allowed me to make it through this PhD process. I would not be the person I am today without you and I could not imagine experiencing the most incredible journeys or spending my life with anyone else. We are so incredibly fortunate to have each other, lived in Scotland and to have travelled Europe together, I am so unbelievably excited to marry you and spend the rest of my life with your love, support and friendship. Gunther, you truly are man's best friend and thank you for enduring 12 hour flights across the Atlantic Ocean to be our loving, cuddling companion who is always able to cheer me up when I am down. Who knew a Newfie only needs to come halfway across the world to Scotland to figure out his innate love for the sea. You both make me incredibly happy, I am lucky to have you and I love you to pieces.

## Author's Declaration

I declare that no portion of the work in this thesis has been submitted in support of any application for any other degree or qualification of this or any other university or institute of learning. I also declare that the work presented in this thesis is entirely my own contribution unless otherwise stated.

Marnie Feder

## Definitions and Abbreviations

SuDS - Sustainable urban Drainage Systems

BMP - Best management practice

PAH's - Polycyclic aromatic hydrocarbons

EMC - Event mean concentration

AADT - Annual average daily traffic

SSF - Slow sand filtration

EPS - Extracellular polymeric substances

SEPA - Scottish Environment Protection Agency

CIRIA - Construction Industry Research and Information Association

MCHW - Manual of Contract Documents for Highway Works

DETR - Department of Environment, Transport and the Regions

BRE - Buildings Research Establishment

DMRB - Design Manual for Roads and Bridges

MRI - Magnetic resonance imaging

nZVI - nano zero valent iron

SEM - Scanning electron microscope

EDS - Energy-dispersive X-ray spectroscopy

DI - Deionized water

AAS - Atomic Absorption Spectroscopy

BET - Brunauer-Emmett-Teller

SI - Saturation indices

STP - Standard temperature and pressure

$D$  - Dispersion coefficient

$k$  - Loss term

RMSE - Root mean squared error

NMR - Nuclear magnetic resonance

$B_0$  - Applied magnetic field

$M$  - Net magnetization

$\omega$  - Larmor frequency

$\gamma$  - Magneticgyric ratio

RF - Radio frequency

$T_1$  - Longitudinal relaxation

$T_2$  - Transverse relaxation

PAR - Photosynthetically active radiation  
RARE - Rapid acquisition relaxation enhanced  
TE - Echo time  
TR - Repetition time  
ROI - Region of interest  
EPA - (US) Environmental Protection Agency  
BOD - Biochemical oxygen demand  
AMD - Acid mine drainage  
NTU - Nephelometric turbidity units  
E0 - Standard electrode potentials  
RMG - Rinsed microgabbro  
IOCG - Iron oxide coated gravel  
UMG - Unrinsed microgabbro  
SMG - Scrubbed microgabbro  
MGD - Microgabbro dust  
DG - Dolomite gravel  
GQG - Gray quartz gravel  
RQG - Rose quartz gravel  
SG - Sandstone gravel  
MLG - Mixed lithology gravel  
BLL - BioLightLong  
BDL - BioDarkLong  
BLS - BioLightShort  
BDS - BioDarkShort  
Sand - Unmodified sand  
1nZVI - 1% nZVI enhanced sand  
5nZVI - 5% nZVI enhanced sand  
10nZVI - 10% nZVI enhanced sand  
1nC - 1% nanoclay enhanced sand

# 1

## Introduction

### 1.1 Background

Urbanization and development have led to a loss of the earth's natural drainage routes and permeable surfaces while at the same time increasing contaminant load from surface water runoff. This contaminant laden runoff has the potential to be discharged into watercourses without suitable treatment and can have devastating effects on the ecosystem and human health. In order to meet environmental and social requirements, sustainable urban drainage systems (SuDS) are designed to reduce the effects of urban development to the environment through improvement of runoff water quality, and safe discharge.

While historically, surface water in urban areas could be managed with grey-infrastructure such as pipes, mechanical systems, and treatment plants, there is a need to move away from these complicated and deteriorating infrastructure systems and towards a more simple, environmentally friendly and sustainable solution (Scholz et al. 2006). SuDS, also referred to as best management practices (BMP's) in the United States and water sensitive urban design in Australia, are an easily manageable alternative and important means of controlling pollution close to point sources throughout the world.

SuDS are increasingly being used as a first defence for treatment of surface water runoff which can contain a variety of pollutants such as heavy metals, polycyclic aromatic hydrocarbons (PAH's), and organic or inorganic particulates (Seelsaen et al. 2006; Ichiki et al. 2008). Many types of SUDS are used such as detention ponds, filter drains or strips, permeable surfaces, and infiltration basins. Each of these systems is designed to remove harmful pollutants from the water runoff that enters them before it is released back to the environment. Without any such means in place, surface water runoff can carry pollutants to watercourses. While many types of SuDS exist, of particular interest are filter

drains; these are roadside trenches backfilled with gravel that play a dual role of filtering contaminants and attenuating road runoff volumes (Woods-Ballard et al. 2007).

Simple, low-cost technologies utilising filtration have been used to treat potable water and wastewater in developed and developing countries throughout the world. While it is known that these technologies are effective at removing certain pollutants, the mechanisms behind them tend to be poorly understood. This project aims to characterize the naturally-occurring geochemical and biogeochemical mechanisms involved in such treatment systems in order to optimise for pollutant removal, particularly heavy metals, within SuDS. Comprehensive research with regards to specific pollutant removal capacity of SuDS systems is lacking, which, unfortunately, reflects in design guidelines and is evidenced by a wide range of treatment capacities for pollutants reported (Woods-Ballard et al. 2007). Also, while much of the initial research into potable and wastewater treatment has been done with smaller particles of fine sand media, this research aims to provide some of the first novel research concerned with the fundamental mechanisms of larger coarse grained gravel media.

## **1.2 Sustainable urban drainage systems**

SuDS have become a logical progression towards simple, low-cost treatment of diffuse non-point pollution. The need for SuDS has become increasingly important as the detrimental effects of urbanization become clear. Specifically, loss of greenspace, habitat and natural infiltration routes results in increased surface water runoff that eventually leads to higher peak flow, erosion and flooding (Brezonik and Stadelmann 2002). This, combined with a build-up of pollutants on impermeable surfaces being washed and accumulating untreated into watercourses, has led to development of the SuDS philosophy, with the overall aim to design systems that mimic natural drainage before development. The premise of SuDS systems is three-fold: improve water quality, maximise amenity and biodiversity while providing attenuation capacity during high precipitation events (Woods-Ballard et al. 2007). While traditional drainage options may meet certain components of this philosophy, SuDS systems are designed to address all three functions as highlighted by the SuDS triangle (Fig. 1.1).

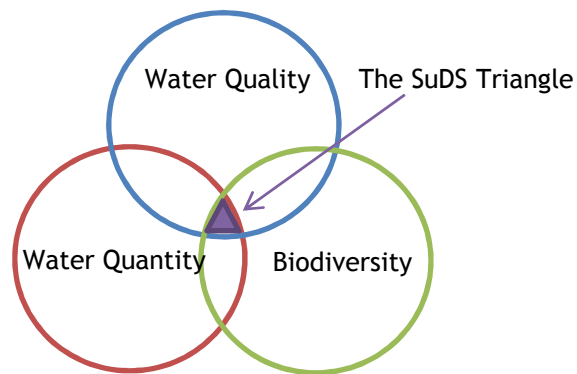


Figure 1.1. The SuDS triangle

### 1.2.1 Types of SuDS

Many types of SuDS exist and their use is dependent on location, taking into account scenarios of hydrological capacity and pollutant load expected. Comprehensive details of all types of SuDS can be found in the SuDS Manual (Woods-Ballard et al. 2007). The following is a list and description of typical SuDS in place throughout the UK.

- Filter strips - areas of grass or vegetation that treat runoff from adjacent impermeable surfaces.
- Swales - channels of grass or vegetation that allow for storage and conveyance of water and infiltration into the ground
- Infiltration basin - depression of land that stores runoff water and allows infiltration into the ground over time
- Ponds - basins that provide water quality treatment for a permanent source of water as well as providing temporary storage for excess runoff
- Detention basin - normally dry depression of land designed to provide water quality treatment for a for a specific volume of runoff water
- Constructed wetland - ponds with added wetland vegetation for enhanced pollutant removal and wildlife habitat
- Filter drains - trench filled with permeable material allowing for filtration, storage and conveyance of runoff from adjacent impermeable surfaces
- Infiltration device - designed to temporarily store runoff from a development and allow infiltration over time

- Porous pavement - surfaces that allow rainwater to infiltrate through to a storage layer for subsequent infiltration to the ground
- Sand filters - structure filled with sand that allows for treatment of surface water through filtration and temporary storage via surface ponding
- Bioretention - shallow landscaped areas with underdrainage and engineered soils and vegetation aimed towards enhancing pollutant removal and reducing runoff
- Green roofs - roofs with a cover of vegetation over a drainage layer

### 1.2.2. SuDS Performance

All types of SuDS benefit from a variety of pollutant removal mechanisms for improved water quality, though treatment capacity of the systems is not well defined. There are numerous reasons for this including limited field data available and over extended periods of time (Scholes et al. 2008), efficiency being highly dependent on design and location, and a lack of understanding of mechanisms at a fundamental level. Because of this, many removal efficiencies of target pollutants in SuDS systems are estimated and listed as simply high, medium or low (Clayton and Schuleler 1996). An example of the range of pollutant removal capacities of different types of SuDS design is shown in Table 1.1 as adapted from the U.S. EPA Handbook on Urban Runoff Pollution Prevention and Control Planning. This high level of uncertainty has led to the recommendation that several types of SuDS, or a ‘treatment train’, be utilized so that the level of redundancy in treatment assures removal over a series of SuDS (Pittner and Allerton 2009). While this philosophy may be effective, it is believed that a better understanding of removal mechanisms and thus removal capacities of SuDS systems can lead to better SuDS design.

SuDS Type	Typical Pollutant Removal (percent)				
	Suspended Solids	Nitrogen	Phosphorus	Pathogens	Metals
Detention Basin	30 - 65	15 - 45	15 - 45	< 30	15 - 45
Pond	50 - 80	30 - 65	30 - 65	< 30	50 - 80
Constructed Wetland	50 - 80	< 30	15 - 45	< 30	50 - 80
Infiltration Basin	50 - 80	50 - 80	50 - 80	65 - 100	50 - 80
Filter Drain	50 - 80	50 - 80	15 - 45	65 - 100	50 - 80
Porous Pavement	65 - 100	65 - 100	30 - 65	65 - 100	65 - 100
Swales	30 - 65	15 - 45	15 - 45	< 30	15 - 45
Filter Strips	50 - 80	50 - 80	50 - 80	< 30	30 - 65
Sand Filter	50 - 80	< 30	50 - 80	< 30	50 - 80
Other Media Filter	65 - 100	15 - 45	< 30	< 30	50 - 80

**Table 1.1.** Range of pollutant removal percentages for SuDS US EPA (1993)

For the sake of this research, focus will be narrowed to filtration based filter drains (Fig 1.2) in order to examine pollutant removal mechanisms typically associated with low-cost potable water treatment systems for SuDS applications. Filter drains are trenches filled with gravel filter media intended to store and treat runoff from the adjacent roadway. Critical to road runoff is the drains potential to filter and treat vehicular pollutants including suspended solids, polycyclic aromatic hydrocarbons (PAHs), and an array of heavy metals (Ward 1990; Liu et al. 2001; Liu et al. 2005; Seelsaen et al. 2006; Genc-Fuhrman et al. 2007; Gan et al. 2008) at concentrations above regulatory limit. Thus, in the United Kingdom, treatment via SuDS is mandatory prior to discharge into nearby watercourses. It is therefore not surprising that filter drains are increasingly being fitted for urban drainage schemes, highlighting their widespread use even though an understanding of pollutant treatment mechanisms and performance is limited.

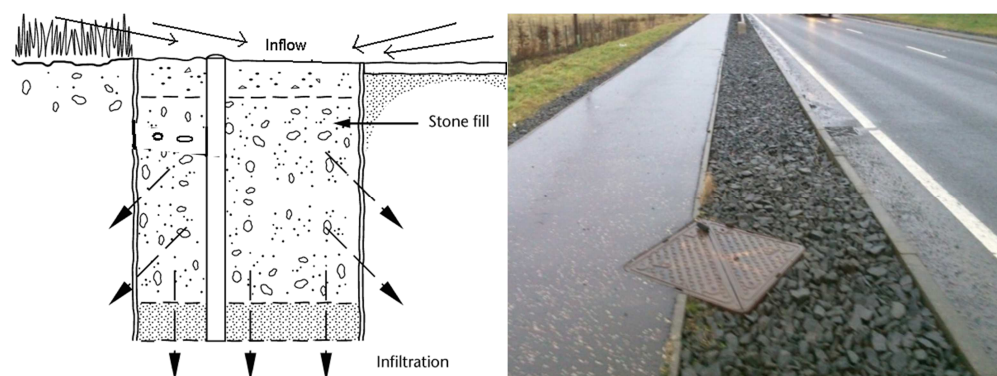


**Figure 1.2.** Schematic of a filter drain (Netregs.org.uk) and photo of a filter drain

Pratt (2004) summarized the initial research into filter drain function which highlighted that Perry and McIntyre (1986) determined a working filter drain parallel to the M1 motorway significantly reduced effluent pollutant concentrations when compared to untreated runoff but efficiency varied between storm events and seasons. Subsequent research by Sansalone (1999) was carried out to compare performance of bench-scale experiments to a field partial exfiltration trench which combines porous pavement and porous media in a filter drain. While it was demonstrated that the trench could be used as an effective trap for suspended solids, breakthrough of particulate-bound heavy metals was found to be a controlling factor in design life. The SuDS Manual (Woods-Ballard et al., 2007) lists the pollution removal of filter drains as high for heavy metals and suspended solids and low to medium for nutrients. As with most published research on filter based SuDS, they are listed as a promising pollutant removal system, especially for particulate pollutants (Clayton and Schuleler 1996) though most research highlights a that a high clogging potential and poor maintenance are the main disadvantages of filter based SuDS systems (Jefferies 2004). While the clogging potential will influence the lifespan of filter drains, Hatt et al. (2007) demonstrated that the treatment capacity of gravel filter media for stormwater treatment remains high up until the point of clogging, and that a 0.5m depth can be effective for treating suspended solids and heavy metals, but not effective in treating nutrients, corroborating with the SuDS manual. While previous SuDS studies have demonstrated effective treatment of metals, the specific geochemical removal mechanisms and effect of lithology and biofilm growth has not yet been addressed.

### **1.3 Runoff and heavy metal pollution**

Surface water runoff is considered diffuse pollution in that an assortment of contaminants arise from many different sources of land-use activity and are dispersed across a catchment rather than being from specific effluent discharge points (Campbell et al. 2004). Sources of diffuse runoff pollution generally include deterioration of the built environment in combination with transportation processes of combustion and wear and tear of vehicles as well as inappropriate waste disposal. Table 1.2 summarizes typical diffuse pollutants and their possible sources (Duncan 1999; Gan et al. 2008), though the list of

potential chemicals and compounds in diffuse runoff from industry, agriculture, construction and the built environment is endless.

<b>Diffuse Pollutants</b>	<b>Possible Sources</b>
<b>Heavy metals</b> - Br, Cd, Ce, Co, Cr, Cu, Mn, Mo, Ni, V, Zn	General urban runoff Vehicle wear and tear
<b>Polycyclic aromatic hydrocarbons (PAH's)</b> - Oil - Grease	Traffic emissions Disposal or spills Vehicle maintenance
<b>Nutrients and organic wastes</b> - Nitrogen - Phosphorous	Agricultural fertilizers/waste Traffic emissions Detergents
<b>Suspended solids</b>	Construction Road surface wear Erosion Street gritting
<b>Microorganisms</b>	Surfaces, soil Sewage overflow Wildlife/pet faecal matter
<b>Various toxic compounds and chemicals</b> - Solvents - Pesticides	Road salting Industrial wastes/cleaning Weed and agricultural control

**Table 1.2.** Typical diffuse pollutants found in runoff and their possible sources

Of the possible pollutants found in road runoff, heavy metals tend to be of most concern due to their prevalence and persistence in the environment coupled with a highly toxic nature (Bergbäck et al. 2001). Metals have the potential to come from many sources, but the most common metal pollutants arise from vehicle maintenance, wear and tear. Table 1.3 summarizes the possible metals typically found in road runoff, the frequency of some metals detected throughout a national US urban runoff monitoring programme (Cole et al. 1984) and the possible sources of metals due to vehicular transportation purposes (Ward 1990).

Metal	Prevalence (%)	Possible Metal Source			
		Wear of tires and brakes	Corrosion of welded metal plating	Combustion of lubricating oils	Signs and barriers
Cadmium (Cd)	55	X		X	
Cerium (Ce)			X		
Chromium (Cr)	57		X		
Copper (Cu)	96	X		X	
Iron (Fe)			X		X
Lead (Pb)	96	X	X	X	X
Manganese (Mn)		X			
Molybdenum (Mo)				X	
Nickel (Ni)	48		X		
Vanadium (V)			X	X	
Zinc (Zn)	95	X		X	

**Table 1.3.** Typical metals found in runoff, prevalence throughout a monitoring program (Cole et al. 1984) and possible sources of metal pollutants (Ward 1990)

Since metals can pose a threat to the ecosystem and are a major concern in road runoff, the current research will focus on removal of heavy metals in gravel based filter drains. Not only are heavy metals a key contributor to road runoff in dissolved form, but also as particulate-bound metals which are commonly attached to suspended solids, also prevalent in road runoff (Lau and Stenstrom 2005). While the different forms of metals may be removed within a filter drain by varying processes, e.g. settling or filtering of particulates versus adsorption of dissolved metals to filter media, Sansalone (1999) found similar removal efficiencies in a field filter drain and porous pavement system with dissolved Cu > 85%, versus particulate-bound Cu 85-95%, dissolved Pb 70-95%, versus particulate-bound Pb 85-95% and dissolved Zn > 95% versus particulate-bound Zn 75-95% (Pratt 2004). A literature review of metal concentrations found in runoff studies and monitoring programs can be found in Appendix A.

Generally, pollutant concentrations of road runoff are expressed as event mean concentration (EMC), though, a precise technique for assessment of pollutant concentrations is difficult and can vary widely between researchers and areas. The difficulty in measuring precise pollutant concentrations of runoff is due to a variety of reasons, most importantly, build-up and deposition of pollutants and sediments during dry periods that are then available for wash-off during rainfall events. This leads to whether to assess pollutants via the controversial phenomenon of the ‘first flush of storm runoff’ versus the concept of EMC.

The EMC is meant to represent the entire runoff event by weighting the average flow concentration throughout and is defined by Sansalone and Buchberger (1997) as total pollutant load divided by total volume of the runoff event for a specified duration. While the EMC is calculated for the whole runoff event, in essence, the first flush implies that a disproportionate concentration of pollutants are seen in the first portion of a runoff event in comparison to the remainder of the event (Schueler 1987). Theoretically this concept makes sense, though confirmation of a first flush and its significance in SuDS design is heavily debated by researchers in that some have found evidence supporting the first flush (Stenstrom and Kayhanian 2005), while others have not (Saget et al. 1996). This may be due to variances and interpretations of the definition of a first flush, as well the possibility that specific pollutants demonstrate a first flush, while others do not. In general, the first flush is assessed by the curve of the cumulative pollutant mass versus the cumulative runoff volume. Researchers then utilize the curves to describe various arbitrary definitions of when a first flush occurs, ranging between 70-80% of the total pollutant mass transported in the first 20-30% runoff volume (Deletic 1998).

Overall, concentrations of pollutants in runoff vary widely between areas, researchers and studies and can be difficult to compare for many reasons including: sample collection methods (including assessment and differing definitions of EMC versus first flush) or time of collection, traffic patterns, land use, geology of surrounding land, and/or street cleaning practices (which have the ability to remove suspended solids to which metals are sorbed) varying between different areas. There are numerous studies aiming to characterize road runoff and impact on water quality (e.g. Cole et al. (1984); Bruen et al. (2006); Kayhanian et al. (2012)) and determine any correlation between the above factors, with some select findings highlighted in the following paragraphs.

After a long-term study of water quality measurements of storm runoff, Deletic and Maksimovic (1998) reported that antecedent dry period had little effect on suspended solids, but that rainfall intensity and overland flow rate influence the suspended solids loading rate and that a first flush of suspended solids was only observed in a limited number of events. Deletic (1998) elaborates that a slight first flush effect can be seen for conductivity whereas no first flush was recorded for pH or temperature. Mangani et al. (2005) evaluated the first flush

of pollutants in stormwater from a highway in Italy and noted that variability is mostly due to site characteristics and rainfall patterns and with regards to heavy metals, Zn tends to be the most abundant while Pb is always present at low concentrations. Interestingly, Sansalone and Buchberger (1995) found a poor correlation between suspended solids and metals for rainfall runoff events but a positive correlation between suspended solids and metals for snow washoff events.

Hjortenkrans et al. (2006) aimed to determine patterns of specific automobile heavy metals compared with specific surrounding factors of traffic such as vehicle speed, road layout, and traffic density around 18 sites in Sweden. It was concluded that Cu and Sb, while relatively new in automobile use in brake linings, are the most important heavy metals for road runoff concern in the future given the 10 fold elevated concentrations in roadside soils. Since it has been observed that traffic patterns can influence heavy metal concentrations in road runoff, Drapper et al. (2000) reported that pollutant concentrations from 21 sites in Southeast Queensland were in similar ranges with other international studies, but that the concentrations would not have been in compliance with the 30,000 daily traffic limit results reported in the United States. It was further reported that traffic volume was not the best indicator of runoff pollutant concentrations, but rather traffic patterns (areas incorporating exit lanes reported higher pollutant concentrations) and interevent duration significantly influenced pollutant concentrations. Thus, rainfall and traffic patterns are important aspects to runoff pollution concentrations and a daily limit cut off may not always hold true for different areas. After a four year pollutant monitoring program, Kayhanian et al. (2003) found no direct correlation between highway pollutant EMC's and annual average daily traffic (AADT), though AADT was determined to have an influence on pollutant concentrations when in conjunction with certain watershed factors such as pollutant build up and wash off. Further runoff characterization was reported in Kayhanian et al. (2007) which determined runoff pollutant EMC's were higher in urban areas than non-urban areas and that the EMC's were influenced by event rainfall, cumulative seasonal rainfall, antecedent dry period, drainage area, AADT, land use and geographic regions.

## 1.4 Filtration

Gravel filtration is a simple and low-cost technology used in numerous applications such as potable water and wastewater treatment (Dorea et al. 2004). A straightforward process allowing contaminated water to flow through filter media has shown an improvement in overall quality of effluent water (Dorea et al. 2004). The ease of use and known ability to remove particulates and contaminants makes this type of treatment an ideal choice as a first defence against contaminants in road runoff. Thus, media filtration in stormwater treatment is increasingly being used as a best management practice.

Filter drains rely on basic principles of filtration that are equivalent to slow sand filtration and horizontal gravel (roughing) filters widely-used for potable and wastewater treatment in both developed and developing countries e.g. Dorea (2004). Extensive literature on slow sand filtration and subsequently gravel filtration for potable and wastewater treatment is available with many focussed on operation and underpinning specific and complex biological (Weber-Shirk and Dick 1997a) and/or physical-chemical processes (Weber-Shirk and Dick 1997b) involved in the systems. The following processes are summarized to be the most important in slow sand filtration systems (Huisman and Wood 1974) and are therefore inferred to be important in filtration based SuDS.

### Biological:

- Straining and attachment to extracellular polymeric substances (EPS) and breaking down of organics by the *schmutzdecke*, a thin layer of biological material that forms at the top of the system
- A biological coating of rotifers and protozoa that has formed feeds and grazes on impurities

### Physical-chemical:

- Straining and settling of particles occurs throughout the sand media and trapped sediments
- Chemical reactions of adsorption, mass attraction and electrostatic forces bind particles to the sand grains

While sand filtration is an effective treatment step in conventional systems, the addition of gravel pre-treatment has been researched to help improve overall

water quality for potable and wastewater treatment. Adapting from the highly effective filtration through a sand media, the same principle is used with larger gravel in order to remove larger particle contaminants. While there are different layouts to a gravel pre-treatment system, horizontal flow gravel filters for treating potable water and wastewater (Fig 1.3) are of particular interest due to the similarity with SuDS filter drains. Horizontal gravel filters are usually designed with three compartments filled with three different sizes of gravel from coarse to fine (Ochieng et al. 2004). It is thought that the primary removal force for particles is sedimentation, though many other mechanisms are possible for removal of pollutants as discussed in Section 1.5 (Boller 1993).

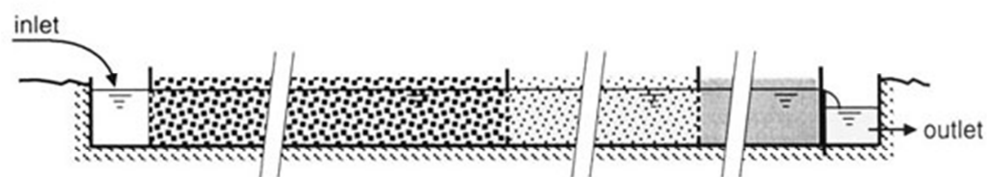


**Figure 1.3.** Schematic of a horizontal gravel filter for potable and wastewater treatment (Wegelin 1996)

While filtration has been utilized in water treatment for over a century (Urbonas 1999) and a large volume of literature exists for its use in potable and wastewater treatment, little research exists for filtration use in urban drainage of road runoff. While the processes are inferred to be similar between the two and water treatment based filtration offers a starting point for overall filtration theory, the main difference between filters for potable water treatment and filtration based SuDS are the operating regime and the pollutants to be treated. While potable and wastewater treatment filters operate under a constant influent flow and are primarily focussed at removing pathogens, SuDS filter drains operate in highly irregular flow conditions and are inundated with a wide range of pollutants of different particle sizes and chemical attributes. Hence, there is a need for research on filtration mechanisms specific to SuDS systems.

## 1.5 Geochemical and Biogeochemical removal mechanisms

All SuDS address water quality improvement through a combination of pollutant removal mechanisms including (Scholes et al. 2008):

- 
- Settling
  - Filtration
  - Volatilization
  - Adsorption
  - Flocculation
  - Precipitation
  - Ion exchange
  - Photolysis
  - Plant and algal uptake
  - Microbial degradation

Passive filter drain systems most importantly rely on fundamental hydraulic, geochemical and biochemical processes, including sedimentation of particulates, adsorption and precipitation, and biological assimilation for the remediation of pollutants (Huisman and Wood 1974). However, in all systems the actual (bio)geochemical processes are inherently complex; multiple removal mechanisms occur simultaneously and are specific to the pollution type and loading experienced. Moreover, much of what we assume occurs in a SuD systems is based on our knowledge of other filtration systems (such as potable and wastewater), rather than a detailed study of SuDS. Thus, for SuDS filters, our understanding of the underpinning processes and their relative importance remains poor, potentially leading to inefficient operation due to non-optimal design. In general, the succeeding paragraphs summarize the mechanisms believed to be the most important in filtration based SuDS.

Physical-chemical removal of pollutants is thought to occur in two steps. First, physical transportation mechanisms bring particles and dissolved contaminants in contact with filter media for possible subsequent removal from solution. These physical forces include (Huisman and Wood 1974):

- Straining or screening - acts to intercept and retain large particles within pores of the media, mostly at the surface
- Sedimentation - the act of particles settling on and in between the media
- Inertial and centrifugal forces - a force of gravity from a larger particle that acts to pull a particle from the water flow

- Diffusion - the act that brings particles and dissolved phases into contact with the media

Once transport mechanisms bring pollutants in contact with the filter media, the following attachment mechanisms hold particles and dissolved phases to the surface and can be regarded under the general term of adsorption (Huisman and Wood 1974):

- Electrostatic attraction - attraction between two opposite electrical charges, mainly an attraction force holding particles and dissolved phases to the surface of the media but can also contribute to transportation mechanisms
- Van der Waals forces - weak mass attraction that draws particles and dissolved phases from water and holds to media surface, more effective as an attraction mechanism but can also contribute to transport mechanisms
- Adhesion - deposition and adherence of particles and pollutants to sticky gelatinous film of biological growth (*schmutzdecke* in slow sand filtration, biofilm in other aqueous environments such as a filter drain)

Victor Goldschmidt first put forth the concept of metal adsorption to mineral surfaces in the 1930's when lower than expected heavy metals were observed in seawater and experimentation showed uptake by iron and manganese oxides (Bradl 2005). Many geochemical factors influence the adsorption of heavy metals onto mineral surfaces, most importantly, pH, ionic strength, metal speciation and competition.

Another potential mechanism of heavy metal removal that may occur in filter drains is precipitation. Precipitation occurs in aqueous systems when a change in geochemical conditions occur which cause the aqueous system to become supersaturated with respect to an insoluble solid phase, often in the form of hydroxides (the most common form for precipitated metals at low temperature), chlorides, sulfates, carbonates or sulfides (Bradl 2005; Kurniawan et al. 2006). Supersaturation is commonly reached by a shift in pH, Eh or an increase in concentration of dissolved constituents. Precipitation is generally considered an irreversible process

Other possible immobilization mechanisms within runoff include metals undergoing complexation with natural organics such as humic and fulvic acid, or synthetic agents such as EDTA, and is possible in SuDS filter drains due to the natural occurrence of dissolved organics ubiquitous to aquatic systems and pollutants in runoff (Schlesinger 1979).

Finally, due to the typically hydrated environment that filtration based SuDS offer, it is possible that biological growth in the form of biofilms may occur and thus contribute to metal removal. The role of biofilms in pollutant removal by SuDS has yet to be examined in detail. However, based on other non-SuDS based examination of bacteria-metal interactions, possible biological mechanisms for metal removal in a filter drain include:

- Adsorption and adhesion to cell surfaces and extracellular polymeric substances (EPS) (Beveridge and Murray 1980; Mittelman and Geesey 1985; Mullen et al. 1989; Fein et al. 1997; De Philippis et al. 2001; Konhauser 2007)
- Active internalization of metals for cell function (Konhauser 2007)
- Accumulation in naturally occurring biofilms (Meylan et al. 2003; Serra et al. 2009; Ancion et al. 2010)

## 1.6 Regulation and guidelines

Overall, SuDS are regulated through the following legislation in Scotland:

- **Water Framework Directive 2001** - European Union directive requiring member states to obtain good ecological and chemical status for ground and surface water within the EU by 2015. While SuDS are not mentioned specifically, they may be considered towards achieving this goal.
- **Water Environment and Water Services Act (Scotland) 2003** - Transposes the Water Framework Directive into Scottish legislation while also amending the Sewerage (Scotland) Act 1968. The first legislation mentioning SuDS as a drainage system, giving Scottish Water responsibility for public SuDS (not including SuDS limited to road drainage) and legally protecting public SuDS.

- **Water Environment (Controlled Activities) (Scotland) Regulations 2011** - The main legislation that regulates surface water discharge in Scotland and makes treatment of surface water through SuDS a legal requirement for all new developments (except for single dwellings or where discharge is direct to coastal water) for the first time.
- **Flood Risk Management (Scotland) Act 2009** - Requires local authorities and governing bodies to assess and reduce flood risk through sustainable flood risk management.

Typically, the Scottish Environmental Protection Agency (SEPA) is instrumental in implementation of the Water Framework Directive through reviewing applications, issuing licenses and ensuring compliance. Though, when it comes to SuDS specifically, design and construction is based on a series of guidelines and is left to the responsibility of the local authorities.

The main design guidance in Scotland for all types of SuDS can be found in The SuDS Manual (CIRIA Manual C697 - Woods-Ballard et al. (2007)) which provides overall best management practice for all aspects of SuDS implementation including planning, selection, siting, design, specifications, construction, maintenance and operation. Specific filter drain design and specifications can be found in Chapter 9 on Trenches (pages 239-249) where the following Table (1.4) summarizing the advantages versus disadvantages as well as performance, cost and maintenance implications can be found.

<b>ADVANTAGES</b>	<b>PERFORMANCE</b>
▪ Significant reduction of runoff rates and volumes	Peak flow reduction: Medium
▪ Important hydraulic benefits achieved	Volume reduction: Low
▪ Significant reduction in pollutant load discharged to receiving watercourse	Water quality treatment: High
▪ Incorporated easily into landscaping and besides roads	Amenity potential: Low
	Ecology potential: Low
<b>DISADVANTAGES</b>	<b>TREATMENT TRAIN SUITABILITY</b>
▪ High clogging potential without effective pre-treatment	Residential: Yes
▪ Build-up of pollution and blockages difficult to ascertain	Commercial/Industrial: Yes
▪ High historic failure due to poor maintenance or high debris input	High density: Yes
▪ High cost to replace filter material when blockages occur	Retrofit: Yes
▪ Limited to small catchments	Contaminated sites or above vulnerable groundwater: Yes
<b>KEY MAINTENANCE REQUIREMENTS</b>	<b>COST IMPLICATIONS</b>
▪ Regular inspection for signs of clogging	Land-take: Low
▪ Removal of sediment from pre-treatment	Capital Cost: Low/Medium
▪ Removal and cleaning or replacement of stone	Maintenance burden: Medium
	<b>POLLUTANT REMOVAL</b>
	Total suspended solids: High
	Nutrients: Low/Medium
	Heavy metals: High

**Table 1.4.** Summary of filter drain and trench performance taken from the SuDS Manual (Woods-Ballard et al. 2007)

Important design specifications for filter drains from the SuDS manual include:

- Excavated trench should be between 1-2 m deep filled with stone aggregate
- Filter drains must be designed in combination with a pre-treatment SuDS such as a detention basin, sediment trap, vegetated filter strip, swale or channel in order to alleviate sediment and fine silt build-up, clogging and eventual failure
- Filter drains should be incorporated within a treatment train of other SuDS for effective conveyance of flows from high storm events
- Perforated pipe can be utilized to distribute inflow or collect outflow and maximize attenuation while geotextile may be used to provide pre-treatment and prevent soil erosion
- Best sited adjacent to impervious surfaces such as roads and car parks
- Contact time of runoff to aggregate and void ratio should be maximized for effective pollutant removal and storage

- Aggregate is specified as granular 40 - 60mm graded stone/rock to be locally sourced if possible. Further specifications for grading and geometrical requirements of aggregate are found in the Manual of Contract Documents for Highway Works (MCHW) Volume 1: Specification for Highway Works Series 500: Drainage and Service Ducts (2009) specifying Type B gravel be utilized as follows (Table 1.5):

Type B Filter Drain Material:		Sieve size, mm	Percentage of mass passing
Standard	BS EN 13242	80	100
Size, mm	20/40	63	98-100
Grading and oversize categories	$G_c80-20$	40	80-99
Category for tolerances at mid-size sieves	$GT_{NR}$ (no requirement)	20	0-20
Category for maximum fines	$GT_{NR}$ (no requirement)	10	0-5

**Table 1.5.** Type B filter drain material grading and geometric requirements as established in MCHW Volume 1 Series 500 (2009) document. The left hand column shows descriptive requirements, while the right hand column the recommended grain size distribution for the gravel.  $G_c80-20$  = coarse graded aggregate with minimum 80% to pass upper limiting sieve size and maximum 20% to pass the lower limiting sieve size.

- Construction and implementation of filter drains should abide by the following:
  - Infiltration drainage - manual of good practice (Report R156) CIRIA, London (Bettess 1996)
  - Construction (Design and Management) Regulations Department of Environment, Transport and the Regions (DETR) (1994)
  - Buildings Research Establishment (BRE) Digest 365: Soakaway Design (1991)
  - Design Manual for Roads and Bridges (DMRB) and the Manual of Contract Documents for Highway Works (MCHW) provide the official standards for design of UK trunk roads including filter drains
- Maintenance required includes:
  - Regular - monthly or annually to remove litter, debris, roots, weeds
  - Occasional - half-yearly removal of sediment and for high pollutant load areas wash filter media and geotextile (if present) every 5 years
  - Remedial - clear blockages, rehabilitate filtration surface, clean and replace filter media if clogging is apparent, excavate trench walls if infiltration falters, inspect for overall clogging, blockages and damage as necessary

- Plans and schedules for maintenance should be developed during the design phase
- Waste sediment and spent filter material from residential or standard road applications is generally not hazardous and can typically be disposed of in landfills, though protocols should be confirmed through consultation with an environmental regulator. While waste sediments and filter media from industrial runoff purposes must be tested for appropriate disposal.

## 1.7 Thesis Overview

### 1.7.1 Aims

It is hypothesized that determining geochemical and biogeochemical mechanisms responsible for pollutant removal, and in particular heavy metals, can be utilized towards more efficient design of filtration based SuDS in the long term. This is increasingly important with SuDS being required by law in Scotland for all new developments, yet, design criteria is based upon removal mechanisms that are still poorly understood and specific removal rates typically estimated and not based on scientific evidence.

With this in mind, the following are the main aims of the research:

1. Determine if a chemical coating to gravel filter media has the ability to enhance heavy metal immobilization of SuDS filter drains through addition of a natural mineral amendment, specifically, an iron oxide coating
2. Analyze the recommendation in the SuDS manual (Woods-Ballard et al. 2007) that any locally sourced gravel is sufficient. This recommendation assumes that all lithologies will perform the same. This work will therefore test whether different lithologies of filter drain gravel effect rates and overall heavy metal immobilization as well as determining geochemical mechanisms involved
3. Assess if biological growth on gravel media in experimental flow cells has any effect on the heavy metal immobilization. Assess biological community structure of biofilms as well as influence of gravel lithology on microbial community structure.

4. Gauge the suitability of magnetic resonance imaging (MRI) to image biofilm growth in experimental gravel flow cells and evaluate whether growth has any effect on heavy metal transport through MR imaging of Cu tracer flow experiments

5. Utilize nanoparticle technology to further enhance heavy metal removal by mixing stable nano zero-valent iron (nZVI) powder with sand for use in filtration based SuDS sand filters

With an overall objective of pinpointing and harnessing the most relevant (bio)geochemical pollutant removal mechanisms in filtration based SuDS and utilizing this for better informed and scientifically backed design criteria to reduce non-point sources of pollution and their adverse effects on the water environment.

## 1.7.2 Thesis Outline

Four experimental chapters follow as:

Chapter 2 investigates heavy metal removal capacity of uncoated microgabbro gravel (utilized by local filter drain contractors) against a further five lithologies of gravel as well as gravel amended with an iron oxide coating. Determination of specific removal mechanisms involved including adsorption and precipitation are investigated through geochemical modelling in the PHREEQC program. Scanning electron microscopy (SEM) is utilized to determine specific rock forming minerals and subsequent weathering minerals responsible for adsorption of metals onto the microgabbro gravel.

Chapter 3 explores the influence of biological community growth on heavy metal removal in a laboratory SuDS system. Biofilms from filter drain gravels were inoculation into experimental flow chambers for use in heavy metal breakthrough experiments. Heavy metal breakthrough curves were collected and analyzed with an advection diffusion model. Bacterial communities were evaluated through clone library analysis to assess influence of lithology on community structure.

Chapter 4 describes the work undertaken to research a method of imaging inside an experimental gravel filter with magnetic resonance imaging (MRI). Gravel filter flow chambers were allowed to colonize with biofilm for subsequent imaging to determine if biofilm grown over gravel could be imaged with MRI. Cu flow experiments were also performed to image transport of a tracer through a gravel filter flow cell with and without biofilm growth.

Chapter 5 examines the possibility of utilizing nano zero-valent iron (nZVI) for enhanced heavy metal removal in sand filter SuDS. Sand was amended with different concentrations of nZVI and the impact of this amendment on heavy metal removal was examined. Metal removal mechanisms were investigated through PHREEQC geochemical modelling and standard electron potential analysis.

Chapter 6 summarizes the conclusions and recommendations for future research and direction.

## 1.8 REFERENCES

- Highways Agency. Design Manual for Roads and Bridges.
- Highways Agency. Manual of Contract Documents for Highway Works.
- Buildings Research Establishment. Soakaway Design. (1991)
- U. S. EPA. Handbook: Urban Runoff Pollution Prevention and Control Planning. (1993)
- Department of the Environment, Transport and the Regions. The Construction (Design and Management) Regulations (1994)
- Manual of Contract Documents for Highway Works. Volume 1: Specification for Highway Works. Series 500: Drainage and Service Ducts (2009)
- Filter Strips and Filter Drains. Retrieved 1 April 2010, from <http://www.netregs.gov.uk/netregs/102069.aspx>.
- Ancion, P. Y., et al. (2010). "Three common metal contaminants of urban runoff (Zn, Cu & Pb) accumulate in freshwater biofilm and modify embedded bacterial communities." Environmental Pollution **158**(8): 2738-2745.
- Bergbäck, B., et al. (2001). "Urban metal flows - A case study of Stockholm." Water, Air, and Soil Pollution **1**: 3-24.
- CIRIA. Infiltration Drainage - Manual of Good Practice. (1996)
- Beveridge, T. J. and R. G. E. Murray (1980). "Sites of metal-deposition in the cell-wall of *Bacillus subtilis*." Journal of Bacteriology **141**(2): 876-887.

- Boller, M. (1993). "Filter mechanisms in roughing filters." Aqua (Oxford) **42**(3): 174-185.
- Bradl, H. B. (2005). Heavy Metals in the Environment: Origin, Interaction and Remediation. Neubrucke, Germany, Elsevier Academic Press.
- Brezonik, P. L. and T. H. Stadelmann (2002). "Analysis and predictive models of stormwater runoff volumes, loads, and pollutant concentrations from watersheds in the Twin Cities metropolitan area, Minnesota, USA." Water Research **36**(7): 1743-1757.
- Bruen, M., et al. (2006). Impact assessment of highway drainage on surface water quality. **2000-MS-13-M2**.
- Campbell, N., et al. (2004). Diffuse Pollution: An Introduction to the Problems and Solutions. London, U.K., IWA Publishing.
- Claytor, R. A. and T. R. Schuleler (1996). Design of Stormwater Filtering Systems. Ellicott City, MD, The Center for Watershed Protection: 1-220.
- Cole, R. H., et al. (1984). "Preliminary findings of the priority pollutant monitoring project of the nationwide-urban-runoff-program." Journal Water Pollution Control Federation **56**(7): 898-908.
- De Philippis, R., et al. (2001). "Exopolysaccharide-producing cyanobacteria and their possible exploitation: A review." Journal of Applied Phycology **13**(4): 293-299.
- Deletic, A. (1998). "The first flush load of urban surface runoff." Water Research **32**(8): 2462-2470.
- Deletic, A. B. and C. T. Maksimovic (1998). "Evaluation of water quality factors in storm runoff from paved areas." Journal of Environmental Engineering-Asce **124**(9): 869-879.
- Dorea, C. C., et al. (2004). "Performance of a rural multi-stage filtration plant after its handover." Water Policy **6**(6): 559-570.
- Drapper, D., et al. (2000). "Pollutant concentrations in road runoff: Southeast Queensland case study." Journal of Environmental Engineering-Asce **126**(4): 313-320.
- Duncan, H. P. (1999). Urban stormwater quality: A statistical overview, Cooperative Research Centre for Catchment Hydrology: 1-134.
- Fein, J. B., et al. (1997). "A chemical equilibrium model for metal adsorption onto bacterial surfaces." Geochimica Et Cosmochimica Acta **61**(16): 3319-3328.
- Gan, H. Y., et al. (2008). "Quality characterization and impact assessment of highway runoff in urban and rural area of Guangzhou, China." Environmental Monitoring and Assessment **140**(1-3): 147-159.
- Genc-Fuhrman, H., et al. (2007). "Simultaneous removal of As, Cd, Cr, Cu, Ni and Zn from stormwater: Experimental comparison of 11 different sorbents." Water Research **41**(3): 591-602.
- Hatt, B. E., et al. (2007). "Treatment performance of gravel filter media: Implications for design and application of stormwater infiltration systems." Water Research **41**(12): 2513-2524.

- Hjortenkrans, D., et al. (2006). "New metal emission patterns in road traffic environments." Environmental Monitoring and Assessment **117**(1-3): 85-98.
- Huisman, L. and W. E. Wood (1974). Slow Sand Filtration. Geneva, Switzerland, WHO.
- Ichiki, A., et al. (2008). "Runoff characteristics of highway pollutants based on a long-term survey through a year." Water Science and Technology **57**(11): 1769-1776.
- Jefferies, C. (2004). SUDS in Scotland - The Monitoring Programme, SNIFFER: 1-92.
- Kayhanian, M., et al. (2012). "Review of highway runoff characteristics: Comparative analysis and universal implications." Water Research **46**(20): 6609-6624.
- Kayhanian, M., et al. (2003). "Impact of annual average daily traffic on highway runoff pollutant concentrations." Journal of Environmental Engineering-Asce **129**(11): 975-990.
- Kayhanian, M., et al. (2007). "Characterization and prediction of highway runoff constituent event mean concentration." Journal of Environmental Management **85**(2): 279-295.
- Konhauser, K. (2007). Introduction to Geomicrobiology. Oxford, UK, Blackwell Publishing.
- Kurniawan, T. A., et al. (2006). "Physico-chemical treatment techniques for wastewater laden with heavy metals." Chemical Engineering Journal **118**(1-2): 83-98.
- Lau, S. L. and M. K. Stenstrom (2005). "Metals and PAHs adsorbed to street particles." Water Research **39**(17): 4083-4092.
- Liu, D. F., et al. (2005). "Comparison of sorptive filter media for treatment of metals in runoff." Journal of Environmental Engineering-Asce **131**(8): 1178-1186.
- Liu, D. F., et al. (2001). "Surface characteristics of sorptive-filtration storm water media. I: Low-density ( $\rho(s) < 1.0$ ) oxide-coated buoyant media." Journal of Environmental Engineering-Asce **127**(10): 868-878.
- Mangani, G., et al. (2005). "Evaluation of the pollutant content in road runoff first flush waters." Water Air and Soil Pollution **160**(1-4): 213-228.
- Meylan, S., et al. (2003). "Accumulation of copper and zinc in periphyton in response to dynamic variations of metal speciation in freshwater." Environmental Science & Technology **37**(22): 5204-5212.
- Mittelman, M. W. and G. G. Geesey (1985). "Copper-binding characteristics of exopolymers from a freshwater-sediment bacterium." Applied and Environmental Microbiology **49**(4): 846-851.
- Mullen, M. D., et al. (1989). "Bacterial sorption of heavy metals." Applied and Environmental Microbiology **55**(12): 3143-3149.
- Ochieng, G. M. M., et al. (2004). "Performance of multistage filtration using different filter media against conventional water treatment systems." Water Sa **30**(3): 361-367.

- Perry, R. and A. E. McIntyre (1986). Impact of motorway runoff upon surface water quality. Chichester, West Sussex, PO19 1EB, UK, Ellis Horwood Limited.
- Pittner, C. and G. Allerton (2009). SUDS for Roads, SUDS Working Party, SCOTS, SEPA, Scottish Water, WSP: 174.
- Pratt, C. J. (2004). Sustainable Drainage - A review of published material on the performance of various SUDS components, Coventry University: 40.
- Saget, A., et al. (1996). "The first flush in sewer systems." Water Science and Technology **33**(9): 101-108.
- Sansalone, J. J. (1999). "In-situ performance of a passive treatment system for metal source control." Water Science and Technology **39**(2): 193-200.
- Sansalone, J. J. and S. G. Buchberger (1995). "An infiltration device as a best management practice for immobilizing heavy-metals in urban highway runoff." Water Science and Technology **32**(1): 119-125.
- Sansalone, J. J. and S. G. Buchberger (1997). "Partitioning and first flush of metals in urban roadway storm water." Journal of Environmental Engineering-Asce **123**(2): 134-143.
- Schlesinger, R. B. (1979). "Natural Removal Mechanisms for Chemical Pollutants in the Environment." BioScience **29**(2): 95-101.
- Scholes, L., et al. (2008). "A systematic approach for the comparative assessment of stormwater pollutant removal potentials." Journal of Environmental Management **88**(3): 467-478.
- Scholz, M., et al. (2006). "Decision support model for sustainable urban drainage system management." Proceedings of the Second IASTED International Conference on Advanced Technology in the Environmental Field: 94-99.
- M. W. C. o. Governments. Controlling urban runoff: a practical manual for planning and designing urban BMP. (1987)
- Seelsaen, N., et al. (2006). "Pollutant removal efficiency of alternative filtration media in stormwater treatment." Water Science and Technology **54**(6-7): 299-305.
- Serra, A., et al. (2009). "Copper accumulation and toxicity in fluvial periphyton: The influence of exposure history." Chemosphere **74**(5): 633-641.
- Stenstrom, M. K. and M. Kayhanian (2005). First Flush Phenomenon Characterization. Sacramento, CA, California Department of Transportation, Division of Environmental Analysis.
- Urbanas, B. R. (1999). "Design of a sand filter for stormwater quality enhancement." Water Environment Research **71**(1): 102-113.
- Ward, N. I. (1990). "Multielemental contamination of British motorway environments." Science of the Total Environment **93**: 393-401.
- Weber-Shirk, M. L. and R. I. Dick (1997a). "Biological mechanisms in slow sand filters." Journal American Water Works Association **89**(2): 72-83.
- Weber-Shirk, M. L. and R. I. Dick (1997b). "Physical-chemical mechanisms in slow sand filters." Journal American Water Works Association **89**(1): 87-100.
- Wegelin, M. (1996). Surface water treatment by roughing filters - A design, Construction and Operation manual. Duebendorf.

---

Woods-Ballard, B., et al. (2007). The SuDS Manual. London, England, CIRIA: 606.

## Treatment of heavy metals by iron oxide coated and natural gravel media in Sustainable urban Drainage Systems

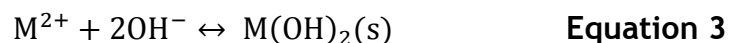
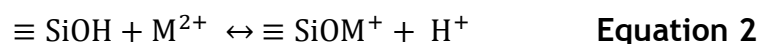
### ABSTRACT

SuDS filter drains are simple, low-cost systems utilized as a first defence to treat road runoff. However, the mechanisms involved in pollution attenuation are poorly understood. This work aimed to develop a better understanding of these mechanisms to facilitate improved SuDS design. Since heavy metals are a large fraction of pollution in road runoff, this study aimed to enhance heavy metal removal of filter drain gravel with an iron oxide mineral amendment to increase surface area for heavy metal scavenging. Experiments showed that amendment-coated and uncoated (control) gravel removed similar quantities of heavy metals. Moreover, when normalized to surface area, iron oxide coated gravels showed poorer metal removal capacities than uncoated gravel. Inspection of the uncoated gravel (microgabbro) indicated that clay particulates on the surface (a natural product of weathering of this material), augmented heavy metal removal, generating metal sequestration capacities that were competitive compared to iron oxide coated gravels. Furthermore, when the weathered surface was scrubbed and removed, metal removal capacities were reduced by 20%. When compared to other lithologies, adsorption of heavy metals by microgabbro was 3-80% higher, indicating that both the lithology of the gravel, and the presence of a weathered surface, considerably influence its ability to immobilize heavy metals. These results contradict previous assumptions which suggest that gravel lithology is not a significant factor in SuDS design. Based upon these results, weathered microgabbro is suggested to be an ideal lithology for use in SuDS where treatment of heavy metals in road runoff is important.

## 2.1 INTRODUCTION

### 2.1.1 Gravel lithology

As discussed in Chapter 1, certain aspects to SuDS design recommendations are lacking scientific evidence. One example is with regard to engineered filter drains where “locally sourced graded rock/stone” is advocated in the design SuDS Manual (Woods-Ballard et al 2007) based on the ill-considered assumption of gravel as an inert media. This assumes the lithology of the gravel is irrelevant. It is possible, however, that different types of gravel media will have different characteristics that would affect the ability of the material to react with heavy metal contaminants, most importantly being mineral composition, surface area and charge (Lindgren 1996). Since filter drain gravel utilized in Glasgow is a locally sourced microgabbro, its properties and composition are focussed on within the current chapter. Microgabbro is defined by the BGS as a medium grained crystalline intrusive rock with a mineralogy of > 65% plagioclase feldspar, < 20% quartz and an overall SiO<sub>2</sub> content < 52%. When silicon dioxide minerals are in the presence of water, the surfaces are typically covered in hydroxyl groups that are able to bind metal ions, with adsorption rates dependant on factors such as pH and competing ions (Stumm 1992). Surface reactions with SiO<sub>2</sub> in the presence of water (Equation 1) follow either adsorption to surface sites (Equation 2) or precipitation (Equation 3), where ≡ represents a surface site and M<sup>2+</sup> represents metal ions (Lindgren 1996).



**Equation 1:** Simplified example of the surface of silica oxide in presence of water in which surfaces are typically covered in hydroxyl groups (≡ represents a surface site) **Equation 2:** Example of an adsorption reaction at surface sites (other adsorption reactions are possible) **Equation 3:** Example of a precipitation reaction (other precipitation reactions are possible)

## 2.1.2 Amendments to gravel

Intensive research has been carried out on naturally reactive materials found throughout soil and sediment systems as they can play an important role in the fate and transport of contaminants (Jerez and Flury 2006). Since metal-oxides, are known to react with target contaminants such as heavy metals, it is aimed to take these materials one step further and utilize them as an enhancement to SuDS filter drain gravel. Iron oxides have been well documented and characterized in many studies and have thus been a focus in research to improve heavy metal removal (Edwards and Benjamin 1989; Benjamin et al. 1996; Xu and Axe 2005). Natural iron oxide coatings exist in the environment, in particular, within soil systems which receive iron compounds due to weathering of minerals (Scheidegger et al. 1993). Since iron oxides are well understood with regards to surface charge, structure and synthesis, are found naturally within the environment and have been shown to increase adsorption of heavy metals, it would appear to be an ideal amendment for heavy metal removal in SuDS (Schwertmann and Cornell 2000). This approach builds on previous use of iron oxides in water and wastewater treatment technologies. For example, iron salts have commonly been added as coagulants within such systems to act as adsorbents for heavy metals (Benjamin et al. 1996). Further to this, iron oxides have been coated onto granular material to enhance heavy metal removal while also filtering particulates (Benjamin et al. 1996).

Iron oxide coating of granular material has been shown to improve heavy metal immobilization but has typically been used to coat finer media in the size range of 0.5-1mm (sand) or 2-5mm (polyethylene beads). (Edwards and Benjamin 1989; Lo et al. 1997; Liu et al. 2001). The current research aims to utilize a coarser material typically used in filter drains as both a source of adsorption for heavy metals as well as a filtration material. Fine granules would not be suitable for use in field scale filter drains due to clogging concerns, thus we aim to use similar iron oxide coatings on natural gravel filter media for use in these systems.

### 2.1.3 Motivation

This chapter aims to test the assumption that all gravel material is inert by examining the rates and capacities of heavy metal removal by a range of gravel lithologies. In addition, we test whether heavy metal adsorption capacities can be artificially enhanced by engineering iron oxide coatings to gravel. The motivation of this study is to provide engineers with a greater understanding of heavy metal removal by gravel filter media, thus providing critical knowledge needed to optimise filter efficiency and implement scientifically-informed SuDS design and policy.

## 2.2 MATERIALS AND METHODS

### 2.2.1 Uncoated filter drain gravel

Filter drains along roadways near Glasgow, Scotland (U.K) use gravel sourced from the Skene Group Ltd Cowdenhill Quarry, Falkirk Scotland, and hence this material was used in this study. While filter drain gravel is typically 40mm ‘graded rock material’ (Woods-Ballard et al. 2007), smaller gravel of the same lithology was obtained for use in scaled laboratory experiments (Fig 2.1). This was rinsed thoroughly with tap water, then deionized (DI) water and subsequently sieved to 8-11.2 mm. The lithology of the gravel was determined to be microgabbro and is referred to herein as rinsed microgabbro (RMG).



**Figure 2.1.** Rinsed microgabbro

## 2.2.2 Amended filter drain gravel

In order to enhance metal removal from runoff, iron oxide coatings were chosen as a mineral amendment to gravel due to their ability to scavenge heavy metals (Bradl 2005). Iron oxide coated gravel (IOCG) (Fig 2.2) was produced by adapting the process (precipitation of iron oxides by alkali treatment) described in Liu et al. (2001) for use with microgabbro gravel instead of polyethylene beads. To produce the IOCG, 500g  $\text{Fe}(\text{NO}_3)_3$  was dissolved in 1 liter DI water and mixed with 3 liters of rinsed microgabbro. After the mixture was dried in the oven at  $90^\circ\text{C}$  for 48 hours, the gravel was mixed with 5 liters of 5M (later changed to 0.5M) NaOH and let sit for 24 hours followed by 24 hours in the  $90^\circ\text{C}$  oven. The gravel was extensively rinsed under tap and DI water with the aim to obtain a neutral pH of the rinse water (this proved to be difficult and is discussed further in Section 2.3.1).



**Figure 2.2.** Iron oxide coated gravel

## 2.2.3 Further refinement with uncoated gravel

A further three variations of microgabbro were compared to the rinsed microgabbro gravel (RMG), namely: unrinsed microgabbro gravel (UMG), direct from the quarry such that the dust and particulate matter remained on the surface; scrubbed microgabbro gravel (SMG), scrubbed with a brush so that all the dust and particulate matter was removed from the surface; and finally the microgabbro dust and particulate matter collected from the rinsed gravel and then dried and sieved to  $> 106 \mu\text{m}$  (MGD). Further rock samples (Fig 2.3) were used for comparison with the microgabbro and sourced as follows: dolomite

gravel (DG), gray quartz gravel (GQG), rose quartz gravel (RQG), sandstone gravel (SG) and a mixed lithology gravel (MLG). All gravels were rinsed thoroughly under tap water and then DI water, dried and sieved to 8-11.2 mm.



**Figure 2.3.** Rock samples for comparison to microgabbro from left to right: microgabbro, sandstone, gray quartz, mixed lithology, dolomite, rose quartz

## 2.2.4 Batch and column experimental setup

Batch and column experiments were run to determine the metal removal rates and capacities of IOCG and rinsed microgabbro (RMG) samples with relation to Cu, Pb and Zn, as these metals are the dominant pollutants in road runoff (Liu et al. 2001). 1000ppm heavy metal solutions were prepared by dissolving metal salts of Copper(II) nitrate ( $\text{Cu}(\text{NO}_3)_2 \cdot 3\text{H}_2\text{O}$ ), Lead(II) nitrate ( $\text{Pb}(\text{NO}_3)_2$ ) and Zinc nitrate ( $\text{Zn}(\text{NO}_3)_2 \cdot 6\text{H}_2\text{O}$ ) (Sigma-Aldrich) in deionized (DI) water. Stock solutions were then diluted to 5 ppm solutions using pond water (PW) collected from a pond adjacent to the main roadway (A77) in Fenwick, Scotland (Fig 2.4a) that receives road runoff from the parallel filter drain (Fig 2.4b). Note that complete water chemistry of the pond water including anions, cations and trace elements was not determined. All experiments were run as single metal solutions for each metal. All glassware, batch bottles and columns were acid-rinsed with 0.01 M nitric acid followed by DI prior to use.



**Figure 2.4.** (a) Pond outflow where water for experiments was collected (b) parallel filter drain

First, batch experiments (Fig 2.5a) were conducted by agitating 50g IOCG and natural gravel samples at 100 rpm on an orbital shaker with 500 mL 5 ppm metal solutions in polypropylene bottles. These were sampled at regular intervals (hourly up to 8 hours and daily up to 48 hours) for pH measurements and analysis of dissolved metal concentrations by atomic adsorption spectroscopy (AAS). Samples were centrifuged at 3000g for 2 minutes to separate the aqueous phase from any fine sediments still in solution for AAS analysis.

Second, to test whether gravel could adsorb metals continually during repeat exposure, column (flow through) experiments (Fig 2.5b) were run for RMG and IOCG using a 1 litre capacity column filled with closely packed filter gravel, subjected to a 4ml/min flow of 5 ppm Zn solution. This flow rate equated to a residence time for water-gravel contact of 2 hours with the experiment lasting 9 hours, or a total of 4.5 pore volumes. As Zn is one of the main constituents of road runoff and typically seen at higher concentrations to other metals (Appendix A), it was chosen to be run in the column experiment. Zn concentrations and pH were measured at the outflow (base of the column) every 10 minutes.



**Figure 2.5.** (a) Batch experiment setup (b) column experiment setup

It is important to note that in all experiments controls were performed without gravel to determine stability of the metals in solution. In all cases heavy metal removal in the controls were negligible.

In order to check experimental analytical precision of batch experiments, the method was tested by collecting and analyzing hourly triplicate aliquots from RMG and IOCG batch experiments. The analytical precision of triplicate zinc concentration analysis was found to have a standard deviation  $< 0.07$  ppm. In order to verify the experimental repeatability, the experiment was tested by running duplicate sets of batch experiments for UMG, RMG and SMG. Duplicates were found to be extremely similar and therefore experiments were considered to be repeatable and representative between batch experiments. Full replicate analysis of experiments was not logistically feasible in the current study and experimental repeatability and analytical error graphs with standard deviation can be found in Appendix B.

## 2.2.5 Instrumentation

Total dissolved heavy metals were analyzed on a Perkin-Elmer Atomic Absorption Spectrometer (AAnalyst 400) with an air-acetylene flame, triplicate sample analysis and a detection limit of  $1.5 \mu\text{g/L}$  for Cu,  $15 \mu\text{g/L}$  for Pb and  $1.5 \mu\text{g/L}$  for Zn (Perkin Elmer Manual). pH was measured on a Thermo Orion 5-Star pH meter. Surface characterization of gravel and coatings were analyzed by backscattered electron imaging on a Zeiss Sigma field-emission analytical Scanning Electron Microscope (SEM) with a beam intensity of 20 kV. Cross sectional polished thin

section samples were carbon coated and analyzed under a high vacuum mode, whereas gravel surface samples were analyzed under variable pressure mode. Surface area analyzed on powder collected from the surfaces and small grains of RMG and IOCG (between 1-4 mm due to limitations of the instrument) using the Brunauer-Emmett-Teller (BET) method (Brunauer et al. 1938) on a Micrometrics Gemini surface area instrument using nitrogen physisorption. As a comparison between two types of gravel, zeta potential (surface charge) analysis was done on the fine particles from the surface of RMG and dolomite gravel (DG) only, on a Malvern Zetasizer Nano ZS90.

## 2.3 RESULTS

### 2.3.1 Uncoated filter drain gravel vs. amended filter drain gravel

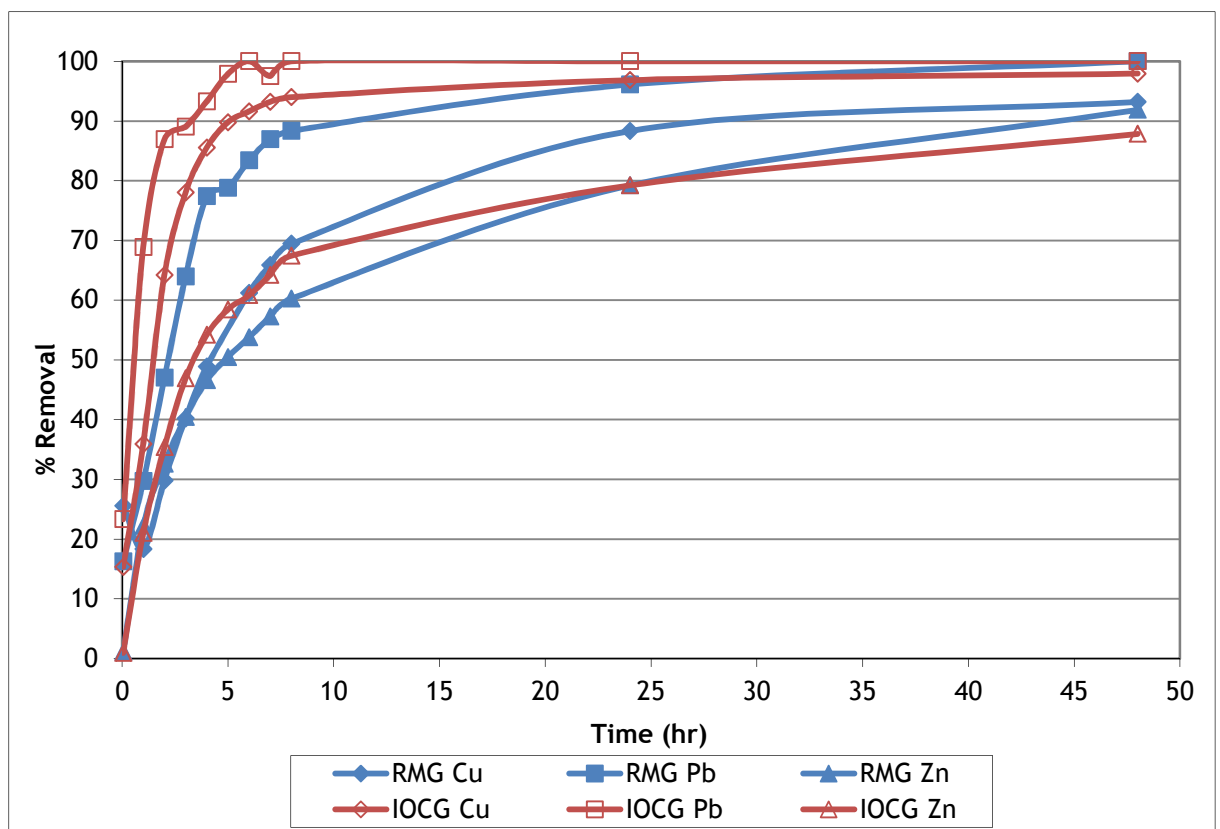
Attempts to coat the gravel with iron oxide using the Liu et al. (2001) method revealed this process was unpredictable and produced highly variable results. Even after extensive rinsing, some batches of amended gravel buffered the experimental metal solutions to a pH of 3 while others buffered the solutions to a pH of 10. Critically, neither pH is desirable for output into waterways if used in SuDS. Consequently, even though the high pH conditions showed good metal removal due to precipitation of metals driven by supersaturation (saturation indices with respect to  $Zn(OH)_2$  were much greater than 1), this system would not be suitable for SuDS due to the need to avoid the release of excessively high pH wastewaters into the environment. Amending the coating method to use 0.5M NaOH rather than 5M NaOH still frequently generated high pH buffering gravels (although some were circumneutral).

Table 2.1 and figure 2.6 illustrates the results once a neutral pH (through continuous rinsing under running water for days) was achieved for IOCG with the removal preference for metals following  $Pb > Cu > Zn$ . While IOCG did demonstrate elevated removal of Cu and Pb when compared to RMG within the first 8 hours, all uncoated and coated gravel removed between 93 - 100% metals after a 48 hour contact time. IOCG enhanced Cu removal by up to 25% and Pb up to 12% over RMG at 8 hours. Zn removal was consistently within 10% difference between IOCG and RMG throughout with IOCG demonstrating a maximum of 7%

enhanced Zn removal at 8 hours but RMG removed 4% better Zn overall after 48 hours. The batch experiment results suggest that while IOCG may have an increased adsorption capacity for metals to start, RMG shows similar and close to 100% removal after an extended contact time.

			% Removal 8 hours	% Removal 48 hours	Removal (mg/g)/h
Rinsed	(RMG)	Cu	69	93	9.98E-04
Micro-		Pb	88	100	1.04E-03
Gabbro		Zn	60	92	9.71E-04
Iron Oxide	(IOCG)	Cu	94	98	1.03E-03
Coated		Pb	100	100	1.04E-03
Gravel		Zn	67	88	9.35E-04

**Table 2.1.** Percentage removal of heavy metals by RMG and IOCG after 8 and 48 hours



**Figure 2.6.** RMG vs. IOCG percentage removal of Cu, Pb and Zn over 48 hours in batch experiments

To verify batch experiment data, flow through column experiments with a residence time of 2 hours within the gravel filter media were run. Figure 2.7 shows similar quantities of metal were removed by both IOCG and RMG but the column experiment indicates that RMG removes higher levels of Zn in a

continuous flow through system than IOCG. At the breakthrough peak, RMG removes about 70% Zn and continues to maintain an average of 85% throughout the experiment while IOCG removes about 60% at the breakthrough peak and maintains an average of 77% thereafter.

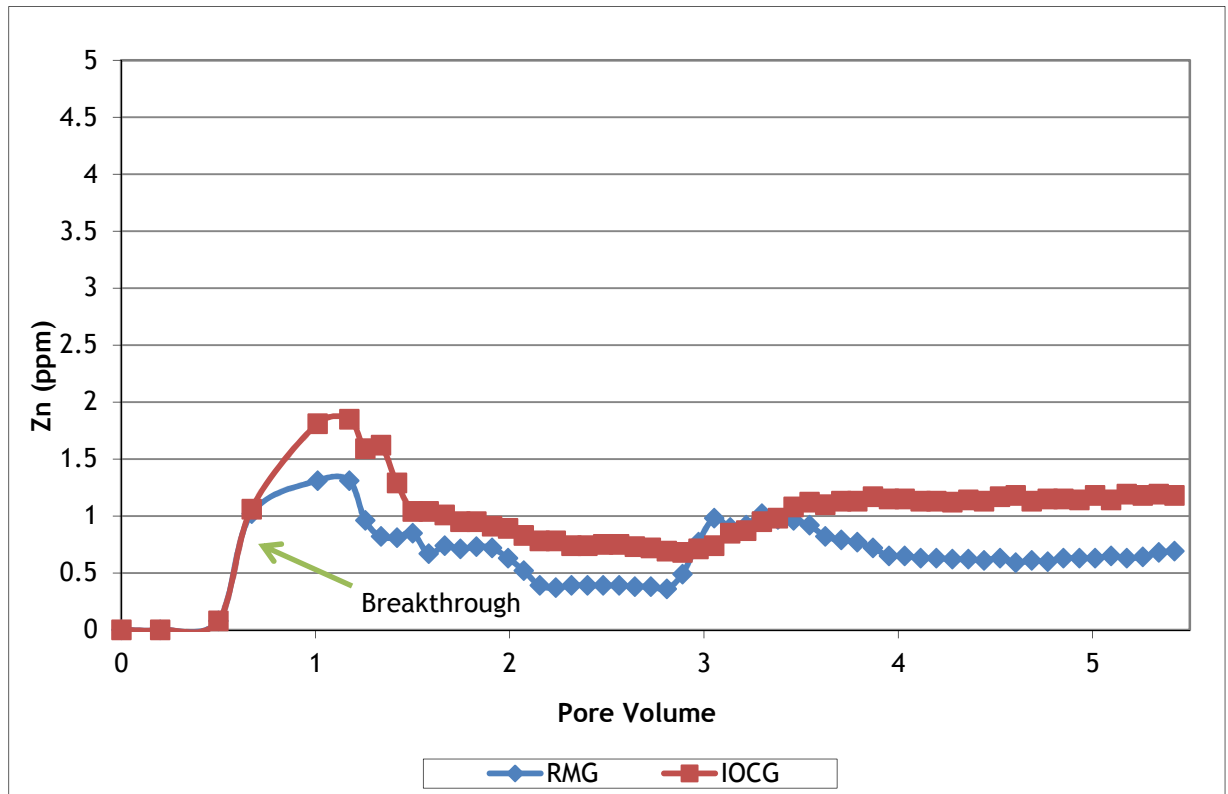


**Figure 2.7.** Flow through column experiments with a residence time of 2 hours within the gravel filter media. RMG vs. IOCG Zn concentrations over 5.5 pore volumes. Injection concentration = 5 ppm Zn.

SEM images were collected in order to unravel the reason behind the similarity in performance of the coated and uncoated gravels. While coated gravel (IOCG, Fig 2.8a) does indeed show a high surface area due to the iron oxide coating, the surface of the uncoated gravel (RMG, Fig 2.8b) can also be considered to have a high surface area when compared to IOCG. RMG is highly heterogeneous in fabric and roughness, with particles of 1-100  $\mu\text{m}$  diameter attached to localized patches of the surface. These particles are hypothesized to be weathered aluminosilicate clay minerals from the surface of the microgabbro. Clay minerals also have a high affinity for heavy metals and are thus believed to be contributing to the removal efficiency of the uncoated gravel.

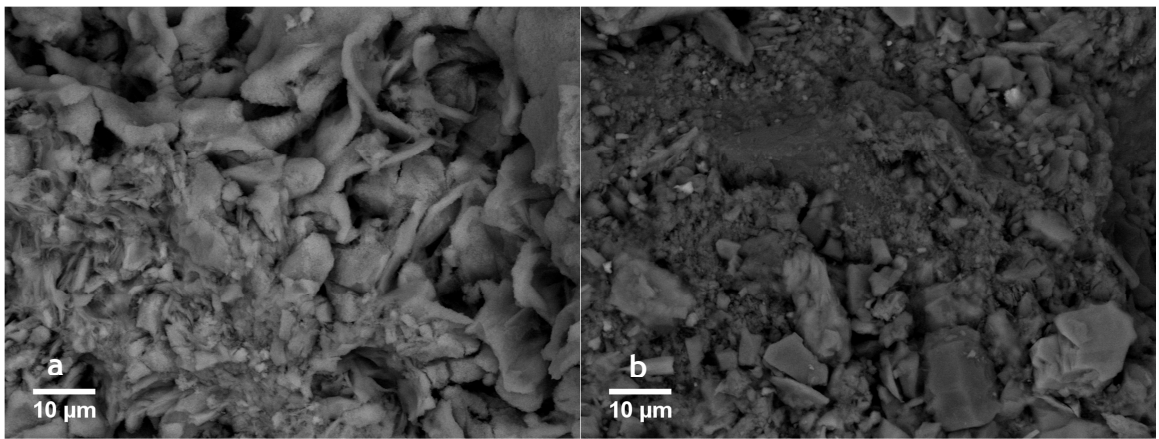


**Figure 2.8.** SEM image of the surface of (a) IOCG - 3140x magnification and 10 µm scale and (b) RMG - 3150x magnification and 10µm scale

### 2.3.2 Further refinement with uncoated gravel

Following the hypothesis that naturally occurring aluminosilicate minerals on the surface of microgabbro immobilize similar amounts of heavy metals to an iron oxide coating, batch experiments were run to determine if the particulate matter on the surface of the gravel affects removal of Cu, Pb and Zn. Different microgabbro samples were prepared as described in the methods Section 2.2.3, and Table 2.2 and Figures 2.9-2.11 shows the results of metal removal by the different forms, in which a few distinct trends emerge. First, the fastest metal removal rates were displayed by the weathered surface dust taken from the microgabbro (MGD, in purple) with > 90% of all three metals being removed after 1 hour, > 97% removed after 8 hours and > 99% removed after 48 hours. Second, Pb removal followed the same trend no matter what form of microgabbro surface was present (not including microgabbro dust) (Fig 2.10). This cluster of Pb for unrinsed (UMG), rinsed (RMG) and scrubbed (SMG) gravel (Fig 2.10) demonstrate a higher degree of removal than Cu or Zn (Fig 2.9 & 2.11) and reaches 87 - 93% by 8 hours and 100% by 48 hours. Finally, for both Cu and Zn, a distinct order of removal efficiency of UMG (red) > RMG (blue) > SMG (green) is realized (Fig 2.9 and 2.11). UMG, in which the dust and particulate coating direct from the quarry is left on the surface of the gravel, removed between 78-79% up to 8 hours and 93% (Cu) - 100% (Zn) after 48 hours. RMG removed about 10% less Cu and Zn up to 8 hours but within 1% overall removal to UMG after 48 hours. In comparison to UMG, SMG, in which the dusty particulate surface was scrubbed off, removes 18% less Zn at 8 hours and 29% less Cu at 8 hours while removing within 5% overall levels of metals up to 48 hours.

		% Removal 8 hours	% Removal 48 hours	Removal (mg/g)/h
Rinsed	(RMG) Cu	69	93	9.98E-04
Micro-	Pb	88	100	1.04E-03
Gabbro	Zn	68	99	9.71E-04
Unrinsed	(UMG) Cu	78	93	9.98E-04
Micro-	Pb	87	100	1.04E-03
Gabbro	Zn	79	100	1.04E-03
Scrubbed	(SMG) Cu	49	88	9.63E-04
Micro-	Pb	93	100	1.04E-03
Gabbro	Zn	61	97	1.02E-03
Micro-	(MGD) Cu	98	98	1.03E-03
Gabbro	Pb	99	100	1.04E-03
Dust	Zn	99	100	1.04E-03

**Table 2.2.** Percentage removal of heavy metals by RMG, UMG, SMG and MGD after 8 and 48 hours

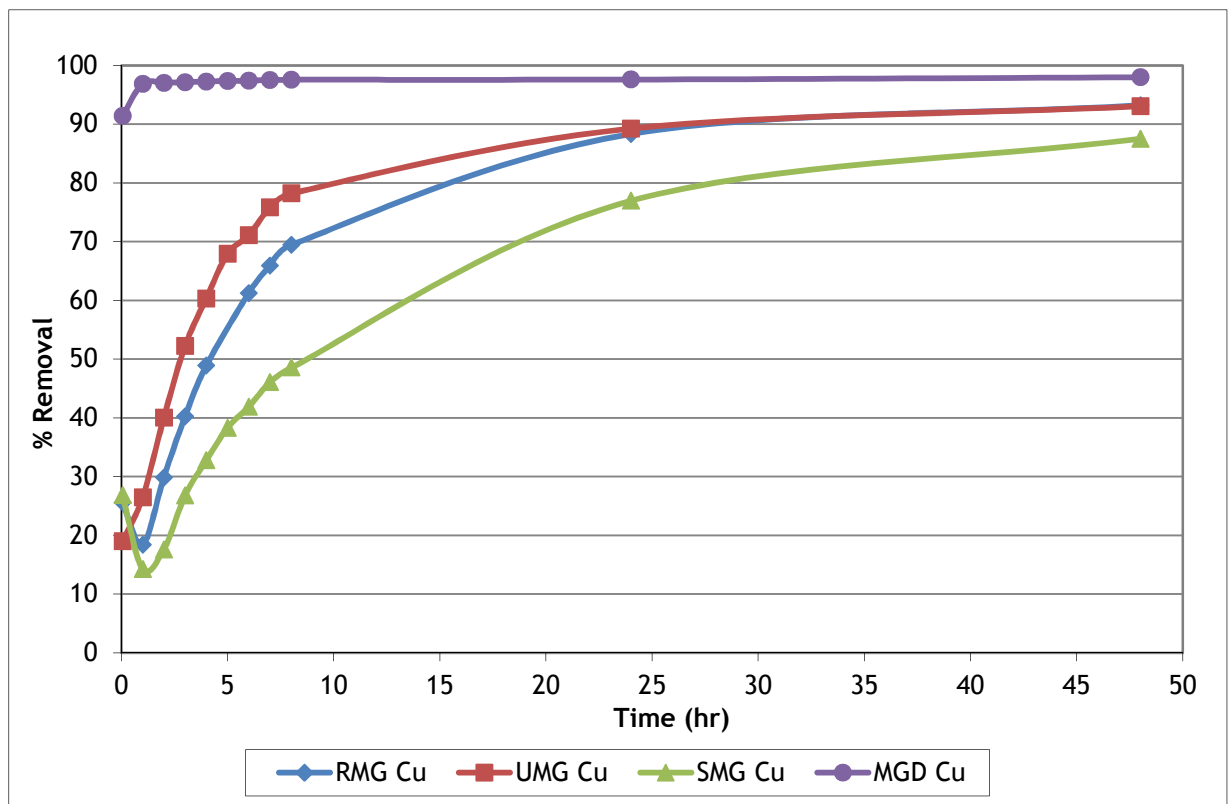


**Figure 2.9.** MGD vs. UMG vs. RMG vs. SMG percentage removal of Cu over 48 hours.

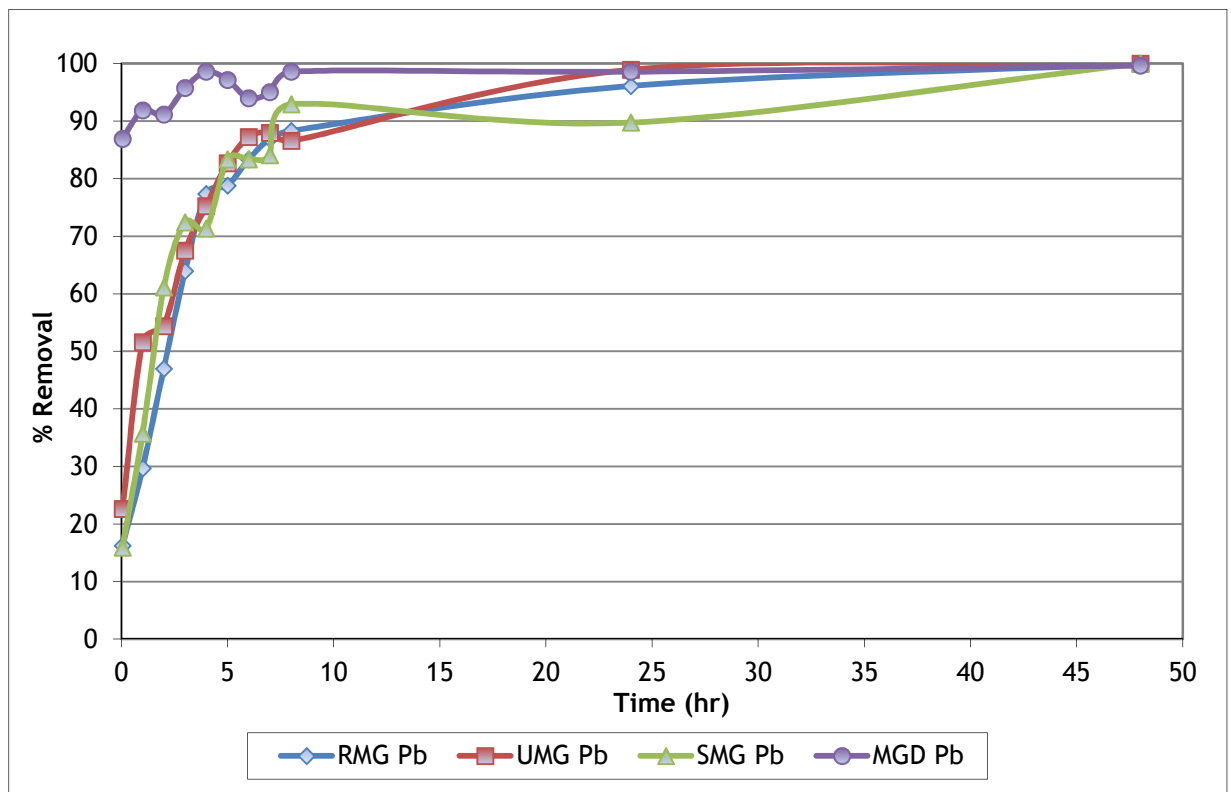


**Figure 2.10.** MGD vs. UMG vs. RMG vs. SMG percentage removal of Pb over 48 hours.

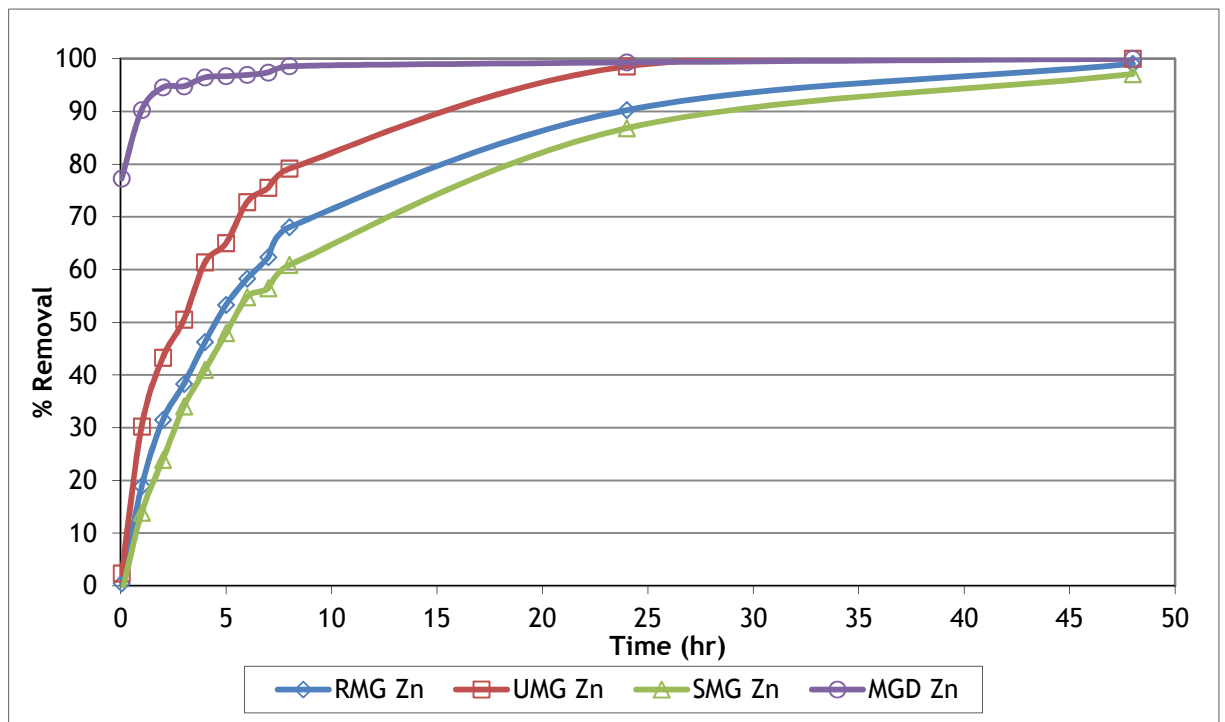


**Figure 2.11.** MGD vs. UMG vs. RMG vs. SMG percentage removal of Zn over 48 hours.

SEM thin section polished blocks were prepared to image the surfaces of UMG and SMG in order to reveal their surface characteristics which may impact metal removal. Figure 2.12a shows a cross section of unrinsed microgabro (UMG)

compared to scrubbed microgabbro (SMG) in Figure 2.12b. These images show that UMG displays an abundance of surface particulate material, while SMG displays a clean surface.

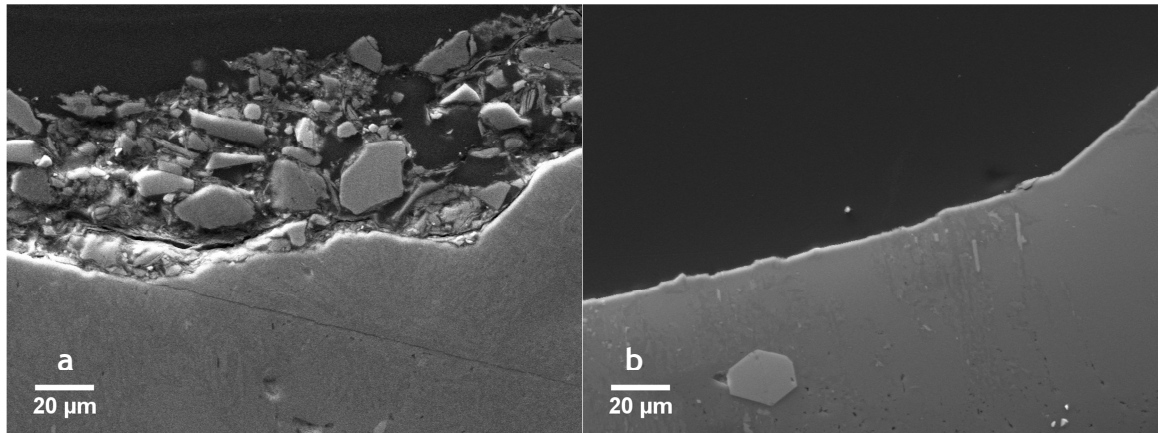


**Figure 2.12.** SEM image of a cross section of the surface of (a) UMG - 1500 magnification and 20 µm scale and (b) SMG - 1500 magnification and 20µm scale

Batch experiments were then run with other lithologies of gravel described in the methods (Section 2.2.3) to determine the impact of gravel lithology on heavy metal removal. Batch experiment results for six types of gravel are shown in Table 2.3 and graphs of percentage removal of Cu (Fig 2.13), Pb (Fig 2.14) and Zn (Fig 2.15). While removal rates and performance of specific gravel types vary between the different metals, it is evident from the figures that the microgabbro (RMG) does indeed immobilize the highest percentage of all three metals in the order of 100% Pb > 99% Zn > 93% Cu after 48 hours. It is also clear that rose quartz (RQG) was consistently the worst for metal immobilization, removing 63% Pb > 44% Cu > 20% Zn after 48 hours. The order of efficiency between metals for the remaining four lithologies is not as clear. Dolomite gravel (DG) demonstrated poor removal for both Cu and Zn but removed one of the highest percentages of Pb after 48 hours, specifically: 87% Pb > 53% Cu > 28% Zn. Gray quartz (GQG), mixed lithology (MLG) and sandstone (SG) had removal rates within 14% of each other for the three metals with the following order of metal efficiency after 48 hours: GQG immobilizing 89% Cu > 80% Zn > 78% Pb, MLG immobilizing 84% Pb > 79% Cu > 73% Zn, and SG immobilizing 90% Cu > 82% Pb > 67% Zn.

		% Removal 8 hours	% Removal 48 hours	Removal (mg/g)/h
Rinsed	(RMG) Cu	69	93	9.98E-04
Micro-	Pb	88	100	1.04E-03
Gabbro	Zn	68	99	9.71E-04
Dolomite	(DG) Cu	23	53	7.44E-04
Gravel	Pb	74	87	9.67E-04
	Zn	20	28	6.83E-04
Rose	(RQG) Cu	24	44	6.85E-04
Quartz	Pb	39	63	8.23E-04
Gravel	Zn	6.3	20	3.58E-04
Gray	(GQG) Cu	53	89	9.50E-04
Quartz	Pb	65	78	9.13E-04
Gravel	Zn	62	80	9.38E-04
Mixed	(MLG) Cu	46	79	8.67E-04
Lithology	Pb	76	84	9.50E-04
Gravel	Zn	48	73	9.02E-04
Sand-	(SG) Cu	63	90	9.68E-04
Stone	Pb	75	82	9.33E-04
Gravel	Zn	49	67	8.71E-04

Table 2.3. Percentage removal of heavy metals by RMG, DG, RQG, GQG, MLG, and SG after 8 and 48 hours

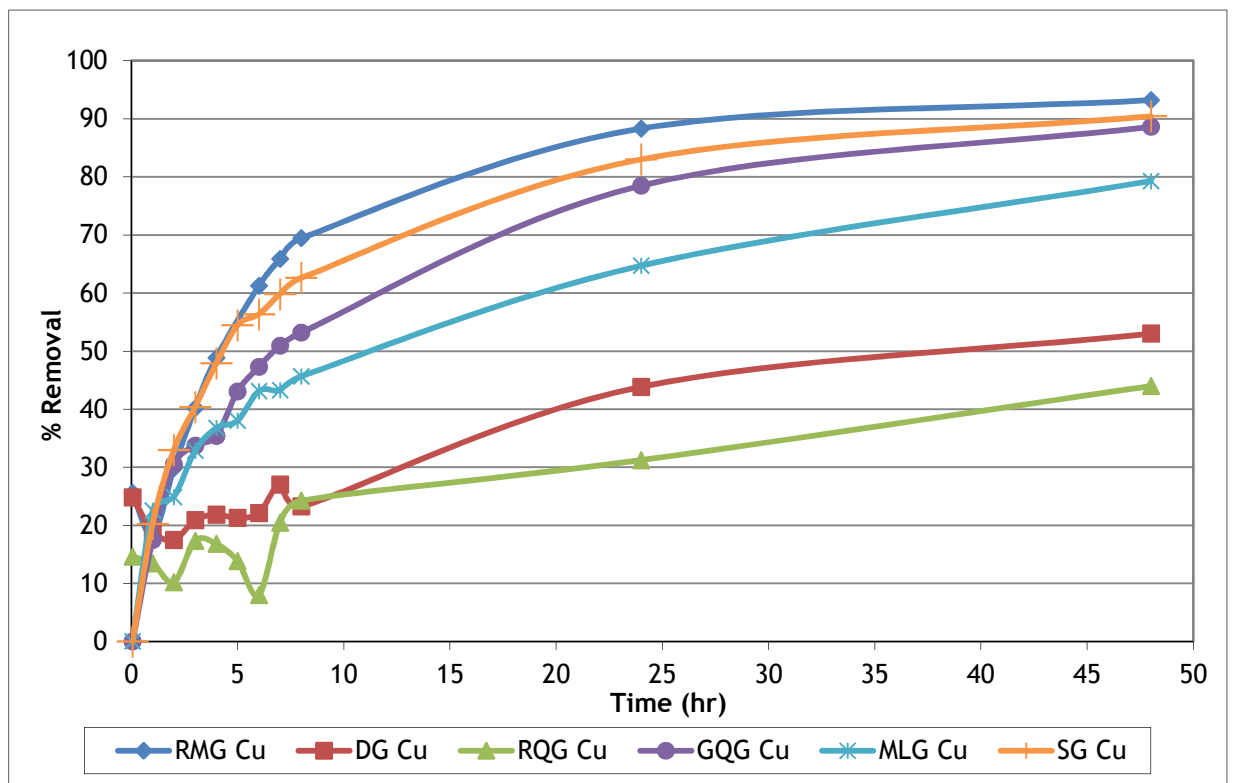


Figure 2.13. RMG compared to DG, RQG, GQG, MLG and SG percentage removal of Cu over 48 hours in batch experiments

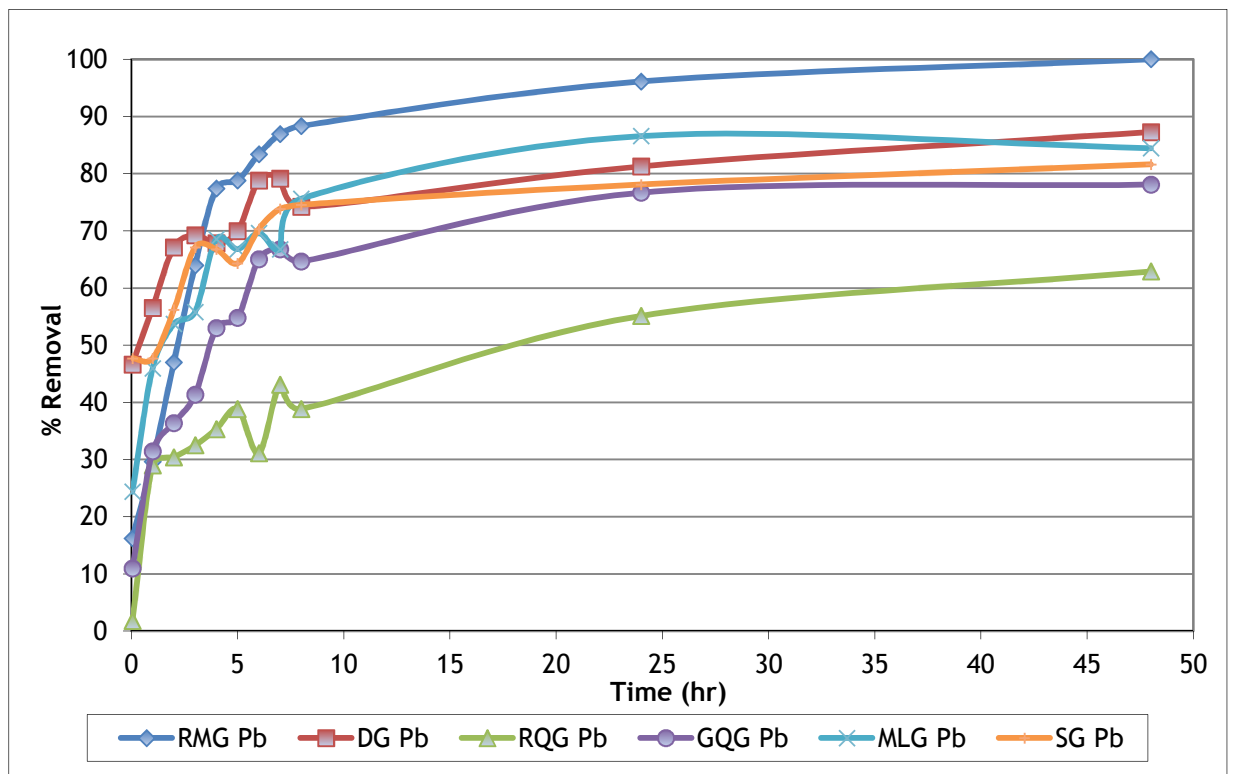


Figure 2.14. RMG compared to DG, RQG, GQG, MLG and SG percentage removal of Pb over 48 hours in batch experiments

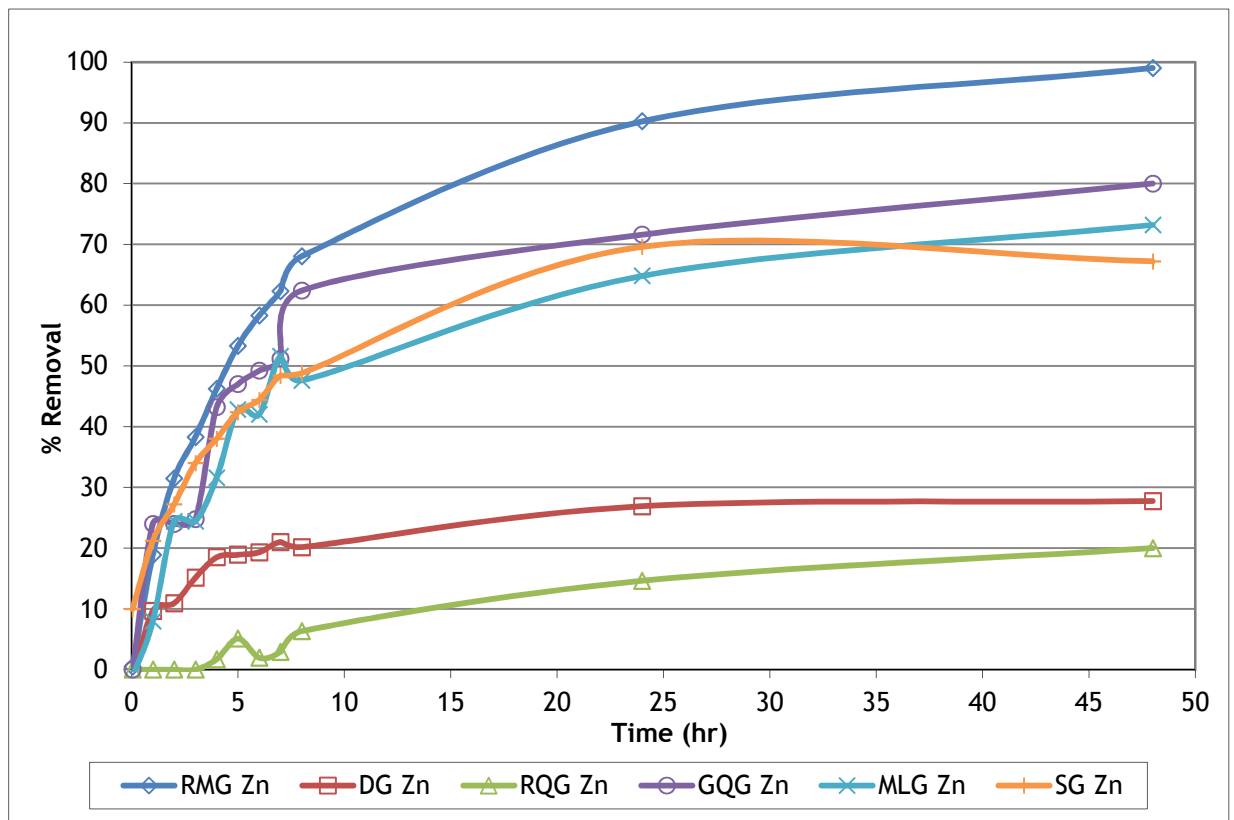


Figure 2.15. RMG compared to DG, RQG, GQG, MLG and SG percentage removal of Zn over 48 hours in batch experiments

### 2.3.3. PHREEQC modelling

Geochemical parameters were calculated using the program PHREEQC for beginning and end experimental solution conditions and can be seen in Table 2.4. The pH range, start and end saturation indices for the dominant phases [Cu(OH)<sub>2</sub>, Pb(OH)<sub>2</sub> and Zn(OH)<sub>2</sub>] and dominant dissolved species found at the initial and final solution conditions are summarized. Note that solution pHs were not adjusted to identical values in each experiment. Instead, solutions were allowed to equilibrate with the gravel in order to allow pHs to develop that would occur in a natural filter drain. The pH's are reported in Table 2.4 and fluctuated a maximum of +/- 0.3 within each system throughout the batch experiments. Also note that only known geochemical parameters were input to the modelling program (pH, temperature, metal and nitrate concentrations) and thus, the modelling results reported may differ from modelling results had the complete water chemistry profile been established. Sample PHREEQC input can be found in Appendix C. The pe indicates the redox potential of the solution and a pe of 4 was used as the PHREEQC default that is typical of oxic surface water. The main findings from PHREEQC modelling are considered in the discussion (Section 2.4.2).

Sample	ID	Cu(OH) <sub>2</sub> Dominant			Cu(OH) <sub>2</sub> Dominant			Pb(OH) <sub>2</sub> Dominant			Pb(OH) <sub>2</sub> Dominant			Zn(OH) <sub>2</sub> Dominant			Zn(OH) <sub>2</sub> Dominant		Zeta Potential
		Cu pH	Start SI	Species	End SI	Species	Pb pH	Start SI	Species	End SI	Species	Zn pH	Start SI	Species	End SI	Species	End SI	Species	
Rinsed microgabbro gravel	RMG	7.9 ± 0.2	0.65	Cu(OH) <sub>2</sub>	-0.50	Cu(OH) <sub>2</sub>	8.1 ± 0.2	2.44	PbOH <sup>+</sup>	*	*	8.1 ± 0.2	0.5	Zn <sup>+2</sup>	-1.34	Zn <sup>+2</sup>	-24		
Iron oxide coated gravel	IOCG	7.0 ± 0.1	0.63	Cu(OH) <sub>2</sub>	-1.17	Cu(OH) <sub>2</sub>	7.2 ± 0.2	2.01	PbOH <sup>+</sup>	*	*	7.8 ± 0.3	0.35	Zn <sup>+2</sup>	-2.11	Zn <sup>+2</sup>			
Unrinsed microgabbro gravel	UMG	7.9 ± 0.2	0.65	Cu(OH) <sub>2</sub>	-0.50	Cu(OH) <sub>2</sub>	8.2 ± 0.1	2.57	PbOH <sup>+</sup>	*	*	8.0 ± 0.3	0.35	Zn <sup>+2</sup>	-0.83	Zn <sup>+2</sup>			
Scrubbed microgabbro gravel	SMG	7.9 ± 0.2	0.65	Cu(OH) <sub>2</sub>	-0.24	Cu(OH) <sub>2</sub>	8.2 ± 0.2	2.57	PbOH <sup>+</sup>	*	*	8.1 ± 0.2	0.5	Zn <sup>+2</sup>	-0.75	Zn <sup>+2</sup>			
Microgabbro dust	MGD	8.1 ± 0.1	0.66	Cu(OH) <sub>2</sub>	-0.98	Cu(OH) <sub>2</sub>	8.4 ± 0.1	2.80	PbOH <sup>+</sup>	0.37	PbOH <sup>+</sup>	8.1 ± 0.2	0.64	Zn <sup>+2</sup>	*	*			
Dolomite gravel	DG	8.0 ± 0.2	0.65	Cu(OH) <sub>2</sub>	0.33	Cu(OH) <sub>2</sub>	8.3 ± 0.1	2.69	PbOH <sup>+</sup>	2.03	PbOH <sup>+</sup>	8.1 ± 0.2	0.27	Zn <sup>+2</sup>	0.13	Zn <sup>+2</sup>	-4.1		
Rose quartz gravel	RQG	7.9 ± 0.2	0.65	Cu(OH) <sub>2</sub>	0.41	Cu(OH) <sub>2</sub>	8.2 ± 0.2	2.57	PbOH <sup>+</sup>	2.26	PbOH <sup>+</sup>	8.1 ± 0.2	0.5	Zn <sup>+2</sup>	-0.07	Zn <sup>+2</sup>			
Grey quartz gravel	GQG	7.9 ± 0.2	0.74	Cu(OH) <sub>2</sub>	-0.18	Cu(OH) <sub>2</sub>	8.1 ± 0.2	2.69	PbOH <sup>+</sup>	2.04	PbOH <sup>+</sup>	8.0 ± 0.2	0.29	Zn <sup>+2</sup>	-0.72	Zn <sup>+2</sup>			
Sandstone gravel	SG	8.1 ± 0.3	0.74	Cu(OH) <sub>2</sub>	-0.26	Cu(OH) <sub>2</sub>	8.2 ± 0.3	2.44	PbOH <sup>+</sup>	2.29	PbOH <sup>+</sup>	8.0 ± 0.1	0.43	Zn <sup>+2</sup>	-0.68	Zn <sup>+2</sup>			
Mixed lithology gravel	MLG	8.0 ± 0.2	0.74	Cu(OH) <sub>2</sub>	0.10	Cu(OH) <sub>2</sub>	8.1 ± 0.2	2.69	PbOH <sup>+</sup>	1.64	PbOH <sup>+</sup>	8.0 ± 0.1	0.43	Zn <sup>+2</sup>	-0.59	Zn <sup>+2</sup>			
Pond water control	PW	8.0 ± 0.3	0.65	Cu(OH) <sub>2</sub>	0.43	Cu(OH) <sub>2</sub>	8.2 ± 0.2	2.38	PbOH <sup>+</sup>	2.63	PbOH <sup>+</sup>	7.9 ± 0.3	-0.38	Zn <sup>+2</sup>	0.42	Zn <sup>+2</sup>			

**Table 2.4.** Gravel samples, pH range of solutions during batch experiments, saturation indices (SI) for metal hydroxides and dominant dissolved species found during conditions at the beginning and end of batch experiments. \* indicates all metals were removed during batch experiments leaving zero metals within the end solution. Zeta potential is surface charge for the gravel.

## 2.4 DISCUSSION

### 2.4.1 Iron oxide coated gravel

Once a neutral pH was established for the IOCG coating method, results appeared mixed with regards to iron oxide coated gravel's effectiveness at enhancing metal removal. On one hand, batch results indicate quicker removal rates for IOCG when compared to RMG up to 8 hours for Cu and Pb, while on the other, after extended periods of up to 48 hours, removal rates between IOCG and RMG have more or less equalized to between 93-100%. Initial Cu removal rates over the first few hours were roughly double, while Pb demonstrated around 10% better removal in the IOCG compared to RMG, and the rate of metal removal by IOCG only slowed once almost all the Cu and Pb was removed. This may suggest the binding sites of the surface of the IOCG were not yet saturated with Cu and Pb. Despite displaying a slower rate of removal, RMG still successfully removed almost all Cu and Pb from the system after 48 hours. Zn removal between the amended and uncoated gravel were similar with both removing 90% Zn after 48 hours. Though, during a flow-through column experiment, which is a more realistic representation of how gravel will react with metals in a filter drain, RMG consistently removes around 10% more Zn than IOCG.

Overall, these results indicate iron oxide coatings do not considerably enhance the metal binding capacity of microgabbro gravel. This is further surprising considering surface area analysis of gravel determined IOCG ( $11.15 \text{ m}^2/\text{g}$ ) to be over 6 times higher in surface area than RMG ( $1.68 \text{ m}^2/\text{g}$ ). While, surface powder from IOCG ( $71.63 \text{ m}^2/\text{g}$ ) was up to 20 times higher in surface area than surface powder of RMG ( $3.72 \text{ m}^2/\text{g}$ ).

It is therefore evident that the initial hypothesis of iron oxide coated gravel removing more heavy metals than uncoated RMG is flawed; in explanation, either the IOCG removal is poorer than expected or the RMG removal is better than expected. As the IOCG does exhibit the expected increased surface area, it is thought that RMG removal is better than expected and thus it is prudent to focus on the nature of the RMG removal to determine whether the consensus of this material as being 'inert' is actually valid.

Considering the similar metal removal results between RMG and IOCG and extended time, resources, and money needed to produce an iron oxide coating, it is clear that the process of coating gravel for use in SuDS applications is unnecessary and not recommended. Though, while the current research has demonstrated that IOCG looks to be unsuitable for use in filter drains when considering Cu, Pb and Zn metal pollutants, IOCG may provide enhanced treatment for other pollutants of concern.

## 2.4.2 Gravel lithology and heavy metal removal

In order to investigate the better than expected metal removal capacity of RMG, the SEM image of the surface of microgabbro in Figure 2.8b gives the first indication in that it clearly shows that the surface is weathered and not pristine. The weathered surface may go some way to explaining the relative good performance of the RMG and why the removal of metals from natural SuDS water was similar to IOCG. As the microgabbro utilized was crushed rock sourced from a quarry, the aluminosilicate minerals on the surface could be continuously grinding to clay minerals and thus, may present a self-perpetuation of surface minerals that promote heavy metal adsorption.

When examining the mineral makeup of microgabbro visually and in the literature, two notable fractions are prevalent within the mafic igneous rocks; pyroxene and plagioclase feldspar (or simply plagioclase). Pyroxenes are a silicate group of rock forming minerals that can consist of a variety of proportions and combinations of cations, generally following the formula of  $M_2M_1(Si^{4+}, Al^{3+})_2O_6$ , to which  $M_2$  represents the larger cation site that determines the subgroup the mineral belongs, being rich in  $Mg^{2+}$ ,  $Fe^{2+}$ ,  $Mn^{2+}$ ,  $Na^+$ ,  $Ca^{2+}$ , or  $Li^+$  and  $M_1$  represents a smaller cation site that can be either  $Fe^{3+}$ ,  $Al^{3+}$ ,  $Ti^{4+}$ ,  $Cr^{3+}$ ,  $V^{3+}$ ,  $Ti^{3+}$ ,  $Zr^{4+}$ ,  $Sc^{3+}$ ,  $Zn^{2+}$ ,  $Mg^{2+}$ ,  $Fe^{2+}$ , or  $Mn^{2+}$  (Morimoto et al. 1988). Plagioclases are an abundant crystalline rock forming mineral whose composition ranges between albite ( $NaAlSi_3O_8$ ) to anorthite ( $CaAl_2Si_2O_8$ ) with sodium and calcium able to alternate within the crystal lattice and form slightly different variations in density and makeup (Smith 1974).

These rock-forming minerals observed on the surface of the microgabbro have the ability to chemically weather to smectite clay minerals (Banfield and

Eggleton 1990; Velbel and Barker 2008). Smectite minerals are classified as 2:1 phyllosilicate structures consisting of 2 tetrahedral sheets (Si, O, OH) and 1 octahedral sheet (Al, Mg, O, OH) contributing to lattice layers of negatively charged oxygen atoms with various positively charged cations ( $\text{Al}^{3+}$ ,  $\text{Fe}^{2+}$ ,  $\text{Fe}^{3+}$ ,  $\text{Mg}^{2+}$ ,  $\text{Li}^+$ ,  $\text{Na}^+$ ,  $\text{Ca}^{2+}$ ) occupying positions in the interlayer (Odom 1984). The most common smectite is montmorillonite which has the chemical composition of  $M_y^+ n\text{H}_2\text{O} (\text{Al}_{2y}\text{Mg}_y) \text{Si}_4\text{O}_{10}(\text{OH})_2$  (Odom 1984). The interlayer cations are exchangeable, contributing the high cation exchange capacity of this type of clay. This unique smectite property, along with the net negative charge of the clay, contributes to the high affinity for metal adsorption (Odom 1984).

The chemical weathering of minerals has the potential to occur in rocks, and specifically igneous rocks that tend to be less stable near the surface of the earth due to typically being formed in vastly different conditions under the earth's surface. When the rocks minerals encounter higher levels of water or oxygen they are usually unstable at standard temperature and pressure (STP) on earth's surface, and thus, the minerals react to form more stable minerals in the new environment (Colman 1986). Weathering processes that may occur include oxidation and most relevant to this study, hydrolysis, in which  $\text{H}^+$  or  $\text{OH}^-$  ions replace an ion in the mineral. The common residual minerals left after chemical weathering of feldspars and pyroxenes are aluminosilicate clay minerals (Colman 1986), which is noteworthy since clay is known to exhibit significant heavy metal adsorption capacities (Bailey et al. 1999). Clay's affinity for heavy metals is a result of the negative surface charge of the silicate minerals that can become neutralized with positively charged heavy metal cations adsorbing to the surface (Odom 1984; Bailey et al. 1999). This affinity for metal capacity is also increased due to the small size of clay minerals exhibiting a large surface area up to  $800 \text{ m}^2/\text{g}$  (Bailey et al. 1999). Both rock-forming minerals are reported to weather to smectites, a group of clay minerals that have the smallest crystals and thus, largest surface areas capable of increased metal cation exchange leading to a high adsorption capacity (Bailey et al. 1999). It is thus hypothesised that microgabbro may be weathering to aluminosilicate clay minerals on the surface which would in turn act as a natural enhancement to the gravel. Crucially, this shows that the type of gravel put into filter drains is critical to operational

efficiency when considering contaminant removal, and that gravel high in surface clay minerals such as granite or basalt should be recommended for SuDS.

This hypothesis is supported with batch experiments that compare different variations of microgabbro which were prepared with different amounts of weathered material on their surfaces (UMG - unrinsed microgabbro with dusty surface coating left in place, RMG - rinsed microgabbro with water, SMG - scrubbed microgabbro whose dusty surface coating was removed, and MGD - microgabbro dust removed from the surface) (Fig 2.9). Overall, these experiments demonstrated that a greater abundance of surface weathered material enhanced heavy metal removal. Thus the natural abundance of aluminosilicate clay minerals on the surface are enhancing the heavy metal removal of the gravel without any chemical amendments needed.

Visualization of the weathered surface coating can be found as a cross sectional surface SEM image for UMG in Figure 2.12a as compared to SMG in Figure 2.12b. UMG shows a great deal of weathering from the surface, while in comparison, it can be seen that all the weathered particulates have been removed from the SMG surface, and thus, an explanation for its reduced metal removal. Further analysis by energy dispersive spectroscopy (EDS) determined a range of species consistent with pyroxene, feldspar and aluminosilicate clay minerals as outlined in Figures 2.16a-h. The EDS function of the SEM allows for determination of chemical makeup by x-ray analysis that is able to discern the energy states of the elements present within the sample and create a spectrum representative of the composition. Element maps are shown in figure 2.16 for the surface of UMG. The bulk compositions of the areas inside the different coloured boxes are summarized in Table 2.5. Note that the specific percentage of elements shown on the EDS maps could not be determined and that the subsequent EDS analysis is purely qualitative.

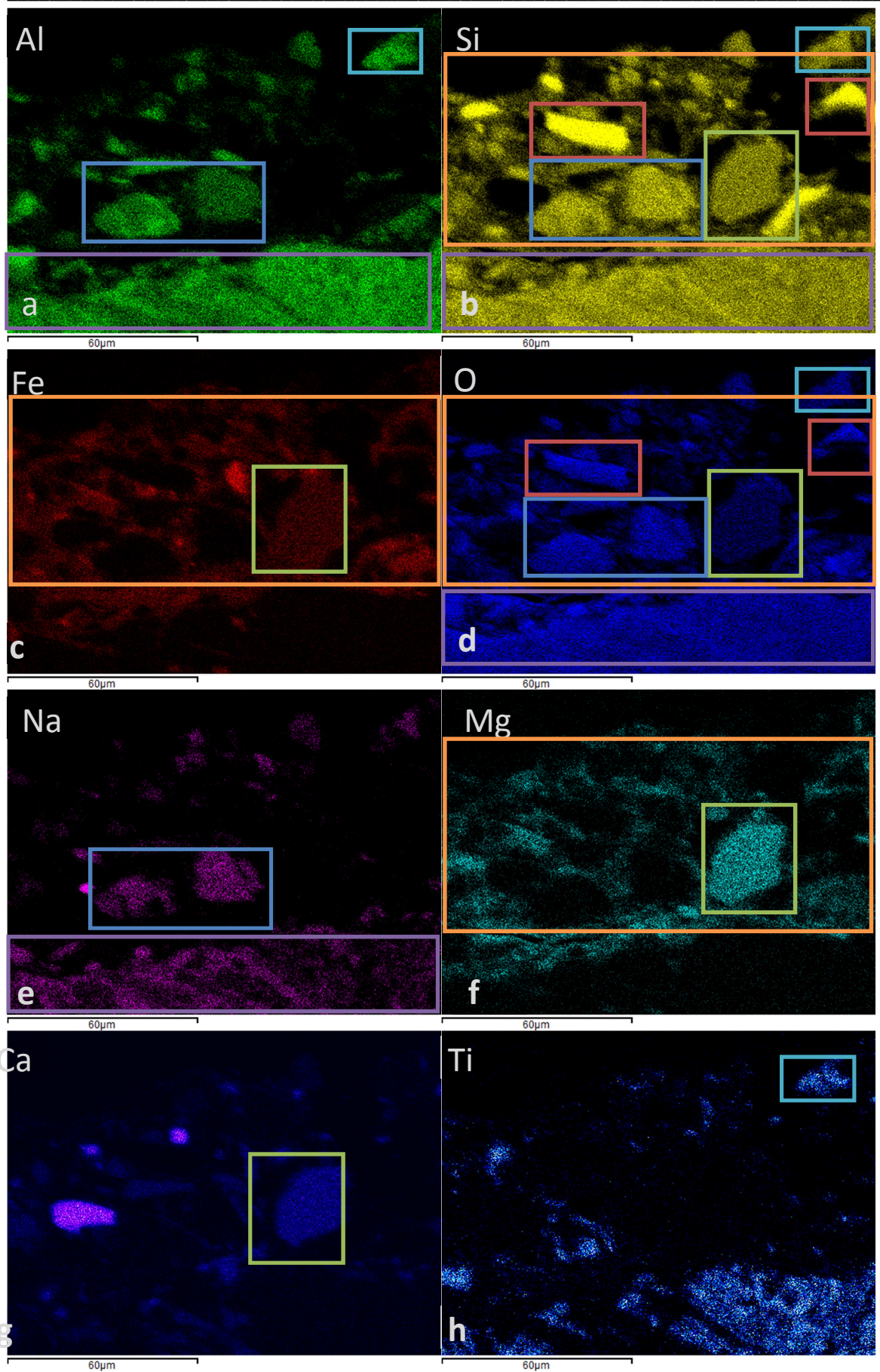


**Figure 2.16.** EDS elemental analysis for cross sectional surface of UMG for (a) Al, (b) Si, (c) Fe, (d) O, (e) Na, (f) Mg, (g) Ca, (h) Ti

Area of UMG	Element Present								Possible UMG Surface Mineral			
	Al	Si	Fe	O	Na	Mg	Ca	Ti	Smectite	Pyroxene	Plagioclase	Quartz
Blue	X	X		X	X				X	X	X	
Red		X		X								X
Green		X	X	X		X	X		X	X		
Purple	X	X		X	X				X	X	X	
Teal	X	X		X				X		X		
Orange		X	X	X		X			X	X		

**Table 2.5.** Summary of elements present within a section of UMG surface as determined by EDS analysis and possible minerals these analyses may represent

As is evident from Figure 2.16 and Table 2.5 the EDS analysis confirms that particles on the surface of the unrinsed microgabbro have the composition of elements consistent with pyroxenes, feldspars and smectite minerals. Since the elements in the primary mineral are the same as the residual aluminosilicate clay minerals, it is not known for sure from the EDS element maps which particulates are the rock forming minerals or the weathered clay minerals. The purple box in the lower part of images, a,b,d,e area corresponds to the sub-surface of the UMG and is thought to be mostly pyroxene with the possibility of plagioclase, while the areas above this represent the weathered surface particles that are a mix of pyroxenes, plagioclase and smectities.

Clay minerals are also an important constituent of sediments which have the ability to help control contaminants in aquatic systems (Liu and Gonzalez 1999). Clay has been used as a reactive surface and a source of containment in environmental remediation such as landfill liners and wastewater treatment (Jerez et al. 2006; Roberts and Shimaoka 2008). But due to the low hydraulic permeability of clay minerals, their use in filter systems is nearly impossible (Jerez et al. 2006). Jerez et al., 2006 developed a process to coat coarse media such as gravel with clay in order to harness the remediation capabilities of clay but reduce the issue of low permeability. However, an engineered clay coating process for gravel was not necessary within the current study as constituents of the surface of the microgabbro utilized appear to naturally weather to clay minerals. Thus, it is evident that the types of minerals on the gravel surface impact heavy metal uptake. This suggests that lithology of the gravel is important, despite engineering guidelines suggesting otherwise. Following this,

experiments were undertaken to examine the impact of a range of lithologies on heavy metal removal.

Due to the inherent nature of the fine crystal minerals that compose the microgabbro (as opposed to gabbro which is composed of coarse grained crystals > 1mm), the multitude of different minerals on the surface may also affect the reproducibility of batch removal results. Though, within the multi-lithology batch experiments, the data still demonstrates that the RMG microgabbro removes more heavy metals (between 93-100% after 48 hours) than other lithologies. After the 48 hour batch experiment, RMG enhanced Cu removal by 3-49% over other lithologies, Pb removal by 13-37% over other lithologies and Zn removal by 19-79% over other lithologies. With rose quartz (RQG) consistently removing the least percentage of metals, for the remaining four types of gravel, a consistent order of efficiency is not clear when comparing between metals, suggesting that specific surfaces react with the three metals to different degrees. While sandstone (SG), mixed lithology (MLG) and gray quartz (GQG) all react similarly between the three lithologies and between the 3 metals (probably because all three are dominated by the mineral quartz), dolomite (DG) demonstrates poor removal of Cu (53% after 48 hours) and Zn (28% after 48 hours) but removes the second highest concentration of Pb, 87% after 48 hours. This variance in removal capacity between different gravel surfaces as well as different metals is likely due to the geochemical properties of each gravels mineralogy which induce different complexation reactions with the dominant species in the metal solutions which was determined through PHREEQC geochemical modelling to be  $\text{Cu}(\text{OH})_2$ ,  $\text{PbOH}^+$  and  $\text{Zn}^{+2}$  throughout the duration of the experiment. This also clearly indicates that not all gravel lithologies are equal with regards to geochemical mechanisms responsible for heavy metal removal. While the specifics of the different complexation reactions are not known, the variations seen cannot be explained solely by gravel surface charge. Quartz is known to exhibit a negative surface charge, while a negative surface charge (zeta potential) was measured in this study for microgabbro and a near neutral charge was measured for dolomite (Table 2.4). So, for example, the near neutral surface charge of dolomite may explain poor removal of the positive charged  $\text{Zn}^{2+}$ , but not its strong affinity for  $\text{Pb}(\text{OH})^+$ .

Overall then, gravels cannot be considered as inert geology, nor should they be considered to offer equivalent performance, as there is strong dependency between lithology and removal capacity. Guidelines may therefore need to move beyond the simple recommendation to use locally sourced gravel.

The saturation indices (SI) are an important geochemical parameter that can help determine mechanisms of metal removal in solutions. When  $SI > 0$  the solution is considered supersaturated with respect to the metal phase and when  $SI < 0$  the solution is considered undersaturated with respect to the metal phase. Typically, it can be thought that when a solution is supersaturated, precipitation of metals from solution is more likely, while when the solution is undersaturated, precipitation is unlikely and adsorption would be the dominant removal process. PHREEQC results show that all batch systems were supersaturated with respect to metal hydroxides at the start of the experiment. At first, this would appear to suggest that precipitation (due to supersaturation) would be the key removal mechanism for these metals. However, closer inspection suggests this is not the case. Firstly, if saturation driven precipitation was the key metal removal mechanism, systems with higher SI values would induce most rapid metal removal. However, as seen throughout this study, this is not the case. Systems with lower starting SI values can generate the most rapid removal rates and highest removal capacities while systems with supersaturated end conditions do not significantly reduce concentrations as would be typical during precipitation. Secondly, final SI values for Cu and Zn are often much less than zero and saturation driven precipitation would only drive final SI values down to zero. Due to this, it is evident that adsorption is also a key process of heavy metal removal in these gravel systems. Therefore, differences in metal removal capacities between different lithologies is likely due to variations in surface reactivity. While the PHREEQC modelling does give insight into the geochemical mechanisms within the current study, please note that to completely understand water-mineral interactions, a comprehensive analysis of the water chemistry of the pond water solutions including anions, cations and trace elements is needed and was not compiled within the current study.

## 2.5 CONCLUSIONS

Iron oxide coated gravel removed similar amounts of metals compared to uncoated gravel at the conclusion of batch experiments and within column experiments, despite the surface area of the iron oxide coated gravel being 6x higher. Considering this, along with the difficult and costly process of coating the gravel and the relative difficulty in producing coatings that induce an undesirable pH, it is evident iron oxide mineral coatings are unsuitable for gravel SuDS.

Overall, it is evident from all batch and column experiments that microgabbro demonstrated increased affinity for heavy metal removal compared to other lithologies. Microgabbro showed 3-80% enhancement of heavy metal removal compared to other lithology gravels. This shows that the lithology of the gravel used in filter drains does influence heavy metal removal and must be considered a critical component to SuDS design in the future. The key to heavy metal removal by microgabbro appeared to be the abundance of weathering products such as aluminosilicate clays, well-known to have a high affinity for heavy metals, upon its surface. These are produced from the weathering of the mafic minerals of pyroxenes and plagioclase feldspars, and thus, surface enhancement from weathering products would only be expected in lithologies containing these parent minerals. Based on this, microgabbro gravel, especially with a weathered surface, is recommended for use in filter drains to benefit heavy metal removal from road runoff.

## 2.6 REFERENCES

- Bailey, S. E., et al. (1999). "A review of potentially low-cost sorbents for heavy metals." Water Research **33**(11): 2469-2479.
- Banfield, J. F. and R. A. Eggleton (1990). "Analytical transmission electron-microscope studies of plagioclase, muscovite, and K-feldspar weathering." Clays and Clay Minerals **38**(1): 77-89.
- Benjamin, M. M., et al. (1996). "Sorption and filtration of metals using iron-oxide-coated sand." Water Research **30**(11): 2609-2620.
- Bradl, H. B. (2005). Heavy Metals in the Environment: Origin, Interaction and Remediation. Neubrucke, Germany, Elsevier Academic Press.
- Brunauer, S., et al. (1938). "Adsorption of gases in multimolecular layers." Journal of the American Chemical Society **60**: 309-319.

- Colman, S. M., Dethier, David P. (1986). Rates of chemical weathering of rocks and minerals, Elsevier Science.
- Edwards, M. and M. M. Benjamin (1989). "Adsorptive filtration using coated sand - A new approach for treatment of metal-bearing wastes." Research Journal of the Water Pollution Control Federation **61**(9-10): 1523-1533.
- Jerez, J. and M. Flury (2006). "Humic acid-, ferrihydrite-, and aluminosilicate-coated sands for column transport experiments." Colloids and Surfaces a-Physicochemical and Engineering Aspects **273**(1-3): 90-96.
- Jerez, J., et al. (2006). "Coating of silica sand with aluminosilicate clay." Journal of Colloid and Interface Science **294**(1): 155-164.
- Lindgren, A. (1996). "Asphalt wear and pollution transport." Science of the Total Environment **189**: 281-286.
- Liu, A. and R. D. Gonzalez (1999). "Adsorption/Desorption in a System Consisting of Humic Acid, Heavy Metals, and Clay Minerals." Journal of Colloid and Interface Science **218**(1): 225-232.
- Liu, D. F., et al. (2001). "Surface characteristics of sorptive-filtration storm water media. I: Low-density ( $\rho(s) < 1.0$ ) oxide-coated buoyant media." Journal of Environmental Engineering-Asce **127**(10): 868-878.
- Lo, S. L., et al. (1997). "Characteristics and adsorption properties of iron-coated sand." Water Science and Technology **35**(7): 63-70.
- Morimoto, N., et al. (1988). "Nomenclature of pyroxenes." American Mineralogist **73**(9-10): 1123-1133.
- Odom, I. E. (1984). "Smectite clay minerals - properties and uses." Philosophical Transactions of the Royal Society a-Mathematical Physical and Engineering Sciences **311**(1517): 391-+.
- Roberts, A. A. and T. Shimaoka (2008). "Analytical study on the suitability of using bentonite coated gravel as a landfill liner material." Waste Management **28**(12): 2635-2644.
- Scheidegger, A., et al. (1993). "Coating of silica sand with goethite: preparation and analytical identification." Geoderma **58**(1-2): 43-65.
- Schwertmann, U. and R. M. Cornell (2000). "Iron oxides in the laboratory: preparation and characterization." Iron oxides in the laboratory: preparation and characterization(Ed.2): xviii + 188 pp.
- Smith, J., V. (1974). Feldspar Minerals. Berlin, Springer-Verlag.
- Stumm, W. (1992). Chemistry of the Solid-Water Interface. New York, Wiley.
- Velbel, M. A. and W. W. Barker (2008). "Pyroxene weathering to smectite: conventional and cryo-field emission scanning electron microscopy, Koua Bocca ultramafic complex, Ivory Coast." Clays and Clay Minerals **56**(1): 112-127.
- Woods-Ballard, B., et al. (2007). The SuDS Manual. London, England, CIRIA: 606.
- Xu, Y. and L. Axe (2005). "Synthesis and characterization of iron oxide-coated silica and its effect on metal adsorption." J Colloid Interface Sci **282**(1): 11-19.

## 3

## Influence of biofilms on heavy metal immobilization in Sustainable urban Drainage Systems

### ABSTRACT

Biological activity and its effect on contaminant transport within SuDS systems is relatively unknown and thus the influence of naturally occurring biofilm growth on heavy metal removal in a gravel filter was sought. Experimental flow columns were constructed to determine removal of Cu, Pb and Zn by microgabbro and dolomite gravel, with and without biofilm growth. It was determined that biofilm growth within the columns enhanced heavy metal removal between 8-29% depending on metal and gravel utilized. Gravel lithology also affected bacterial communities of the biofilm as determined through clone library analysis. Biofilm grown from locally collected filter drain gravel was composed of 71% *cyanobacteria* while inoculation into microgabbro reduced *cyanobacteria* composition to 25%, with 54% *proteobacteria* and 20% *bacteroidetes* while dolomite retained 47% *cyanobacteria* composition, followed by 25% *proteobacteria* and 22% *bacteroidetes*. An advection diffusion equation successfully modelled the metal and conservative tracer transport within the columns with biofilm growth columns fitting the model slightly better (root mean squared error (RMSE) between 0.17-0.47) versus non-biofilm columns (RMSE between 0.29-0.61). The model determined a permanent loss term ( $k$ ) for metal tracers between 0.01 - 1.05 that correlates to the observed percentage of metals removed (8-65%) within the column breakthrough experiments. While specific immobilization mechanisms cannot be ascertained from the current model, permanent loss is speculated to be due to a combination of adsorption and precipitation in the Blank columns and biosorption, precipitation and bioaccumulation in the Bio columns. Overall, results indicate that naturally occurring biofilm growth within a SuDS filter drain system has the possibility to enhance heavy metal removal from road runoff.

## 3.1 INTRODUCTION

### 3.1.1 Biofilms

Biofilms are communities of microorganisms that occur in any natural, engineered or medical system that offers sufficient moisture for survival. Biofilms are constituted of a variety of species of bacteria and can also include protozoa, fungi, algae and debris, typically giving rise to a spatially heterogeneous community (Cao et al. 2012). Biofilms form by producing a slimy glue-like substance called extracellular polymeric substances (EPS), which act to bind the community together and stick to surfaces (Fig 3.1). Once microorganisms initially attach to a surface, the biofilm colonizes and grows with reproduction by microorganisms within the EPS matrix to produce a dense community.

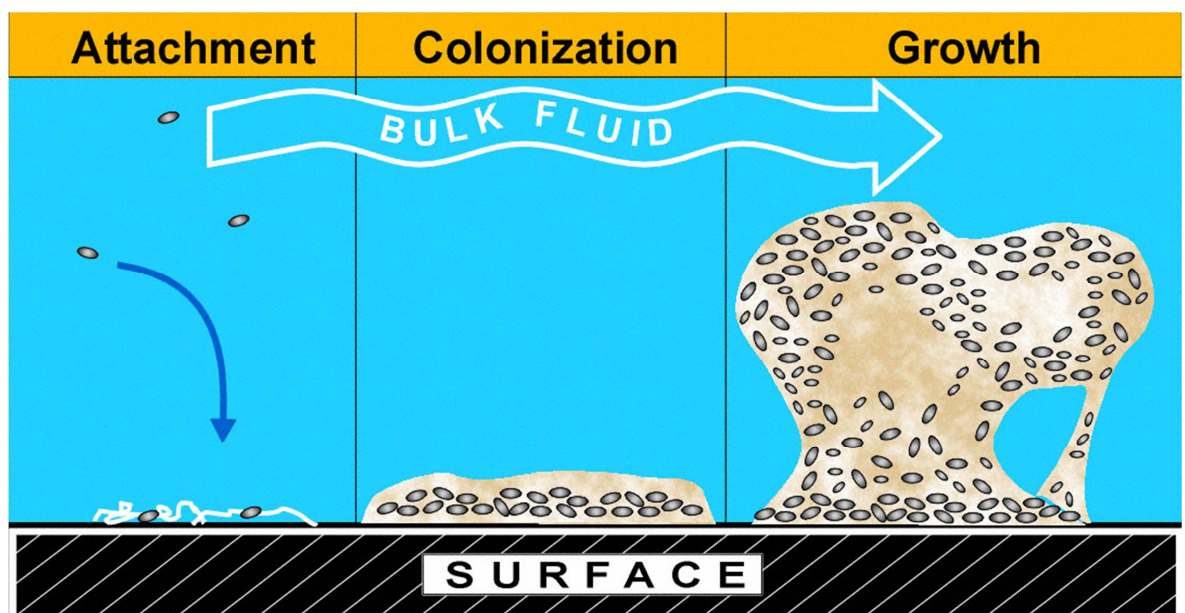


**Figure 3.1.** Biofilm formation (Via Montana State University's Center for Biofilm Engineering)

Biofilms are ubiquitous, with over 99% of earth's microorganisms living within a biofilm (Vu et al. 2009). Since biofilms can form in any hydrated environment, they are important as both a beneficial entity in biotechnical processes such as bioremediation, water treatment and energy production (Roeselers et al. 2008) as well as detrimental in causing bio-fouling, bio-corrosion and infections (Davies 2003). Owing to their fundamental impact on numerous processes across many

disciplines, biofilm processes are intensely studied in order to diminish their harmful effects while harnessing their use for beneficial purposes.

### 3.1.2 Bacteria-metal and Biofilm-metal interactions

Understanding all of the processes in which microorganisms react with metals is an important aspect in many environmental applications including contaminant transport and bioremediation. Due to the ubiquitous nature of microbes on surfaces in aqueous environments, they have the possibility to constitute a majority of the organic fraction of the subsurface (Konhauser 2007). Their presence is therefore significant in metal immobilization and transport. The formation of a biofilm by microbe colonization via electrostatic adhesion and subsequent excretion of EPS then forms a highly reactive coating over mineral surfaces that has been shown to be beneficial for metal immobilization by increasing the surface area and enhancing the metal binding capacity of the surface (Yee and Fein 2002). This is an important aspect in the current contaminant transport research due to biofilm formation over a SuDS gravel substratum. The processes by which microorganisms contribute to bioremediation of metals in the environment are summarized in Figure 3.2.

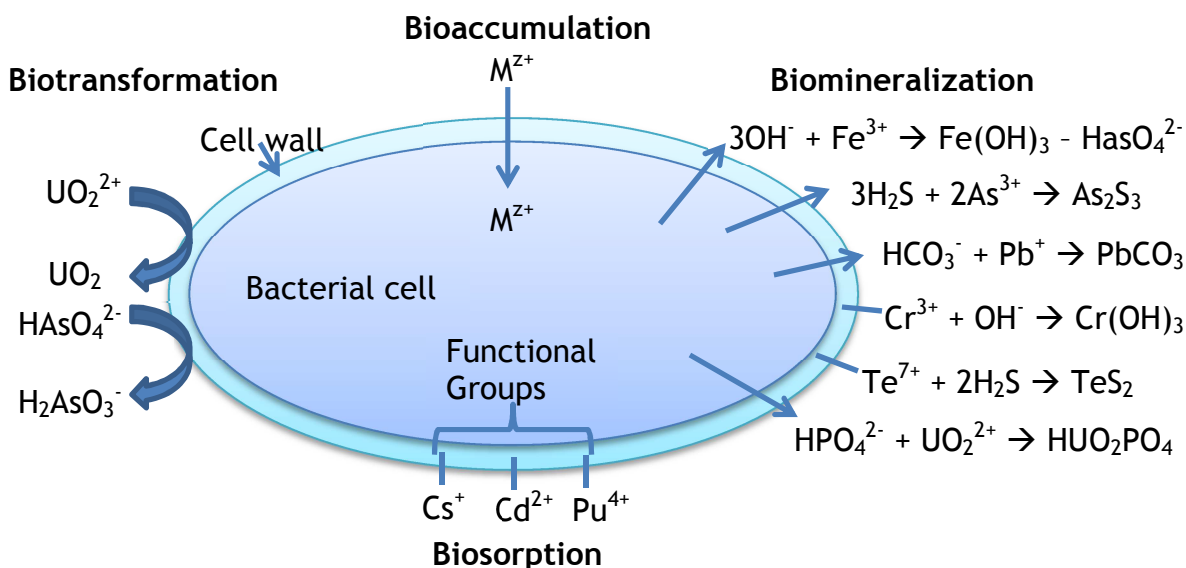


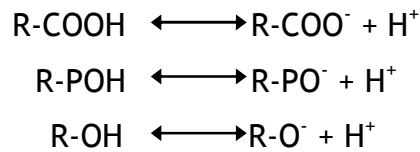
**Figure 3.2.** Summary of microbe-metal interactions that contribute to bioremediation of toxic metals in the environment (adapted from Lloyd and Macaskie (2000) via Konhauser (2007))

### 3.1.2.1 Biosorption

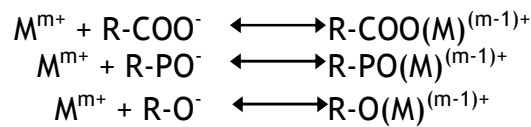
Adsorption involves the complexation of dissolved metals onto anionic functional groups on the cell surface. This inherent structure of bacterial cell walls contains surface functional groups such as carboxylic, amino, hydroxyl and phosphate sites that will determine metal binding capacity (Beveridge and Murray 1980). By determining specific parameters regarding these organic functional groups, including abundance on the cell wall deprotonation and metal-organic stability constants of the groups and metals, Fein et al. (1997) was able to quantify and model the effect of bacteria on metal adsorption. The functional groups were found to contribute to the acid/base properties, and thus metal uptake ability of the bacteria and specifically, that phosphate and carboxyl sites showed strongest affinity for heavy metals.

As well as the cell wall, some bacteria exhibit supplemental layers such as sheaths, or extracellular polysaccharides, which can be extremely diverse between microorganisms and environments, but are commonly composed of sugar monomers, uronic acids, proteins (Konhauser 2007), as well as phosphates, sulphates, fatty acids and amino acids (Weckesser et al. 1988). These complex gel-like structures also contribute to the metal-binding capacity of the bacteria as well as controlling the concentrations of metals reaching the cell (Konhauser 2007). These surface coatings contribute to the EPS that protects, enables adhesion and facilitates aggregation of the microorganisms and stabilizes the biofilm community (Yang et al. 2013). Both the cell surface and EPS are then able to sequester positively charged metals due to exhibiting negatively charged surfaces within the natural environment (Harden and Harris 1953; Mittelman and Geesey 1985; Yang et al. 2013).

The negatively charged surfaces result from the deprotonation of the hydroxyl, phosphate and carboxyl surface functional groups (Beveridge and Murray 1980) which follow the three equations in Equation 3.1. Deprotonation progresses as pH increases; the surfaces becoming increasingly electronegative, thus increasing metal binding capacity. As a result, at the circumneutral pH's typical in environmental settings cells display significant metal binding capacity. Metal cation binding to the deprotonated functional groups on the surface of the bacterial cell then follows the equations in Equation 3.2.



**Equation 3.1.** Deprotonation reactions for the three surface functional groups from Fein et al. (1997). R represents the bacterial surface.



**Equation 3.2.** Reactions of metal cations (M) binding to deprotonated functional groups on the bacterial surface (R)

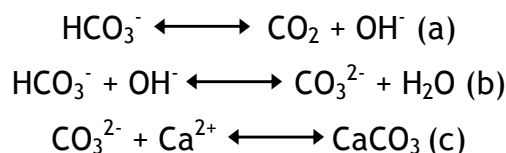
### 3.1.2.2 Biomineralization

Metals binding to the cell wall may act as a nucleation site for further metal deposition via mineral precipitation. Biomineralization is important in geochemical cycling and can occur as either “biologically induced biomineralization” in which surface mineral phases are produced as a byproduct of normal cellular processes or in response to the surrounding environment (Lowenstam 1981) or “biologically controlled biomineralization” in which mineral phases are produced to serve a purpose to the cell (Konhauser 2007).

One of the most common (and relevant) examples of biomineralization is the formation of iron hydroxides created by microbial biomass in association with iron(II) water (for example in water distribution systems, mining wastes, hydrothermal systems, springs and aquifers) that comes into contact with O<sub>2</sub> (Konhauser 2007). Iron hydroxide biomineralization may form through many active or passive process and typically undergo numerous stages including Fe adsorption to cell surfaces, nucleation of iron hydroxide grains and even possible full encrustation of the cell (Konhauser 2007).

In another classic example of biologically induced biomineralization, microorganisms have been contributing to carbonate sedimentation for billions of years, specifically; *cyanobacteria* metabolically fixate carbon leading to increased pH and supersaturation that is coupled with cation adsorption to the cell surface (Konhauser 2007). In neutral or alkaline environments, the carbon source utilized for photosynthesis is bicarbonate which leads to a byproduct of

hydroxyl ions (Equation 3.3a) and subsequent areas of alkalinity around the cell to change the speciation towards carbonate anions (Equation 3.3b). Different carbonate phases follow through metal complexation to reactive ligands offered by the *cyanobacteria* (Equation 3.3c).



**Equation 3.3.** (a) Utilization of bicarbonate during photosynthesis creates hydroxyl ions (b) increased pH creates carbonate anions (c) which then react with ligands to form carbonate phases such as calcite (Konhauser 2007)

### 3.1.2.3 Bioaccumulation

While many metals are immobilized due to passive complexation to the cell surface, it is important to note that bacterial cells also actively respond to metals for internalization or protection. First, bacteria require certain metals for a multitude of cellular functions and thus, actively manipulate the cell wall and surface functional groups in order to uptake metals intracellularly for cell growth and health. Secondly, the microbes may also actively expel metal binding chelates in order to protect from toxic metals within their vicinity (Konhauser 2007).

### 3.1.2.4 Biotransformation

Microorganisms have the ability to contribute to bioremediation through biotransformation processes of both oxidation of low valence metals to higher valence species and reduction of high valence metals to lower valence insoluble species. Biotransformations by bacteria therefore have the capacity to alter the solubility and mobility of harmful radionuclides such as in the classic examples of reduction of mobile U(VI) to insoluble U(IV) as a treatment strategy for immobilizing uranium in contaminated aquifers or reduction of adsorptive arsenate (As(V)) to more mobile arsenite (As(III)) which has led to groundwater contamination by sediment derived arsenic (Konhauser 2007).

### 3.1.3. Motivation

While bacteria and biofilms clearly have the capacity to immobilize heavy metals, their propensity to do so in SuDS systems, and in particular filter drains, has yet to be investigated. If biofilms do have a positive impact on the pollutant removal of the systems, their natural presence could be harnessed for further treatment capacity of the SuDS. This understanding of the influence of biofilms in heavy metal removal within gravel filter drains can help to better engineer the systems for enhanced performance of contaminant treatment.

## 3.2 MATERIALS AND METHODS

### 3.2.1 Biofilm growth

In order to facilitate colonization of a biofilm that would be typical of a filter drain, SuDS gravel collected from a working filter drain located adjacent to the A77 roadway in Fenwick, Scotland (Fig 2.4a) was placed in a sterilized and rinsed laboratory scale vertical flow cell. Filter drain gravel falls under Volume 1 Specifications for Highway Works, Series 500 which specifies that Type B graded filter drain material with a 40mm single size crushed drainage stone be used in highway filter drains. In this case, the gravel was crushed igneous rock and it is worth noting that when the gravel was collected, it had a noticeable slimy layer covering most grains. Water collected from a pond that receives road runoff from the parallel filter drain (Fig 2.4b) was subsequently allowed to recirculate within the column for 10 months. Note that since the water chemistry was not known and the water was recirculated over the 10 months, this meant that only one carbon source was available to the biofilm communities and thus, a depletion of the organic carbon could have rendered the results substrate limited.

Nothing was added to aid growth and the column was placed in a laboratory at room temperature which had access to natural sunlight. Figure 3.3 shows biofilm growth within the column (a) and the influent recirculated pond water feed (b) after 10 months of growth as well as an example of collected filter drain gravel (c).



**Figure 3.3.** (a) Growth chamber after 10 months growth (b) Recirculating pond water after 10 months growth (c) SuDS filter drain gravel ~40mm grain size

The vertical Perspex flow cell column (Fig 3.4) was designed to hold a 1 liter volume of gravel material in between 2 mesh diffuser plates and mixing chambers on either side. The inner diameter of the Perspex was 100mm while the gravel filter area was 135mm high with 25mm high mixing chambers at the top and bottom. To disperse the flow, there were four inlets at the bottom and outlets at the top of the column connected together by tubing. Water was pumped on a Watson-Marlow 323S/D peristaltic pump at ~4ml/min and flowed from the bottom of the column to the top.

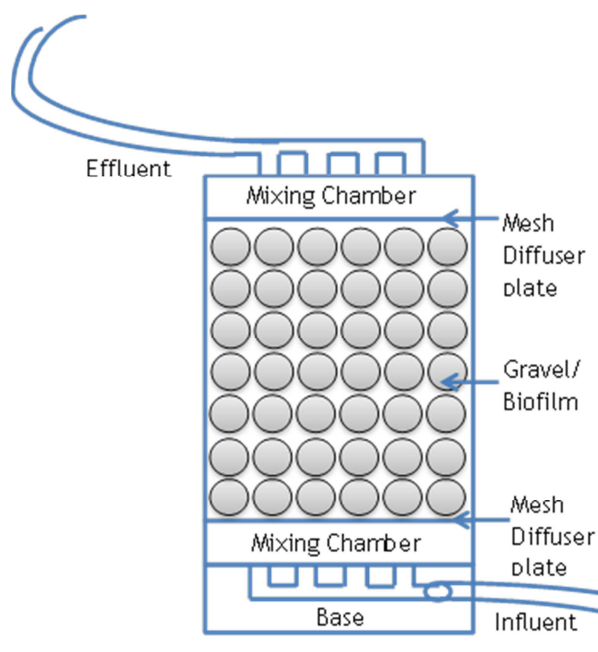


**Figure 3.4.** Schematic of flow cell

After 10 months of recirculating SuDS pond water through the column containing filter drain gravel, a thick, green, phototrophic biofilm formed both within the

column as well as the bottle of influent water feed. Samples of this biofilm, in the form of sections of biomass collected from the bottle and column, were then utilized to inoculate a further source of influent pond water for further experimental columns. Each section of biomass was cut in half and put into two 2 liter bottles of SuDS pond water so that each bottle had the same source of biomass to start with. A total of four columns were prepped (sterilized with Virkon laboratory disinfectant and rinsed with DI water) for biofilm growth and subsequent heavy metal breakthrough curve experiments. Two of the four columns contained DI rinsed, autoclaved, 8-11.2mm sieved dolomite gravel while the other two columns contained DI rinsed, autoclaved, 8-11.2mm sieved microgabbro gravel. Gravel, column, and tubing was all sterilized beforehand to make sure any biological growth was due to the biomass obtained from the SuDS gravel system. Microgabbro (Columns A and B) and dolomite (Columns C and D) was loosely packed into the chambers. Once columns were sterilized and filled with gravel, the influent solution of SuDS pond water with SuDS gravel biomass was recirculated with a Watson Marlow 323S/D pump at a constant rate ~4ml/min for a total of 8 months. Each set of columns (2 microgabbro, 2 dolomite) had their own influent source water as seen in Figure 3.5 which shows the experimental setup after 2 months of growth.



**Figure 3.5.** Experimental column setup with recirculating influent after 2 months

### 3.2.2 Breakthrough experiments

After 8 months of SuDS pond water recirculation, biofilm growth was present in all four columns and ready for breakthrough experiments (Fig 3.6). Both a conservative tracer and heavy metal solution were run through the biofilm

growth columns to obtain eight breakthrough curves, termed 'Bio' experiments. After the conservative and metal breakthrough curves were run on the biofilm growth columns, the columns were cleaned, sterilized with Virkon® disinfectant, rinsed with DI, dried and filled with autoclaved dolomite or microgabbro. The columns were filled with the same weight of gravel to recreate the conditions of the previous columns but without biofilm growth. These were used as a blank experiment for comparative purposes, thus enabling the effect of biofilm on heavy metal removal to be determined. The conservative and metal breakthrough experiments were run on the non-biofilm growth columns which produced a further eight breakthrough curves, termed 'Blank' experiments. Each set of breakthrough experiments was run for a total of 4.5 hours, of which, the first 3 hours was the pulse of tracer (metal or conservative) while the final 1.5 hours was without a tracer to determine the tail end of the curve. All columns had a flow rate of 15-16.5 ml/min resulting in a residence time of one hour. 10mL samples were taken every 5 minutes from the outflow at the top of each column into polypropylene falcon tubes for subsequent analysis.



**Figure 3.6.** Biofilm growth columns after 8 months of growth

First, a conservative tracer was needed that would not react with the gravel or biofilms within the columns nor alter the conditions of the column before the heavy metal experiments. Typically, solutions of salts are ideal as conservative tracers as they are not removed by any process and ion concentrations are easily measured by electrical conductivity (Worch 2012). This allows for the conservative tracer to be used as a blank which reveals transport due to advection and diffusion alone without tracer immobilization. Heavy metal breakthrough curves are then compared to the blank; any differences are thus

due to immobilization of heavy metals. Since the SuDS pond water already recirculating within the columns has a naturally high background conductivity of  $\sim 1800 \mu\text{s}/\text{cm}$ , deionized (DI) water, which has a conductivity of  $5\text{-}20 \mu\text{s}/\text{cm}$ , was used as a tracer. This allowed measurement of conductivity in  $\mu\text{s}/\text{cm}$  which could then be converted to concentration of sodium (Na) in ppm and an inverse breakthrough curve to represent a conservative tracer. The initial concentration of Na of the pond water equalled  $\sim 300$  ppm and conductivity readings taken every 5 minutes were corroborated with Flame Photometer Na analysis on the collected samples to within 5%. The elevated background Na concentration in the pond water is thought to be due to collection during the winter when precipitation and runoff from the nearby road is high.

Second, heavy metal breakthrough experiments were run in which one microgabbro column and one dolomite column had a pulse of 5 ppm Cu, while one microgabbro and one dolomite column had a pulse of a mix of 5 ppm Cu, Pb, and Zn. Cu, Pb and Zn were chosen as they are the most common heavy metal contaminants in road runoff (Lau et al. 2000; Ancion et al. 2010; Beck et al. 2011). All metal solutions were prepared using River Kelvin water following the method described in Section 2.2.4. Note that complete water chemistry of the river water including anions, cations and trace elements was not determined. An overview of experimental conditions of all columns can be found in Table 3.1, each column listed had a DI tracer experiment run first, followed by the metal breakthrough experiment.

Column	Gravel Type	Metals	Biofilm Growth
BioGabbroCu	Microgabbro	Cu	8 months
BioGabbroMix	Microgabbro	Cu, Pb, Zn	8 months
BioDolMix	Dolomite	Cu, Pb, Zn	8 months
BioDolCu	Dolomite	Cu	8 months
BlankGabbroCu	Microgabbro	Cu	none
BlankGabbroMix	Microgabbro	Cu, Pb, Zn	none
BlankDolMix	Dolomite	Cu, Pb, Zn	none
BlankDolCu	Dolomite	Cu	none

**Table 3.1.** Experimental conditions of columns

### 3.2.3 Instrumentation

Total dissolved heavy metals were analyzed on a Perkin-Elmer Atomic Absorption Spectrometer (AAAnalyst 400) with an air-acetylene flame, triplicate sample analysis and a detection limit of 1.5 µg/L for Cu, 15 µg/L for Pb and 1.5 µg/L for Zn (Perkin Elmer Manual). pH was measured on a Thermo Orion 5-Star pH meter while conductivity was measured on a Hach HQ40d multi-parameter meter and Na was measured on a Sherwood Scientific M410 Flame Spectrometer.

### 3.2.4 Breakthrough curve analysis and modelling

In order to determine the concentration of metals that passed through the column, percentages were obtained by calculating the area under the curve with the trapezoidal rule and comparing each experimental curves area to a theoretical breakthrough of 100%.

Transport of contaminants within porous media can be described by the advection diffusion equation for solutes within a homogeneous medium at steady state flow (Van Genuchten and Parker 1984; Pang and Close 1999; Tang et al. 2010; Jaiswal et al. 2011). To account for immobilization of heavy metals within the column, a linear loss term was incorporated into the diffusion-advection equation (Equation 3.3).

$$\frac{\partial c_r}{\partial t} = D \frac{\partial^2 c_r}{\partial x^2} - v \frac{\partial c_r}{\partial x} - kc_r$$

**Equation 3.3.** Advection-diffusion equation where  $c_r$  is the resident concentration,  $D$  is the dispersion coefficient,  $v$  is the average pore water velocity,  $x$  is the distance,  $t$  is time and  $k$  is the loss term

A Matlab code was written to calibrate an advection diffusion equation that solved the initial boundary condition for the breakthrough curves in one dimension. The code solves the advection diffusion equation assuming any heavy metal loss is by permanent immobilization (i.e. permanent precipitation or adsorption with no opportunity to remobilize) and theoretical breakthrough curves following the equation are plotted against experimental curves. The Matlab code can be found in Appendix D.

### 3.2.5 DNA extraction and clone library construction

Note that all DNA extraction and clone library analysis was undertaken by Sarah Haig in the Environmental Engineering laboratory at the University of Glasgow.

In order to determine community composition of the biofilms in each column, total bacterial DNA was extracted from 0.5 g biomass from each system using the Fast DNA Spin kit for soil as described in the manufacturer's instructions (MP Bio-Medical, Cambridge, UK). 16S rDNA was amplified using PCR with the following reaction mix: 200 ng SuDS DNA, 25  $\mu$ l Bioline PCR mix, 12.5 pmol forward primer 27f (5'-GAGTTTGATCCTGGCTCAG-3') and reverse primer 1392r (5'-ACGGGCGGTGTGTRC-3'). PCR was carried out in a Gene Pro Thermal Cycler (Bioer Technology, UK) with the following protocol: 95 °C for 5 min, followed by 30 cycles of 94 °C for 1min, 62 °C for 1min and 72 °C for 1min and a final extension of 72 °C for 10 min.

Amplified PCR fragments were purified using a gel purification kit (Qiagen) and cloned using the TOPO TA kit (Invitrogen) following manufacturer's instructions. One hundred clones from each library were screened using amplified ribosomal DNA restriction analysis (ARDRA), with the restriction enzyme HaeIII (promega). Operational taxonomic units (OTUs) were identified, based on restriction cleavage patterns and clones representing the OTUs selected for sequencing.

For the phylogenetic analysis, clone sequences were compared to the GenBank nucleotide data library (<http://www.ncbi.nlm.nih.gov/blast/blast.cgi>) and taxonomy assigned using RDP Classifier with confidence interval of >90% (Cole et al. 2009). All sequences were analyzed in the context of the complete data set using Bellerophon to identify chimeras, of which none were found.

The 16S rDNA gene sequences were aligned along with representative of all bacterial phyla using Clustal (<http://www.ebi.ac.uk/Tools/msa/clustalw2/>). All sequences were used for Phylogenetic tree reconstruction with the MrBayes v. 3.2 software program (Ronquist et al. 2012). A general time-reversible gamma-distributed rate variation model was specified. A Markov chain Monte Carlo analyses (MCMC) was performed for 1000000 generations with sampling every 1000 generations to create a posterior probability distribution of 7000 trees. The

average standard deviation of split frequencies as well as convergence diagnostics for the posterior probabilities of bipartitions (Stdev(s)) and branch lengths potential scale reduction factor (PSRF) of Gelman and Rubin (1992) were used in all cases to check for convergence. Clone library sequences were submitted to the NCBI GenBank database through Bankit under the accession numbers KM263145-KM263186.

## **3.3 RESULTS AND ANALYSIS**

### **3.3.1 Breakthrough curve analysis**

Conductivity was corroborated with flame photometer Na measurements and as results were entirely consistent (Appendix E), conductivity measurements were utilized for determining the blank breakthrough curves due to ease of measurement. Results comparing the conservative tracer for all Bio experiments can be seen in Figure 3.7, while results from the Blank experiments can be seen in Figure 3.8. For the Bio experiment, there are slight differences (within 3% total breakthrough) in the curves, thought to be due to the biofilm coating on the gravel, as when compared to the extremely similar curves within 1% difference in the Blank experiment. Even though the curves look slightly different within the Bio experiment, all DI results indicate that 100% of the conservative pulse broke through the column with 0% being retained in both the Bio and Blank experiments.

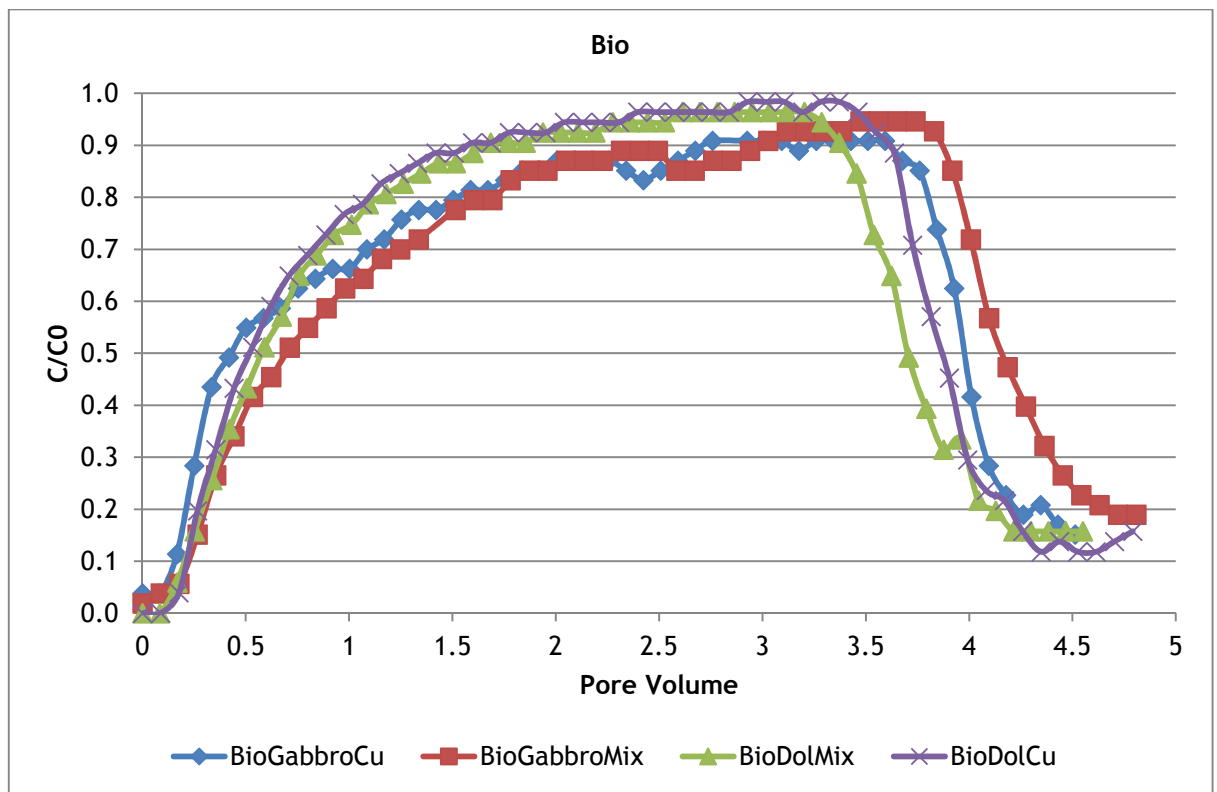


**Figure 3.7.** Comparison of conservative DI tracer breakthrough curves between four Bio growth columns. Refer to table 3.1 for details of each experiment

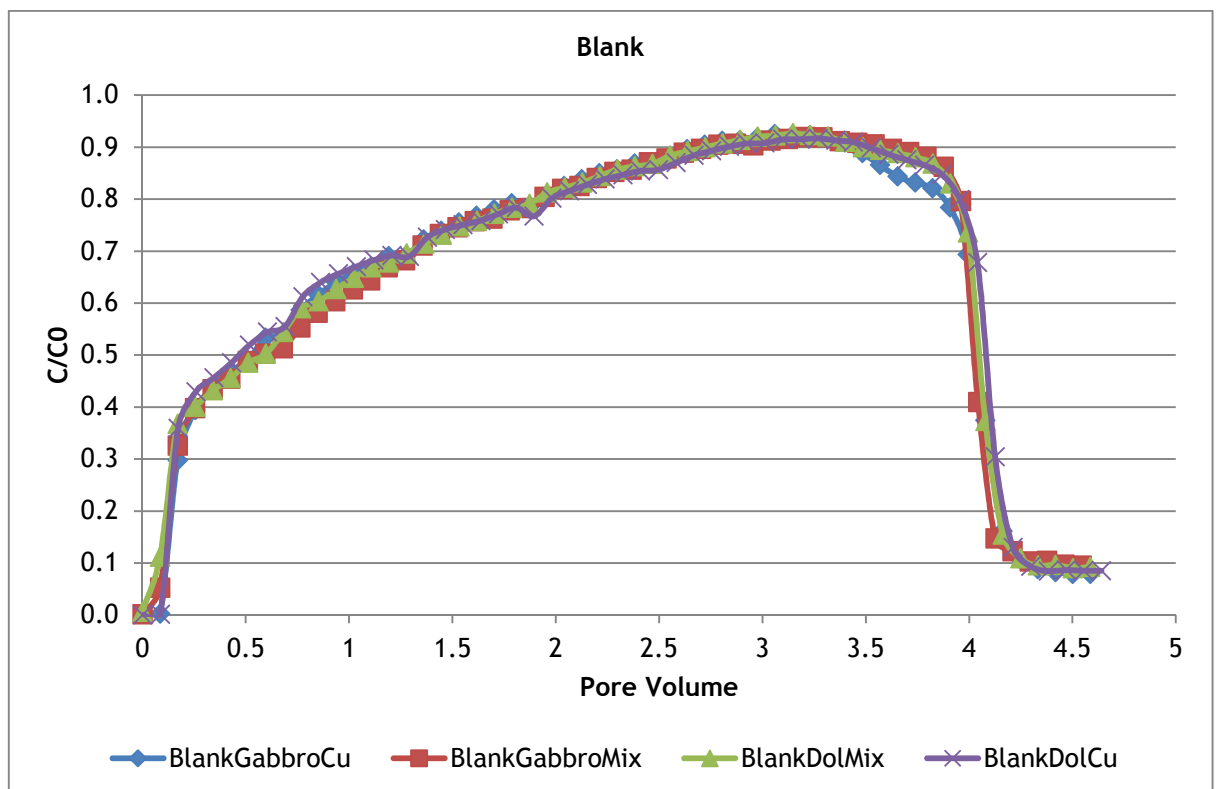


**Figure 3.8.** Comparison of conservative DI tracer breakthrough curves between four Blank columns.

Breakthrough curves which compare both the DI conservative tracer and the non-conservative tracer of either Cu or the mix of Cu, Pb and Zn of the Bio and Blank experiments are shown as follows: GabbroCu (Fig 3.9), GabbroMix (Fig 3.10), DolMix (Fig 3.11), DolCu (Fig 3.12). This data is summarized in Table 3.2 which shows the percentage of metal retention in both Bio and Blank columns.

% Metals Retained	GabbroCu	GabbroMix			DolCu	DolMix		
	Cu	Cu	Pb	Zn	Cu	Cu	Pb	Zn
Bio	61	59	65	59	45	29	38	8.4
Blank	44	37	51	51	16	8.4	24	11
Bio-Blank	17	22	14	8	29	20.6	14	2.6

**Table 3.2.** Percentage of metals retained within the columns between the Bio and Blank experiments. Bio-Blank shows the difference between the Bio and Blank columns.

Results demonstrate that blank and bio columns removed heavy metals from the water. Bio columns retained more metals than the Blank columns in all but one case (Zn removal in the DolMix column). In both Blank and Bio systems, Gabbro columns were more efficient at heavy metal removal than the Dolomite columns. Overall, the extent to which biofilms enhanced heavy metal removal (i.e. compared to blanks) was similar between gabbro and dolomite for mixed metal experiments, while in the Cu only systems, enhancement by the biofilm was almost double that of the gabbro system.

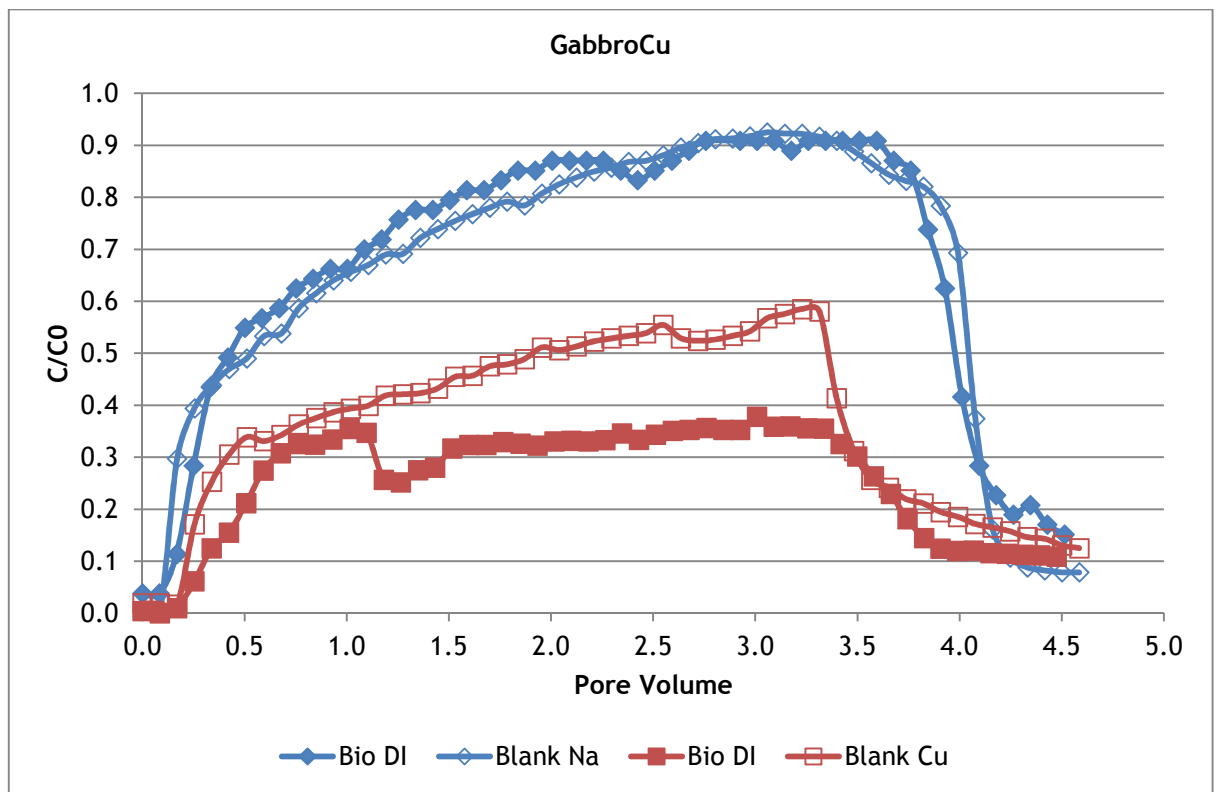


**Figure 3.9.** Comparison of DI water and Cu breakthrough between the microgabbro Bio and Blank experiments

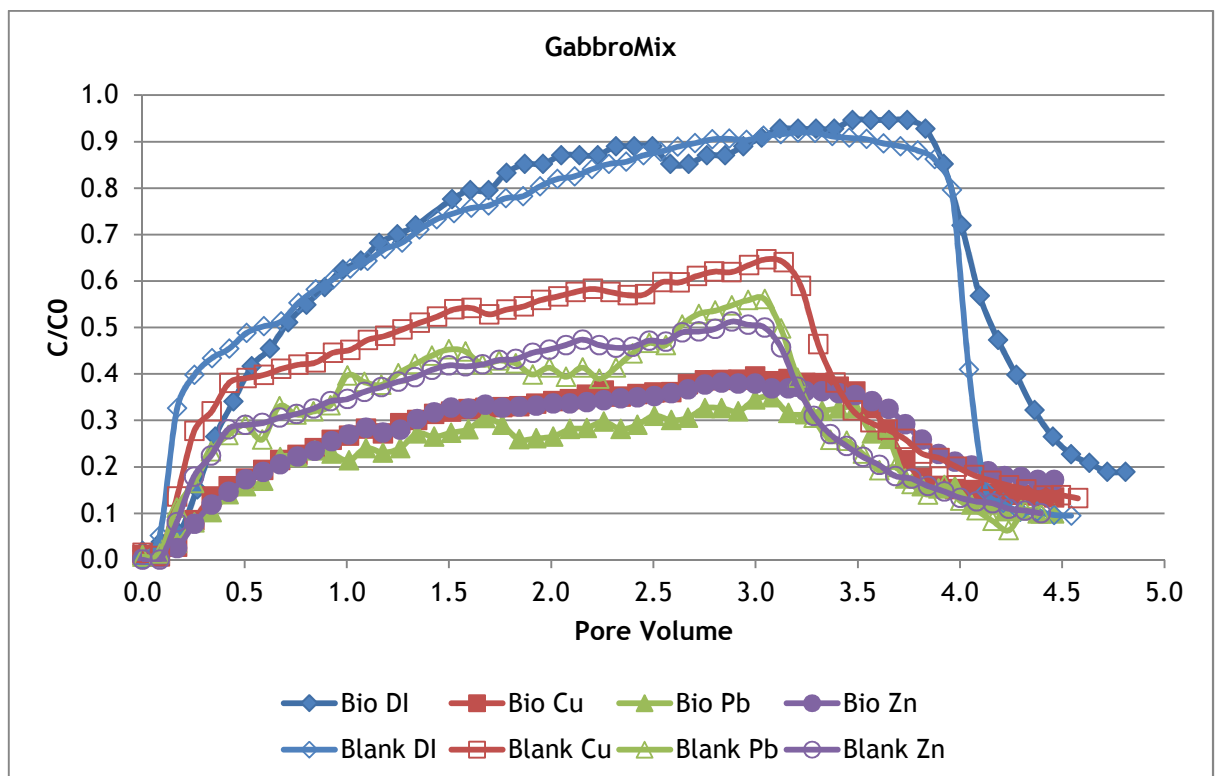


**Figure 3.10.** Comparison of DI, Cu, Pb and Zn breakthrough between the microgabbro Bio and Blank experiments

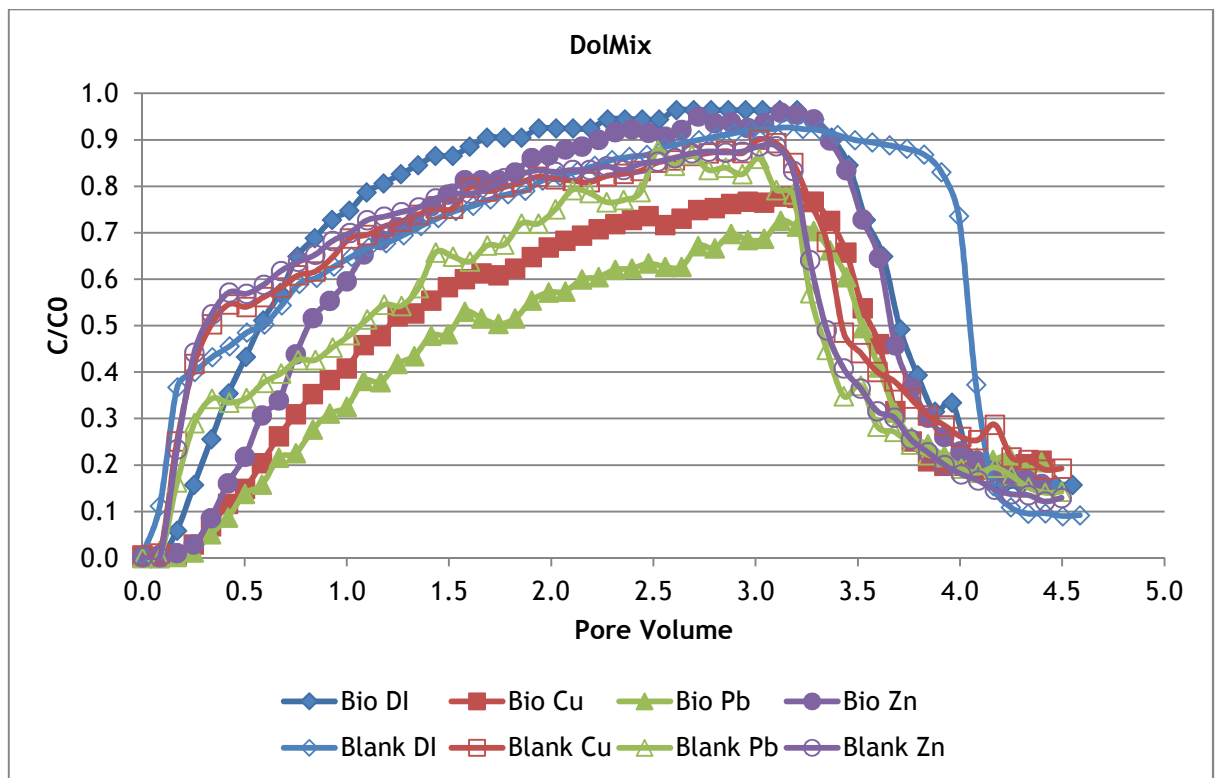


**Figure 3.11.** Comparison of DI, Cu, Pb and Zn breakthrough between the dolomite Bio and Blank experiments

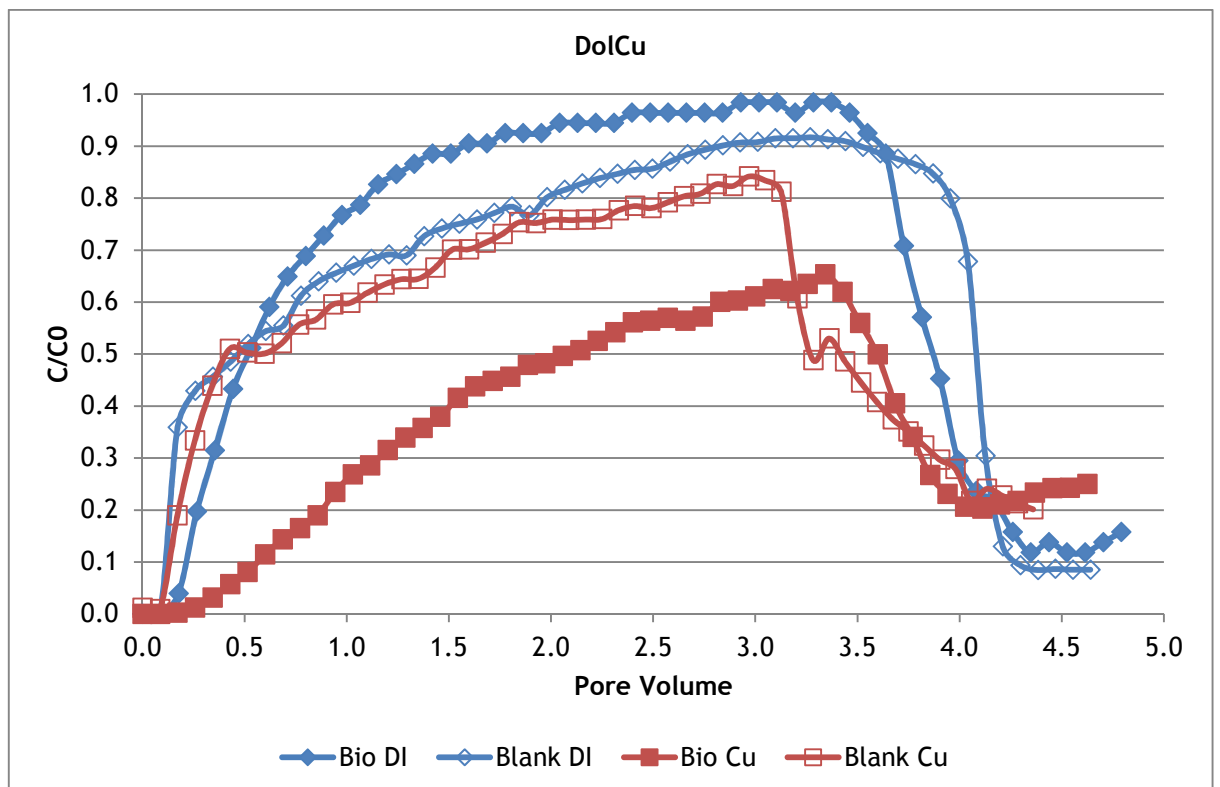


**Figure 3.12.** Comparison of DI and Cu breakthrough between the dolomite Bio and Blank experiments

Microgabbro columns performed better overall whether biofilm growth was present or not. BioGabbro columns retained concentrations of metals between

59-65% with an order of efficiency of Pb (65%) > Cu (59%) ≥ Zn (59%) in the mixed metal solution and Cu removal in the single metal solution (61%) was within 2% of the mixed metal solution. BlankGabbro columns retained between 37-51% with an order of efficiency as Zn (51%) ≥ Pb (51%) > Cu (37%) and Cu removal in the single metal solution (44%) was within 7% of the mixed metal solution. This resulted in the BioGabbro columns enhancing Cu removal by 17% (single metal) to 22% (multiple metal), Pb removal by 14% and Zn removal by 8% compared to the blank.

BioDol columns retained between 8-45% metals with an order of efficiency of Pb (38%) > Cu (29%) > Zn (8.4%) and 16% better Cu removal in the single metal solution (45%). BlankDol columns retained between 8-23% metals with an order of efficiency of Pb (24%) > Zn (11%) > Cu (8.4%) and 7.6% better Cu removal in the single metal solution (16%). This resulted in the BioDol columns enhancing Cu removal by 20.6% (multiple metal) to 29% (single metal), Pb removal by 14%, while Zn removal was 2.6% less in the Bio column compared to the Blank column. Though, both dolomite columns removed very little Zn overall, retaining only 8.4-11% Zn.

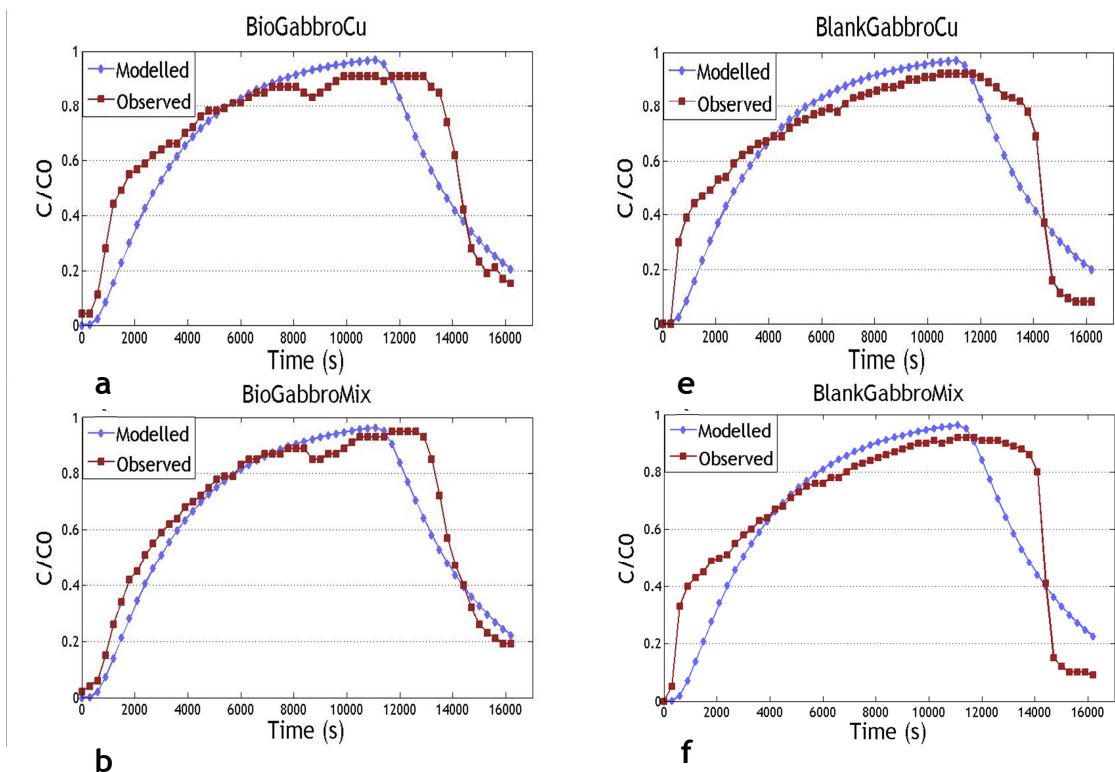
### 3.3.2 Breakthrough curve modelling

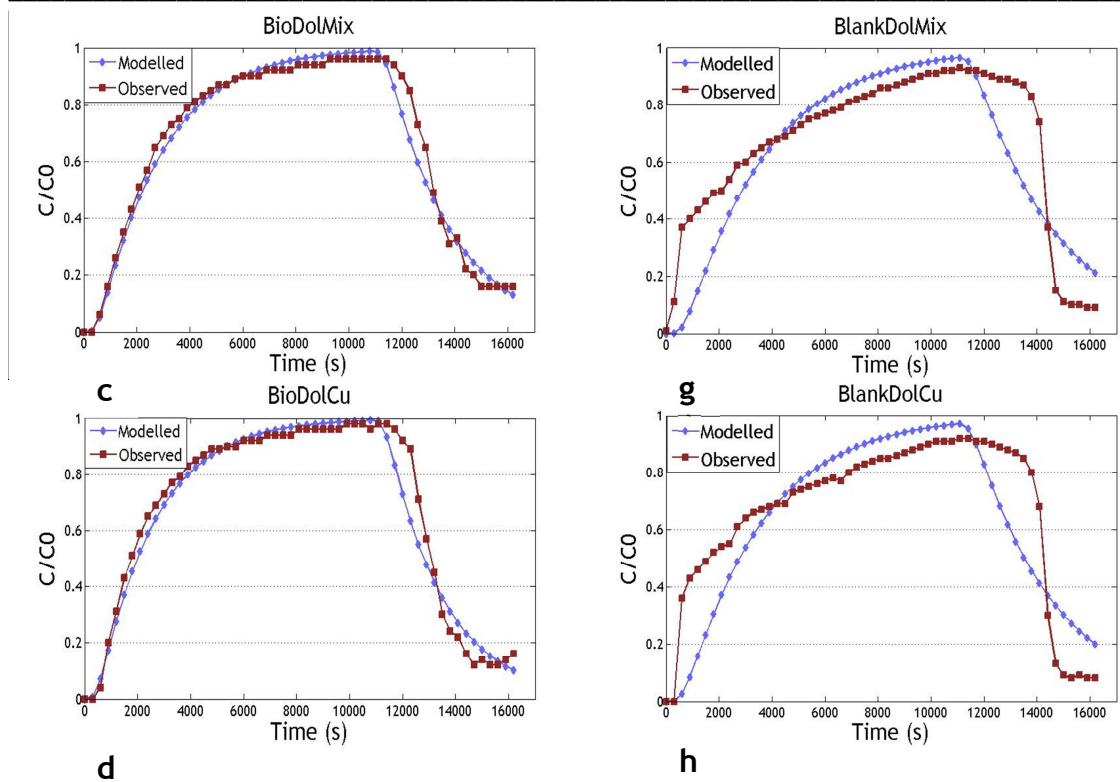
Table 3.3 summarizes the results of the advection diffusion model which solves the equation for the dispersion coefficient ( $D$ ,  $m^2/s$ ) and the loss term for the metal tracers ( $k$ ,  $(mg/l)/s$ ). The root mean squared error (RMSE) has also been determined as a measure of goodness of fit between the observed and modelled breakthrough curves. Note that  $k$  was fixed at zero when modelling the Blank experiments.

		<i>D</i> - Dispersion Coeff. ( $m^2/s$ )		<i>k</i> - Loss Term (( $mg/l/h$ ))		Root Mean Squared Error	
		BIO	BLANK	BIO	BLANK	BIO	BLANK
GabbroCu	DI	2.93E-06	2.94E-06	0.00	0.00	0.047	0.055
	Cu	3.58E-06	5.00E-06	1.05	0.82	0.027	0.042
GabbroMix	DI	2.78E-06	2.76E-06	0.00	0.00	0.033	0.061
	Cu	2.67E-06	5.26E-06	0.71	0.68	0.020	0.038
	Pb	2.51E-06	4.44E-06	0.84	0.91	0.020	0.029
	Zn	2.32E-06	4.28E-06	0.60	0.88	0.028	0.030
DolMix	DI	3.60E-06	2.84E-06	0.00	0.00	0.017	0.060
	Cu	3.54E-06	6.33E-06	0.22	0.17	0.028	0.052
	Pb	2.99E-06	5.35E-06	0.28	0.34	0.025	0.044
	Zn	4.34E-06	7.65E-06	0.01	0.26	0.038	0.043
DolCu	DI	3.99E-06	2.96E-06	0.00	0.00	0.022	0.060
	Cu	2.70E-06	5.41E-06	0.37	0.24	0.023	0.056

**Table 3.3.** Advection diffusion model results for dispersal coefficient (*D*), loss term (*k*) in (mg/l/h) and goodness of fit (RMSE)

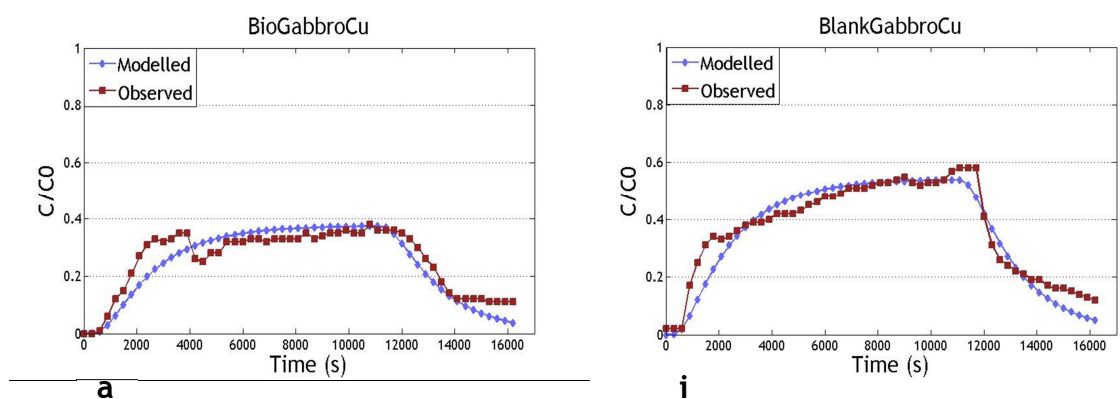
The breakthrough curves for the observed results of the DI tracer as reported as  $C/C_0$  versus time in seconds are plotted against the modelled curve as determined by the advection diffusion model results in Figures 3.13a-d for the Bio experiments and 3.13e-h for the Blank experiment. These graphs are shown for completeness. However, due to the large amount of data shown in the graphs, it is recommended the reader simply refer to Table 3.3 for the salient points.

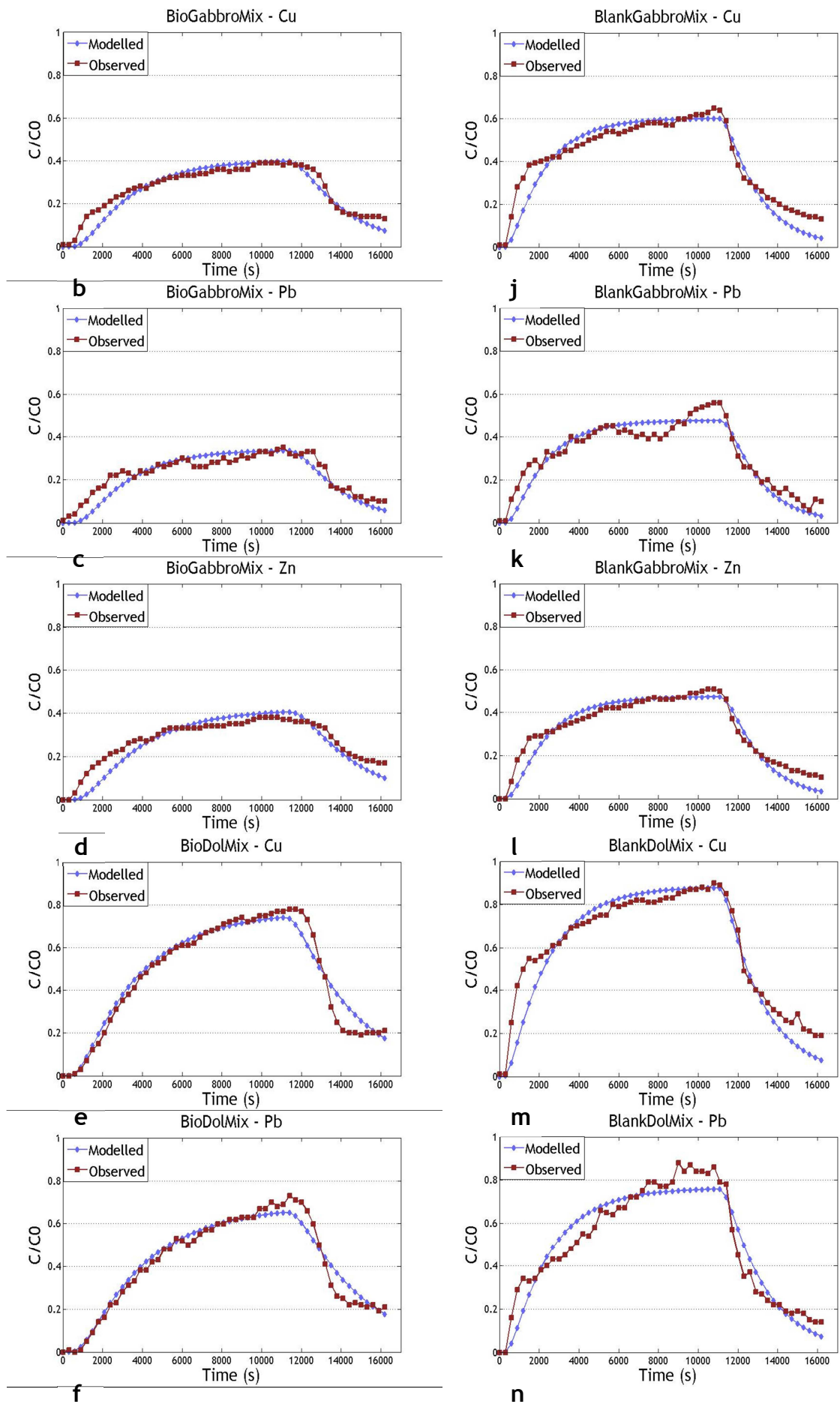




**Figure 3.13** (a) BioGabbroCu (b) BioGabbroMix (c) BioDolMix (d) BioDolCu (e) BlankGabbroCu (f) BlankGabbroMix (g) BlankDolMix (h) BlankDolCu predicted advection diffusion curve compared to observed results for the Na conservative tracer

Modelled advection diffusion results compared to the observed results for all Bio metal breakthrough experiments can be seen in Figures 3.14a-h, while the Blank metal breakthrough experiments can be seen in Figures 3.14i-p.





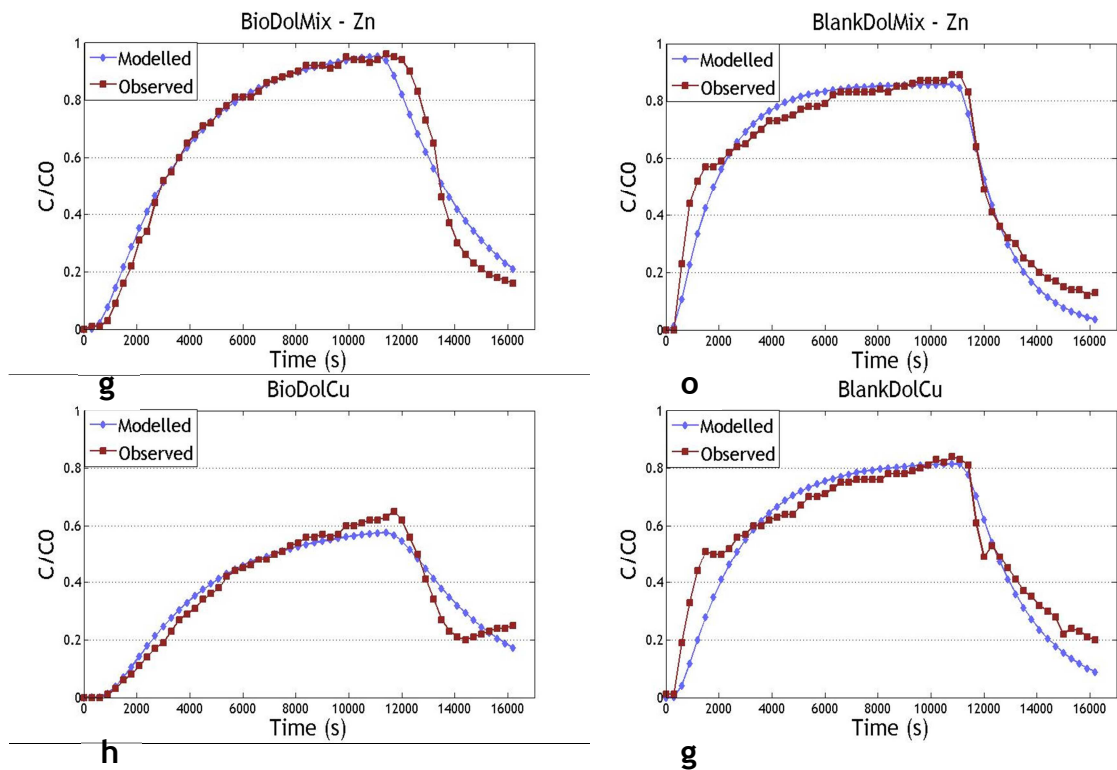


**Figure 3.14** (a) BioGabbroCu (b) BioGabbroMix - Cu (c) BioGabbroMix - Pb (d) BioGabbroMix - Zn (e) BioDolMix - Cu (f) BioDolMix - Pb (g) BioDolMix - Zn (h) BlankDolCu (i) BlankGabbroCu (j) BlankGabbroMix - Cu (k) BlankGabbroMix - Pb (l) BlankGabbroMix - Zn (m) BlankDolMix - Cu (n) BlankDolMix - Pb (o) BlankDolMix - Zn (p) BlankDolCu predicted advection diffusion curve compared to observed results for the Cu, Pb or Zn non-conservative tracers

Overall, the modelled versus observed breakthrough curves have a good measure of fit visually, and while there is no specific criterion for a good RMSE value, it is acknowledged that the smaller the value the better the fit. It is also apparent that the metal tracer experiments fit the modelled breakthrough curves better than the conservative tracer experiments. Since the conservative tracer model had the loss term ( $k$ ) fixed at 0, it is believed that the extra parameter of  $k$  that the metal model had to work with was able to produce a better goodness of fit due to having the option to adjust the extra term. From Figure 3.15, it is confirmed that the  $k$  term determined from the model does follow a linear trend and correlates with the observed percentage of metals removed within the column, though better in the Blank metal experiments ( $R^2 = 0.97$ ) than the Bio metal experiments ( $R^2 = 0.83$ ).

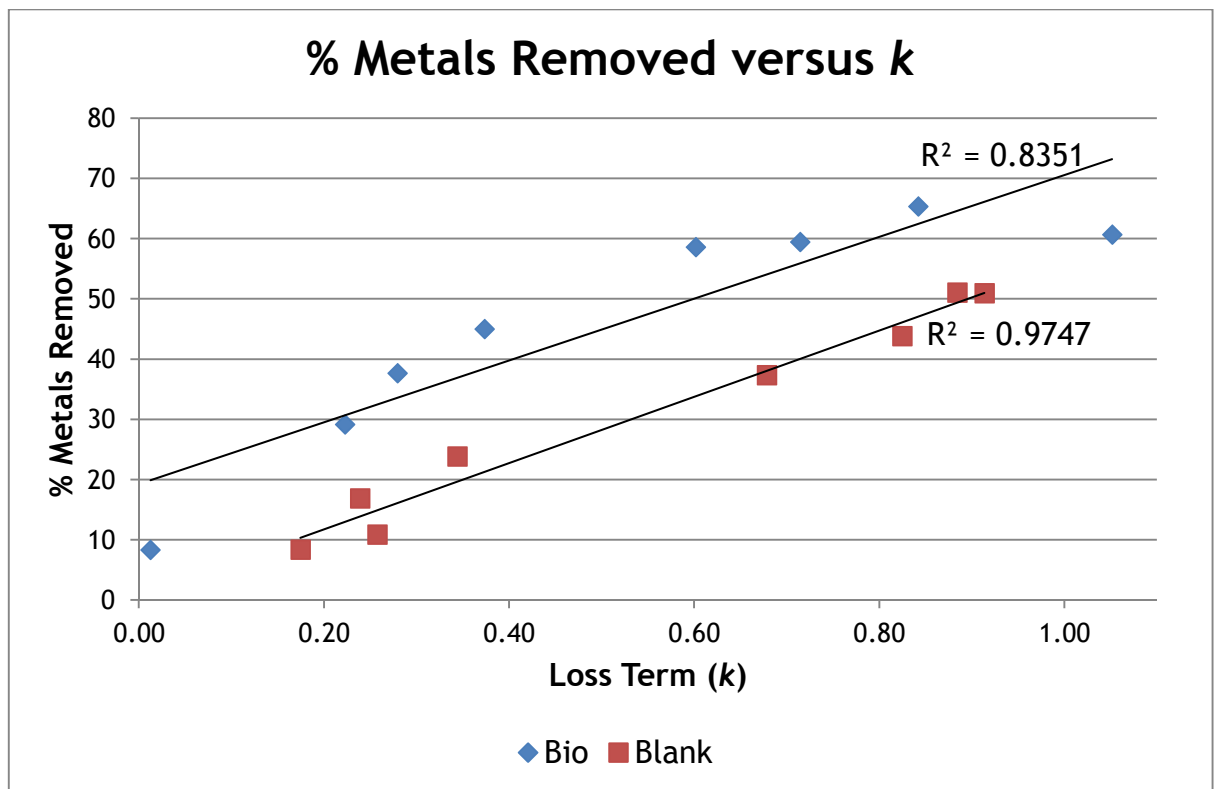


**Figure 3.15.**  $k$  loss term determined from model correlating to percentage of metals retained in experimental columns.

### 3.3.3 Clone library

A clone library of the initial biofilm growth column containing filter drain gravel was performed on a 10 month old sample of biofilm (Fig 3.16) taken from the column (Fig 3.3a) and influent bottle (Fig 3.3b) and subsequently used to inoculate the four experimental biofilm growth columns.

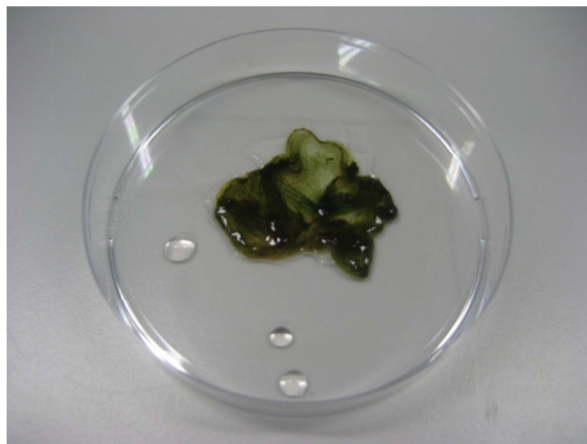


**Figure 3.16.** Sample of biofilm used for clone library analysis and to inoculate Bio columns.

The results of the clone library and breakdown of phyla can be seen in Figure 3.17, which shows that the initial filter drain biofilm growth is composed of 71% *Cyanobacteria*, followed by 9% *Firmicutes*, 5% *Proteobacteria* and all other phyla listed representing less than 15% of the biofilm makeup at values lower than 5%. Clone library frequency and classification can be found in Appendix F.

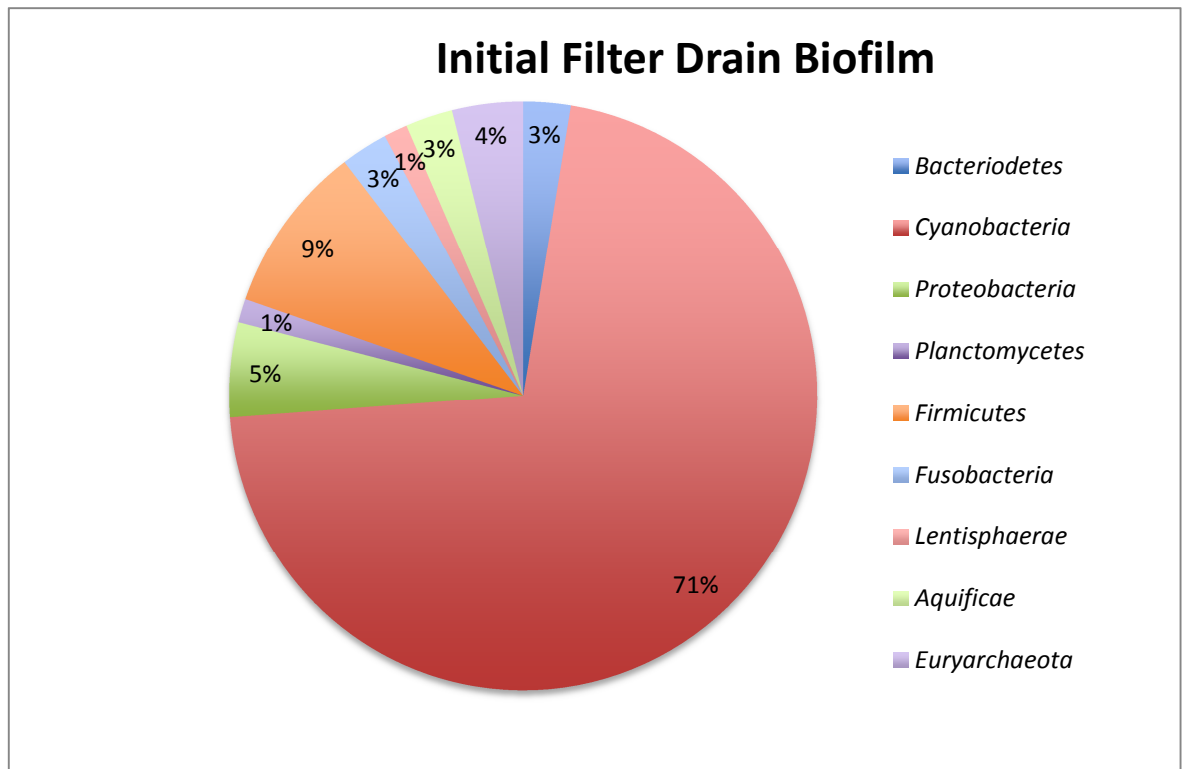


**Figure 3.17.** Graph of representative phyla of bacteria for initial filter drain biofilm growth as determined by clone library analysis.

Once a section of biomass of the initial filter drain biofilm was separated for clone library analysis, the remaining biomass was split into two as inoculant within SuDS pond water for a set of microgabbro and a set of dolomite for growth within the experimental columns. After 8 months growth and breakthrough experiments were run on the Bio columns, two samples of biomass were collected from throughout the column of each set of microgabbro columns and each set of dolomite columns. Samples from throughout the columns were combined together for clone library analysis. Results for the composition of microgabbro biofilm and dolomite biofilm clone libraries are summarized in Figures 3.18a and 3.18b respectively. Both microgabbro and dolomite gravel columns show reduced diversity compared to the original biofilm inoculum, with a majority of both biofilms being composed of three main phyla of bacteria: *bacteroidetes*, *cyanobacteria* and *proteobacteria*. Each of the different gravel

clone libraries demonstrates that about half is composed of a dominant phyla, while the other two phyla are similarly split between 20-25% and *planctomycetes* and *crenarchaeota* contributing a minor 1-4% overall. While the dolomite biofilm is still composed of a majority of *cyanobacteria* at 47% (Fig 3.18b), followed by 25% *proteobacteria* and 22% *bacteriodetes*, the majority of the microgabbro biofilm has shifted towards *proteobacteria* at 54% (Fig 3.18a) followed by 25% *cyanobacteria* and 20% *bacteriodetes*. Further breakdown of the distribution of classes of *proteobacteria* can be found in Appendix G. The phylogenic tree of all bacteria identified within the experimental growth columns can be found in Appendix H. Classification of clones and clone library breakdown data can be found in Appendix F.

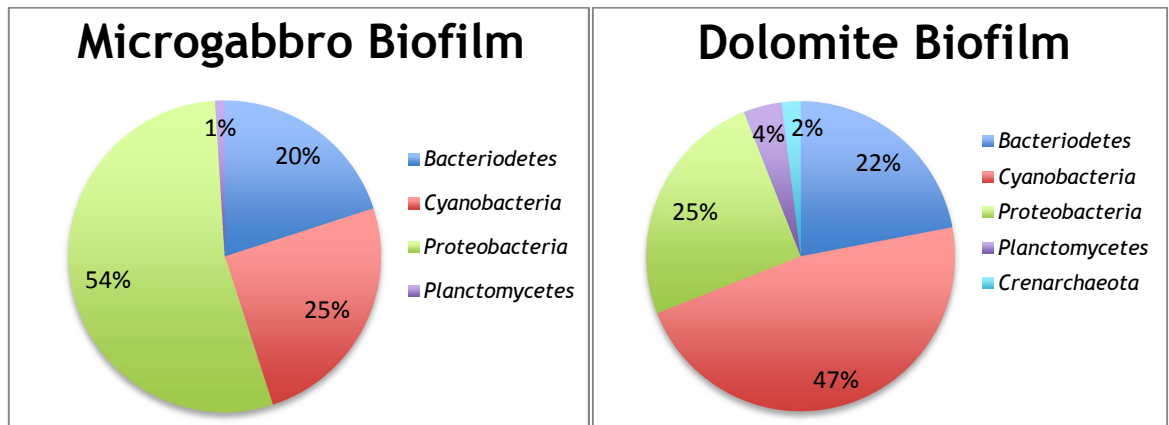


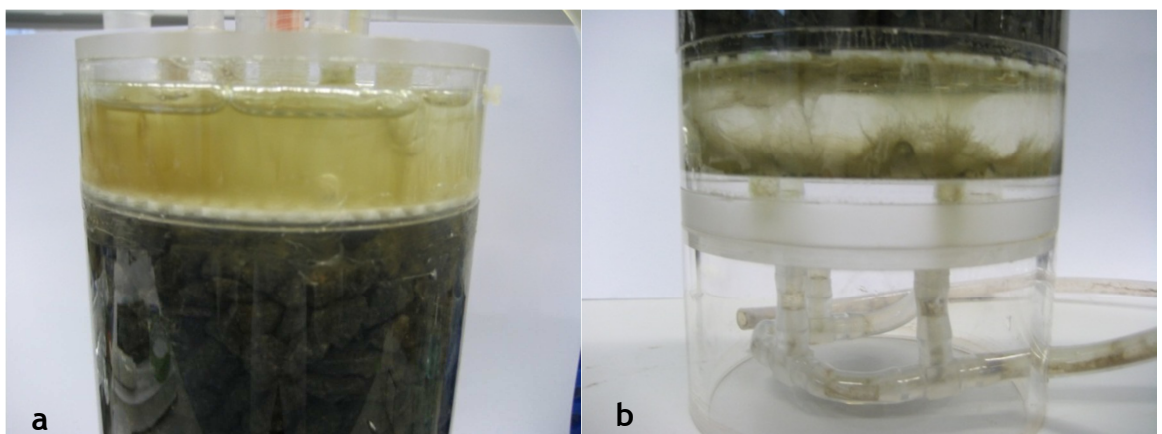
**Figure 3.18.** Graph of representative phyla of bacteria for (a) microgabbro and (b) dolomite experimental column biofilm growth as determined by clone library analysis.

Due to the same biomass inoculant utilized for each of the different gravel experimental columns and the resulting shift in bacterial community, the clone library results indicate that biofilm composition is indeed influenced in some part by gravel lithology. Not only did the clone library analysis reveal different bacterial communities between the microgabbro and dolomite columns, photos of columns during the growth period show very different conditions (Fig 3.19a), notably that the dolomite columns produced a bright red-orange recirculated pond water (Fig 3.19b). The properties of the biofilms consistency and structure were also different when the columns were dismantled to collect the clone library samples. Noted properties of the microgabbro columns were that the biofilms were more slimy and brown in color at the top of columns (Fig 3.20a) while stringy at the bottom of the column (Fig 3.20b-c) and that a thick brown

biofilm grew on the mesh diffuser plate (Fig 3.20d) and along the Perspex sides of the columns. While for the dolomite columns, the biofilm appeared to be brownish but with flecks of green (Fig 3.21a) in sticky clumps that grew around individual grains of dolomite (Fig 3.21b-c), filamentous along the Perspex and a thick uniform layer over the mesh diffuser plate (Fig 3.21d). Photos of the biofilm collected from each growth column can be seen in Figures 3.22a-b.



**Figure 3.19.** (a) Dolomite (back) and microgabbaro (front) columns after 4 months growth. (b) influent/recirculated water feed for dolomite (left) and microgabbaro (right)



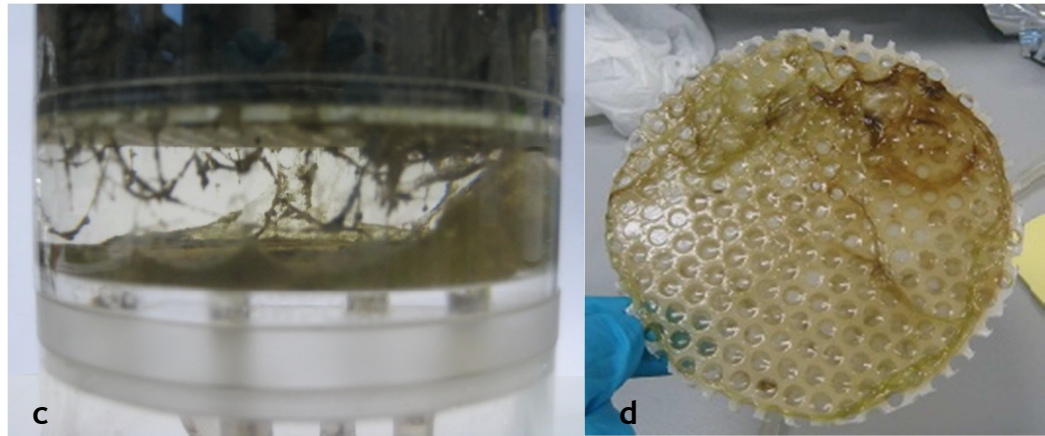


**Figure 3.20.** (a) Biofilm growth near the top of the microgabbro column (b-c) biofilm growth near the bottom of the microgabbro columns (d) biofilm growth on the mesh diffuser plate in the microgabbro column



**Figure 3.21.** (a) Biofilm growth in the dolomite column (b-c) biofilm growth around individual dolomite grains (d) biofilm growth on the mesh diffuser plate in the dolomite column

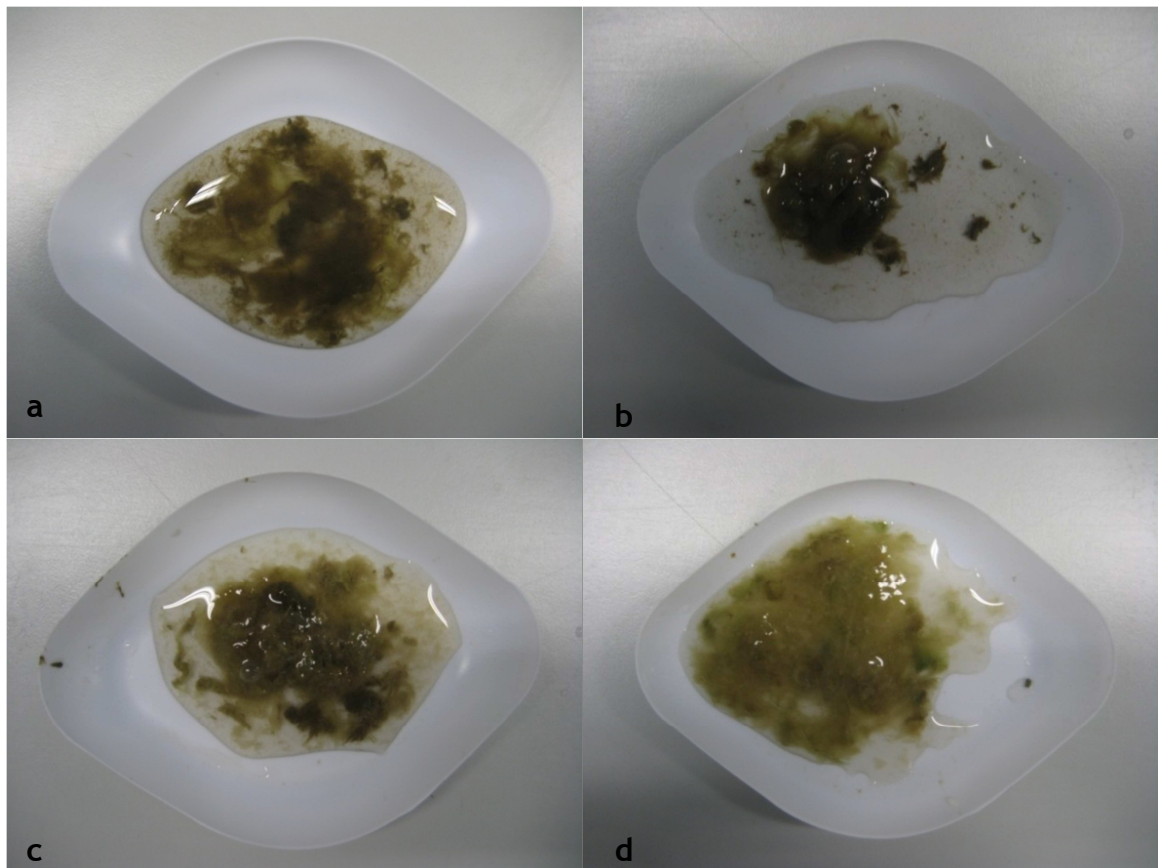


**Figure 3.22.** (a) Biofilm collected from BioGabbroCu (b) biofilm collected from BioGabbroMix (c) biofilm collected from BioDolMix (d) biofilm collected from BioDolCu

## 3.4 DISCUSSION

### 3.4.1 Breakthrough curve analysis

The conservative tracer of DI in both Bio and Blank columns demonstrated 100% breakthrough, as expected from a conservative tracer. Blank columns exhibited very similar breakthrough curves for the conservative tracer indicating identical dispersion (the combination of advection and diffusion) occurred during transport in all blank columns. Although again very similar, slightly larger differences in breakthrough curves were observed when biofilms were present, indicating the biofilms had a small, but measurable impact on dispersion within the column. While the Bio columns illustrated slightly different curve shapes between columns (within 3% of total breakthrough) all still demonstrated 100% breakthrough. Blank columns also had a slightly different shape curve to the Bio columns but when the gravel columns had no biofilm growth, the conservative tracer curves were very similar, within 1% difference of each other. It could therefore be assumed that all 4 Blank columns exhibited the same solute

transport conditions, and that the small differences within the Bio columns was due to biofilm growth. Since all columns still exhibited 100% conservative tracer breakthrough, differences in metal breakthrough could thus be considered due to reactivity of the gravel media and biofilm growth respective to each column.

Metal breakthrough curves collected for a set of biofilm-coated porous media columns compared to a set of porous media columns without biological growth clearly demonstrated enhanced heavy metal removal due to the presence of biofilm. When comparing percentages of metals retained within the columns as determined by calculating the area under the breakthrough curves, all but one biofilm growth column (DolMix - Zn) showed improved metal removal between 7-29%, depending on type of gravel and metal involved.

All concentrations of metals retained in the blank dolomite columns were lower than the microgabbro columns indicating that microgabbro has a better metal binding capacity to dolomite. This corroborates with results from Chapter 2 and is discussed in detail in Section 2.4.2 which outlines that certain rock forming minerals in microgabbro weather to clay minerals, enhancing heavy metal uptake when compared to dolomite, whose surface elicits inherently different metal complexation.

Examination of the mixed metal experiments demonstrates that Cu is removed less than Pb and Zn in the blank columns suggesting that certain removal mechanisms are occurring for Pb and Zn that are not available for Cu. However, when the columns were amended with biofilm, the biofilm improved copper removal more than it did for Pb and Zn. In short, blank systems have a relatively low affinity for Cu while biofilms have a relatively high affinity for Cu. This is significant as the addition of the biofilm to the system helps to overcome the weakness in Cu absorption by the blank system: the combined gravel-biofilm system is thus synergistic. While the addition of biofilm appears to increase adsorption within the experimental setup of the current study, some have suggested that biofilm may lead to the opposite effect by smothering reactive sites on minerals, in turn leading to decreased adsorption (Kulczycki et al. 2005; Anderson et al. 2006). Thus, if masking of binding sites is occurring, it must be significantly less than the additional benefits of the biofilm.

### 3.4.2 Breakthrough curve modelling

The advection-diffusion model was utilized to assess the experimental breakthrough curves against the partial differential equation typically used to describe one-dimensional transport of reactive solutes within a homogenous medium during steady state flow (Equation 3.3). All modelled curves fit the experimental breakthrough curves well, and the RMSE values in Table 3.3 are used as an indication of goodness of fit of the two curves. RMSE values ranged between 0.017 - 0.061 for all Bio and Blank columns in both the conservative and reactive tracer experiments. Although fits for both Bio and Blank columns are good, the model fit for Bio columns were slightly better with lower RMSE values between 0.017 - 0.047 (average 0.027) while Blank values were slightly higher between 0.029 - 0.061 (average 0.047). The lower RMSE values for the Bio columns indicate that the mechanisms integral to the advection diffusion model are slightly better suited for describing the breakthrough curves in the Bio columns over the Blank columns. The very low RMSE values indicate the model was very effective at describing both the dispersion ( $D$ ) and metal immobilization ( $k$ ) of the system.

The linear loss term,  $k$ , describes permanent immobilization of metals, as opposed to a retardation factor which describes non-permanent immobilization (i.e. metals are only briefly stopped but then allowed to progress further through the column). The excellent quality of fit indicates metal immobilization mechanisms are permanent within the column. Metal immobilization processes such as precipitation, bioaccumulation (the uptake of metal inside the cell) or strong adsorption can be considered permanent at the time scales of this experiment. Although adsorption is an equilibrium process and thus reversible, adsorption constants for metals onto minerals and bacteria are high with stability constants for metal-carboxyl surface complexes in metal-bacteria adsorption experiments reported as 4.2 for Pb and 4.3 for Cu in Fein et al. (1997), indicating metal complexation is extremely stable. The significant changes in environmental conditions (such as acidification to pH's below 3-5, depending on metal and geochemical parameters involved) required to remobilize significant quantities of adsorbed metals did not occur in these experiments, again supporting the notion that adsorption can be considered permanent here. While precipitation, bioaccumulation and adsorption could all

be at play here, more advanced models and further experimentation would be required to decipher the relative contribution of each.

Gabbro columns removed between 0.60 - 1.05 ppm of Cu, Pb or Zn per hour while Dolomite columns removed between 0.01 - 0.37 ppm of Cu, Pb or Zn per hour. The  $k$  value determined from the model can be used in support of the overall percentages of metals retained within the columns, as shown in Figure 3.16, in which a linear correlation is demonstrated between an increase in percentage removal with increasing  $k$  values.

Dispersion coefficients are typically between  $10^3 - 10^4$  (Schnoor 1996) and while all gravel columns exhibited lower dispersion at values of  $10^{-6}$ , this could be due to the mixing zones in the experimental flow cell on either end of the gravel filter. While the dispersion coefficients may not compare to other gravel systems in the literature, it was assumed that the zones without gravel were well mixed and thus, coefficients are comparable between column experiments within this study. Dispersion for the metal tracers in the Bio columns was between  $D = 2.32 \times 10^{-6} - 4.34 \times 10^{-6}$  (average  $3.08 \times 10^{-6}$ ) while for the Blank columns  $D$  values were between  $4.28 \times 10^{-6} - 7.65 \times 10^{-6}$  (average  $5.47 \times 10^{-6}$ ). Dispersion of metal tracers increased in all Blank columns compared to the Bio columns, upholding the thought that biofilm growth in porous media would be expected to decrease pore space, velocity and hydraulic conductivity (Taylor and Jaffe 1990; Vandevivere and Baveye 1992b; Vandevivere and Baveye 1992a; Yang et al. 2013) while increasing path length and friction.

The RMSE values along with visual validation of a goodness of fit between predicted and experimental breakthrough curves indicates that the advection-diffusion equation can be used to describe contaminant transport within experimental gravel filters (with or without biological activity). The equation is therefore suitable for analyzing metal removal in the gravel column system and determining the dispersion coefficient ( $D$ ) and loss term ( $k$ ) for specific column experiments. Potential mechanisms of permanent immobilization includes precipitation, bioaccumulation, and biosorption (Section 3.4.3) that are therefore consistent with the  $k$  term, although determination of which specific mechanism are responsible for metal removal in a particular system is very difficult and depends on a multitude of biochemical factors involved (De

Philippis et al. 2011). The advection-diffusion equation is a simpler approach to modelling breakthrough curves as precise mechanisms are not discriminated for, though, the model has proven to fit the data set effectively and therefore, a more advanced model discerning removal mechanisms was not sought as it goes beyond the scope of this research. Importantly, the goodness of fit of the model indicates it may be used to predict contaminant transport within gravel SuDS systems.

### **3.4.3 Biofilm enhancement of metal-immobilization**

There are many forces believed to be involved with metal immobilization within the systems, including adsorption and precipitation. Metals are removed from solution due to adsorption to the gravel media, as discussed in Chapter 2 and precipitation due to supersaturated conditions present for Cu and Pb. As mentioned earlier, biofilm interactions with heavy metals are widely reported in the literature. The observed enhanced metal removal of columns with biofilm growth compared to columns without biofilm growth is therefore believed to be due to microorganisms sequestering heavy metals more readily than the gravel subsurface. This enhanced metal binding can be due to many factors including cellular processes as well as reactions of the cellular wall and surrounding bacterial surface layers including EPS.

The bacterial surface of the microorganisms within the biofilm is considered to be an important aspect to the enhanced metal binding capacity of the Bio columns. Moreover, due to the observed presence of biofilm growth with an abundant coating of slimy EPS, it is believed that the EPS was integral to enhanced metal binding in the Bio columns. EPS is naturally excreted by microorganisms in order to protect the cells while also promoting aggregation and stabilization through adhesion to surfaces and formation of a biofilm community. The EPS may act both as a barrier for toxic substances through immobilization on the surface as well as controlling what metals are internalized for cell function. EPS also exhibits a negative surface charge in the circumneutral situations encountered in many environmental applications, and as such, the metal binding capacity of EPS with positively charged metal ions has been well documented (Harden and Harris 1953; Mittelman and Geesey 1985; De Philippis et al. 2001; De Philippis and Vincenzini 2003; Micheletti et al. 2008; De

Philippis and Micheletti 2009; Pereira et al. 2011; Yang et al. 2013). When considering bioremediation, as in the current study, to which biofilms were subjected to an elevated concentration of heavy metals, it is thought that the negative surface charge of the cell surface and EPS sequestered positively charged metals.

Other cellular processes could be involved in bacterial metal removal including active internalization of metals (bioaccumulation). While it is not known the degree to which metals could have actively been taken into bacterial cells versus passive adsorption to surfaces, this is a question for future research. Further, due to the phototrophic nature of the microbial communities in the biofilms, the process of photosynthesis may play a role in metal removal within the systems. During photosynthesis,  $\text{HCO}_3^-$  is consumed resulting in production of hydroxyl ions that are released from the cell, increasing the pH of the system and the possibility of metal precipitation (Merz 1992). This process may lead to surface mineralization of precipitated minerals and metals on the cell surface and within the EPS. If, and when, biomineralization would occur within a SuDS filter drain biofilm is also a question for future research.

pH measurements before and after recirculation of pond water within the Bio columns did indicate an elevated pH after biofilm growth in the columns from the initial pH of 7.4 to 8.6 measured in the bottle of recirculated pond water after 8 months, hence, it is likely that the phototrophic biofilms did increase pH and the potential for metal precipitation in the systems. While an increase in pH was seen within the current experimentation, it is also possible that precipitation effects may be more pronounced at a localized level where increases in pH within EPS of photosynthetic biofilms could cause localized increases in metal saturation (and thus precipitation) without markedly increasing pH and saturation of the bulk of the system (Phoenix et al. 2000). Though, initial pH of the Influent metal solution conditions were input into the PHREEQC geochemical modelling program had already determined that all (single and multiple metal) Cu ( $\text{Cu}(\text{OH})_2$  SI = 0.74 - 0.86) and Pb ( $\text{Pb}(\text{OH})_2$  SI = 1.67 - 1.70) solutions were supersaturated (saturation index, SI > 1) while Zn ( $\text{Zn}(\text{OH})_2$  SI = -0.89 - -0.91) solutions were undersaturated (SI < 1) at the circumneutral influent pH. Therefore, it is believed that the undersaturation within the Zn experiment may contribute to the reduced Zn removal observed,

while precipitation may contribute to the Cu and Pb removal to some degree. Since the influent metal solutions and SI's were equivalent in the Blank versus Bio experiments, any precipitation due to supersaturation would be comparable between the two. Though, the elevated pHs within the Bio columns (due to the photosynthetic process) may have contributed to the overall metal removal enhancement within the systems through precipitation. The precise concentration of metals removed due to either adsorption to cell surfaces or precipitation due to elevated pH or supersaturation is not necessarily realized within the current study, as such, is a further question for future research.

### 3.4.4 Clone library

Clone library results indicate that a biofilm grown from SuDS filter drain gravel and pond water consisted of a majority of *cyanobacteria* at 71% followed by a variety of eight other bacterial phyla at lower occurrences. It is not surprising that the green, slimy biofilm grown (Fig 3.16) in the initial column (Fig 3.3a) with filter drain gravel (Fig 3.3c) is made up mostly of *cyanobacteria*, which are aquatic and phototrophic organisms. *Cyanobacteria*, also known as blue-green algae, are a diverse group of prokaryotic bacteria that produce oxygen during photosynthesis. Furthermore, *cyanobacteria* commonly produce an abundance of extracellular polymeric substances (EPS) in the form of sheaths, capsules and/or slimes typically formed of polysaccharides (Pereira et al. 2011). This EPS has been widely reported in the literature as effectively removing heavy metals through biosorption from aqueous solutions (De Philippis et al. 2001; De Philippis and Vincenzini 2003; De Philippis and Micheletti 2009). Though, De Philippis et al. (2011) points out that determining a general mechanism for biosorption of metals by EPS is very difficult and relies on numerous biochemical factors. Therefore, the characteristic properties of *cyanobacteria* seen and genetically identified in the slimy-green filter drain biofilm and subsequently inoculated and identified in the microgabbro and dolomite columns are believed to contribute to the enhanced metal removal exhibited in the Bio column experiments. Also worth noting is that there is a likely possibility that algae may contribute to the overall biofilm community but due to limitations in expertise and time constraints it was not possible to determine this for certain.

Once this filter drain biofilm was inoculated into the experimental microgabbro and dolomite columns, the distribution of microorganisms changed, presumably in response to the different composition of gravel. While specific bacterial dynamics and aggregation on any surface can be considered a complex subject, two main aspects are postulated within the current study as to why the observed differences in community (both visually and genetically identified) are seen within two different types of gravel. First, microgabbro and dolomite have very different chemical makeups, and the specific minerals distinctive to each type of gravel may influence bacterial community population specifically. While dolomite is made up of a single mineral (calcium magnesium carbonate -  $\text{CaMg}(\text{CO}_3)_2$ ), microgabbro may be made up of a multitude of rock forming minerals, as previously discussed in Chapter 2, such as feldspars, pyroxenes or olivine, all containing different microelements such as magnesium, iron, silicon, aluminium, calcium or sodium. The different minerals and elements within each lithology of gravel may offer specific nutrients or conditions to specific types of microorganisms and thus, some bacterial populations may prosper better within each type of gravel. For example, dolomite may experience some dissolution in water in which carbonate ions are released, thus increasing the alkalinity and the potential for specific organisms to colonize. Research by Gleeson et al. (2006) found strong evidence that the chemical composition of specific mineral groups extracted from granite were able to selectively influence bacterial populations, and as such, it is believed that the different chemical compositions of gravel within the current study are affecting the bacterial communities in a similar manner. Second, differences in surface characteristics of each type of gravel may have similar effects on bacterial communities in that they may favour one community over another. Since different microorganisms produce different EPS, biofilm attachment by various communities may be preferential towards a specific surface charge (dolomite is positive, microgabbro exhibits an array of different charges as it is multimineralic), preferentially colonize on that surface.

In depth information on bacterial communities within filter drains or SuDS systems is scarce within the literature and thus, is difficult to compare the community composition found here with other SuDS systems. It is likely that filter drains and SuDS systems would contain quite different communities of

microorganisms depending on environmental conditions, gravel type and influents to the system. Limitations of the current study including the growth conditions in natural light, the recirculated pond water, the unknown evolution of the biofilm over time in the laboratory and the fact that algae may contribute to the biofilm community further make it difficult to compare to natural SuDS systems. Even so, determination of bacterial communities of biofilm within this study enabled a better look at what is possible within a locally collected filter drain biofilm as well as set a baseline to determine effects of gravel lithology on communities within the experimental column experiments. While the model demonstrated permanent immobilization mechanisms, such as precipitation, adsorption and bioaccumulation were likely present, it is not possible to directly link these mechanisms to any specific taxa. However, the fact that two quite different bacterial communities both helped enhance metal removal to a broadly similar extent, and that both could be explained by the same simple permanent loss model is encouraging. It tentatively suggests that despite the expectation of different bacterial communities in different SuDS systems, broadly similar immobilization process will occur.

### 3.5 CONCLUSION

Biofilm growth columns revealed a 8-29% enhancement of heavy metal immobilization in when compared to Blank columns. Microgabbro columns demonstrated better metal removal over dolomite in both Blank and Bio experiments corroborating with batch experiments from Chapter 2.

Even though the degree to what metal removal mechanisms are involved within the systems is not determined in the model used, the advection diffusion equation was successfully fit to the experimental breakthrough curves and demonstrated a slightly better fit in the Bio growth columns. Thus, the advection diffusion equation can be utilized to describe conservative and metal tracers within an experimental gravel filter column and has the potential to be utilized for further SuDS applications.

Bacterial communities of a biofilm grown from locally collected filter drain gravel and pond water was found to be 71% *cyanobacteria*, verifying that the slimy green phototrophic biofilm is, not surprisingly, made up of a majority of

the 'blue-green algae' bacteria. When inoculated into microgabbro or dolomite columns the bacterial communities changed, presumably due to the different minerals available to the microorganisms on the surfaces of the different lithologies of gravel. Microgabbro columns were constituted of 54% *proteobacteria*, 25% *cyanobacteria* and 20% *bacteroidetes* while dolomite columns were constituted of 47% *cyanobacteria*, 25% *proteobacteria* and 22% *bacteroidetes*.

Based on the successful fit of the model, the permanent removal mechanisms of adsorption, precipitation and bioaccumulation are thought to be mechanisms involved in heavy metal removal within the gravel filter columns. In addition to precipitation, adsorption to the gravel media results in metals being retained within the Blank columns with more metals being adsorbed to the microgabbro than the dolomite due to clay surface minerals (discussed in Chapter 2). Supersaturated conditions in the initial solution for Cu and Pb may have increased the observed metal removal in both the Blank and Bio columns due to precipitation while undersaturated conditions for Zn may have inhibited Zn removal. While a higher pH measured in the recirculated pond water may be indicative of photosynthetic activity within the Bio columns increasing the pH and thus further supersaturation and precipitation. Overall, experimental results in the current study indicate that naturally occurring biofilms have the potential to enhance metal removal from road runoff within filter drains. Further, it may be possible to stimulate biological activity (up until the point of biofouling) for use in bio-augmented porous filtration to be harnessed for contaminant removal in other in situ bioremediation systems.

### 3.6 REFERENCES

- Ancion, P. Y., et al. (2010). "Three common metal contaminants of urban runoff (Zn, Cu & Pb) accumulate in freshwater biofilm and modify embedded bacterial communities." Environmental Pollution **158**(8): 2738-2745.
- Anderson, C., et al. (2006). "Autoradiographic comparisons of radionuclide adsorption between subsurface anaerobic biofilms and granitic host rocks." Geomicrobiology Journal **23**(1): 15-29.
- Beck, A. J., et al. (2011). "The influence of phototrophic benthic biofilms on Cd, Cu, Ni, and Pb transport in permeable sediments." Biogeochemistry **102**(1-3): 167-181.

- Beveridge, T. J. and R. G. E. Murray (1980). "Sites of metal-deposition in the cell-wall of *Bacillus subtilis*." Journal of Bacteriology **141**(2): 876-887.
- Cao, B., et al. (2012). "Biofilm shows spatially stratified metabolic responses to contaminant exposure." Environmental Microbiology **14**(11): 2901-2910.
- Cole, J. R., et al. (2009). "The Ribosomal Database Project: improved alignments and new tools for rRNA analysis." Nucleic Acids Research **37**: D141-D145.
- Davies, D. (2003). "Understanding biofilm resistance to antibacterial agents." Nature Reviews Drug Discovery **2**(2): 114-122.
- De Philippis, R., et al. (2011). "Exopolysaccharide-producing cyanobacteria in heavy metal removal from water: molecular basis and practical applicability of the biosorption process." Applied Microbiology and Biotechnology **92**(4): 697-708.
- De Philippis, R. and E. Micheletti (2009). Heavy metal removal with exopolysaccharide-producing cyanobacteria. Heavy Metals in the Environment. L. K. Wang, J. P. Chen, Y.-T. Hung and N. K. Shamma. Boca Raton, USA, CRC Press.
- De Philippis, R., et al. (2001). "Exopolysaccharide-producing cyanobacteria and their possible exploitation: A review." Journal of Applied Phycology **13**(4): 293-299.
- De Philippis, R. and M. Vincenzini (2003). "Outermost polysaccharidic investments of cyanobacteria: Nature, significance and possible applications." Recent Research Developments in Microbiology, Vol 7, Pt 1 **7**: 13-22.
- Fein, J. B., et al. (1997). "A chemical equilibrium model for metal adsorption onto bacterial surfaces." Geochimica Et Cosmochimica Acta **61**(16): 3319-3328.
- Gelman, A. and D. B. Rubin (1992). "Inference from Iterative Simulation Using Multiple Sequences." Statistical Science **7**(4): 457-472.
- Gleeson, D. B., et al. (2006). "Characterization of bacterial community structure on a weathered pegmatitic granite." Microbial Ecology **51**(4): 526-534.
- Harden, V. P. and J. O. Harris (1953). "The isoelectric point of bacterial cells." Journal of Bacteriology **65**(2): 198-202.
- Jaiswal, D. K., et al. (2011). "Analytical solution to the one-dimensional advection-diffusion equation with temporally dependent coefficients." Journal of Water Resource and Protection **3**(1): 76-84.
- Konhauser, K. (2007). Introduction to Geomicrobiology. Oxford, UK, Blackwell Publishing.
- Kulczycki, E., et al. (2005). "Sorption of cadmium and lead by bacteria-ferrihydrite composites." Geomicrobiology Journal **22**(6): 299-310.
- Lau, Y. L., et al. (2000). "Use of a biofilter for treatment of heavy metals in highway runoff." Water Quality Research Journal of Canada **35**(3): 563-580.
- Lloyd, J. R. and L. E. Macaskie (2000). "Bioremediation of radionuclide-containing wastewaters." Environmental Microbe-Metal Interactions: 277-327.
- Lowenstam, H. A. (1981). "Minerals formed by organisms." Science **211**(4487): 1126-1131.

- Merz, M. E. (1992). "The biology of carbonate precipitation by cyanobacteria." Facies **26**(1): 81-101.
- Micheletti, E., et al. (2008). "Selectivity in the heavy metal removal by exopolysaccharide-producing cyanobacteria." Journal of Applied Microbiology **105**(1): 88-94.
- Mittelman, M. W. and G. G. Geesey (1985). "Copper-binding characteristics of exopolymers from a freshwater-sediment bacterium." Applied and Environmental Microbiology **49**(4): 846-851.
- Pang, L. P. and M. E. Close (1999). "Non-equilibrium transport of Cd in alluvial gravels." Journal of Contaminant Hydrology **36**(1-2): 185-206.
- Pereira, S., et al. (2011). "Using extracellular polymeric substances (EPS)-producing cyanobacteria for the bioremediation of heavy metals: do cations compete for the EPS functional groups and also accumulate inside the cell?" Microbiology-Sgm **157**: 451-458.
- Phoenix, V. R., et al. (2000). "Cyanobacterial viability during hydrothermal biomineralisation." Chemical Geology **169**(3-4): 329-338.
- Roeselers, G., et al. (2008). "Phototrophic biofilms and their potential applications." Journal of Applied Phycology **20**(3): 227-235.
- Ronquist, F., et al. (2012). "MrBayes 3.2: Efficient Bayesian Phylogenetic Inference and Model Choice Across a Large Model Space." Systematic Biology **61**(3): 539-542.
- Schnoor, J. L. (1996). Environmental modeling: fate and transport of pollutants in water, air, and soil.
- Tang, G., et al. (2010). "CXTFIT/Excel-A modular adaptable code for parameter estimation, sensitivity analysis and uncertainty analysis for laboratory or field tracer experiments." Computers & Geosciences **36**(9): 1200-1209.
- Taylor, S. W. and P. R. Jaffe (1990). "Biofilm growth and the related changes in the physical properties of a porous medium 1. Experimental investigation." Water Resources Research **26**(9): 2153-2159.
- Van Genuchten, M. T. and J. C. Parker (1984). "Boundary conditions for displacement experiments through short laboratory soil columns." Soil Science Society of America Journal **48**: 703-708.
- Vandevivere, P. and P. Baveye (1992a). "Effect of bacterial extracellular polymers on the saturated hydraulic conductivity of sand columns." Applied and Environmental Microbiology **58**(5): 1690-1698.
- Vandevivere, P. and P. Baveye (1992b). "Relationship between transport of bacteria and their clogging efficiency in sand columns." Applied and Environmental Microbiology **58**(8): 2523-2530.
- Vu, B., et al. (2009). "Bacterial Extracellular Polysaccharides Involved in Biofilm Formation." Molecules **14**(7): 2535-2554.
- Weckesser, J., et al. (1988). "Isolation and chemical-analysis of the sheaths of the filamentous cyanobacteria *Calothrix parietina* and *C. scopulorum*." Journal of General Microbiology **134**: 629-634.
- Worch, E. (2012). Adsorption Technology in Water Treatment: Fundamentals, Processes, and Modeling, Walter de Gruyter.

- 
- Yang, S. Y., et al. (2013). "Coupled interactions between metals and bacterial biofilms in porous media: Implications for biofilm stability, fluid flow and metal transport." Chemical Geology **337**: 20-29.
- Yee, N. and J. B. Fein (2002). "Does metal adsorption onto bacterial surfaces inhibit or enhance aqueous metal transport? Column and batch reactor experiments on Cd-Bacillus subtilis-quartz systems." Chemical Geology **185**(3-4): 303-319.

# 4

## Utilizing MRI to image biofilm growth and pollutant transport within gravel bed systems

### ABSTRACT

MRI (magnetic resonance imaging) was investigated as a potential method for determining black-box processes within SuDS; specifically, biofilm growth, flow patterns, and metal (Cu) immobilization in a gravel filter. MRI can image non-invasively inside porous media, and therefore exhibits potential to spatially resolve dynamic bio-physical processes and unlock their complexity. Gravel flow cells were constructed to run 3D high resolution MRI scans as well as 2D Cu tracer flow scans. First, the 3D images were utilized along with ImageJ software to determine that the average porosity of a dolomite gravel bed was between 32-34%, correlating with porosity values for dolomite and coarse gravel in the literature. Second, 3D images were utilized to determine if biofilm growth within a gravel bed could be differentiated from the water and gravel portion. Whilst all columns showed small-scale rearrangement of particles to a more stable packing arrangement under pore pressure, further image processing steps suggest that regions of biofilm growth are present in the column exposed to light over the long term. High resolution MR images indicate a reduction in MRI signal that corroborates with observations prominent in the literature in which biofilms reduce the  $T_2$  relaxation time of water molecules. Similarly, binary data shows that 6 months of natural biofilm growth can reduce the cross-sectional average porosity of the gravel filter by up to 8.8% near the inlet of the water source (representative of the surface of the SuDS) and up to 49% in local regions of interest close to the light source. Such local 'blockage' of pores at the SuDS surface is an important consideration for filter efficiency and design. Finally, Cu transport within a gravel bed was imaged, concluding that a plug flow system is not apparent within a horizontal flow cell; this has implications for its assumption within modelling of contaminant transport in porous media.

## 4.1 INTRODUCTION

### 4.1.1 MRI Principles

The following is a basic overview of MRI principles, though extensive literature on MRI theory is widely available and more comprehensive information can be found from the following sources: Morgan and Hendee (1984); Callaghan (1993); Haacke et al. (1999); Liang and Lauterbur (1999); Levitt (2008).

The nucleus of an atom defines many properties for specific elements. Along with determining the mass and charge of an element, the nucleus also possess intrinsic properties of spin angular momentum and possible magnetic moment as determined by the spin quantum number. While all particles have spin, only atoms with uneven spin angular momentum possess a magnetic moment. It is the magnetic moment that allows for some elements to experience nuclear magnetic resonance (NMR). Of specific importance for MRI use and the current research is the  $^1\text{H}$  nucleus which possesses a spin quantum number ( $s$ ) of  $\frac{1}{2}$ , making it NMR active. The packed gravel column utilized in this study is saturated with water (which contains an abundance of  $^1\text{H}$ ), and thus,  $^1\text{H}$  based MRI is utilized with the hydrogen nucleus being regarded as a nuclear “spin”. The interaction of these spins with an applied magnetic field,  $B_0$ , leads to a split in energy levels proportional to the magnetic field which is known as Zeeman splitting (Fig 4.1).

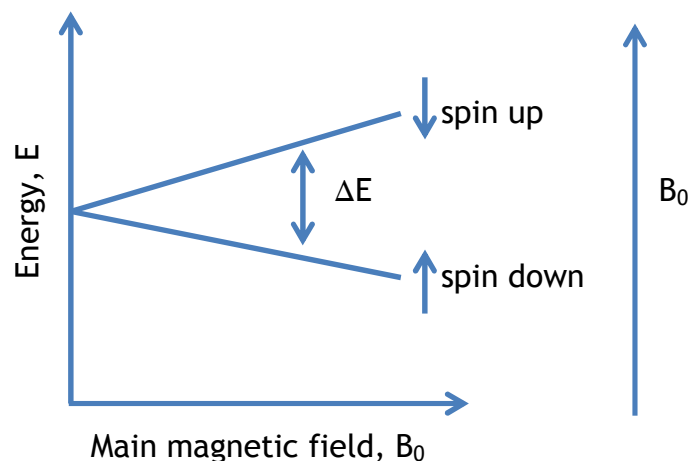


**Figure 4.1.** Zeeman splitting (adapted from Ramanan (2011))

Due to fundamental quantum properties, hydrogen atoms are able to experience two states when a magnetic field is applied. Spin-up is a lower energy state that occurs when the magnetic moment aligns with the applied magnetic field,  $B_0$ ,

while spin-down is a higher energy state that occurs when the magnetic moment aligns against  $B_0$ . These different spin states follow the Boltzmann distribution such that slightly more nuclei align with the lower energy level and end up in the spin-up state than the spin-down state. A net magnetization ( $M$ ) then occurs when the excess spins align in the longitudinal direction of  $B_0$ , or z-axis (Fig 4.2). Also, when a magnetic moment is placed in an applied magnetic field the spins precess about the axis. The frequency of this spin precession is known as Larmor frequency,  $\omega$ , which is equal to  $\gamma B_0$  where  $\gamma$  is the magneticgyric ratio, a constant that is the property of the specific nucleus (42.58 MHz/T for  $^1\text{H}$ ) (Werth et al. 2010).

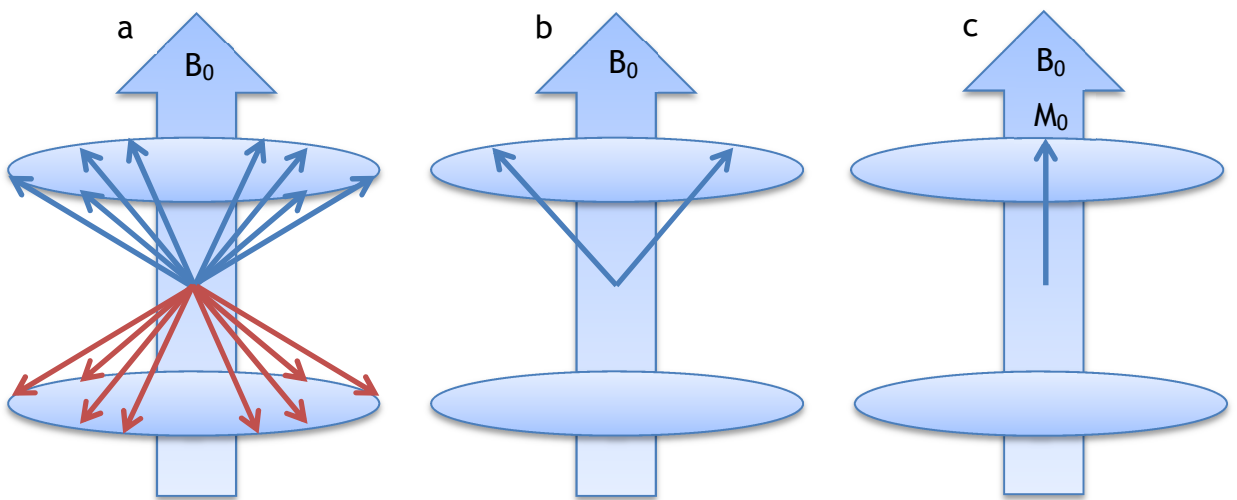


**Figure 4.2.** (a) Spin up and spin down alignment (b) excess spin alignment along direction of magnetic field (c) net magnetization (adapted from Ramanan (2011))

In order to manipulate the spins, an electromagnetic radiation pulse induced by a coil that is equal to the Larmor frequency is applied perpendicular to the net magnetization, referred to as the radio frequency (RF). As a result of this RF pulse, the net magnetization fluctuates away from equilibrium and the resulting energy absorption of the spin, known as NMR effect, is the phenomena exploited in MR imaging. Once the RF pulse has terminated, the net magnetization returns to equilibrium, resulting in the process known as relaxation. During relaxation, there are two distinct processes occurring; first, longitudinal relaxation is the recovery of the longitudinal net magnetization, or  $T_1$  relaxation, in which the spins begin to lose energy absorbed from the excitation to the surrounding environment (Fig 4.3). Second, transverse relaxation is the decay of the spins

transverse phase coherence, or  $T_2$  relaxation and thus allowing the net magnetization to decay over time (Fig 4.4). The resulting MR signal is due to the oscillating current created by the transverse magnetization of the spins in the excitation phase at the resonance frequency in the coil (Fig 4.5) (Haynes et al. 2009).

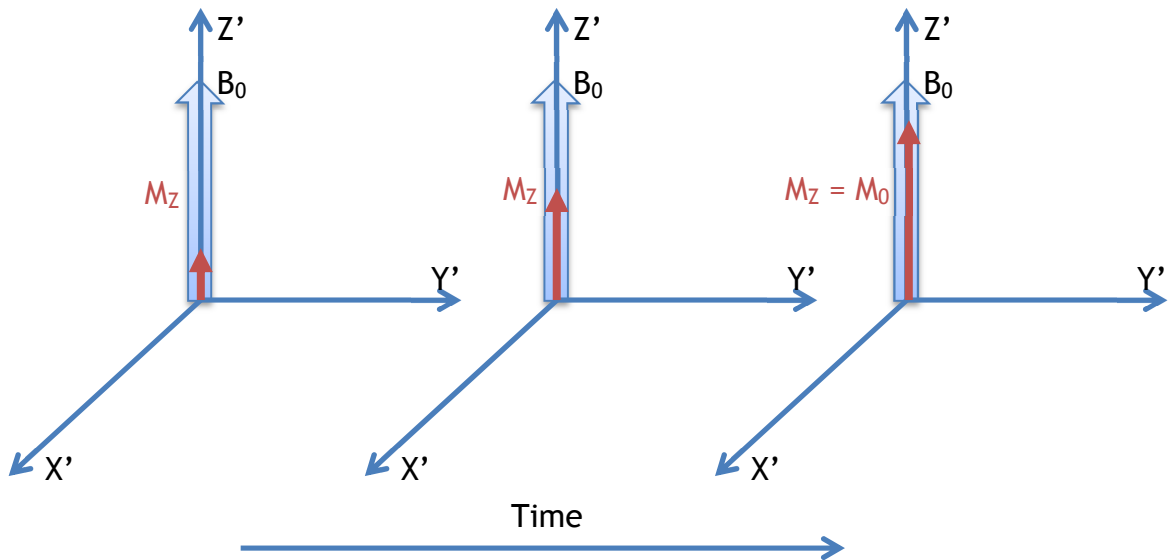


**Figure 4.3.** Longitudinal relaxation following an excitation pulse in which longitudinal magnetization ( $M_z$ ) at time ( $t$ ) is described by the relaxation time constant ( $T_1$ ) and given as  $M_z = M_0(1 - e^{-t/T_1})$  (adapted from Ramanan (2011))

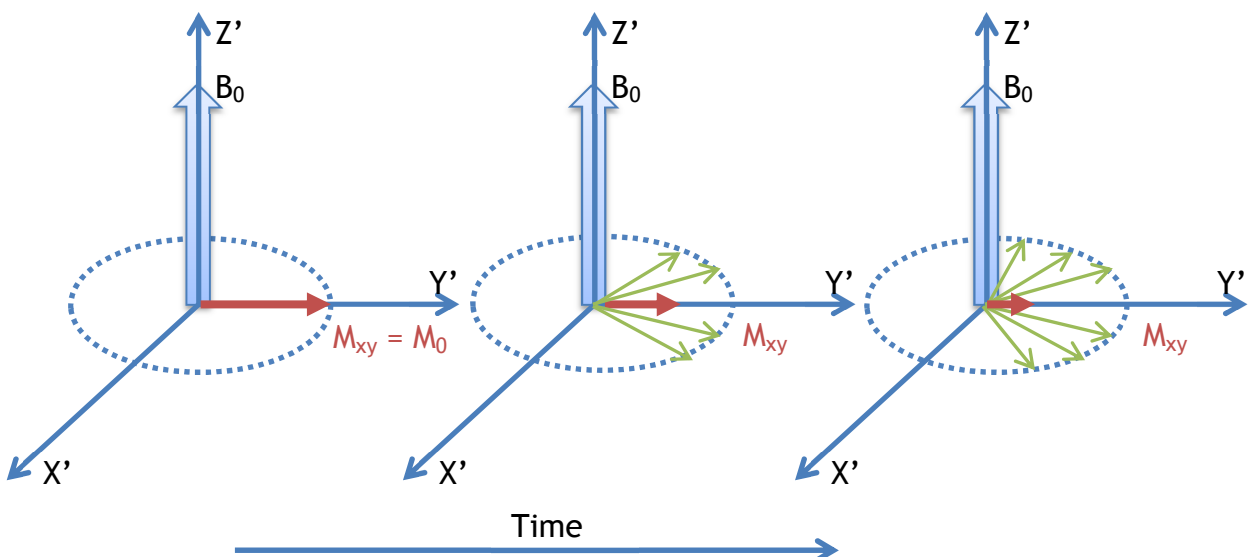


**Figure 4.4.** Transverse relaxation following an excitation pulse in which transverse magnetization ( $M_{xy}$ ) at time ( $t$ ) is described by the relaxation time constant ( $T_2$ ) and given as  $M_{xy} = M_0 e^{-t/T_2}$  (adapted from Ramanan (2011))

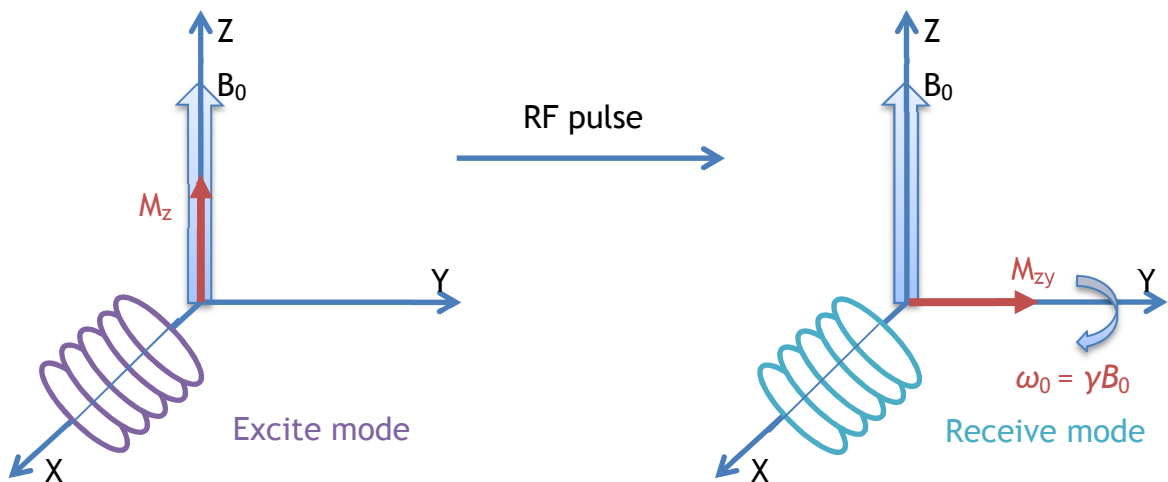


**Figure 4.5.** Excitation by RF pulse equal to the Larmor frequency ( $\omega_0$ ) and subsequent detection of MR signal (adapted from Ramanan (2011))

Imaging occurs when linear magnetic field gradients are applied to the sample. Due to  $B_0$  being consistently uniform, applied pulses of gradients are needed to produce a varying magnetic field across the sample, which causes the spins at varying locations to resonate at different frequencies. With the spatial positions of each nucleus labelled, the  $T_2$  relaxation is detected by the RF coil which can then be mapped to create an image. The resolution of the image depends both on the diameter of the RF coil (smaller diameter coils generate higher resolution) as well as the strength of the gradients (higher gradients also generate better resolution) (Phoenix and Holmes 2008).

### 4.1.2 MRI for use in contaminant hydrogeology

While MRI has traditionally been used in the medical field for non-invasive imaging of humans or animals, engineers and scientists have begun to tap into this valuable technology for non-invasive imaging of transport and structural parameters inside water systems, due to the abundance of  $H^1$  nuclei (in  $H_2O$ ). Research on contaminant transport and fate traditionally relies on sampling at the outlet of the system thus producing breakthrough curves which are used to elucidate transport and removal processes (Pang and Close 1999; Liu et al. 2005; Hatt et al. 2007; Werth et al. 2010). However, this approach cannot reveal the spatial heterogeneity of structure and transport inside the system which often hold the key to its behaviour. MRI has allowed researchers concerned with water systems such as rivers (Haynes et al. 2009), filter membranes and water

treatment systems (von der Schulenburg et al. 2008a; von der Schulenburg et al. 2008b; Creber et al. 2010a; Creber et al. 2010b; Pintelon et al. 2010) and currently SuDS to look inside at the processes involved in flow, biofilm growth and contaminant removal in more detail (Werth et al. 2010).

Early research utilizing MRI in engineering science aimed to look at pore structure and distribution within a porous media, which is important in systems such as oil recovery, remediation of soil or mass transport in packed beds (Baldwin et al. 1996). Localized measurement of porosity of rocks using MRI was first reported in Rothwell and Vinegar (1985), Vinegar (1986), Hall and Rajanayagam (1987), Lamrous et al. (1989) and Merrill (1993) with further characterization methods of void space described in Baldwin et al. (1996) and pore structure and connectivity methods refined in Doughty (1998).

Further research with MRI for characterization within porous media then began to look at fluid transport processes within such systems. Detailed flow mapping of fluids in sandstone was reported in Guilfoyle et al. (1992). Sederman et al. (1997) used MRI imaging and velocity flow measurements to determine structure-flow correlations in a packed bed of ballotini (glass beads), visualizing channelling effects, laminar flow and constant flow depending on the structure of the pore space, concluding that flow is not homogenous within a packed column. Sederman et al. (1998) further advanced this research with enhanced MRI resolution allowing for flow monitoring throughout the column which also demonstrated significant heterogeneity dependent on local pore space geometry and correlated to the local Reynolds number (in reference to flow rate). Nestle et al. (2003) examined the spatial and temporal adsorption of heavy metals within a sand column, successfully visualizing adsorption and remobilization of heavy metal (Cr, Cu and Gd) contaminants. In this guise, further advancing the understanding of heavy metal immobilization processes with MRI, Phoenix and Holmes (2008) investigated Cu transport within a naturally occurring biofilm and was able to demonstrate that MRI could effectively determine biofilm structure, diffusion coefficients, and map Cu concentrations. Cu concentrations were successfully calibrated to spatially describe immobilization of the metal within the biofilm. This enabled the generation of a model which determined the dominant Cu transport and immobilization processes (found to be dominated by diffusion and adsorption as opposed to advection and precipitation). However,

these experiments were undertaken at the small-scale with a 1 cm thick biofilm grown in a 1.5 cm column at 200  $\mu\text{m}$  resolution which is unrealistic for direct application of results to coarse-grained SuDS filters. MRI was also successfully utilized to spatially image distribution of biofilms for detection of biofouling within membrane filtration systems (von der Schulenburg et al. 2008b) and a bioreactor (Seymour et al. 2004a). Here, MRI technology was able to non-invasively quantify effective surface area of the membranes which is key to design and operation of important water treatment in which biofilms can affect mass transport and hydrodynamics of the treatment systems. Yet, again this research was undertaken on a 55 mm filter membrane and 1 mm bioreactor which is unrepresentative of SuDS.

While the specific studies detailed above are directly relevant to the present thesis, it is worth comment of the handful of papers associated to the wider use of MRI for biofilm research (largely motivated by biofouling of medical equipment and thus undertaken at the very small scale of microns through millimeters). For a wider review of biofouling research using MRI in porous media in the medical field papers include: Hoskins et al. (1999); Seymour et al. (2004b); Seymour et al. (2007); Shamim et al. (2013)). Further, related studies on use of MRI to image biofouling in membranes can be found in Seymour et al. (2007); Creber et al. (2010a); Creber et al. (2010b); Pintelon et al. (2010), whilst MRI use for metal transport processes within biofilm can be found in Beauregard et al. (2010); Bartacek et al. (2012); Cao et al. (2012); Schulenburg et al. (2008); Bartacek et al. (2009); Ramanan et al. (2010); Vogt et al. (2012); Ramanan et al. (2013). Finally, studies looking at the structural form and architecture of biofilms themselves include Manz et al. (2003); Neu et al. (2010); Fridjonsson et al. (2011). Whilst all these studies lend important insight into MRI use for biofilm imaging and analysis, they cannot be mapped directly onto SuDS related research due to inappropriateness of scale and material.

Thus, despite a very recent surge in MRI application to flow-pollution processes prevalent in SuDS, the 20+ papers available do not consider the effect of biofouling on filter efficiency for metal removal at coarse-grain scales as required in SuDS design. Importantly, only 2 of the aforementioned studies consider a coarse-grained gravel media set-up appropriate to SuDS research: Ramanan et al. (2012) successfully imaged superparamagnetic nanoparticle

transport through a coarse-grained quartz gravel media in a vertical column. Also, Haynes et al. (2009) was able to image sedimentation of fine-grained sand within a gravel bed, an important aspect to gravel filter drains which encounter significant sedimentation of suspended solids from road runoff. Therefore, precedent exists for successful application of MRI to flow-sediment- pollution studies in coarse-grained media as necessary for gaining insight into SuDS filters, yet its application to biofouling of such a coarse-grain media is without such precedence. This therefore underpins the motivation of the present research.

### 4.1.3 Motivation

Typically, contaminant transport research must rely on outlet measurements to construct breakthrough curves, which are then used to infer the transport and contaminant immobilization processes that occur within the system. When transport and metal immobilization patterns are spatially complex, these can be difficult to unravel with traditional breakthrough curves and therefore it becomes desirable to image inside the system to view transport and immobilization processes within (Ramanan et al., 2012). Transport and immobilization patterns within SuDS may be spatially complex due to the highly open structure generated by the use of coarse gravels and biofilm growth. In response to this, we here examine the potential of MRI to image the spatially complexity of structure, biofilm growth and contaminant (heavy metal) transport within a model SuDS system. This approach could lead to more informed design of filter drains with subsequent optimized performance.

The key goals were: First, to image gravel porous media within an experimental chamber in order to provide porosity measurements of material typical of a filter drain. Second, to determine if naturally occurring biofilms colonized within a gravel-filled column can be imaged and quantified in terms of a porosity loss to the gravel filter. And third, to image spatial heterogeneity in heavy metal contaminant transport within a gravel filter and how this is influenced by gravel structure and biofilms.

## 4.2 MATERIALS AND METHODS

### 4.2.1 Experimental overview

Table 4.1 provides an overview of the experimental programme. Six separate porous media flow cells were constructed with variables including: lithology (i.e. surface charge); lighting; biological inoculation; and time of growth. The detail and rationale for each experimental set-up is provided below:

Experiment	Growth Conditions	Weight of Gravel	PAR Range	Clean Scan	Biofilm Scan	Flow Scan
BioLightLong	Light source/6 months growth	1269.39g	48 - 65 PAR	✓	✓	✓
BioLightShort	Light source/1 month growth	1283.22g	48 - 65 PAR	✓	✓	✓
BioDarkLong	Light source/6 months growth	1256.31g	0.02 - 1.4 PAR	✓	✓	✓
BioDarkShort	Light source/1 month growth	1271.49g	0.02 - 1.4 PAR	✓	✓	✓
ChemDolomite	None	1245.07g	N/A	✓		✓
ChemQuartz	None	1297.81g	N/A	✓		✓

**Table 4.1.** List of MRI experiments. PAR = Photosynthetic Active Radiation ( $\mu\text{moles.m}^{-2}\text{s}^{-1}$ )

The biofilm experiments were undertaken to first determine if natural biofilm growth in a gravel filter could be imaged with MRI. To examine this, each of the four biofilm experiments had a 3D high resolution MRI scan undertaken before biofilm growth, termed ‘Clean’ and a 3D high resolution scan after a prescribed growth period of up to 6 months (Table 4.1), termed ‘Biofilm’. The clean and biofilm scans were then used to determine porosity of the gravel filter and any differences between the two which could potentially be biofilm growth. Columns were incubated under either light or dark conditions to stimulate biofilm growth; it was anticipated that columns incubated under light would promote a greater abundance of phototrophs such as *cyanobacteria* appropriate to representing the exposed surface layers of the SuDS filter, whilst the dark columns were proxies for subsurface gravels below the light-penetration layers. Growth periods of 1 month and 6 months were used to give insight into growth behaviour of a biofilm; these timeframes were considered representative of a newly constructed SuDS filter where early colonisation may have occurred and a more established SuDS filter where mature colonies of biofilm may have developed growth patterns appropriate to local SuDS flow and community structure.

The lithology of the gravel media was either dolomite (Haynes et al, 2012) or rose quartz (Haynes et al., 2009; Ramanan et al., 2010). This comparison was intended both to permit analysis of lithology on MR image quality and, importantly, a comparison of the effect that the different surface charges have on heavy metal removal in filters. Specifically, dolomite has a positive charge whilst quartz has a negative charge. After high resolution scans of porosity were undertaken for the clean gravel columns, all columns were subject to flow imaging experiments within the MRI, to determine the impact of biofilms on flow of a Cu tracer patterns. One column of dolomite (ChemDolomite) gravel without biofilm growth served as a comparison of flow to columns with biofilm growth. Detailed MRI parameters and scans can be found in Sections 4.2.6.

### 4.2.2 Flow cell

The flow cell was constructed out of non-metal materials (metal near the MRI magnet is dangerous and can also affect the signal) so the flow cell was made of Perspex with nylon screws and fittings. The flow cell had an internal diameter of 10cm and a length of 10cm not including inlet and outlet flanges and fittings. The flow cell contained four inlet and four outlet tubes which worked simultaneously (Fig 4.6). A mesh diffuser plate was placed at the inlet to keep gravel in place, diffuse and homogenize the influent water, and aid in matching up images received from the MRI scans. Before each use the chamber and fittings was disinfected with Virkon<sup>®</sup> laboratory surface disinfectant and thoroughly rinsed with ultrapure (18.2 M $\Omega$ ) deionized (DI) water (Millipore).

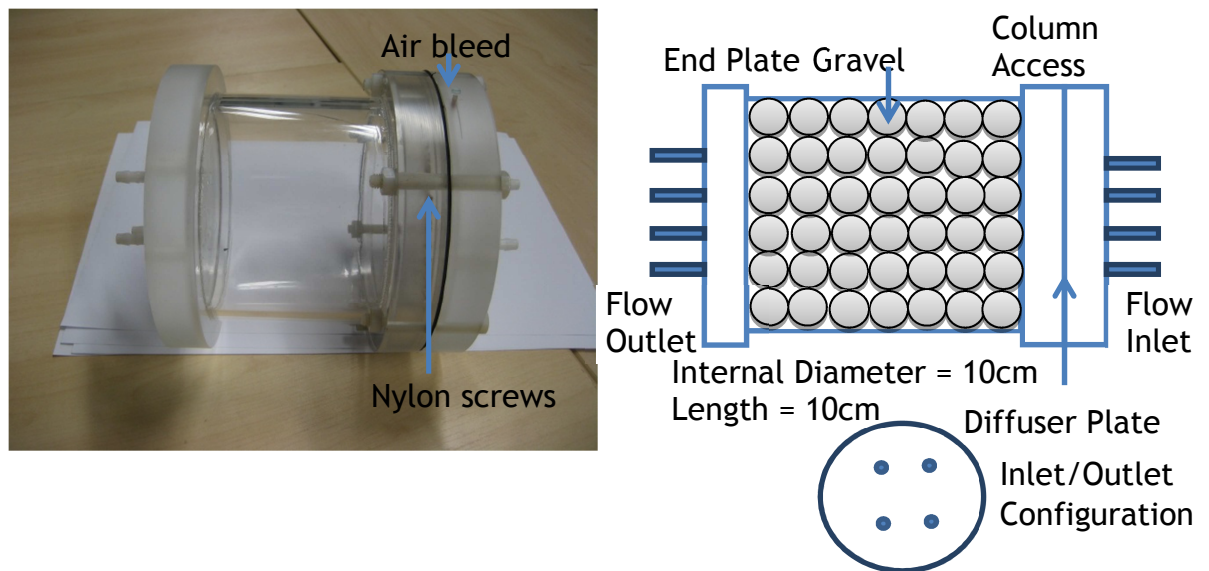


**Figure 4.6.** (a) Photo and (b) schematic of the experimental gravel filter. Detailed specifications can be found in Appendix I.

### 4.2.3 Experimental materials

Care must also be taken to choose a gravel material that does not interfere with the MRI signal. Natural gravel lithology may contain trace metal impurities which can cause distortion or artefacts in an MRI image. When natural sediments contain elements with ferromagnetic properties such as iron, nickel and cobalt, the elements become permanently magnetized by the MRI and cause disruption to the consistency of the surrounding magnetic field ultimately reducing the signal to zero (Haynes et al. 2009). For this reason, a more pure gravel lithology free of ferromagnetic impurities but with a similar sub-angular composition to filter drain gravel was sought. Dolomite gravel has been used successfully in MRI research (Haynes et al. 2012) as it is low in metals and the sieved fraction between 8-11.2mm dolomite was used for all biofilm experiments and one non-biofilm experiment. Dolomite gravel was sterilized by autoclave prior to being placed in the flow cell. Volume of gravel was determined by weight and is recorded in Table 4.1. Rose quartz has also been imaged successfully by MRI (Ramanan et al. 2012) and was used in one non-biofilm experiment in order to compare flow and Cu immobilization with dolomite (dolomite has a positive surface charge while rose quartz has a negative surface charge). Fortunately, most MRI applications utilize  $^1\text{H}$  based MRI. All MRI scans were performed on the columns filled with DI water, or water doped with copper, and hence there was an abundance of  $^1\text{H}$  (in water) making the system ideal for imaging

The imaging of flow through the column was achieved using DI water doped with  $\text{Cu}^{2+}$ . The Cu causes a shortening of the relaxation times ( $T_1$  and  $T_2$ ) of  $^1\text{H}$  in water. As a result, Cu doped water generates a different MRI signal than DI water, and thus the movement of Cu doped water through the column can be imaged. The flow experiment used a copper solution of 50 mg/L (ppm) that was diluted from 1000 ppm stock solution prepared by dissolving Copper(II) nitrate ( $\text{Cu}(\text{NO}_3)_2 \cdot 3\text{H}_2\text{O}$ ), (Sigma-Aldrich) in ultrapure DI.

#### 4.2.4 Biofilm growth

A growth column of a natural SuDS biofilm is described in Section 3.2.1 and it is from this column that a small sample of biofilm was taken to inoculate the pond water used to colonize the MRI experiments. A photo of the original biofilm growth column setup (a) can be seen in Figure 4.7 as well as the biofilm sample (b) placed in the recirculating MRI water.

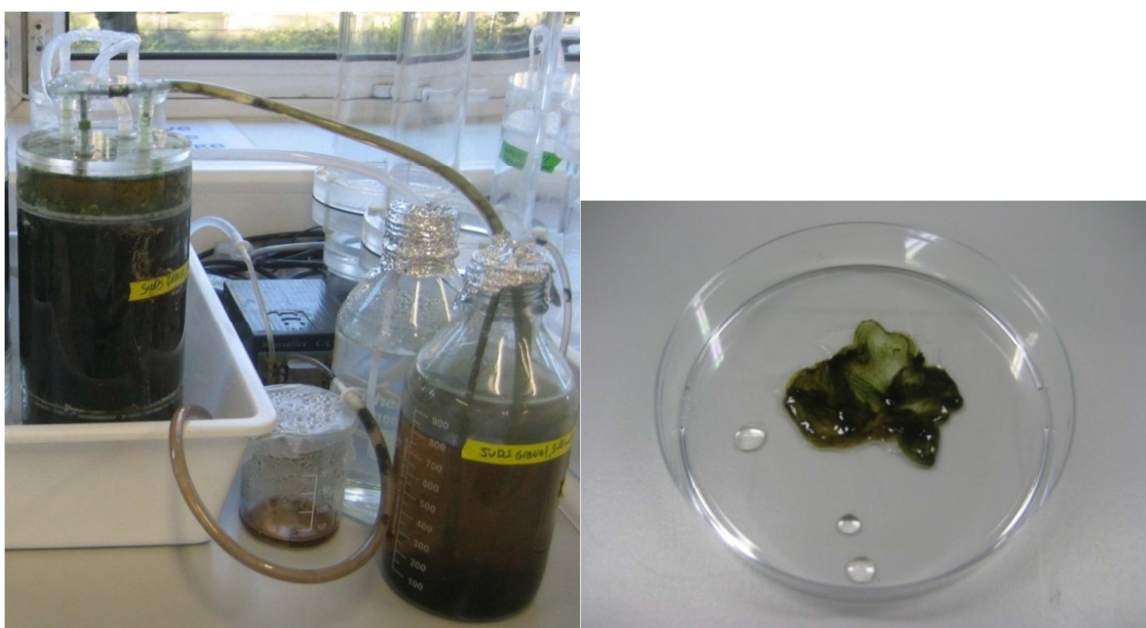


**Figure 4.7.** (a) Original biofilm growth column and (b) biofilm sample inoculated into pond water for MRI columns

With reference to Table 4.1 two columns ('Dark' in Table 4.1) were covered completely with foil for their entire growth period (Figure 4.8a) to ensure dark growth conditions which would be suitable only for non-photosynthetic organisms. While the two columns grown in light conditions ('Light' in Table 4.1) had white fluorescent light directed near the top of the flow cell (to represent where sunlight would typically affect a filter drain) for 12 hours a day (7am-

7pm) (Figure 4.8b). White fluorescent light was chosen as it has a similar wavelength range to visible sunlight (400-700 nm) (Davidson 2003). Photosynthetically active radiation (PAR) measurements were taken on a Macam Q203 PAR meter (Table 4.1) to record how much light each experimental column was getting. In all columns, the biofilm inoculated SuDS pond water was allowed to recirculate 4-5ml/min at room temperature as a means to constantly refresh the water at the lowest flow rate possible on the peristaltic pump. The growth within the columns was set up at the MRI facility in order to reduce disturbances to the gravel within the column during transport.



**Figure 4.8.** (a) Column in 'dark' conditions and (b) 'light' conditions

### 4.2.5 Flow system (Cu transport imaging)

The flow system was set up in which a separate but equal flow of 50 ppm Cu solution was applied via the four inlets with a four cassette peristaltic pump at a total of 6.82 ml/min flow rate (1.7 ml/min for each inlet) which equates to a one hour residence time within the flow cell (a rate needed for visualization of the Cu flow front). Cu was chosen as a tracer due to the heavy metals' prominence as a typical constituent of road runoff (Appendix A) and is suitable for MRI use as it is sufficiently paramagnetic (Phoenix and Holmes 2008). A 50 ppm concentration was needed in order to visualize the Cu in comparison to water and offered the lowest concentration at a relaxation rate differentiable from water. While 50 ppm Cu and a one hour residence time may not be completely representative of concentrations found in road runoff or residence time of a filter drain, these were limitations of the MRI that were needed to carry out the experiments. Tubing was primed with the 50 ppm Cu solution prior to the start of the experiment and connected to a 50 ppm Cu solution reservoir.

Photos of the MRI flow setup can be seen in Figure 4.9, which details the setup outside the MRI room (a), inside the MRI room (b) as well as the view of the column within the bore of the MRI (c).

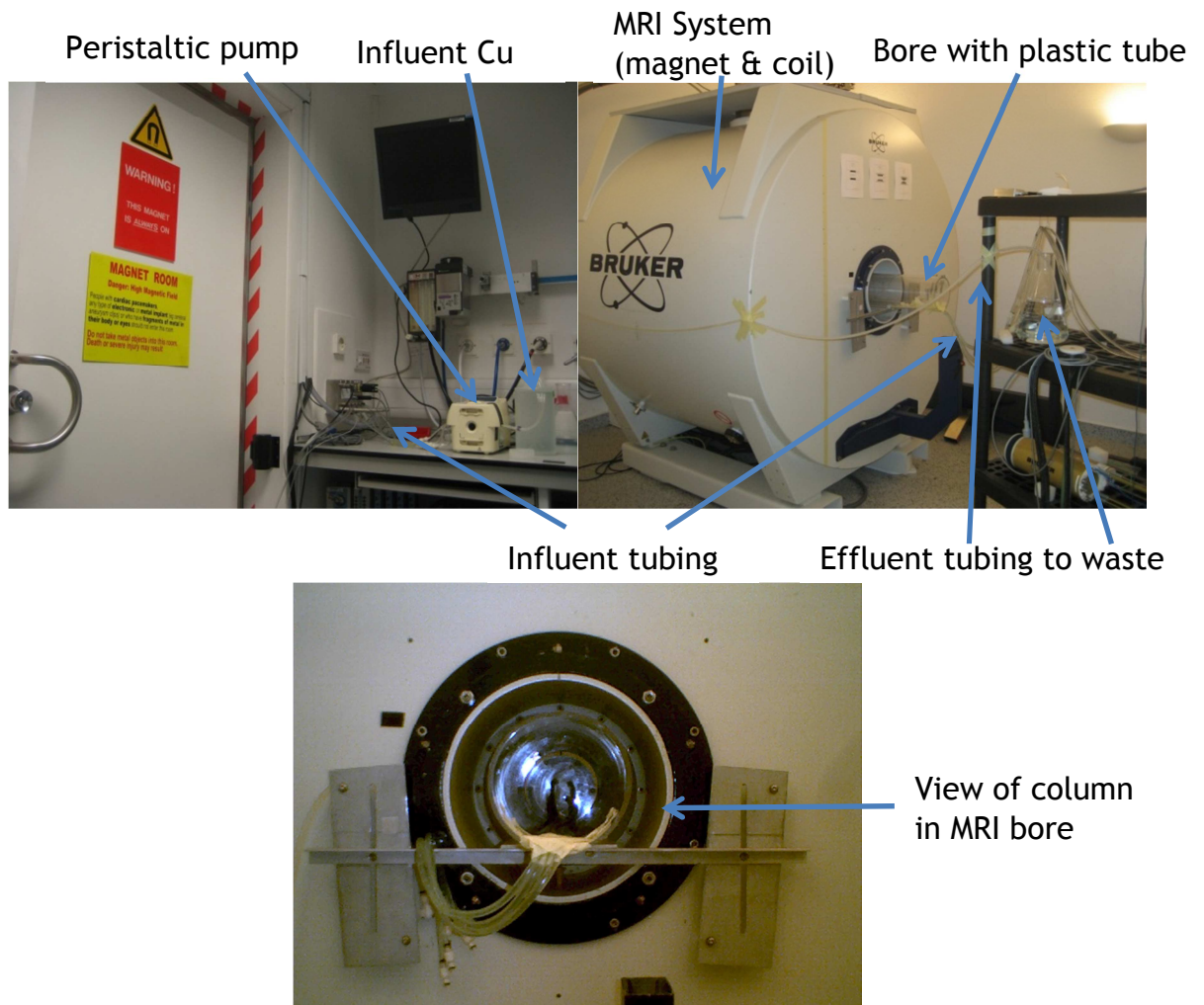


**Figure 4.9.** (a) Setup of peristaltic pump outside MRI room, (b) setup of inlet tubing, column within MRI bore, and outlet tubing, (c) view of column within bore

#### 4.2.6 MRI parameters and image acquisition

This research was performed at the Glasgow Experimental MRI Centre (GEMRIC) on a Bruker Avance Biospin animal scanner with a 7 Tesla magnet with a 15 cm RF coil and a bore size of 152 cm. In order to determine the best parameters for the 3D scans, a pre-scan was run as well as a short, localizer tripilot scan which helps to make sure the column is placed in the most precise position possible between experiments. To obtain the high resolution clean and biofilm scans, a 3-dimensional rapid acquisition relaxation enhanced (RARE) sequence with a resolution of 300 $\mu$ m across the x- y- and z- planes was used to excite the  $^1\text{H}$

nuclei within the sample and thus, image and determine the water and non-water phases of the gravel column. The RARE scan consisted of a train of RF pulses  $90^\circ_x [-t_e -180^\circ_y -t_e -]_n$  with an echo time ( $t_e$ ) of 11 ms, a RARE factor of  $n = 8$ , a repetition time of 4000 ms and a bandwidth set to 200 kHz. While higher resolution scans are possible, this increases the scan time and with the parameters utilized in these 3D scans totalling 20-21 hours, is already sufficiently high. 3D images consisted of 600 vertical slices which are 333 pixels high and 433 pixels wide (Fig 4.10).

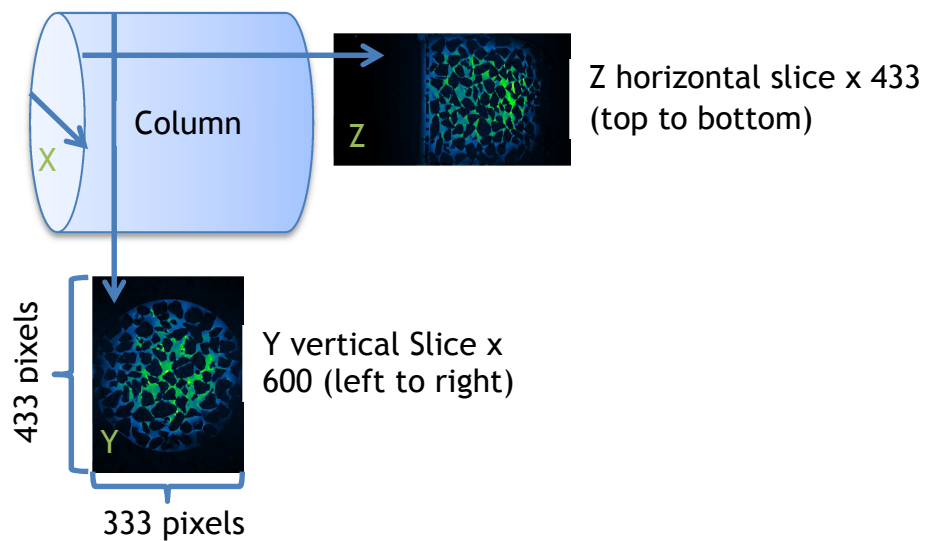


**Figure 4.10.** Orthogonal directions of x, y and z and examples of resulting images obtained from the 3D acquisition

This sequence and setup has been successfully utilized to image gravel sedimentation in Haynes et al. (2009) and was thus used without modification in this study. Since this MR system utilizes a more powerful superconducting 7T magnet for a higher strength magnetic field than typical medical MR, images acquired are more susceptible to distortions or artefacts. Optimized image quality has been augmented with previous work of determining a low metal gravel lithology suitable for MRI use in Haynes et al. (2009); Ramanan et al. (2012) and Haynes et al. (2012) as well as chamber construction and experimental setup by Minto (2013). Thus, the MR images obtained were free from possible distortions due ferromagnetic artefacts or wrap-around effect. Though images obtained did experience gradient non-linearity near the outlet end resulting in a tapering effect in the image (Figure 4.11) as well as intensity inhomogeneity in which signal intensity across the image varies. To address both issues: Firstly, gradient non-linearity was removed for the high resolution 3D

scans by the analysed area being reduced from the original 600 Y slices to the 152 Y slices free of non-linearity distortion (Figure 4.11). This reduced volume was utilized for further processing of porosity data. It is important to note that each Y slice is 88604 pixels, hence even the reduced volume space from 152 slices still contained over 13 million pixels with associated complexity and lengthy analysis requirements. Secondly, intensity inhomogeneity was addressed through utilization of binary processing (described in Section 4.2.7); this is viable as Figure 4.11 indicates that this affects the blue/green wavelengths of the colour spectrum of the fluid signal only; distinction of the solid-fluid boundaries remains clear and thus binary processing can be accurately utilised.

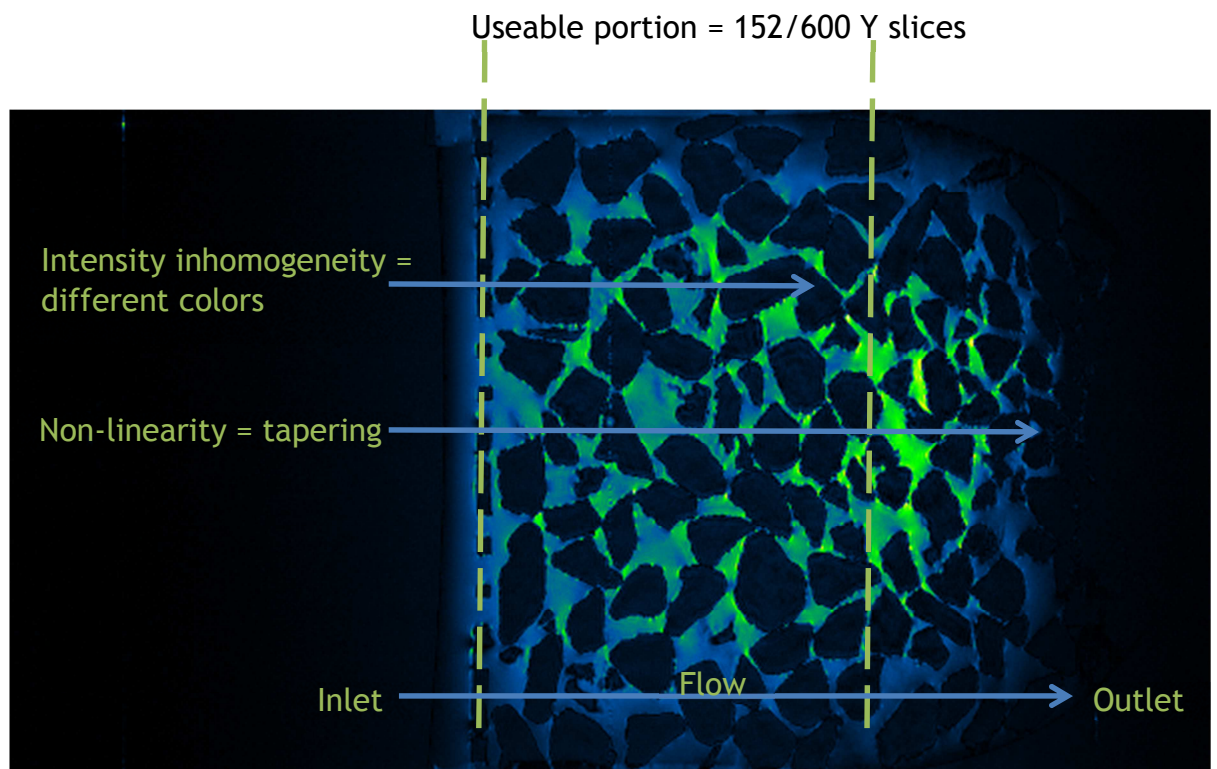


**Figure 4.11.** Example of horizontal Z slice (433 total from top to bottom) from the 3D high resolution scans. Non-linearity can be seen tapering near the outlet end and the different colors show the intensity inhomogeneity. The area between the green lines indicates the useable portion for image processing the porosity and comparison and equals 152 slices vertical Y slices out of the total 600 obtained.

The clean and biofilm scans were run as 3D high resolution scans in order to determine porosity of the gravel and look at possible biofilm growth between the two. Care was taken to match up the scans when placing the column within the MRI after growth periods and was done so with alignment points on the column, the MRI system and the plastic bore as well as comparing between the initial tripilot scans, ensuring the column was imaging in the same location

between the Clean and Bio scans. Once the biofilm scan for the 'Bio' experiments and the clean scan for the 'Chem' experiments was run, the flow scans were run immediately after without movement from the MRI system.

As the high resolution 3D scans took 20 hours to complete (Clean and Bio scans) the flow rate and diffusion/advection of Cu tracer through the column required a far quicker image acquisition time so as to ensure multiple images of tracer movement. With the aim to run a scan frequency of 5 minutes, a maximum scan acquisition timeframe of 2 minutes was chosen as an appropriate compromise for process understanding and MRI set-up. This reduced the number of image slices to 8 horizontal slices through the column (from top to bottom) as visualized in Figure 4.12. Between 12 and 24 scans were taken for time-lapse imaging of tracer movement. Thus, the resulting imaging parameters were set up for the flow experiments; 440  $\mu\text{m}$  resolution, echo time (TE) 170.5 ms, repetition time (TR) 24000 ms, a RARE factor of 48, the field of view was 11 cm with an imaging matrix of 250 x 250 pixels and an 8 pixel slice thickness.

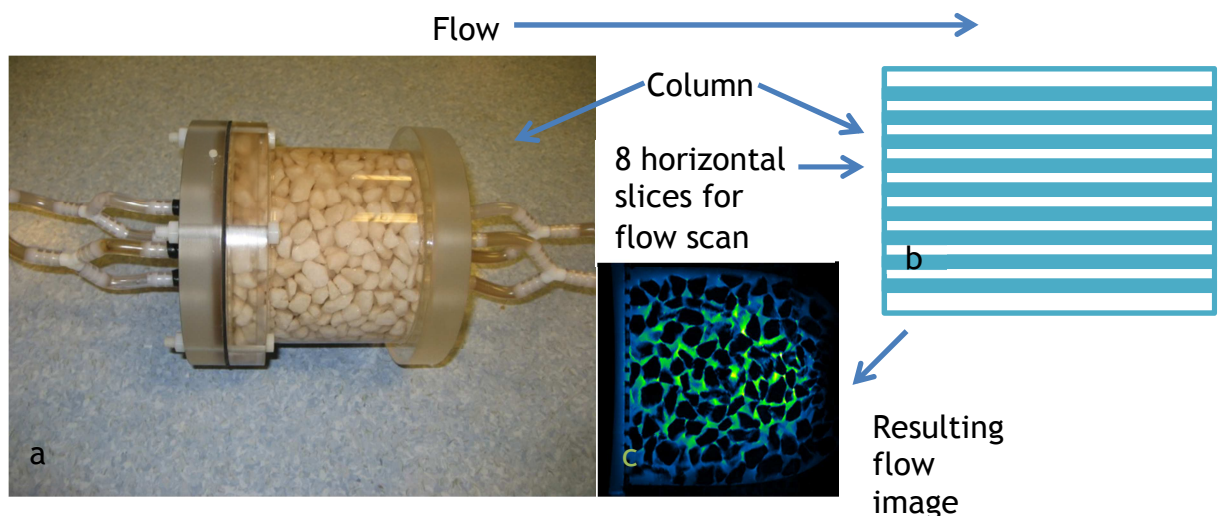


**Figure 4.12.** (a) Photo of the gravel filter column with inlet on the left and outlet on the right, and thus flow applied left to right (b) schematic of the 8 horizontal slices for each flow scan obtained (c) resulting MRI image of once slice

#### 4.2.7 Image processing - clean versus biofilm scans

The first objective of the chapter is to determine the porosity of the dolomite gravel within an experimental filter; while the second objective is to determine

if biofilm growth within this filter could be imaged and quantified in terms of volume and reduced porosity of the filter. Thus, the water and solid (non-water) fraction of the image needs to be segregated from each other using a binary process whereby regions of MR signal (water) image white (1), whilst regions of no signal (solid) image black (0). As it is uncertain as to whether biofilm would return a signal or not (due to variable water content of the bioform), comparison of the Clean and Bio binary images (i.e. before and after growth) was used to determine if there is a third distinguishable fraction of biofilm. While there are innumerable processes of segmentation available (e.g. Sezgin and Sankur (2004); Kaestner et al. (2008); Iassonov et al. (2009)), including difficult, time consuming manual processes and some automated algorithms for many similar applications, all are inherently user subjective due to differing pre- and post-processing steps, different acquisition of images and varying programs to process the images. Yet, there is not a standard process for segmentation in image processing. Thus, the protocol utilized and outlined in this section was that of Minto (2013) who used an identical experimental set-up and MR machine to that of the present thesis. Minto (2013) utilized an exhaustive evaluation procedure to determine the best overall segmentation method out of numerous pre-processing, segmentation and post-processing combinations. In short, the key rationale and benefits of Minto's (2013) process include: qualitative assessment of segmentation quality based on area thresholded, level of noise and separation of particles with further analysis of methods compared against experimentally determined bulk porosity, manual segmentation of slices and manual segmentation of the mesh screen of known value. This evaluation ultimately determined the segmentation process utilized within this chapter to give the best quality results given the experimental setup and MR images acquired.

The segmentation process used to analyze the clean scans of all experiments was done in the image processing software ImageJ with the Bruker plugin installed. The following is a step-by-step process which first creates the useable portion of the 3D scan resulting in the area used to threshold (segment) the water and non-water fractions which is further used to determine porosity and for comparison purposes.

1. The 2Dseq file contains the high resolution MR scan. Once opened in ImageJ it is displayed as 433 horizontal slices which is then resliced to

show the 600 vertical slices (example of grayscale and color are shown in Figure 4.13a and 4.13b) which allows for visualization of the tapering near the outlet end and the start at the diffuser plate.

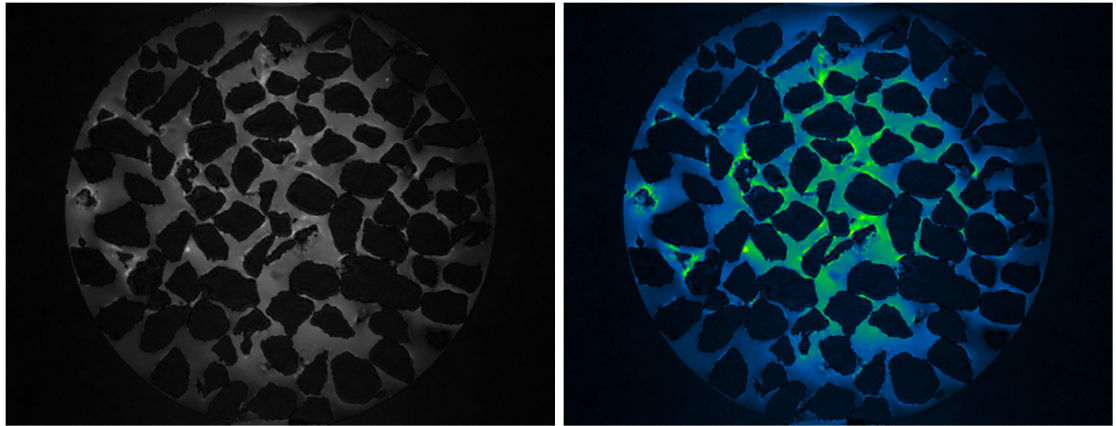


**Figure 4.13.** Example of vertical slices in (a) grayscale (b) colour

2. Before and after scans are matched up as best as possible though are subject to error due to placement within the MR bore between experiments (see Section 4.5.5 summarizing uncertainty). Despite the potential small error, the before-after analysis is essential to review temporal changes which have occurred within the column; hence a substack (Fig. 4.14) is made of the useable portion of the 152 vertical scans (see Section 4.2.6) termed the region of interest (ROI). In all cases 3 slices in the middle of the scan are taken out due to an inherent signal interference from the MR instrument visible in all high resolution images.

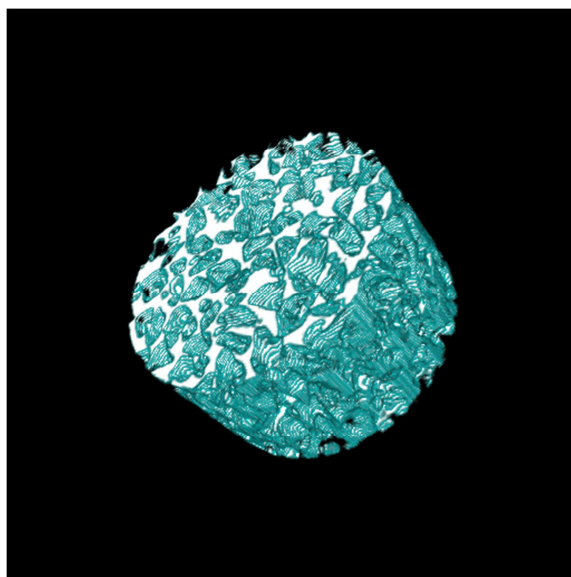


**Figure 4.14.** 3D visualization of useable ROI of experimental gravel filter

3. The image was segmented by using a thresholding plugin called 'Auto Local Threshold' in which each pixel is thresholded individually according to a radius around it. The specific thresholding option used for this data was the Niblack method with a radius of 20, which follows the algorithm:  
$$pixel = ( pixel > mean + k * standard\_deviation - c ) ? object : background$$
A radius of 20 was chosen since both water and gravel was needed within a region for the algorithm to work correctly. Since the gravel was ~10mm or ~34 pixels across and thus a 17 pixel diameter, a radius of 20 ensured that both water and gravel fractions would be within a region (and not only one or the other) for the algorithm to segment.
4. Once the image has been thresholded, noise outliers are automatically removed for the dark and bright pixels using nearest neighbour functions, so as to remove any erroneous data that may affect the porosity value. The edges of the column are also cropped so as to not include any edge effects in the porosity measurements. The resulting image is shown in Figure 4.15 in which the segmentation of the water fraction is seen as white (assigned a value of 255) while the non-water (gravel) fraction is seen as black (assigned a value of 0)

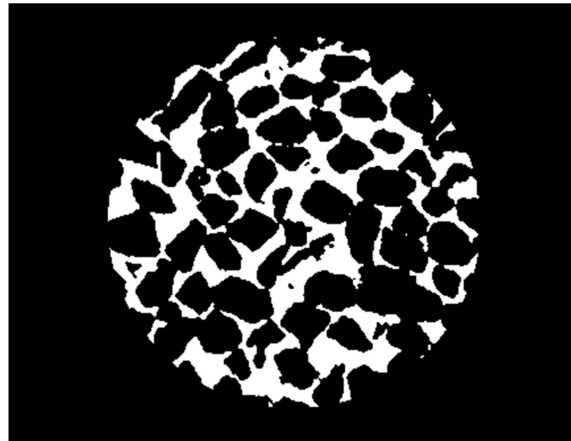


**Figure 4.15.** Middle slice of 3D scan thresholded in ImageJ.

5. Following the segmentation process, the porosity is determined by measuring the percentage area (%area) in ImageJ. This returns a list of the porosity measurements for each of the 152 slices in which the percentage of white pore spaces to black grains of gravel is calculated. This fulfils our first aim of determining the porosity of a gravel filter column via MRI.

Subsequently, the thresholded high resolution scans are used to determine differences between the before Clean scans and the after Biofilm scans of the four Bio experiments. In ImageJ a thresholded image is segmented into two values of 0 (black) and 255 (white) as seen in Figure 4.15. So to determine differences between two images the following methodology is employed:

- (i) the initial clean stack of slices is divided by 2 such that the water-filled pore areas give a value of 127 (coloured green, Figure 4.16a);
- (ii) the final Bio stack is divided by 4 to give water-filled pore-spaces a value of 64 (coloured blue, Figure 4.16b). The uncropped images are used for this step to ensure any biofilm growing at the edges were captured

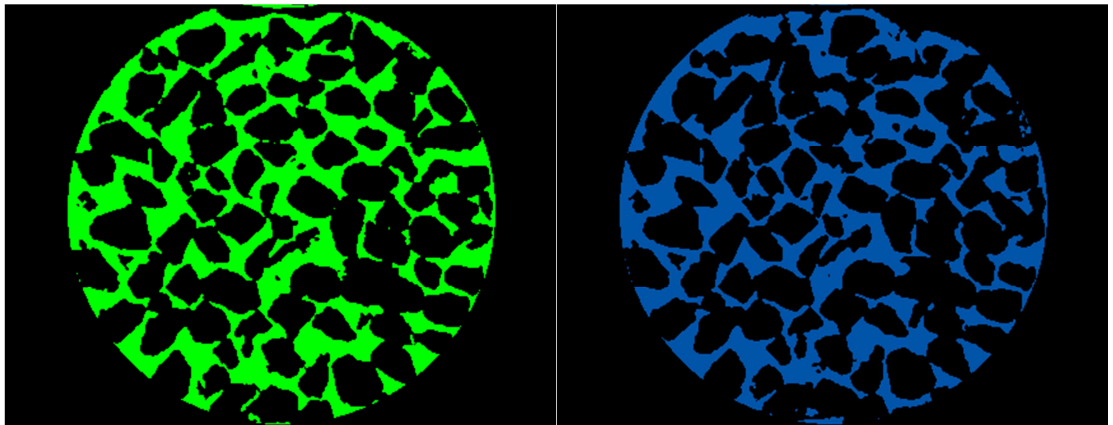


**Figure 4.16.** (a) Middle slice of a clean thresholded stack divided by 2 (b) middle slice of a biofilm thresholded stack divided by 4

6. Thus, by adding the two divided images together we are able to determine four regions (Figure 4.17):  $0+0=0$  indicates gravel in both images (black),  $0+64=64$  indicates gravel in the clean image but water in the biofilm image (blue),  $127+0=127$  indicates water in the clean image but solid in the biofilm image (green) and  $127+64=191$  indicates water in both images (white). Thus, values of 64 (blue) may indicate local movement of gravels away from that location due to settlement/rotation in the column in a manner appropriate to enhanced packing under fluid pore pressures. Similarly, values of 127 (green) may indicate local movement of gravels into that location or potential biofilm growth. Deciphering the green regions in more detail forms subsequent analysis in this Chapter (Section 4.3) and seeks to fulfil the second aim of

determining the viability of using MRI to image biofilm growth within a gravel filter column.

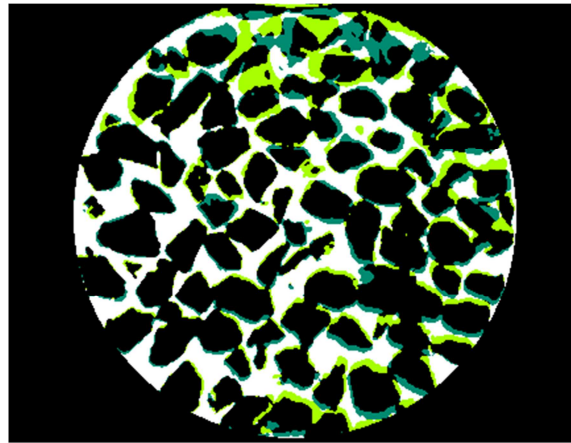


**Figure 4.17.** Resulting image from adding Clean  $\div$  2 with Bio  $\div$  4

7. In order to determine the percentage of green versus blue regions for each experiment, a region of interest of the initial 152 slices (with 3 middle interference slices removed) was reduced to 140 slices to eliminate the mesh screen area near the inlet. These 140 slices were then used to obtain the total number of pixels of the stack of images for each colour; green, blue, black and white. Percentages of each specified colour region were then determined from comparing against the total pixels of the circular column area.

#### 4.2.8 Image processing - Cu transport scans

The third aim of this research was to look at the suitability of MRI to image Cu transport processes within a horizontal gravel filter. A single reference scan was taken before flow commenced in order to use as a 'blank' to subtract from subsequent scans. Since Cu alters the relaxation time of water, it impacts the MRI signal and thus can be used as a contrasting agent, allowing for visualization of the incoming Cu front. Flow patterns can be discerned by subtracting the reference image of the column filled with DI water from scans obtained as Cu doped water migrates through the column. The patterns were then compared between experiments to determine any differences or, if biofilm growth occurred, if any effects on flow path network can be determined. Bruker Paravision software utilized for initial image acquisition and processing from the MR system was used for this analysis step; this permitted direct comparison of the brightness intensity data accounting for colour-spectrum variability due to

inhomogeneity (Figure 4.11) and is important to note, as the same function was not possible in ImageJ due to a built-in automated correction for colour-spectrum for individual images (which precluded direct comparison of images). In view of the results obtained and discussed in the next section (4.3), this simple analysis of the flow scans was reasoned sufficient for the flow system analysis as modelling or concentration maps for the system were considered difficult to achieve from the resulting Cu transport in this particular column due to complexity of transport patterns.

## 4.3 RESULTS AND ANALYSIS

### 4.3.1 Clean and Biofilm image analysis

The results of the clean and biofilm high resolution scans are summarized with regards to porosity and percentage of total pixels of the differentiating images with further analysis investigating differences between the clean and biofilm scans of specific experiments thereafter. All image analysis was done in ImageJ. For ease of analysis *bulk* porosities and biophysical data over the entire volumetric space of length equivalent to 140 slices is provided first; subsequent *local* analysis is presented in order to better explain detailed biophysical processes.

#### 4.3.1.1 Bulk porosity data

The porosity of each experimental column as estimated by the thresholding method in ImageJ and is summarized in Table 4.2.

Experiment	Clean	Clean	Bio	Bio	% difference Clean vs. Bio Average
	Porosity Min/Max	Porosity Average	Porosity Min/Max	Porosity Average	
BioLightLong	31/36	34	31/35	33	2.5
BioDarkLong	29/37	32	30/37	32	-1.7
BioLightShort	29/42	33	29/38	33	-0.90
BioDarkShort	29/41	32	29/41	32	0.18
ChemDolomite	31/36	33			
ChemQuartz	24/29	27			

**Table 4.2.** Summary of porosity (% area of pore spaces) of experimental columns as determined by ImageJ. Average porosity reported was the average of all slices through the ROI.

From Table 4.2 two findings are clear: Firstly, lithology influences porosity significantly. The average porosity of all dolomite columns was 33% +/- 1; this is in line with the upper values cited in the literature (Morris and Johnson 1967) and appropriate given that wall-effects reduce packing density in these regions. Yet, the average porosity of the quartz column was 27%; this reflects more angular grain shapes which increase imbrication and packing densities. Thus, grain shape is an important control on porosity and a factor to consider in SuDS filter efficiency in terms of both flow rate and pollution assimilation. The following debate is therefore valid: in situations where pollution assimilation is the primary objective of the SuDS, larger residence time and slower flow rates would be preferred and a more angular material of lower porosity would be most beneficial. However, where treatment volume and storage are crucial then larger porosities (and potentially enhanced permeabilities) of a more rounded material would be preferential. Given that this chapter is focussed upon biophysical clogging potential and the impact of metal removal, there is further argument for selection of material with a reduced clogging risk; this dictates a preference towards more rounded materials offering larger pore spaces that promote greater likelihood of throughflow.

Secondly, dolomite columns indicate only limited changes in average bulk porosity data and porosity range following biological growth tests. Table 4.2 shows that the longest lit experiment of 6 months (BioLightLong) clearly shows a reduction in average bulk porosity of 2.5%; notably, this is the only column to visually exhibit phototrophic (green) biofilm growth (Fig 4.18) near the exposed chamber walls and clearly shows the associated pore filling process. This

indicates the importance of both light and extended growth durations. Thus, it can be deduced that an established SuDS filters would be subject to surface growth of biofilm and associated blockage potential.

Visual data from the BioDarkLong experiment gives some suggestion that biological clogging potential is not just restricted to the surface of a filter. Specifically, the BioDarkLong column showed regions of ‘slimy’ appearance (mostly near the top of the column and the inlet) that appeared to resemble a non-phototropic biofilm after 6 months of growth. Whilst the presence of this biofilm is irrefutable, bulk porosities indicate an increase in porosity. These findings are counterintuitive and further analysis (see Figure 4.19 in next section) does suggest that local shifts in gravel grains due to either column movement or misalignment of repeat scans were sufficiently pronounced to cause notable distortion of the before-after subtracted images. In defence of this, the BioDarkShort experiment appears less affected by gravel movements and clearly indicates a bulk porosity loss of 0.18% even after just one month of non-phototropic growth. Whilst the bulk clogging effects of this non-phototropic biofilm after 1 month are therefore an order of magnitude less than those of the phototropic ones left for 6 months, it is an important effect to note as it means that SuDS are subject to biological blockage over the full depth of the filter independent of lighting.

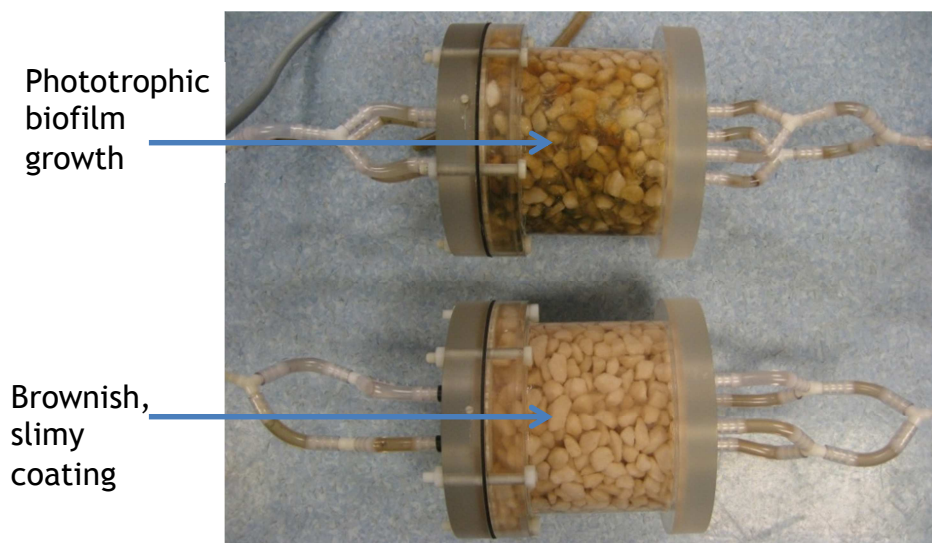


**Figure 4.18.** BioLightLong column after 6 months growth indicating phototrophic biofilm growth mostly around the top and right where light source focussed for first half of growth period (top) and BioDarkLong column after 6 months growth indicating a slightly slimy appearance near the top (bottom)

### 4.3.1.2 Bulk bio-physical data

The process outlined in steps 6 and 7 of Section 4.2.7 was used to visualize differences between the Clean and Bio scans. Figure 4.19a-d illustrates the results for the middle slice of the ROI of each experiment as an example of the column data.

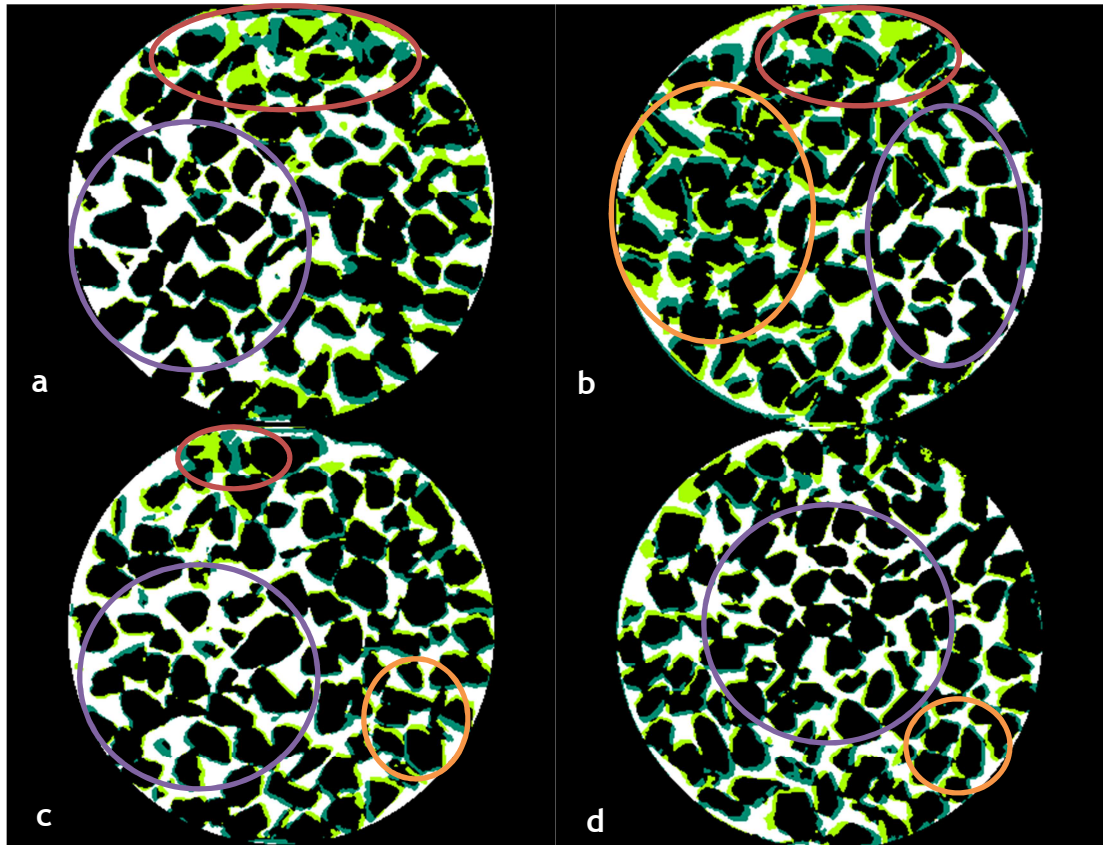


**Figure 4.19.** Differentiating image between Clean and Bio scans for (a) BioLightLong (b) BioDarkLong (c) BioLightShort (d) BioDarkShort in which blue and green indicates differences between the before and after scans and white and black indicate areas where the solid and liquid fraction were consistent between the before and after. A red circle indicates an area that does not match up between scans, a purple circle indicates an area where the two scans align well and an orange circle indicates an area where the gravel can be seen as shifting between the two scans

Two main observations are apparent from Figure 4.19: Firstly, in all of the experiments individual grains of gravel seemed to have shifted between the Clean and Bio scans. This is evident when the shape of the grain remains, but one side of the grain shows a green area and the other an equivalent blue area (Fig 4.20a). The size of these coloured regions need not be exactly identical as grain movements are in 3D space and may not occur planar to the image slice. Analysis indicates that for the majority of movements the displacement is

equivalent to 1 pixel (0.3mm). Whilst this is equivalent to the estimated error possible from manual misalignment of the column in the MRI bore (Section 4.4.5), it is clear that this effect is only present for some, not all, of the grains and varies within slices from 1-5 pixels in displacement length; thus, image acquisition cannot be responsible for these changes. Instead, such movement are likely a result of the unstable grains moving locally; this may be due to: instability under pore-pressure; vibrations during manual removal of the column from the MRI between scans; or, disturbance due to pressure exerted when connecting the flow system to the column. This problem appears most pronounced on the BioDarkLong (Figure 4.19b) experiment and may explain the unexpected porosity data of Table 4.2 (discussed above).



**Figure 4.20.** (a) Example of local movement of grain (b) distinct area of green without blue compensation

Secondly, it is clear from Figure 4.19 that partial or entire pore filling (green regions) is prevalent in the wall regions of the chambers. Fig 4.20b shows that this is not compensated locally by pore emptying regions and thus is a process distinct from the aforementioned process of grain movement. This is believed to represent biofilm growth areas responsible for pore clogging. Visual examination of MRI slices (e.g. Figure 4.19) shows that local pore filling is most apparent in the upper, right and lower wall regions of the BioLightLong experiment (Figure 4.19a); here 4 pores appear to have entirely filled (100%) over the 6 month growth period. To a lesser extent the BioLightShort (Figure 4.19c) indicates similar locations of growth (all be it to a lesser extent in that only 1 pore is entirely filled; i.e. partial-filling of pores is more common). This data supports the notion of biological growth filling these pores, as phototrophs have preference for lit conditions near the chamber surface. Interestingly, the Dark experiments also indicate regions of biological pore filling in near-wall regions; as growth is not ubiquitous around the circumference of the chamber detailed review of Figure 4.19 appears to show that growth in dark conditions is greatest

in connected, larger pore areas near the wall. Thus, greater porosity in the near-wall region of the column also appears to promote greater fluid exchange/flow and greater probability of biofilm settlement.

In light of the findings above, analysis was undertaken to attempt to quantify the relative importance of the two processes of grain shifts and biological growth. A basic mathematical approach was utilised in that: (i) the coloured (blue or green) area was determined for each of the 140 slices; (ii) its percentage relative to the total area of the slice was then calculated; (iii) bulk average statistics were then calculated for the volume space. Results are provided in Table 4.3. Since much of the green and blue areas are thought to be local movement of grains between the Clean and Bio scans, subtracting the blue area from the green area may be indicative of biofilm growth in the column.

Reported as % Pixels Throughout 140 Slice ROI	Solid/Gravel (Black)	Water/Pore Space (White)	Liquid in Clean Solid in Bio (Green)	Solid in Clean Liquid in Bio (Blue)	% Pore Blockage due to Biofilm
BioLightLong Clean	66	34			
BioLightLong Bio	67	33			
BioLightLong Added	56	23	11	10	1.6
BioDarkLong Clean	68	32			
BioDarkLong Bio	67	33			
BioDarkLong Added	55	21	12	12	-1.2
BioLightShort Clean	67	33			
BioLightShort Bio	66	34			
BioLightShort Added	57	24	8.9	10	-3.7
BioDarkShort Clean	67	33			
BioDarkShort Bio	67	33			
BioDarkShort Added	58	23	9.4	10	-0.57

**Table 4.3.** Percentage area of pixel analysis illustrating differences between the Clean and Bio scans

From Table 4.3 BioLightLong appears to be the only column with more green than blue; that is, there is an increase in solid region over six months of biological growth when analysed over the bulk volume of the chamber. This is surprising, as earlier data from Figure 4.19 undisputedly highlights regions of biofilm growth in all experiments such that porosity losses would be expected in all data sets of Table 4.3. Thus, three issues are raised: (i) are we correct in assuming that biofilm images as a solid? (ii) have we fully considered issues of gravel movement? (iii) are bulk measurements appropriate to quantifying the

---

impact of local biophysical changes in gravel columns? The first two questions are discussed below, whilst the final question requires separate analysis provided in Section 4.3.1.3.

To address the first of these questions, a look at the original high resolution images is needed to demonstrate a correlation with, and reasoning for use of binary analysis as well as correlation with visual evidence of biofilm growth in the BioLightLong experiment. Since image analysis has been done using binary images thus far and has resulted in what appears to be biofilm growth imaging as a solid rather than a liquid, Figures 4.21a-c show an example (BioLightLong) of the original high resolution Clean (a) and Bio (b) scan images followed by the subtraction of Clean from Bio (c) in which similar trends near the top and right of the column can be visualized. Using the original high resolution scans illustrates that the same differences (little change on the left side of the column, major variations at the top of the column, and what appears to be small ‘fuzzy’ changes on the right of the column) are seen between the Clean and Bio scans without being segmented into binary. What is also apparent is the intensity inhomogeneity differences seen between the Clean and Bio Scans. This inherent side effect of the image acquisition (Vovk et al. 2007) is noticeable where higher degrees of green versus blue appear in the Clean scan over the Bio scan. For this reason, histogram analysis and thresholding of the multitude of colours in the original high resolution scans would be difficult and incomparable and thus, why binary image analysis was chosen as a more appropriate method for comparison and determination of biofilm growth.

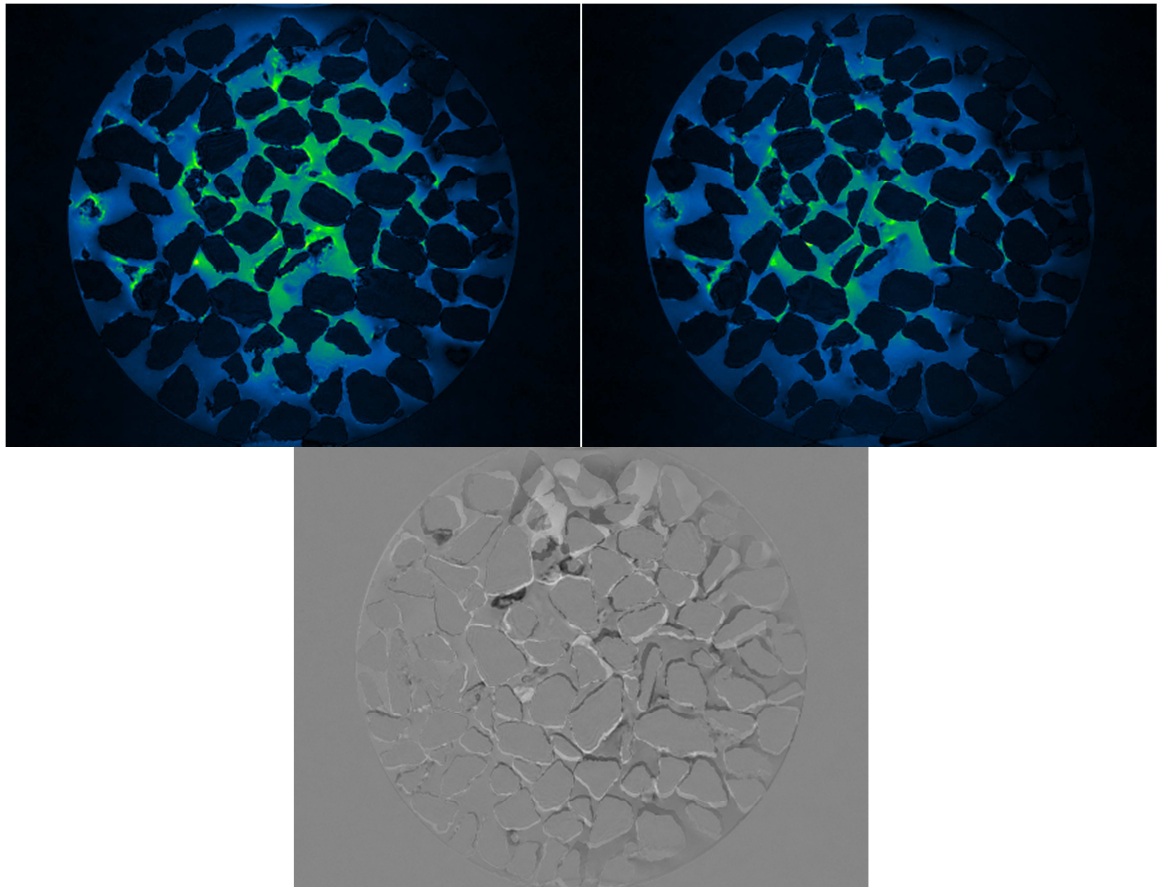


**Figure 4.21.** Original high resolution images of slice 76 of BioLightLong (a) Clean (b) Bio (c) Bio subtracted from Clean

Since BioLightLong was the only column that demonstrated a decrease in porosity and increase in green regions, the following points summarizes the observations and highlights further verification of what is believed to be imaged biofilm growth in BioLightLong:

1. It is speculated that biofilm growth would occur near the edge of the column and near the inlet. Growth around the edge would likely occur as this is the closest area of the column to the light source and growth would occur near the inlet as this is where the first entry of the inoculated pond water occurs, thus enhancing colonization in these areas of the column.
2. The areas where the blue and green variations occur in BioLightLong correlate to where the phototrophic biofilm is seen growing in the column. Figure 4.24 shows photos of the biofilm growth of the column on the right side (a) and the left side (b).

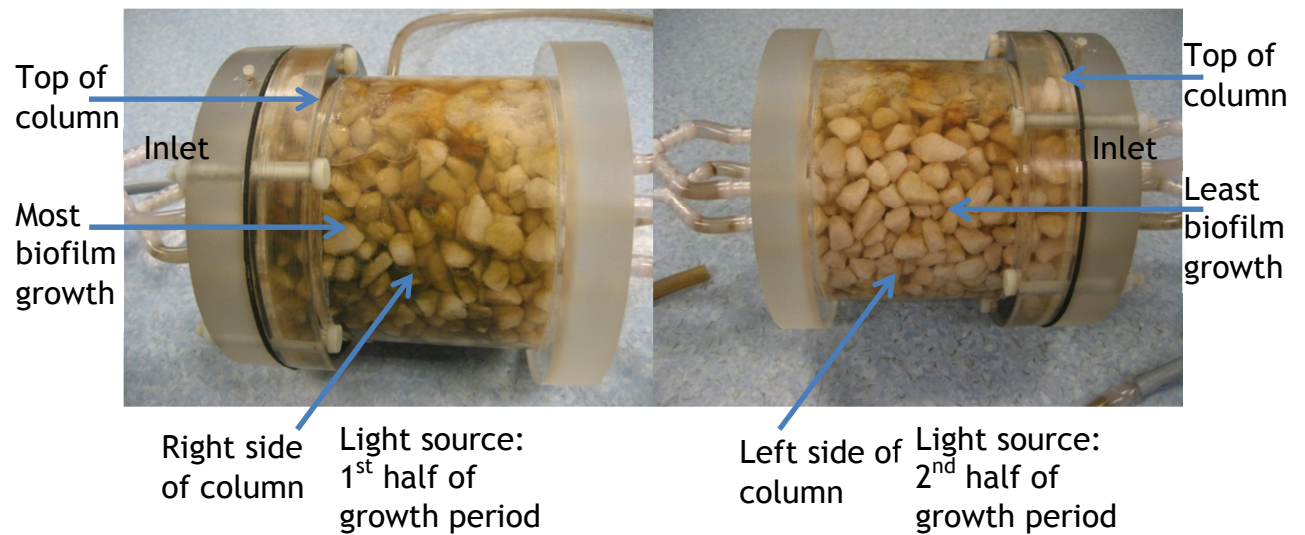


**Figure 4.22.** (a) Photo of the right side of BioLightLong column after 6 month growth period (b) Photo of the left side of BioLightLong column after 6 months growth period.

3. Most of the green variations are seen in the BioLightLong experiment, which is the only experiment where phototrophic biofilm was visually seen to grow as a thick slimy coating. While biofilm may have grown in the other three columns, it was not as visually prominent as BioLightLong.

Thus, for the highlighted reasons above, it does appear that biofilm growth is imaging and thresholding as a solid.

To address the second of the questions casting uncertainty over Table 4.3, the full extent of gravel movement in the columns does appear to be significant. The negative values generated in determining differences between the Clean and Bio scans of BioDarkLong, BioLightShort and BioDarkShort indicate an increase in pore space, even though areas of biofilm growth are clearly seen (in BioDarkLong in particular) and it is not possible for the solid gravel fraction to ‘disappear’. Thus, the pore space gain is thought to be due to each of the columns gravel settling under gravity to different degrees, as well as porewater pressures experienced during recirculation of pond water and vibrations caused by the MRI process. A change in the original packing arrangement due to the freedom of movement of grains then has the possibility to move and image in different 3D slices, calculating as a ‘loss’ of solid gravel. Therefore, the actual settlement is conceived to be higher than the percentage reported in Table 4.3, in which case percentages of calculated biofilm growth are thought to be an underestimate of actual biofilm growth.

### 4.3.1.3 Local bio-physical data

The third question raised in the previous section referred to the appropriateness of using bulk statistics for biophysical changes in gravel filters where local changes are observed to dominate. It has already been exemplified (e.g. Figure 4.19) that individual pores appear subject to 100% blockage due to biofouling and thus, it is important to examine and quantify this process locally if SuDS knowledge is to be better informed. Thus, three methods were employed to examine local biofouling using the binary processed before-after subtracted images used in the previous section: Method (i) analysed individual cross-sectional slices along the column length to assess changes in cross-sectional average porosities from inlet to outlet; Method (ii) re-sliced individual cross-sectional data in concentric circles to analyse local biofouling impact on porosities in the side-wall region (i.e. representative of a SuDS surface); Method (iii) provides visual identification and selection of local ROIs where maximum biofouling appears to be present.

Method (i): From Table 4.3 it is evident that BioLightLong has biofilm growth present. Hence, using similar before-after subtraction methodology on individual cross-sections of this experiment's data indicates the slices nearest the inlet (as in Slice 135) show more biofilm growth as compared to slices near the middle (as in Slice 76) and towards the outlet which is documented by percentage of pore space blockage by biofilm in in Table 4.4 and Figures 4.23 a-h.

% Pore Blockage by Biofilm		
<b>BLL</b>	Slice 76	3.3
	Slice 135	8.8
<b>BDL</b>	Slice 76	-2.4
	Slice 135	2.9
<b>BLS</b>	Slice 76	-3.1
	Slice 135	6.0
<b>BDS</b>	Slice 76	0.38
	Slice 135	1.0

**Table 4.4.** Percentage of pore space blockage by biofilm for Slices 76 versus 135 of each experiment

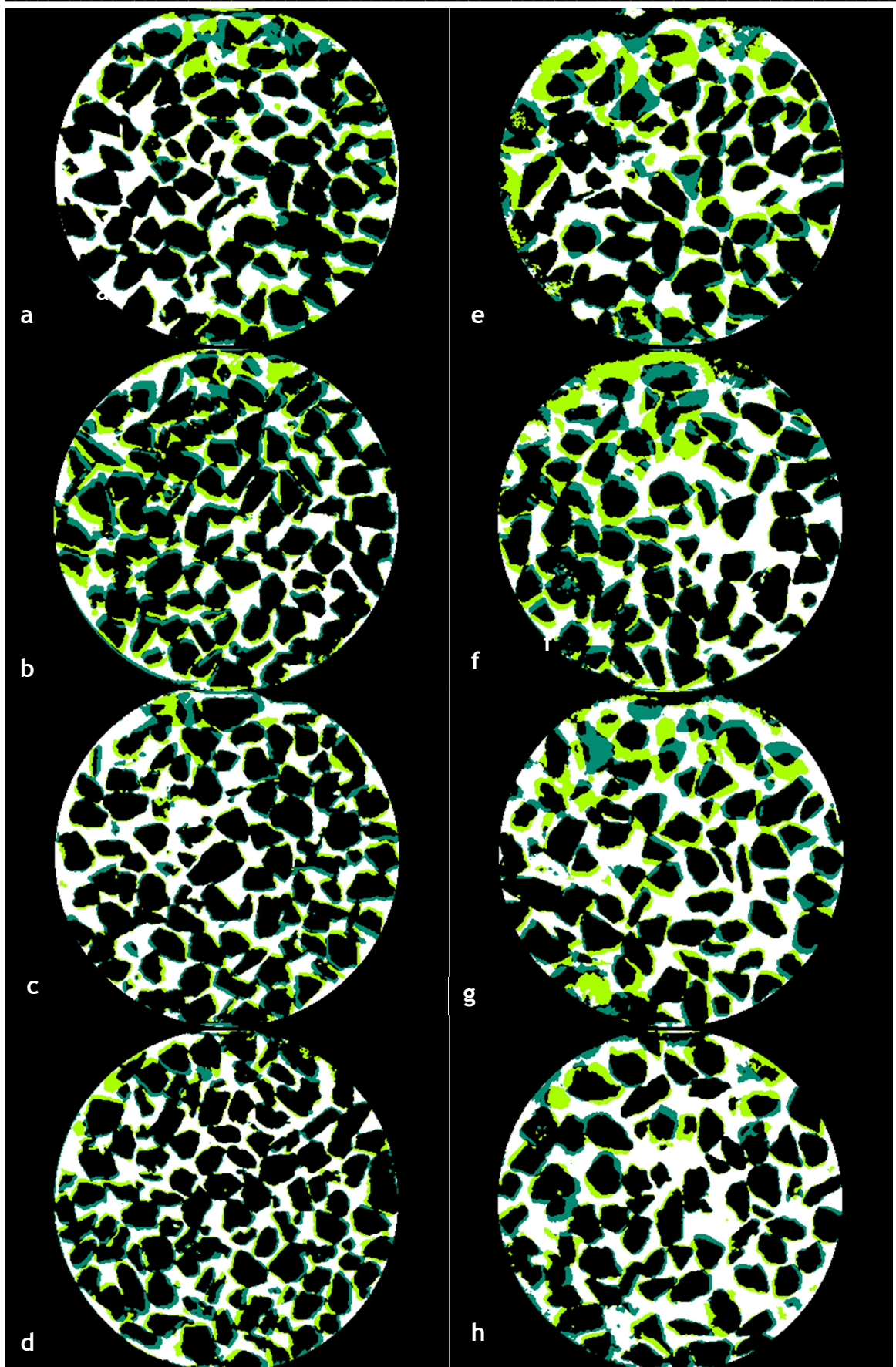
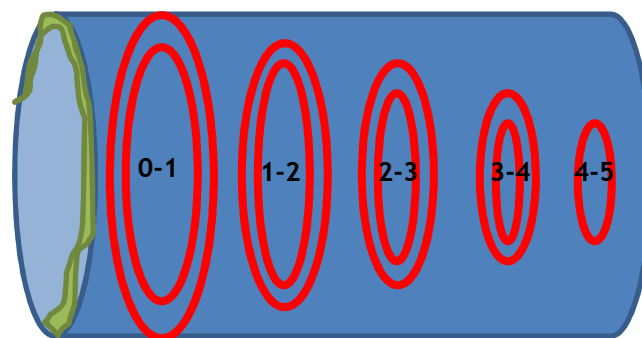


Figure 4.23. a - h. Slice 76 of (a) BLL (b) BDL (c) BLS (d) BDS, Slice 135 of (e) BLL (f) BDL (g) BLS (h) BDS

Thus, it appears that when assessing the slice-average along the longitudinal gradient of the filter, the inlet appears to have a prevalence of biofouling that is likely due to a higher nutrient dose for preferred biological growth. Percentage of pore space blocked by biofilm clearly increases by 0.62-9.1% in slices closer to the inlet than the middle of the column for all four experiments. This statistic is understandable as biofilm would be expected to aggregate and grow at a higher concentration at the point of entry to the column or SuDS system. What is also apparent is that pore blockage due to biofilm is higher in the experiments that had a light source at 8.8% and 6% blockage near the inlet in Slice 135 as opposed to 2.9% and 1% in the dark experiments. Overall, Method (i) was able to demonstrate that even though an overall negative value for percentage of pore space lost to blockage was determined for BioDarkLong, BioLightShort and BioDarkShort, localized areas near the inlet do indicate biofilm growth but that gravel movement throughout the column was more significant. Therefore, the binary analysis used for determining biofilm growth and percentage of biofilm growth over the total ROI's is believed to underestimate the percentage of pore blockage by biofilm due to settling and movement of gravel throughout the experiment.

Method (ii). In order to determine biofilm growth throughout different depths of the column, concentric regions of interest (Fig. 4.24) were established for each column experiment at 0-1, 1-2, 2-3, 3-4 and 4-5 grain diameter (equivalent to ~10mm) distance from the column edge. Results can be found in Table 4.5 and visualized in Appendix J.



**Figure 4.24.** Illustration of concentric ROI of 0-1, 1-2, 2-3, 3-4 and 4-5 grain diameter

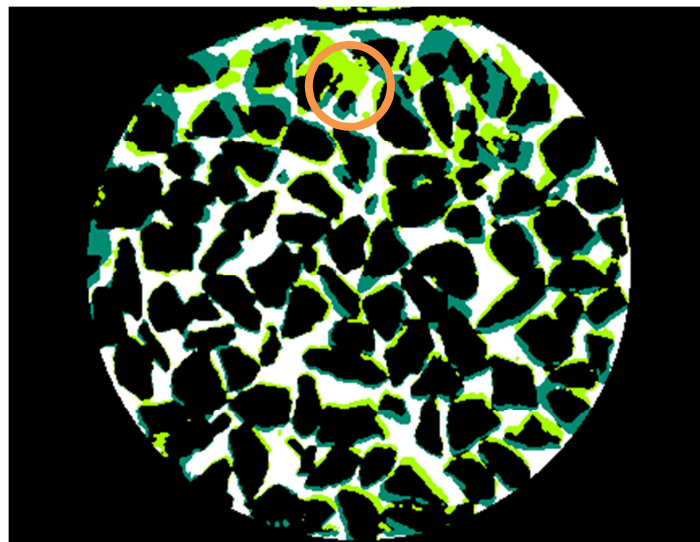
ROI Area	% Pore Blockage by Biofilm			
	BLL	BDL	BLS	BDS
<b>0-1 Stack</b>	0.88	0.38	-8.5	-1.9
<b>Slice 76</b>	1.8	-0.88	-3.3	4.6
<b>Slice 135</b>	7.8	7.8	-2.4	1.5
<b>1-2 Stack</b>	3.9	-2.1	1.0	1.2
<b>Slice 76</b>	9.7	-5.0	-4.3	-5.0
<b>Slice 135</b>	13	-7.7	10	-0.03
<b>2-3 Stack</b>	2.6	-1.1	-0.73	-0.49
<b>Slice 76</b>	-4.5	-3.8	-1.1	0.62
<b>Slice 135</b>	4.6	6.1	13	-1.6
<b>3-4 Stack</b>	2.3	-1.9	-0.69	-0.64
<b>Slice 76</b>	5.6	-2.3	-5.2	1.5
<b>Slice 135</b>	14	2.8	8.3	4.3
<b>4-5 Stack</b>	2.2	-0.11	-2.7	-0.54
<b>Slice 76</b>	-1.8	3.9	3.9	-6.1
<b>Slice 135</b>	-14	4.9	8.6	3.8

**Table 4.5.** Results of concentric ROI for BLL, BDL, BLS and BDS for % pore blockage by biofilm for the entire stack, slice 76 and slice 135

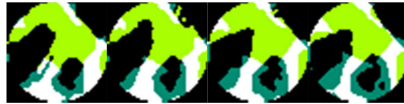
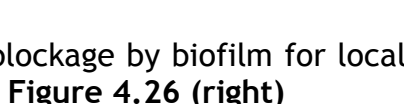
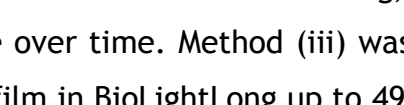
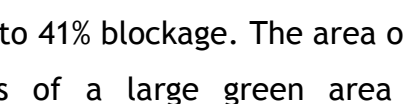
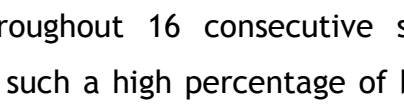
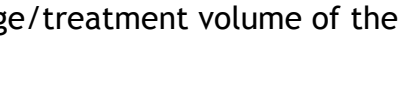
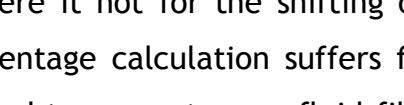
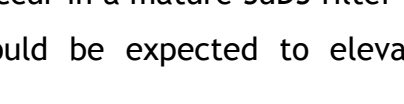
According to the snapshot provided by the data of Slice 76 and 135 in Table 4.5, the following observations can be made: (i) no obvious depth trends are seen in the dark experiments and BioDarkLong continues to demonstrate an overall negative percentage of pore blockage due to biofilm throughout the concentric ROI's except for a small 0.38% at the surface (as illustrated in Figure 4.19b). (ii) All columns demonstrate some form of clear biofouling in the mid-depth zones of 1-4 (up to 14%) indicating definite growth where flow rates are moderated within the porous media and some light may penetrate. (iii) BioLightLong demonstrates pore blockage due to biofilm throughout the concentric ROI's with the ROI at 1-2 grain diameter illustrating the highest percentage of growth at 3.9% total for the stack. It is surprising that in the light, long experiment that the values of biofouling are low (up to only 7.8%) near the edge of the column exposed to the most light. This may be due to the edge effect of the column allowing more movement of grains in this ROI and thus, underestimating the actual biofilm growth at the surface. Or, it may also be due to the initial pore space volume being very large in the wall region, hence, despite significant biofilm growth, the values seem small relative to the initial pore volume. Also, growth is generally localized to the top of the chamber, hence, the circumference method fails to account for the more localized effect, and thus,

why Method (iii) was undertaken. This trend is also seen in BioLightShort and BioDarkShort in which the 0-1 grain diameter edge illustrates the least ‘blockage’ but 1-2 grain diameter illustrates the only positive percentage of biofilm blockage.

Method (iii). A localized area of BLL was identified to which a large portion appeared to be biofilm growth and identified as green in the binary analysis (orange circle in Fig 4.25). Further percentages of biofilm blockage were calculated for this localized ROI over 16 slices (chosen as this is the full pore space that returned the maximum percentage of biofilm blockage through the ROI) with results are summarized in Table 4.6 and Figure 4.26.



**Figure 4.25.** Localized ROI (orange circle) shown on slice 106 of BLL

Local % Pore Blockage by Biofilm		95	96	97	98
Slice 95	27				
Slice 96	36				
Slice 97	43				
Slice 98	44				
Slice 99	45				
Slice 100	49				
Slice 101	48				
Slice 102	45				
Slice 103	44				
Slice 104	42				
Slice 105	42				
Slice 106	45				
Slice 107	43				
Slice 108	39				
Slice 109	33				
Slice 110	26				

**Table 4.6 (left).** Calculated percentage of blockage by biofilm for localized ROI throughout slices 94 - 112 of BLL as shown in Figure 4.26 (right)

This data is specific to illustrating the localised influence of biofouling, specific to examining changes to a single pore space over time. Method (iii) was able to quantify maximum pore blockage due to biofilm in BioLightLong up to 49% on the ROI cross-section and, when Table 4.6 is averaged out over the pore volume it is clear that this pore in its entirety is subject to 41% blockage. The area of biofilm visually identified through binary analysis of a large green area without corresponding blue (which would have been indicative of shifting) maintained between 26-49% pore space blockage throughout 16 consecutive slices of BioLightLong. This in itself is significant, as such a high percentage of blockage reduces the volume and speed of fluid flow within the pore space, reduces pore connectivity and reduces the effective storage/treatment volume of the filter.

However, equally significant is that this blockage value due to biofilm would actually be expected to be even higher, were it not for the shifting of grains locally. To justify this statement, the percentage calculation suffers from the 'blue' region where grains have locally shifted to generate new fluid-filled pore space in Fig 4.26. This effect is unlikely to occur in a mature SuDS filter and thus biofouling of a more stable substrate would be expected to elevate local

biofouling. Crudely, this effect could be removed from the data set above by examining the green area relative to only the white region (long-term fluid), leading to values of up to 85% biofouling (Fig 4.26); whilst this intuitively can be considered a more likely scenario for a stable, mature filter gravel it cannot be conclusively proven from the above data set.

### 4.3.2 Flow image analysis

For the sake of brevity, only the BioLightLong Cu transport experiment (as the Bruker software image of the initial blank scan subtracted from the sequence of scans taken every 5 minutes) is shown in Fig 4.27; this is justified as the data is representative of that observed for all flow experiments. Figure 4.27 illustrates that while it is possible to image metal transport and utilize a Cu tracer within an experimental gravel filter, the transport pathways are too complicated in the current thesis to be modelled or analyzed by basic statistics; rather more complex computational fluid dynamic modelling is required for full interpretation of the (eco)hydraulics, which falls outwith the remit and timescale of the present PhD. Interpretation of Fig 4.27 shows that it is apparent that from the time the tracer pulse started, it took around 15 minutes for the Cu to begin to appear in scan number 4 (20 minutes); the tracer is focussed around the side-walls of the column, indicating earliest breakthrough (i.e. fastest flow) in this region. Given that the packing arrangement of the gravel near the side-wall is looser, leading to larger pore space, this result is to be expected. Analysis of subsequent images (no. 4-9 on Fig 4.27) shows the Cu concentration (intensity of colour contrast) increasing in the side-wall region and expanding towards the centre of the column. This shows either lateral advection of tracer from the side-wall regions or, slower break-through of longitudinal flow in the central region; most likely, a combination of both processes is responsible. Fig 4.27 then indicates that tracer concentrations finally appear homogeneous in concentration across the column between scans 9-20. Thus, it can be concluded that flow within a horizontal gravel filter column does not follow the plug flow regime that is typically assumed in wider flow chamber studies and contaminant transport research (Fetter 2008); this has notable implications for future modelling of transport parameters in such systems.

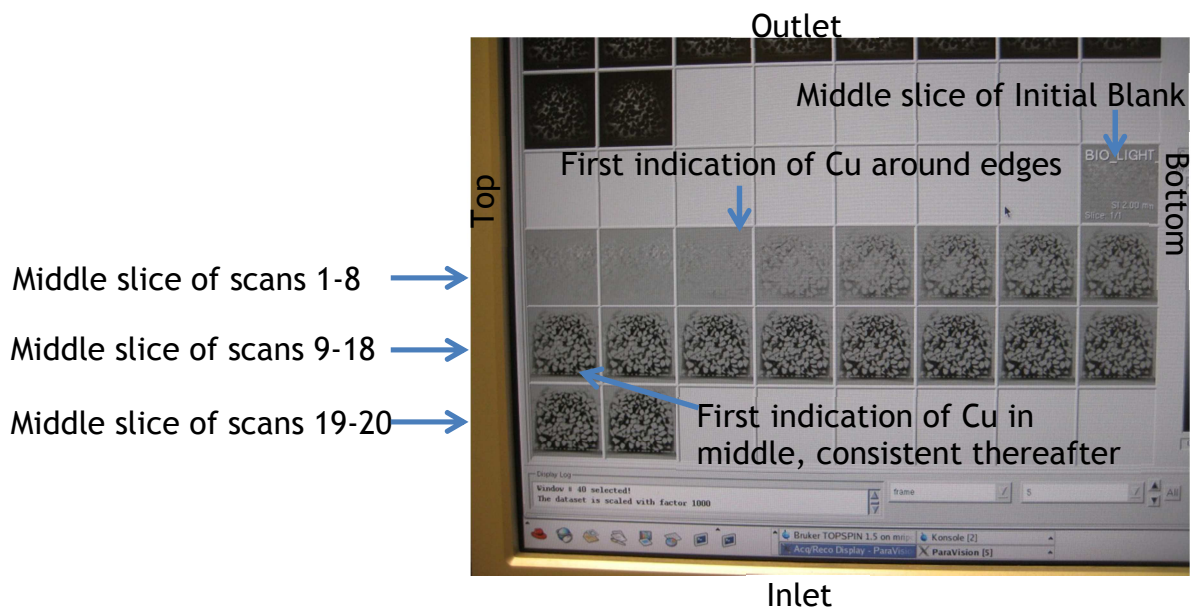


**Figure 4.27.** Bruker Paravision Cu transport experimental results. Data shows the full cross-sectional slice located halfway along the flow chamber. Each consecutive image is at + 5 minutes of the prior image. Cu tracer is illustrated on a grey-scale, where low concentrations image grey and high concentrations tend to black.

## 4.4 DISCUSSION

Since growth of biofilm within a SuDS system is not a well-known process, this research aimed to develop a method for use of MRI to image biofilm grown in a gravel filter. While to this point, much of the biofilm and MRI research focussed on imaging a thicker biofilm (Phoenix and Holmes 2008) or was grown in membranes (von der Schulenburg et al. 2008b) or smaller, uniform porous media (Seymour et al. 2007), it was not known for sure how a biofilm coating grown over ~10mm gravel grains would affect the MR signal. While, MRI has been successfully utilized to image biofilm and metal processes in the past, (Phoenix and Holmes 2008) it has not been utilized specifically in a gravel filter bed and as such, some challenges arose in the ability of MRI for this purpose, though some results do provide some important implications for SuDS based research.

### 4.4.1 Porosity analysis

The first aim of determining porosity of a gravel bed filter through MRI imaging returned successful results. The 3D high resolution scan of the gravel filter bed provided an exceptionally detailed MRI image to work with for further image processing, with the only downside being the 21 hours need to acquire the

image. While higher resolution could have been achieved, the parameters used for this experiment were sufficient for the post-scan processing intended. The porosity method was also one in which the ImageJ processing software was favourable in its ease of use and ability to provide reliable results. A wide range of segmentation processes was researched in order to determine the optimal thresholding method that was ultimately used for this data set and is discussed and reported in Minto (2013). With a thorough evaluation of manual and automatic thresholding methods, it was determined that the post-processing of noise and thresholding with the Niblack algorithm in the Auto Local Threshold Plugin provided the optimal results with low residual noise and clear segmentation of gravel particles in close proximity to one another. The ability of the method to segment a large area quickly and efficiently, matching reasonably well to a manual interpretation performed, was thus considered the overall best method for a variety of quality criteria considered. While all methods will give some uncertainty and discrepancy with interpreting and segmenting the MR signal, the thresholding method described in Section 4.2.7 was chosen as the optimal method for the current data set of images. Following the segmentation process which provided a good thresholded region of interest (ROI) to work with, ImageJ's ability to determine the percentage area of the pore spaces, resulted in a porosity measurement for the gravel filter consistent with the range of porosity typically predicted for coarse gravel or dolomite. As reported in Morris and Johnson (1967), porosity for coarse gravel tends to be in the range of 24 - 37% while dolomite has a porosity range of 19-33%. The average dolomite porosity measurements obtained from the MRI images and percentage area analysis in ImageJ were between 32-34% with most clean and all biofilm average porosities being at 32%. Thus, the ability of MRI to produce high resolution 3D images that can be subsequently processed to segment between the solid gravel fraction and the water fraction to obtain porosity measurements did prove to be a successful method for determining porosity of an experimental gravel filter.

#### **4.4.2 Biofilm imaging with MRI**

Since it was not known how biofilm would image with MRI when grown in a gravel filter column, comparison of porosity between the Clean and Bio scans was used for possible insight into changes before and after the growth period. Since biofilm is mostly composed of water, there was the possibility that it

would image as the water fraction though it was not known whether a thick enough biofilm, consisting of a higher amount of  $^1\text{H}$  nuclei, would grow over the gravel and change the MR signal within the Bio scans. If this were the case, the biofilm growth would image as water, thus increasing the porosity of the Bio scan compared to the Clean scan when thresholded. As discussed in the results section, phototrophic biofilm growth was visually seen in the BioLightLong experiment, while biofilm may have grown in the other three experiments, it was not as visually prominent. When comparing the Clean to Bio scans, the average porosity increased slightly in the experiments where biofilm was not seen: BioDarkLong increased by an average of 1.7% while BioLightShort increased by an average of 0.90% and porosity for BioDarkShort was within 0.18% between the Clean and Bio scans. These slight differences in porosity are thought to be due to the small shifts in the gravel during movement between the Clean and Bio scans in BioDarkLong and BioLightShort, while the BioDarkShort appeared to display the slightest shifts in gravel in Figure 4.19c and is thus affirmed with the average porosity being within 0.18 between the Clean and Bio scans. With the three columns with little visual growth but possible gravel shifting showing slightly higher porosity for the Bio scan over the Clean scan, the BioLightLong column porosity consistently decreased from the Clean scan to Bio scan with an average decrease in porosity of 2.5%. Interestingly, it was hypothesized that due to the high water content of biofilm, the growth over gravel would increase the  $^1\text{H}$  nuclei present and image more like water to increase the porosity of the BioLightLong scan in which phototrophic biofilm was seen, but the porosity calculations indicate otherwise. Thus, after further analysis and review of the literature, the biofilm growth appeared to be reducing the MR signal when compared to water, and thresholded as the solid fraction. This more substantial difference between the before and after biofilm growth scans in BioLightLong is evident in the porosity measurements as well as the differentiating images acquired to compare between the Clean and Bio scans.

Once porosity analysis determined that the column with visual phototrophic biofilm (BioLightLong) indicated a decrease in porosity, the assumption that biofilm growth was being segmented as a solid in the binary thresholded Bio scans was further analyzed with total pixel area of differentiating images. This was subsequently confirmed through analysis of differentiating images between

Clean and Bio scans for each experiment (as seen in Fig 4.19 a-d), to which resulting regions of green, that indicate regions that imaged as liquid in the Clean scan and solid in the Bio scan, were determined to be potential regions of biofilm growth. Once areas of blue, that indicate regions imaged as solid in the Clean scan and liquid in the Bio scan, were subtracted out (as these regions indicate shifting gravel and have equivalent green regions on the opposite side of the grain), BioLightLong was the only column to which resulted in more green regions being distinguished through pixel analysis to determine total area of each fraction (solid - black, liquid - white, and resulting differences between Clean and Bio resulting in blue and green regions). This 1.6% of the bulk volume for the BioLightLong column is thus considered to be the area of initial pore space that has been filled by 6 months biofilm growth. The further three experiments all had negative percentage of biofilm blockage, corroborating with both porosity analysis and the observation that a thick, phototrophic biofilm was not seen to grow within these columns. Thus, green and blue regions in the differentiating images for BioDarkLong, BioLightShort and BioDarkShort and the negative overall percentage of green area is believed to be due to more significant shifts in gravel during movement of the column between the Clean and Bio scan than actual biofilm growth within these experiments.

Since determination of biofilm growth within an experimental gravel flow cell has thus far been done through binary analysis, it is also important to look at the original high resolution scans (example in Figure 4.21). While potential biofilm growth cannot be visualized specifically over the already solid fraction of gravel outright and differences in intensity inhomogeneity are apparent (thus why analysis was done in binary), the main observation illustrated in Figure 4.21 is that the brightness of the signal has been diminished from the Clean to the Bio scan. This observation corroborates with previous studies in which it is reported that biofilms are known to reduce the  $T_2$  NMR relaxation times of water hydrogens (Hoskins et al. 1999; Manz et al. 2003; Seymour et al. 2004a; Seymour et al. 2004b; von der Schulenburg et al. 2008a; von der Schulenburg et al. 2008b). This reduced signal is due to the intracellular water molecules (and thus  $H^1$  atoms) motion being impeded by the surface of the biofilm (Hoskins et al. 1999). Due to the visual appearance of biofilm in BioLightLong along with the resulting decrease in porosity and increase in pore space thresholded as liquid in

the Clean scan and solid in the Bio scan, it is believed that the reduced relaxation signal seen on the high resolution scans is indeed biofilm growth returning a reduced signal to the water in the pore space and ultimately thresholding as a solid in binary analysis. Indeed, while biofilm has a high water content, it could not be expected to completely change the solid fraction signal when grown over gravel (even though it was thought that the high water content could enhance the  $^1\text{H}$  over gravel to a point), nor threshold as a liquid when the relaxation is less than water itself. Since  $T_2$  relaxation time values, mapping and analysis was beyond the scope of the current study, direct comparison to imaging of biofilm within the literature is difficult due to the many studies in which biofilm was successfully imaged and quantified through MRI techniques utilizing  $T_1$  or  $T_2$  reduced relaxation times that correspond to biofilm and biofilm being grown in reactors/membranes (Manz et al. 2003; Seymour et al. 2004a; von der Schulenburg et al. 2008b) or on porous media not comparable to gravel filter media, e.g. glass beads (Hoskins et al. 1999; Seymour et al. 2004b; Seymour et al. 2007; Shamim et al. 2013) or sand (Potter et al. 1996).

What is also important to note is that while BioDarkLong, BioLightShort and BioDarkShort all returned a negative percentage of blockage due to biofilm, it is not thought that biofilm did not grow at all in these columns but rather, a combination of less biofilm growth as compared to BioLightLong and the degree to which gravel movement between the two scans was more significant in these columns. This is apparent when localized analysis is performed on the binary processed Clean and Bio scans in Section 4.3.1.3. In Method (i) it is realized biofouling occurs near the inlet more than the middle of the column in all experiments, though this is only a snapshot of two slices, as analyzing the entire ROI of 140 slices would be laborious and time-consuming. Method (ii) did indicate some trends through concentric ROI in the experiments, though, while it was believed this method would indicate higher biofouling in the near-wall areas where light penetrated most in the light experiments, the method failed to account for the outer-most region having the largest initial pore space, and thus, underestimating the biofouling in this area in relation to the pore space despite significant biofilm growth. Finally, in Method (iii), while the biofilm may represent 100% pore blockage in certain areas, binary analysis of ROI takes into account areas of gravel and water as well, thus returning a nearly 50% pore

space blockage over the local, circular, ROI. Bulk measurements (Section 4.3.1.2) are relatively easy to determine but are not suited to detailed understanding of the biofouling impact on filter flow processes and effect on efficiency, while pore-scale analysis (Section 4.3.1.3) helps to give insight into localized biofouling but is currently laborious and time-intensive. Overall, the data still corroborates that biofilm growth is spatially heterogenic and reacts to local flow paths and light.

Whilst the ROI methodology employed in Section 4.3.1.3 is user defined and judicious in better explaining the processes in the present thesis, its scope is limited in the present thesis. This is justified, as both objectives of (i) methodological use of MRI for biofouling of filters and (ii) quantitative analysis of local biofouling, have been proven. As a more detailed examination of individual pore-space biofouling would require significant (many months) of data analysis and, likely data processing software coding to be generated, it is considered outwith the requirements of this thesis but worthy of future research which, in particular, when concerned with the impact of biofouling on local flow paths or pore connectivity. Even if specific biofouling percentages could not be ascertained from the current research, it is important to note that local blockage of even one individual pore will cause global changes to permeability, local preferential flow paths and velocities and may render large volumes of a filter redundant if pores are filled or isolated. Thus, it is critical that future research sees this more as a local problem with upscaled impact, rather than a bulk volume issue. It is suggested that further local biofouling MRI research be run in conjunction with laboratory studies to determine flow and permeability in porous media through assessment of hydraulic conductivity and loss of hydraulic head (Beach et al. 2005).

### **4.4.3 Biofilm growth**

A number of important observations about growth of biofilm in a gravel filter can be made following the four different growth experiments.

1. With the single light source, a one month growth period did not appear to be sufficient for thick phototrophic biofilm colonization. As visual biofilm

did not grow in the light conditions over one month, neither did biofilm grow in the dark conditions over one month.

2. Once the columns were allowed to recirculate the inoculated pond water for upwards of two months, colonization was seen in the BioLightLong column on the side that the light source was focussed. This initial colonization on the right side of the column resulted in the area where biofilm colonized for the remainder of the experiment even though the light source was moved to the other side midway through the six months. Thus, this initial colonization appears to be significant for the biofilm in that it continues to grow in this area, even though the light had moved.
3. A thick greenish-brown phototrophic biofilm was apparent after six months of growth in the BioLightLong column as a light source was present. While, it is thought that the longer time frame of six months was sufficient to produce patches of a brownish biofilm coating on some of the grains in BioDarkLong experiment (Fig 4.28).



**Figure 4.28.** Photo of the BioDarkLong column after 6 months growth period

4. Once the biofilm started to appear in in BioLightLong after about two months, a bright green coating appeared to coat the grains (Fig 4.29a). Once the biofilm began to grow thicker and colonize (Fig 4.29b), the inoculated pond water began to turn a bright orange-red colour as seen in Figure 4.29c. It is not known why the colour of the water would change, though the chemical makeup of the dolomite is thought to have an effect on the composition of the biofilm growth as discussed in Chapter 3.



**Figure 4.29.** (a) Biofilm growth after 2 months (b) biofilm colonization after 6 months (c) orange colour of inoculated pond water after 6 months growth

5. This orange-red appeared to have coloured the grains of gravel in the BioDarkLong column and can be visualized in Figure 4.29 as compared to the BioLightShort column without any visual biofilm growth.



**Figure 4.30.** Photo of BioLightShort (left) compared to BioDarkLong (right) after growth period showing colour change of the dolomite in BioDarkLong

#### 4.4.4 Data Uncertainty

Even though care was taken to determine the best methodology for processing of the MRI images and data set, certain levels of uncertainty and errors are likely

to remain in the data set and it is important to be transparent in terms of their significance to the data presented above:

- i. As the location of the column in the MRI is repeatable to within  $<1$  slice, before and after scans of individual slices for the biofilm experiments can be overlain for analysis of temporal changes. It is important to note that this process is subject to sub-pixel scale errors of slice alignment: for example, even if there was no change to the column contents, a 0.5 pixel difference in the positioning of the column in the MR bore may lead to a difference in the composition of solid-liquid proportions of the pixel; in its extreme this may mean that a solid pixel in the original scan may become fluid in the repeat scan (or vice versa). As this error will only affect pixels defining the solid-fluid interface of particle boundaries, it is notable that thresholding of particles is subject to a 1 pixel error due to misalignment in the bore. Based on sphere packing of the column, this yields a maximum potential error of 0.36% (or a maximum error in porosity of 0.12). Whilst improved alignment is recommended for future studies, this is difficult to achieve in reality without a pre-scan of finer resolution around a prescribed physical marker (of size greater than the image resolution) placed within the column. Whether the facility or user would be able to justify the expense (financial and time) of a long-duration pre-scan is dubious, and the implications of a physical marker on possible disturbance of internal flows should be seriously considered.
- ii. Image resolution is based upon the signal of either water or gravel within 3D voxels (300  $\mu\text{m}$  cubes) obtained from the MRI. Since it is possible that the resulting 2D pixel used for image analysis may be filled with both water and gravel, the segmentation process must choose to make some pixels with both fractions entirely water or entirely gravel depending on which fraction is a majority ( $> 50\%$ ). This results in some error when segmenting for porosity analysis and can be visualized in Figure 4.31 as illustrated in Minto (2013). If certain pixels are both water and gravel fractions but segmented as one or the other, the porosity measurement is either reduced or exaggerated. Enhancing the resolution from the MRI reduces the area that may be segmented improperly as well as refining the actual gravel/water edges. Though, increasing the resolution within

the current study would require a smaller RF coil, which would reduce the total imageable area and thus experimental gravel filter column capacity, or increase the scan time from ~20 hours to > 70 hours, which is also undesirable. Thus, it was determined that scan time and resolution were optimal for the current study and that error in the edge effects between water and gravel are likely possible in porosity measurements reported. It is not possible to determine actual gravel size versus MRI image thresholded size results due to the angular and unique shape of each individual grain of gravel. Error has been pre-determined by Minto (2013) through analysis of the actual known area of mesh diffuser openings (4.8mm) versus MRI image calculated value of the area of openings in the mesh diffuser screen at the inlet of the column. For each mesh opening, the MRI segmentation method was calculating the area to be 11% smaller than the actual 4.8mm measurement, thus giving an error estimation that the image processing method utilized overestimates the water fraction by 0.44 pixels when presented with a water/gravel interface (Minto 2013). Though, it is thought that the error may be offset by the segmenting process, and therefore, the resolution is the limiting factor between calculated image porosity and measured porosity. Since porosity measurements from image analysis align with porosity for coarse and dolomite gravel in the literature, this uncertainty is thought to be negligible within the results and scope of this work. However, future work should carefully consider the compromise between image resolution, time of scan and strength of the MR instrument; this recommendation and justification is in line with that of Haynes et al. (2009).

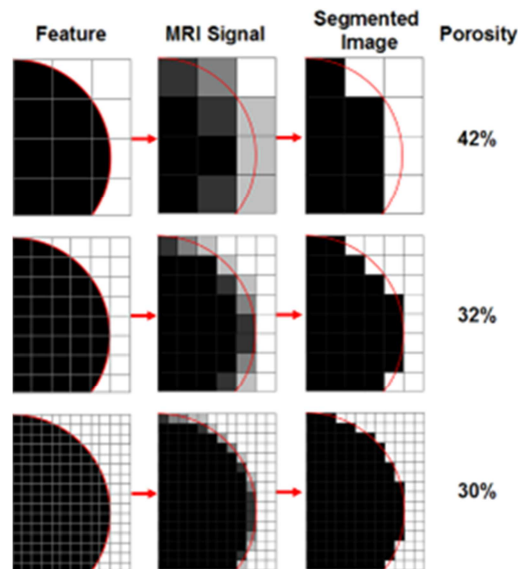


**Figure 4.31.** Example of how image resolution effects porosity measurements during segmentation of water and gravel fractions. Example thresholding analysis done by Minto (2013)

- iii. The segmentation process involved in the binary thresholding for the differentiating images between the Clean and Bio scans will also result in a certain degree of uncertainty for the reasons highlighted in (i). When determining the area of green, errors will exist with edge effects and thresholding of water versus gravel fractions but another degree of uncertainty exists due to movement between the two scans. This is evident in Figures 4.19 but there is also movement in 3D that may not show within the vertical 2D slices utilized for comparison between Clean and Bio scans. Thus, the estimated percentage of biofilm growth within the pore space as 1.6% in BioLightLong is most likely underestimated due to movement within 3D and resulting analysis within 2D. Clearly, reducing the movement of gravel in further experiments would be beneficial. Whilst it is likely that manual movement of columns into and out of the MRI may have the greatest effect, the cost implications of running long-term experiments within the MR-bore preclude entirely non-invasive methodologies. Thus, something worthy of future consideration may be use of a fixed porous media e.g. sourced from 3D printing of an MR-compatible material.

When all these sources of error are considered, even the highest cumulative error is likely to be within 2% porosity calculations; these are comfortably within the tolerances of a project where the objective was primarily to see if biofilm

growth could be MR imaged and subsequent spatio-temporal patterns analyzed in an experimental gravel filter column.

## 4.5 CONCLUSION

The first aim of MRI chapter was successfully fulfilled in that the porosity of a gravel filter was determined through MRI imaging. Key conclusions are:

- MR image processing and thresholding method returned porosity measurements that correlate with the range of porosity typically found in the literature for coarse and dolomite gravel at around 32%.
- Using porosity measurements as an indication of biofilm growth (via subtraction of images taken before and after biofilm growth), phototrophic biofilm growth (BioLightLong) resulted in a decrease in average porosity.
- From BioLightLong data, the assumption that biofilm growth reduces the  $^1\text{H}$  signal of water to segment as a solid fraction appears valid.

Further, the use of MRI has provided clear evidence of spatially heterogenic patterns of biofilm growth and (eco)hydraulics studied by Cu tracer. Specifically:

- Inlet and near-wall regions appear most susceptible to biofilm growth; this appears related to a combination of both, the larger pore spaces with faster flow which causes greater nutrient availability and, the light source (for phototrophic experiments).
- Analysis of biofilm clogging of the filter indicates that it is responsible for the loss of 1.6% of the total effective storage/treatment-volume. Analysis of cross-sectionally averaged MR slices near the inlet suggests that this bulk volume loss rises to 8.8%. However, given that growth is spatially heterogenic across the filter, pore-scale analysis is arguably the most important statistic, with individual pore spaces showing biological blockage of up to 85%. This latter finding is clearly influential on filter storage volume, treatment volume, effective permeability and flow routes within the filter. Thus, it is recommended that biological growth and filter design life are jointly considered in future SuDS design and modelling.

Finally, the flow transport experiments do indicate a successful methodological framework for (eco)hydraulics in filter studies using MRI. The main findings are:

- Cu tracer concentration mapping is appropriate for MRI of pore-scale ecohydraulic analysis, subject to appropriate CFD numerical modelling packages being available (outwith the scope the present PhD).
- Cu tracer data clearly indicates faster flow transport in the side-wall regions of the filter. This is important, as it counters previous assumptions of plug-flow in filter systems and raises doubt regarding the validity of current filter flow modelling practices.

Overall, this Chapter has successfully designed and demonstrated the benefits of MRI in filter design analysis. It has cast doubt upon existing plug-flow modelling of filter flow and highlighted the necessity of considering microbiology in filter design efficiency, particularly over the extended design life of the filter where biological communities may be extensive and well-developed. Whilst it is recognised that these recommendations come from a limited PhD study, the topic and data are novel and crucial for engineers to better design SuDS systems that are effective in water-treatment over the long-term.

## 4.6 REFERENCES

- Baldwin, C. A., et al. (1996). "Determination and characterization of the structure of a pore space from 3D volume images." Journal of Colloid and Interface Science **181**(1): 79-92.
- Bartacek, J., et al. (2012). "The impact of metal transport processes on bioavailability of free and complex metal ions in methanogenic granular sludge." Water Science and Technology **65**(10): 1875-1881.
- Bartacek, J., et al. (2009). "Magnetic resonance microscopy of iron transport in methanogenic granules." Journal of Magnetic Resonance **200**(2): 303-312.
- Beach, D. N. H., et al. (2005). "Temporal changes in hydraulic conductivity of sand porous media biofilters during wastewater infiltration due to biomat formation." Journal of Hydrology **311**(1-4): 230-243.
- Beauregard, D. A., et al. (2010). "Using Non-Invasive Magnetic Resonance Imaging (MRI) to Assess the Reduction of Cr(VI) Using a Biofilm-Palladium Catalyst." Biotechnology and Bioengineering **107**(1): 11-20.
- Callaghan, P. T. (1993). Principles of nuclear magnetic resonance microscopy, Clarendon Press.
- Cao, B., et al. (2012). "Biofilm shows spatially stratified metabolic responses to contaminant exposure." Environmental Microbiology **14**(11): 2901-2910.

- Creber, S. A., et al. (2010a). "Magnetic resonance imaging and 3D simulation studies of biofilm accumulation and cleaning on reverse osmosis membranes." Food and Bioproducts Processing **88**(C4): 401-408.
- Creber, S. A., et al. (2010b). "Chemical cleaning of biofouling in reverse osmosis membranes evaluated using magnetic resonance imaging." Journal of Membrane Science **362**(1-2): 202-210.
- Sources of Visible Light. Retrieved November 11, 2013.
- Doughty, D. A. a. T., L (1998). Pore structure and connectivity of porous rock by high resolution NMR microscopy. Spatially Resolved Magnetic Resonance: Methods, Materials, Medicine, Biology, Rheology, Geology, Ecology, Hardware. B. B. P. Blümler, R. Botto, E. Fukushima, WILEY-VCH Verlag GmbH.
- Fridjonsson, E. O., et al. (2011). "NMR measurement of hydrodynamic dispersion in porous media subject to biofilm mediated precipitation reactions." Journal of Contaminant Hydrology **120-21**: 79-88.
- Guilfoyle, D. N., et al. (1992). "Fluid-flow measurement in porous-media by echo-planar imaging." Journal of Magnetic Resonance **97**(2): 342-358.
- Haacke, E. M., et al. (1999). Magnetic Resonance Imaging: Physical principles and sequence design, Wiley-Liss.
- Hall, L. D. and V. Rajanayagam (1987). "Thin-slice, chemical-shift imaging of oil and water in sandstone rock at 80-MHz." Journal of Magnetic Resonance **74**(1): 139-146.
- Hatt, B. E., et al. (2007). "Treatment performance of gravel filter media: Implications for design and application of stormwater infiltration systems." Water Research **41**(12): 2513-2524.
- Haynes, H., et al. (2012). "A new approach to define surface/sub-surface transition in gravel beds." Acta Geophysica **60**(6): 1589-1606.
- Haynes, H., et al. (2009). "Using magnetic resonance imaging for experimental analysis of fine-sediment infiltration into gravel beds." Sedimentology **56**(7): 1961-1975.
- Hoskins, B. C., et al. (1999). "Selective imaging of biofilms in porous media by NMR relaxation." Journal of Magnetic Resonance **139**(1): 67-73.
- Iassonov, P., et al. (2009). "Segmentation of X-ray computed tomography images of porous materials: A crucial step for characterization and quantitative analysis of pore structures." Water Resources Research **45**.
- Kaestner, A., et al. (2008). "Imaging and image processing in porous media research." Advances in Water Resources **31**(9): 1174-1187.
- Lamrous, O., et al. (1989). "Magnetic-resonance imaging application to study of porous-media." Revue De Physique Appliquee **24**(5): 607-612.
- Levitt, M., H. (2008). Spin Dynamics: Basics of Nuclear Magnetic Resonance, Wiley-Blackwell.
- Liang, Z.-P. and P. Lauterbur, C. (1999). Principles of Magnetic Resonance Imaging: A Signal Processing Perspective, Wiley-IEEE Press.
- Liu, D. F., et al. (2005). "Comparison of sorptive filter media for treatment of metals in runoff." Journal of Environmental Engineering-Asce **131**(8): 1178-1186.

- Manz, B., et al. (2003). "Measuring local flow velocities and biofilm structure in biofilm systems with magnetic resonance imaging (MRI)." Biotechnology and Bioengineering **84**(4): 424-432.
- Merrill, M. R. (1993). "Porosity measurements in natural porous rocks using magnetic-resonance-imaging." Applied Magnetic Resonance **5**(3-4): 307-321.
- Minto, J. (2013). Magnetic Resonance Imaging: a non-invasive tool to characterise and quantify spatial variation in sediment accumulation, University of Glasgow.
- Morgan, C., J. and W. Hendee, R. (1984). Introduction to Magnetic Resonance Imaging. Denver, CO, Multi-Media Pub.
- U. S. G. Survey. Summary of hydrologic and physical properties of rock and soil materials, as analyzed by the hydrologic laboratory of the U.S. Geological Survey, 1948-60. Water Supply Paper (1967)
- Nestle, N., et al. (2003). "Spatial and temporal observations of adsorption and remobilization of heavy metal ions in a sandy aquifer matrix using magnetic resonance imaging." Environmental Science & Technology **37**(17): 3972-3977.
- Neu, T. R., et al. (2010). "Advanced imaging techniques for assessment of structure, composition and function in biofilm systems." Fems Microbiology Ecology **72**(1): 1-21.
- Pang, L. P. and M. E. Close (1999). "Non-equilibrium transport of Cd in alluvial gravels." Journal of Contaminant Hydrology **36**(1-2): 185-206.
- Phoenix, V. R. and W. M. Holmes (2008). "Magnetic resonance imaging of structure, diffusivity, and copper immobilization in a phototrophic biofilm." Applied and Environmental Microbiology **74**(15): 4934-4943.
- Pintelon, T. R. R., et al. (2010). "Validation of 3D Simulations of Reverse Osmosis Membrane Biofouling." Biotechnology and Bioengineering **106**(4): 677-689.
- Potter, K., et al. (1996). "Assay for Bacteria in Porous Media by Diffusion-Weighted NMR." Journal of Magnetic Resonance, Series B **113**(1): 9-15.
- Ramanan, B. (2011). Quantifying mass transport processes in environmental systems using magnetic resonance imaging (MRI). Doctor of Philosophy (Ph.D.), University of Glasgow.
- Ramanan, B., et al. (2010). "Application of Paramagnetically Tagged Molecules for Magnetic Resonance Imaging of Biofilm Mass Transport Processes." Applied and Environmental Microbiology **76**(12): 4027-4036.
- Ramanan, B., et al. (2012). "Investigation of Nanoparticle Transport Inside Coarse-Grained Geological Media Using Magnetic Resonance Imaging." Environmental Science & Technology **46**(1): 360-366.
- Ramanan, B., et al. (2013). "Magnetic Resonance Imaging of Mass Transport and Structure Inside a Phototrophic Biofilm." Current Microbiology **66**(5): 456-461.
- Rothwell, W. P. and H. J. Vinegar (1985). "Petrophysical applications of NMR imaging." Applied Optics **24**(23): 3969-3972.
- Schulenburg, D. A. G. v. d., et al. (2008). "Spatially resolved quantification of metal ion concentration in a biofilm-mediated ion exchanger." Biotechnology and Bioengineering **99**(4): 821-829.

- Sederman, A. J., et al. (1998). "Structure-flow correlations in packed beds." Chemical Engineering Science **53**(12): 2117-2128.
- Sederman, A. J., et al. (1997). "Magnetic resonance imaging of liquid flow and pore structure within packed beds." Chemical Engineering Science **52**(14): 2239-2250.
- Seymour, J. D., et al. (2004a). "Magnetic resonance microscopy of biofilm structure and impact on transport in a capillary bioreactor." Journal of Magnetic Resonance **167**(2): 322-327.
- Seymour, J. D., et al. (2004b). "Anomalous fluid transport in porous media induced by biofilm growth." Physical Review Letters **93**(19).
- Seymour, J. D., et al. (2007). "Magnetic resonance microscopy of biofouling induced scale dependent transport in porous media." Advances in Water Resources **30**(6-7): 1408-1420.
- Sezgin, M. and B. Sankur (2004). "Survey over image thresholding techniques and quantitative performance evaluation." Journal of Electronic Imaging **13**(1): 146-168.
- Shamim, M. F., et al. (2013). "MRI measurements of dynamic clogging in porous systems using sterilised sludge." Microporous and Mesoporous Materials **178**(0): 48-52.
- Vinegar, H. J. (1986). "X-ray CT and NMR imaging of rocks." Journal of Petroleum Technology **38**(3): 257-259.
- Vogt, S. J., et al. (2012). "Detection of biological uranium reduction using magnetic resonance." Biotechnology and Bioengineering **109**(4): 877-883.
- von der Schulenburg, D. A. G., et al. (2008a). "Spatially resolved quantification of metal ion concentration in a biofilm-mediated ion exchanger." Biotechnology and Bioengineering **99**(4): 821-829.
- von der Schulenburg, D. A. G., et al. (2008b). "Nuclear magnetic resonance microscopy studies of membrane biofouling." Journal of Membrane Science **323**(1): 37-44.
- Vovk, U., et al. (2007). "A review of methods for correction of intensity inhomogeneity in MRI." IEEE Transactions on Medical Imaging **26**(3): 405-421.
- Werth, C. J., et al. (2010). "A review of non-invasive imaging methods and applications in contaminant hydrogeology research." Journal of Contaminant Hydrology **113**(1-4): 1-24.

# 5

## Nanoparticle enhanced sand for optimized heavy metal removal

### ABSTRACT

Sand based filtration systems are used in a wide range of water treatment systems, such as slow sand filtration (SSF), SuDS sand filters and SuDS systems that utilize a sand base layer. The potential for enhanced heavy metal removal by incorporation of zero-valent iron nanoparticles into the sand was examined. Nano zero-valent iron (nZVI) enhanced sand columns improved Cu, Pb and Zn removal compared to unamended sand proportional to the percentage of nZVI used. 10% nZVI removed over 98% Cu and Pb from 330 pore volumes of 5 ppm metal solution, while enhancing Zn removal by 17-30%. Considering PHREEQC geochemical modelling results and standard electron potentials of the metals, reduction is thought to be the dominant removal mechanism within the systems with precipitation supplementing the removal of Cu and Pb and adsorption supplementing the removal of zinc.

### 5.1 - INTRODUCTION

#### 5.1.1 - Environmental nanotechnology

Engineered nanoparticles have potential for pollution control in applications including acid mine drainage (Klimkova et al. 2011) contaminated water (Zaspalis et al. 2007; Zhu et al. 2009; Comba et al. 2011; Crane et al. 2011; Engates and Shipley 2011; Scott et al. 2011; Crane and Scott 2012; Parham et al. 2012), drinking water (Huang et al. 2011), groundwater (Kanel et al. 2005; Kanel et al. 2006; Karabelli et al. 2008; Mpenyana-Monyatsi et al. 2012), remediation techniques (Wang and Zhang 1997; Ponder et al. 2000; Ponder et al. 2001; Masciangioli and Zhang 2003; Li and Zhang 2006; Kanel et al. 2007; Li and Zhang 2007; Nabi et al. 2009; Shipley et al. 2011; Khin et al. 2012; Noubactep et al.

2012), stormwater systems (Chang et al. 2008), waste effluent (Dickinson and Scott 2010) and water and wastewater treatment (Hua et al. 2012). With such a wide range of environmental issues requiring attention, many types of bespoke nanoparticles are being developed to target specific environmental problems (Khin et al. 2012).

The key to nanoparticle reactivity lay in their small size range (1-100 nm), which equates to a very high surface area (Hua et al. 2012) of up to  $100\text{m}^2/\text{g}$  (Crane and Scott 2012). With such a high surface area to mass ratio, nanoparticle reactions with pollutants show enhanced reaction capacity and rates (Khin et al. 2012). This increased function at a smaller mass equates to less nanoscale material needed when compared to equivalent macro-scale material for similar applications. This leads to cost and energy savings in the long run (Masciangioli and Zhang 2003; Crane and Scott 2012).

### **5.1.2 Zero valent iron (nZVI) nanoparticles**

The capability of nanoparticles to effectively remediate a vast range of heavy metals has been widely reported, particularly for nano zero-valent iron (nZVI) nanoparticles (Ponder et al. 2001; Li et al. 2006; Li and Zhang 2007; Karabelli et al. 2008; Crane et al. 2011; Klimkova et al. 2011; Scott et al. 2011). The effectiveness of nZVI in treatment of pollutants results from the structure which promotes mechanisms of reduction as well as chemisorption (Fig 5.1). nZVI is composed of a core of zero-valent iron which drives electron donation to the surface, thus enabling reduction of heavy metal contaminants. (Li et al. 2006) Furthermore, the shell of the nanoparticle is composed of iron oxides and hydroxides which promotes adsorption of heavy metals to the surface of the nZVI (Li et al. 2006).

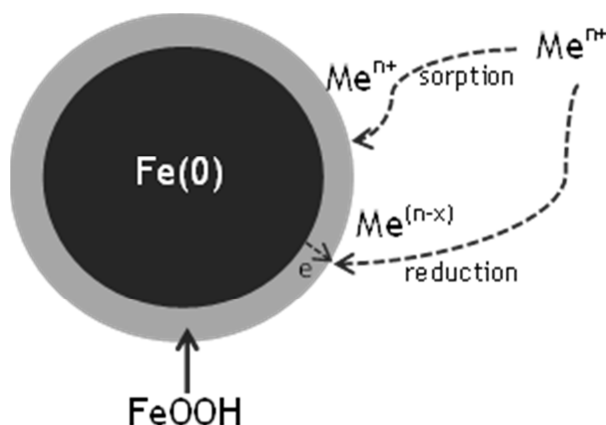


**Figure 5.1.** Schematic showing mechanisms responsible for immobilization of contaminants by nZVI. The zero valent iron core provides electrons to the surface and thus the reducing potential, while the iron oxide/hydroxide shell provides a highly reactive surface for sorption to occur. Adapted from Li et al. 2006.

While many studies have shown nZVI to be highly effective at rapid removal of a wide range of chemical pollutants, most have demonstrated this in batch form, i.e. nanoparticles suspended in liquid media (Karabelli et al. 2008; Klimkova et al. 2011; Scott et al. 2011; Parham et al. 2012). None, however, have incorporated commercially available nZVI powder into a sand filter for treatment of heavy metals. In previous research titanium dioxide nanoparticles have been immobilized in sand for arsenic and pathogen removal (Nabi et al. 2009; Mpenyana-Monyatsi et al. 2012) but immobilized nZVI have yet to be examined.

The considerable potential of nZVI in a wide range of remediation processes has led to production of commercially available nZVI, such as Nanofer. Klimkova et al. (2011) tested the ability of Nanofer in the form of a slurry of nanoiron particles coated in polyacrylic acid (Nanofer 25S) to remediate acid mine drainage resulting from in situ uranium leaching. Batch experiments with undiluted acid mine drainage demonstrated a decrease in all metal contaminants including Al, U, V, Cr, Cu, Ni, Cd, Zn and As while nZVI was able to remove all metals from a diluted sample of acid mine drainage (Klimkova et al. 2011).

### 5.1.3 Slow Sand Filtration

Slow sand filtration (SSF) is an existing, low cost and efficient technology used in water treatment to filter and treat pollutants and particulates from raw water such as pathogens, organic and inorganic contaminants and heavy metals. Not only has SSF been a water treatment technique since the early 1800's, it is also one of

the most cost-effective, simplest and efficient water treatment technologies available for developed as well as developing countries (Huisman and Wood 1974).

The SSF is a simple system incorporating a sand layer with a dense naturally occurring biofilm community on top. SSF has been used since the 1800's as a primary treatment stage in municipal water treatment in the developed world (Huisman and Wood 1974). The main mechanisms at work in a slow sand filter are first straining and degradation of organics by the *schmutzdecke*, which is the thin layer of biological material (biofilm) that forms at the top of the system. Secondly, straining of particles and adsorption of pollutants onto sand grains occurs throughout the sand media. Processes of electrostatic attraction bind particles and dissolved pollutants to the sand grains and biological coatings that have formed (Huisman and Wood 1974). Most work on slow sand filters have focussed on the removal of pathogenic bacteria; the filtering process (straining and adsorption) effectively removing bacterial cells. Heavy metals are filtered less effectively due to quartz's moderate affinity for dissolved metal ions (Mahlangu et al. 2011). As a consequence, it is imperative to enhance the heavy metal removal capacity of SSFs for use in areas of high heavy metal load.

Owing to the documented and effective use of sand for water treatment globally for over two centuries, this research aimed to use sand as a base for an enhanced treatment technology for urban run-off containing high levels of heavy metals. One such use could utilize nanoparticle enhanced sand for stormwater treatment in SuDS applications such as sand filters, or as a laying course for bioretention or permeable paving. Sand based SuDS are generally utilized in areas where the underlying soil cannot cope with influent pollutant concentrations high in biochemical oxygen demand (BOD), suspended solids or faecal coliform (EPA 1999). The United States EPA fact sheet on sand filters notes that the removal capacity of metals is moderate, reporting removal of Pb and Zn at 45%, and thus, heavy metal removal within sand filters has the potential to be improved upon.

Many other SuDS systems utilize sand as a base layer which could potentially use nanoparticle enhanced sand if heavy metals are problematic. For example, bioretention is an engineered SuDS system designed to treat high rainfall events

with landscaped vegetation underpinned with engineered soil and sand providing underdrainage and aerobic conditions as well as offering a final polishing step in the filtration process (Woods-Ballard et al. 2007). Permeable paving systems use grit as a laying course and nanoparticle enhanced sand could also be utilized in this aspect.

Another source of pollution in which high concentrations of heavy metals are a concern is acid mine drainage (AMD). AMD is a major problem throughout the world and results from oxidation of sulphide-rich mining wastes by catalysing bacteria creating a highly acidic water rich in heavy metals that poses a threat to the surrounding environment (Shelp et al. 1995). The use of a nanoparticle enhanced sand filter either designed as a slow sand filter or as a sand filter SuDS system could potentially be utilized in mining areas at risk of heavy metal contamination to the surrounding environment.

### **5.1.4 Motivation**

In the current study, nZVI and nano-bentonite were investigated for enhanced heavy metal (Cu, Pb, and Zn) removal in sand filtration applications. Little work has been done with nanoclays, and thus, nano-bentonite was used as a comparison to nZVI due to clays high affinity for heavy metals (Majdan et al. 2010) as well as being readily available, low cost (£75/kg) and non-hazardous (Sigma-Aldrich MSDS). This study aims to bridge the gap between documented, effective nanotechnology for pollution control with a simple, low cost application for incorporation of nanoparticles into sand filtration for enhanced in-situ removal of critical heavy metals in urban run-off.

## **5.2 MATERIALS AND METHODS**

### **5.2.1 Enhancing sand with nanoparticles**

Sand was enhanced with nanoparticles by dry mixing 0.1-0.3 mm fine marine sand (Specialist Aggregates Ltd., UK) with varying ratios of commercially produced nZVI (Nanofer STAR, Nano Iron s.r.o.) or nanoclay hydrophilic bentonite (Sigma-Aldrich).

Nanofer STAR is commercially stabilized by a thin inorganic layer which protects it against rapid oxidation when exposed to air, enabling transport of pure nanoparticle reactive material, as compared to the liquid suspended slurry mixture of Nanofer containing only 20% nanoparticles to 80% water. A transmission electron microscope image of Nanofer STAR can be seen in Figure 5.2 as referenced directly from Nano Iron, s.r.o.

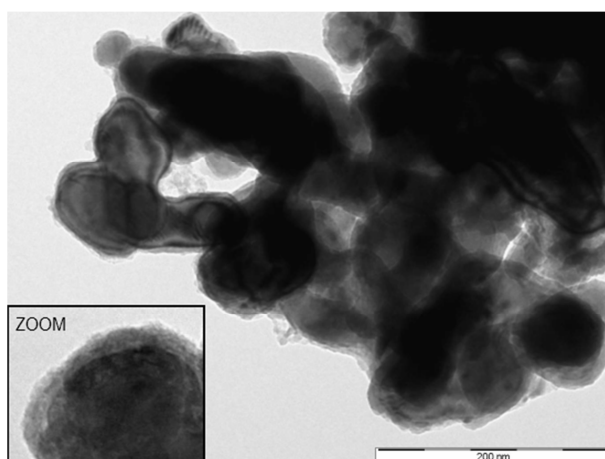


**Figure 5.2.** TEM image of the surface of Nanofer STAR. (Nano Iron Website, 2013)

Initial nanoclay (nC) experiments utilized a coarser grade of sand that measured between 0.5-1mm as well as included use of 5% nanoclay (5nC) and 10% nanoclay (10nC). The overnight DI flush appeared to flush out a notable quantity of nanoclay, generating very cloudy rinse water with high turbidity values and high solids content on drying (Table 5.1).

Column	One Liter DI Rinse Water			Porosity (%)
	Turbidity (NTU)	pH	Weight of nC (g)	
Sand	21	6.99	0.00	30
1nC	389	8.40	0.58	27
5nC	1016	8.99	1.48	26
10nC	1227	8.80	1.88	26

**Table 5.1.** Summary of data for effluent water for preliminary nanoclay experiment. NTU = nephelometric turbidity units, Weight of nC = solids content of effluent water as determined by drying.

This loss of high percentages of nanoclay from the sand matrix would be problematic as it would act as a mechanism by which heavy metals could flush through the column (i.e., bound to mobile clays). In an attempt to remedy this, a finer sand matrix consisting of 0.1-0.3 mm sand particles was used in an attempt to retain more clay. Problematically, once the fine sand matrix was utilized, 5nC and 10nC amendments made the sand filter impermeable, and thus only 1nC amendments were used in future experiments.

In order to determine an effective sand:nanoparticle concentration for heavy metal removal, unmodified sand (sand), 1% nZVI (1nZVI), 5% nZVI (5nZVI), and 10% nZVI (10nZVI) enhanced sand and 1% nanoclay (1nC) enhanced sand was measured out by weight for use in small scale sand column filters. Increased ratios of nanoclay were not used as on initial trial runs these made the filters impermeable. All five sand columns were run with individual metal solutions of 5 ppm Cu, Pb and Zn as well as a mixed solution of 5 ppm Cu, Pb and Zn together.

## 5.2.2 Experimental setup

Small scale sand columns (3.7cm diameter, 10cm length) were constructed from polypropylene syringes to hold a sand volume between 80-90g with a graded base layer 8 mm thick of very course sand (1.4-2 mm) and course sand (0.5-1 mm) to prevent the sand from falling back through the inlet at the base (Fig 5.3). Porosity ranged between 30-50% as determined by the difference in saturated and dry weights of individual columns and can be seen in Table 5.2 along with the total volume of pore space and tubing.

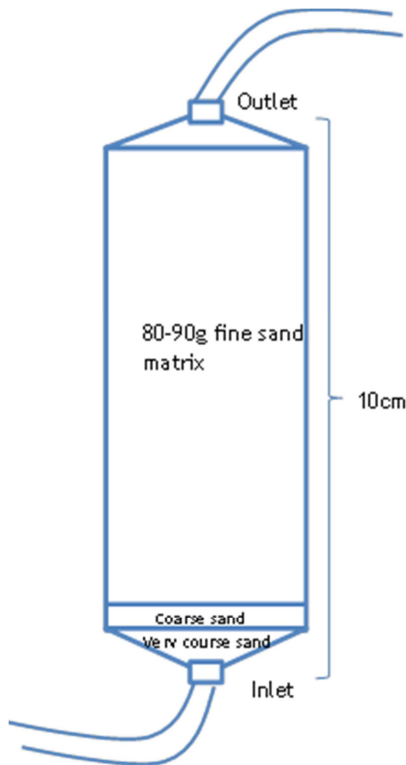


**Figure 5.3.** Schematic of flow cell. The fine sand matrix was either unamended or amended with nanoparticle.

Column	Porosity Volume		Porosity Volume		Porosity Volume		Porosity Volume					
	(%)	(mL)	(%)	(mL)	(%)	(mL)	(%)	(mL)				
Sand	Cu	38	35.22	Pb	42	39.46	Zn	43	38.31	Mix	34	35.13
1nC	Cu	35	33.23	Pb	36	33.24	Zn	34	31.14	Mix	31	33.41
1nZVI	Cu	39	35.72	Pb	37	34.73	Zn	40	36.03	Mix	34	35.44
5nZVI	Cu	46	40.75	Pb	34	31.57	Zn	44	37.96	Mix	33	35.44
10nZVI	Cu	42	37.65	Pb	42	37.93	Zn	50	39.57	Mix	49	41.02

**Table 5.2.** Porosity and total volume of pore space including tubing of each column.

1000ppm heavy metal solutions were prepared by dissolving metal salts of Copper(II) nitrate ( $\text{Cu}(\text{NO}_3)_2 \cdot 3\text{H}_2\text{O}$ ), Lead(II) nitrate ( $\text{Pb}(\text{NO}_3)_2$ ) and Zinc nitrate ( $\text{Zn}(\text{NO}_3)_2 \cdot 6\text{H}_2\text{O}$ ) (Sigma-Aldrich) in deionized (DI) water. These stock solutions were subsequently diluted into locally collected River Kelvin water to final concentrations of 5ppm for use in sand filter column experiments. Local river water was used in order to obtain a naturally occurring, complex, water chemistry that would be more typical of influent water to a SSF system, although the complete water chemistry of the river water including anions, cations and trace elements was not determined. Concentrations of 5ppm were chosen to determine effect and efficiency of the enhanced sand in comparison to un-enhanced sand. Depending on the application, this could be expected as a worst case scenario for a SuDS system which typically sees lower influent metal concentrations (Cole et al. 1984).

Prior to beginning experiments, all columns were rinsed with DI water overnight. Rinse water was collected for turbidity and pH measurements and subsequently dried at 90°C to determine weight of nanoparticles lost during the initial flush. For the final run of experiments, heavy metal solutions were fed through the base of the column with a peristaltic pump at a steady rate of between 1-1.3 ml/min (depending on pore volume for each column) in order to obtain a 0.5 hour residence time for solutions within the columns. Experiments were run for a total pulse of one week (168 hours) of heavy metals in river water. After this, un-spiked river water without metals was flushed through the columns for 16 hours to collect the tail of the breakthrough. Overall, the metal pulse equates to around 330 pore volumes followed by 40 pore volumes of un-spiked river water. Samples were taken at regular intervals from the outlet at the top of the column. Experimental setup can be seen in Figure 5.4.

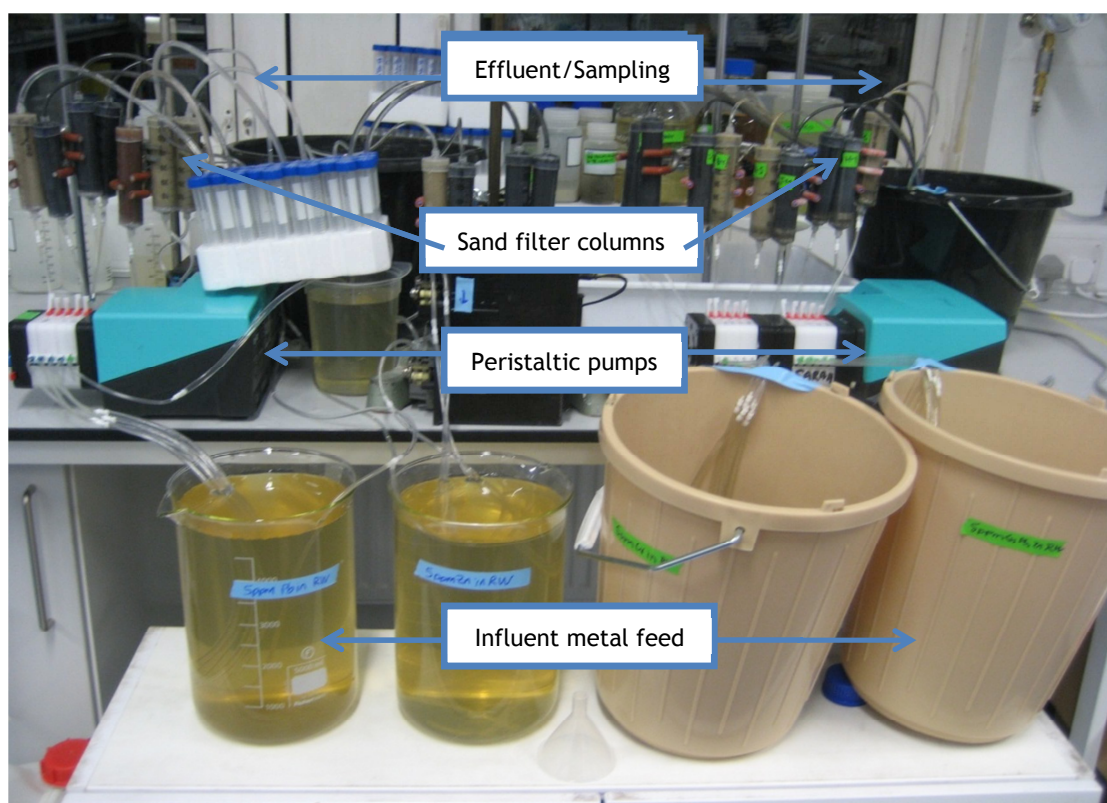


Figure 5.4. Experimental setup of sand filter columns.

### 5.2.3 Instrumentation

Total dissolved heavy metals were analyzed on a Perkin-Elmer Atomic Absorption Spectrometer (AAnalyst 400) with an air-acetylene flame, triplicate sample analysis and a detection limit of 1.5 µg/L for Cu, 15 µg/L for Pb and 1.5 µg/L for

Zn (Perkin Elmer Manual). pH was measured on a Thermo Orion 5-Star pH meter.

### 5.2.4 Breakthrough curve analysis

In order to determine the concentration of metals that passed through the column, percentages were obtained by calculating the area under the curve with the trapezoidal rule and comparing each experimental curves area to a theoretical breakthrough of 100%.

### 5.2.5 Modelling

The PHREEQC program was used to determine the geochemical parameters of metal speciation and saturation indices (SI). Input conditions to PHREEQC used the concentrations of  $\text{Cu}^{2+}$ ,  $\text{Pb}^{2+}$ ,  $\text{Zn}^{2+}$  and  $\text{NO}_3^-$ , while pH measurements recorded at the inlet and outlet were used. Saturation indices were determined for the initial metal solution (i.e. river water amended with metal prior to injection into the column) and for the final solution eluting from the column at the end of the experiment (prior to flushing with unamended water). SI's are reported for the dominant phases determined by PHREEQC as copper hydroxide ( $\text{Cu}(\text{OH})_2$ ), lead hydroxide ( $\text{Pb}(\text{OH})_2$ ), and zinc hydroxide ( $\text{Zn}(\text{OH})_2$ ) phases. PHREEQC was also used to determine dissolved metal speciation.

## 5.3 RESULTS AND ANALYSIS

### 5.3.1 nZVI and nanoclay - Single metal experimental breakthrough curves

Heavy metal immobilization results are reported as total percentage of metals retained within the columns in Table 5.3 followed by breakthrough curve graphs in Figures 5.5 - 5.10 for single and multiple metal experiments. Figure 5.5 shows experimental results of a pulse of Cu fed through the columns containing either unamended sand or sand amended with nZVI or nanoclay for one week (168 hours) followed by 16 hours of river water without Cu. All columns showed significant removal of copper, including the unamended sand. Notably, the quantities of Cu removed increased as the nZVI concentration increased. Sand removed 69%, 1nZVI removed 76%, 5nZVI removed 91% and 10nZVI removed 99%.

In contrast, 1nC (nanoclay) removed only 67% and was therefore slightly less efficient than sand alone. Consistent with trends seen for total Cu removal, peak copper concentrations in the effluent were lower at higher nZVI concentrations. In all systems, no copper eluted from the columns for the first 20 hours and the time until copper appeared in the effluent (i.e. any concentration above zero) occurred later at higher nZVI concentrations. Overall, these results show enhancement in Cu removal due to the presence of nZVI.

% Metals Retained in Column	Cu-		Pb-		Zn-	
	Single	Multiple	Single	Multiple	Single	Multiple
Sand	69	87	77	69	39	20
1nC	67	87	55	74	35	19
1nZVI	76	88	88	85	43	21
5nZVI	91	97	100	100	52	32
10nZVI	99	99	100	100	69	37

**Table 5.3.** Percentage of Cu, Pb and Zn retained within the single and multiple metal experimental columns.

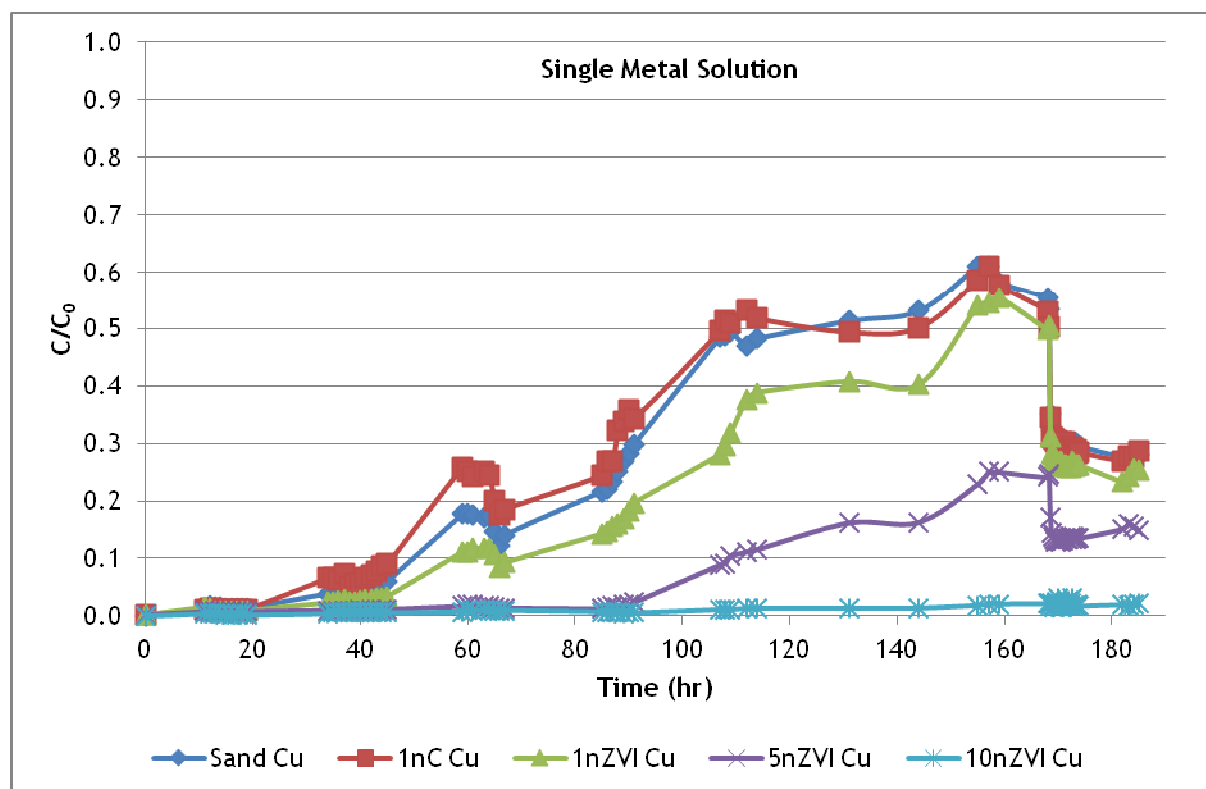


**Figure 5.5.** Cu breakthrough curve in a single element solution for sand, 1nC, 1nZVI, 5nZVI, and 10nZVI showing  $C/C_0$  versus time

Similar trends can be seen within the Pb experiment (Fig 5.6) in that all nZVI enhanced sand, as well as unamended sand retaining between 77-100% Pb, while 1nC continued to show less efficient removal of Pb than sand alone. Removal rates again were proportional to the percentage of nZVI present, with sand retaining 77%, 1nZVI retaining 88%, 5nZVI retaining 100% and 10nZVI retaining 100% Pb. As with Cu, peak Pb concentrations in the effluent were lower at higher nZVI concentrations. Furthermore, the time until Pb appeared in the effluent (i.e. any concentration above zero) occurred later at higher nZVI concentrations. Again, 1nC proved to be less efficient than sand alone with 55% Pb retained within the column. Overall, all the nZVI columns demonstrated improved removal of Pb throughout the weeklong experiment. Note that throughout the breakthrough curves, the consistency in the dips around 64 hours, 85 hours and 128 hours are thought to be an effect of metal solutions being refilled at those times.

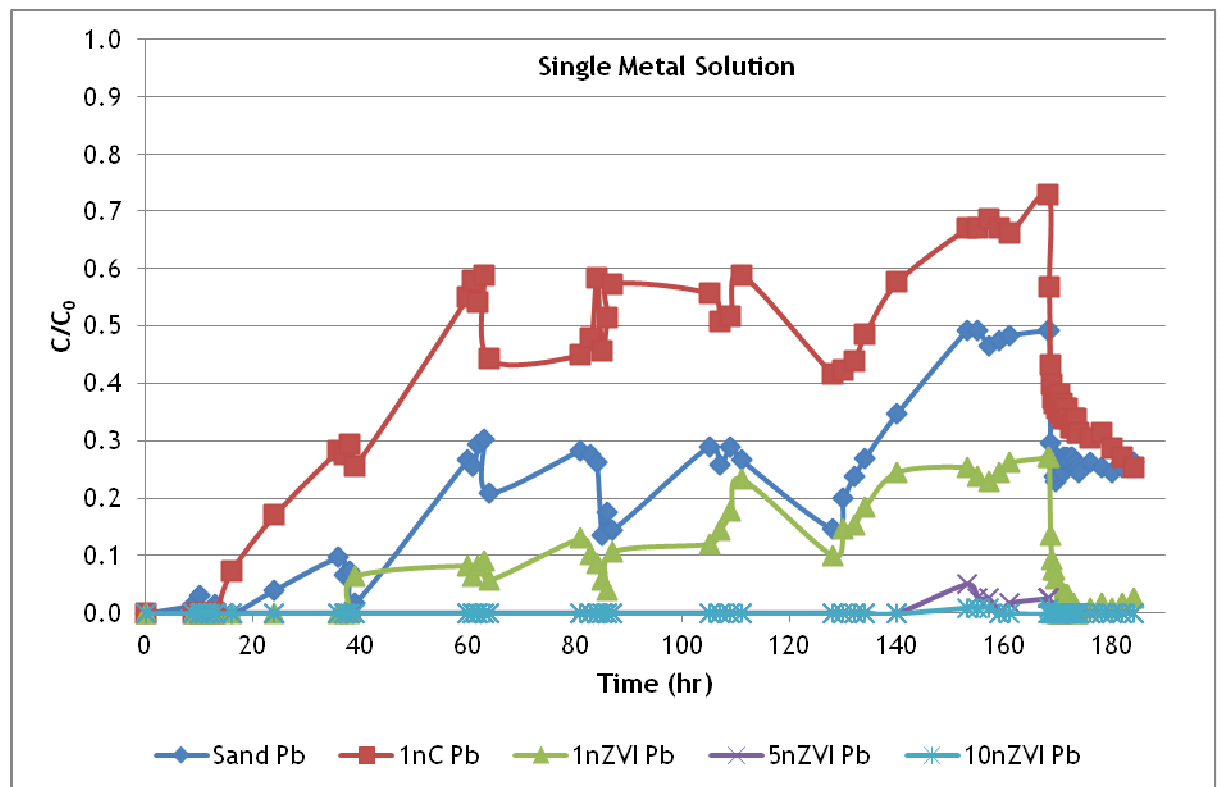


**Figure 5.6.** Pb breakthrough curve in a single element solution for sand, 1nC, 1nZVI, 5nZVI, and 10nZVI showing  $C/C_0$  versus time

Figure 5.7 illustrates the week-long Zn pulse experiment showing the same order of efficiency, with sand retaining 39% Zn, 1nZVI retaining 43% Zn, 5nZVI retaining 52% Zn and 10nZVI retaining 69% Zn. 1nC retained only 35% Zn and was therefore

again less efficient than sand alone. Maximum breakthrough concentration of Zn was similar for the unamended sand and nZVI enhanced sand columns at 82% for sand, 85% for 1nZVI, 80% for 5nZVI and 71% for 10nZVI, while 1nC reached 90%. During the first five days of the Zn pulse, the order of efficiency holds true, but for the remaining 2 days sand,  $C/C_0$  for 1nC, 1nZVI and 5nZVI are all within 10% of each other. While 1nZVI and 5nZVI sand filters initially show enhanced Zn removal over sand, they seem to lose efficiency over time while 10nZVI shows consistent enhanced Zn retention throughout the weekly experiment. The time to initial breakthrough was around 16 hours for 1nC, 24 hours for sand and 1nZVI and 37 hours for 5nZVI and 10nZVI. While Zn showed the highest breakthrough of the three metals, nZVI enhanced sand columns did continue to demonstrate overall improved Zn removal.

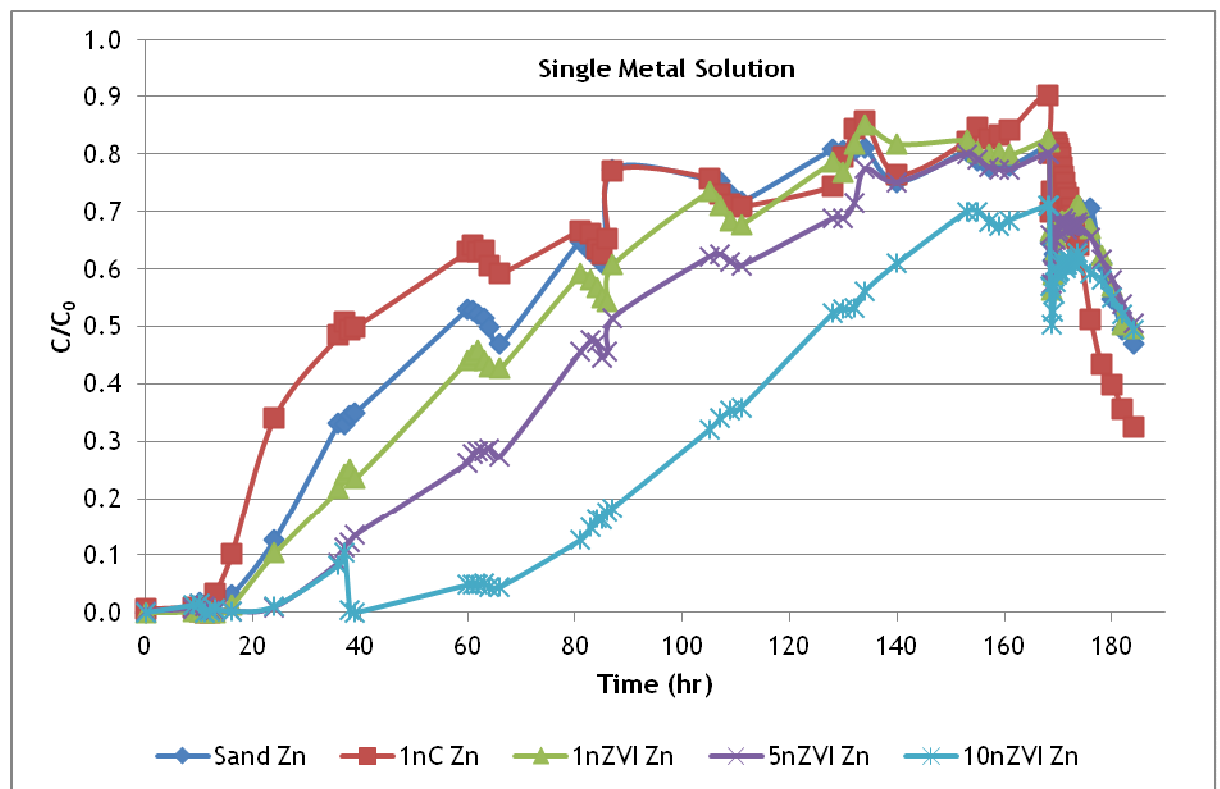


**Figure 5.7.** Zn breakthrough curve in a single element solution for sand, 1nC, 1nZVI, 5nZVI, and 10nZVI showing  $C/C_0$  versus time.

### 5.3.2 nZVI and nanoclay - Multiple metal experimental breakthrough curves

A multi-elemental solution of Cu, Pb, and Zn was also run for a weekly experiment and individual element graphs can be seen in Figures 5.8 (Cu), 5.9

(Pb) and 5.10 (Zn). The mixed solution columns showed overall Cu retention within 1% between sand at 87%, 1nC at 87% and 1nZVI at 88% while overall retention reached 97% for 5nZVI and 99% for 10nZVI (Figure 5.8). Maximum Cu concentrations were within 6% between sand at 41%, 1nC at 35% and 1nZVI at 37% with 5nZVI reaching 7.4% and 10nZVI only 2.6%. Overall, Cu retention in the mixed metal solution was higher than in that of the individual element experiment, ranging from 18% higher in unamended sand, down to 6% higher in systems with 5nZVI (there was no notable difference in 10nZVI systems as both removed almost all copper).

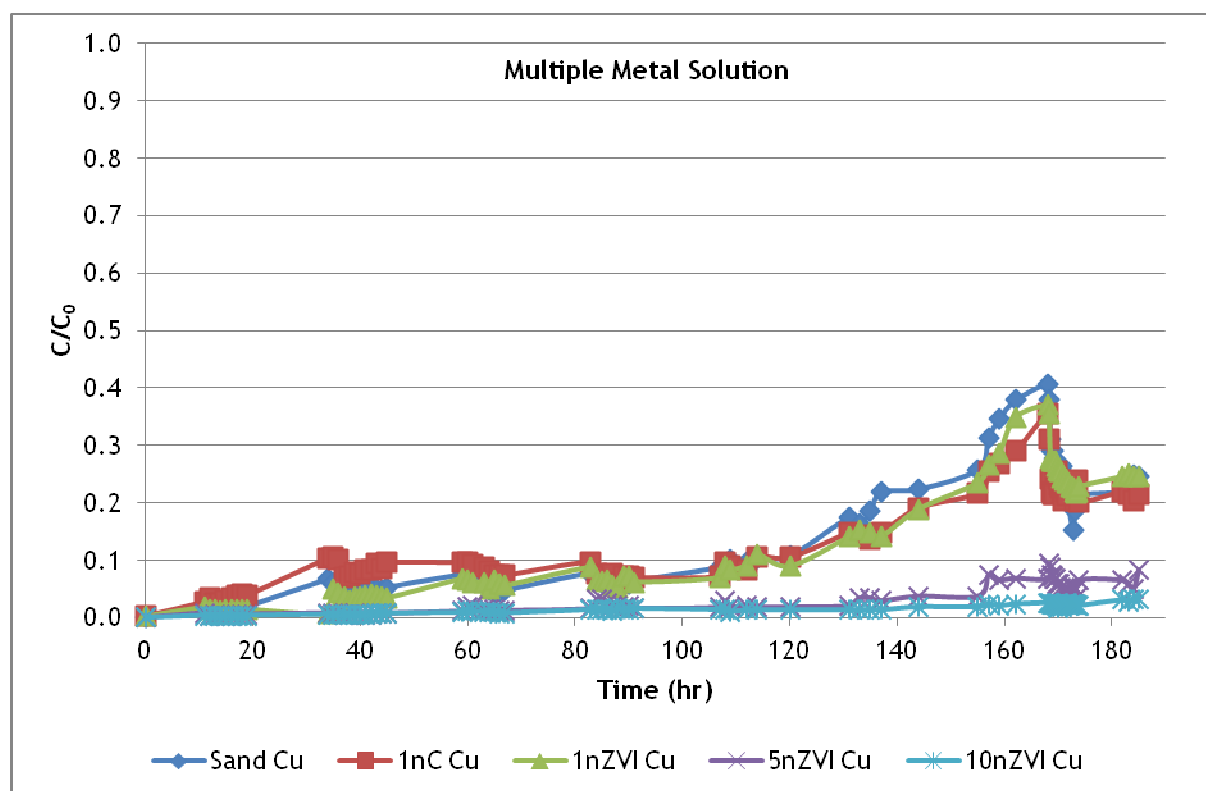


**Figure 5.8.** Cu breakthrough curve in a multi-element solution for sand, 1nC, 1nZVI, 5nZVI, and 10nZVI showing  $C/C_0$  versus time

The mixed solution columns showed an order of efficiency for Pb retention of 1nZVI at 85% > 1nC at 74% > sand at 69% while both 5nZVI and 10nZVI retained 100% of the Pb (Figure 5.9). Again, maximum Pb concentrations followed the same trend with 1nZVI reaching 52%, 1nC reaching 60% and sand reaching 90%. Overall, Pb retention in the mixed metal solution was 3.3% and 7.8% lower for 1nZVI and sand respectively while 1nC demonstrated an increase in Pb retention

of 19% over the individual element experiment (there was no notable difference in 5nZVI and 10nZVI systems as both removed almost all lead).

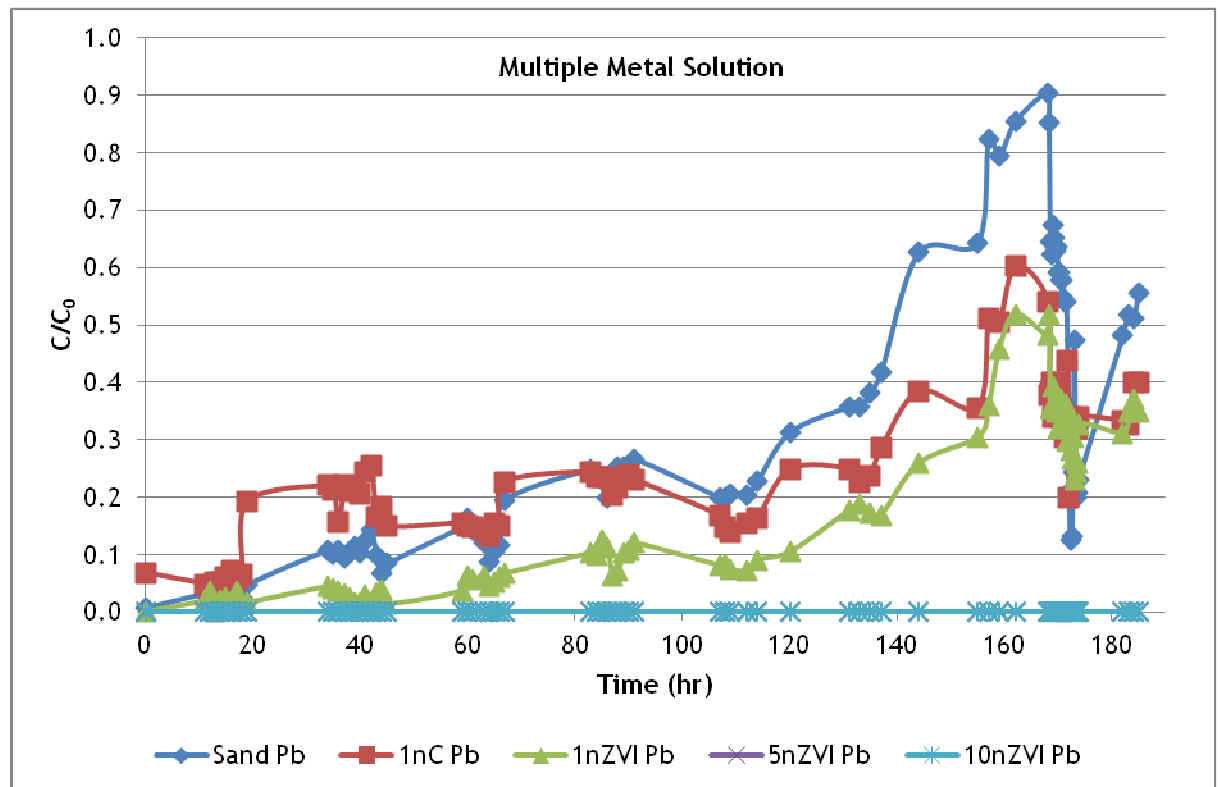


**Figure 5.9.** Pb breakthrough curve in a multi-element solution for sand, 1nC, 1nZVI, 5nZVI, and 10nZVI showing  $C/C_0$  versus time.

Zn in the mixed element solution showed greater breakthrough compared to that in the single element system. This is converse to Pb and Cu which showed less breakthrough in the mixed element system. Sand, 1nC and 1nZVI all show breakthrough curves that reach 100% peak metal concentration after 114 hours, while demonstrating overall retention of 20% for sand, 19% for 1nC and 21% for 1nZVI. 5nZVI and 10nZVI did enhanced Zn removal over sand with total retention of 32% and 37% respectively. Enhanced Zn removal for 5nZVI and 10nZVI is evidenced at the start of the experiment (Fig 5.10) with 10nZVI showing zero breakthrough up to 20 hours and 5nZVI showing zero breakthrough up to 14 hours

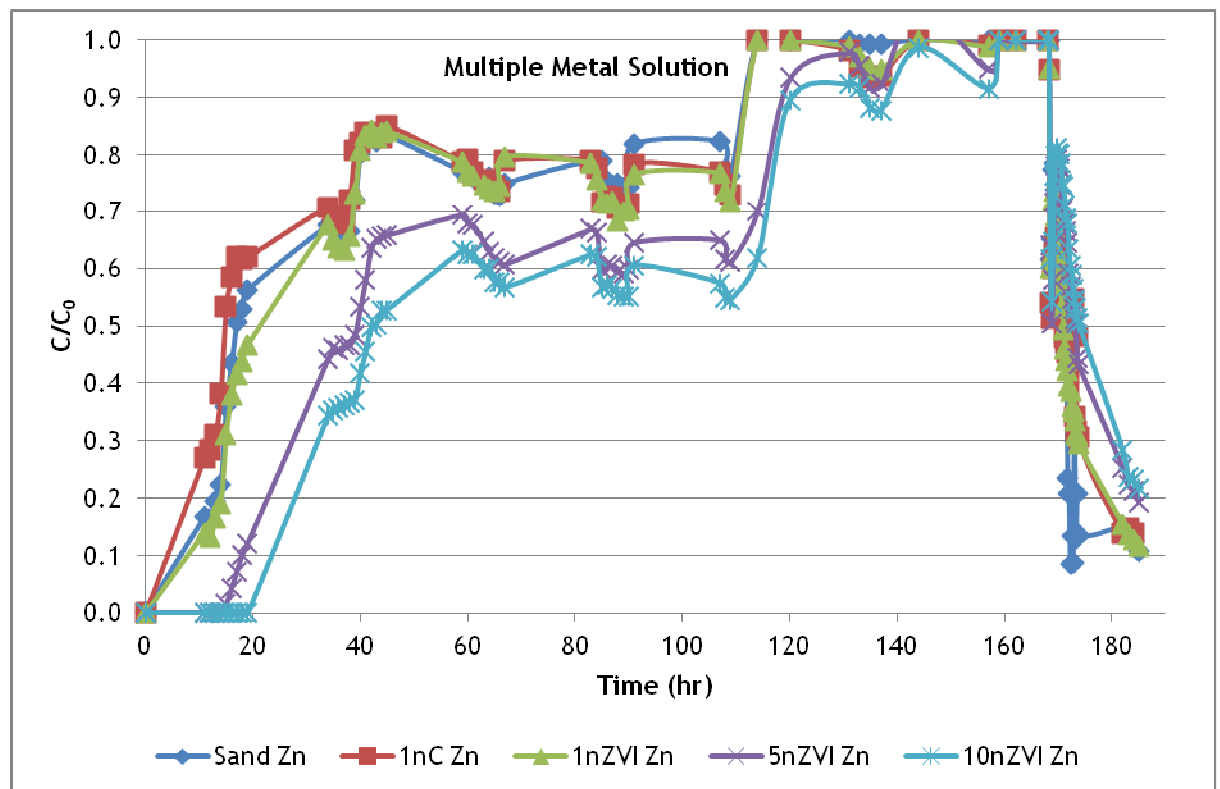


**Figure 5.10.** Zn breakthrough curve in a multi-element solution for sand, 1nC, 1nZVI, 5nZVI, and 10nZVI showing  $C/C_0$  versus time.

## 5.4 DISCUSSION

It is evident that use of nZVI sand in laboratory scale column filters did enhance heavy metal removal compared to unamended sand. The general sequence for metal affinity in the single metal experiments is  $Pb > Cu > Zn$ . This affinity for heavy metals was also found in a study of adsorption on sand (Awan et al. 2003). In the multi-element column experiments, the metal affinity shifts slightly so that  $Cu > Pb > Zn$ , presumably due to changes in competition for removal and/or adsorption sites.

All experiments showed that removal efficiency was proportional to nZVI content, with greater nZVI content leading to greater overall heavy metal removal. The relationship between nZVI concentration and total metal removal for single metal systems is shown in Figure 5.11 and mixed metal systems is shown in Figure 5.12.

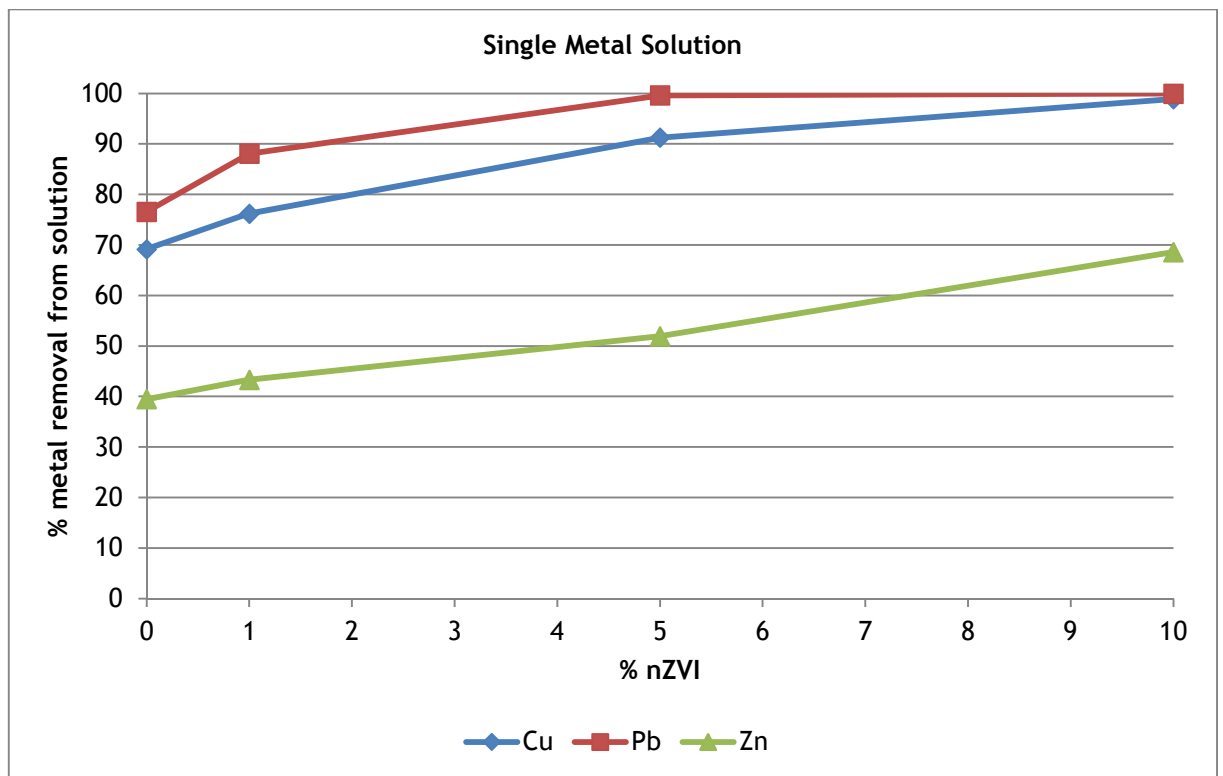


**Figure 5.11.** Summary of percentage of Cu, Pb and Zn removed within the unamended sand, 1%, 5% and 10% nZVI enhanced sand columns for single metal

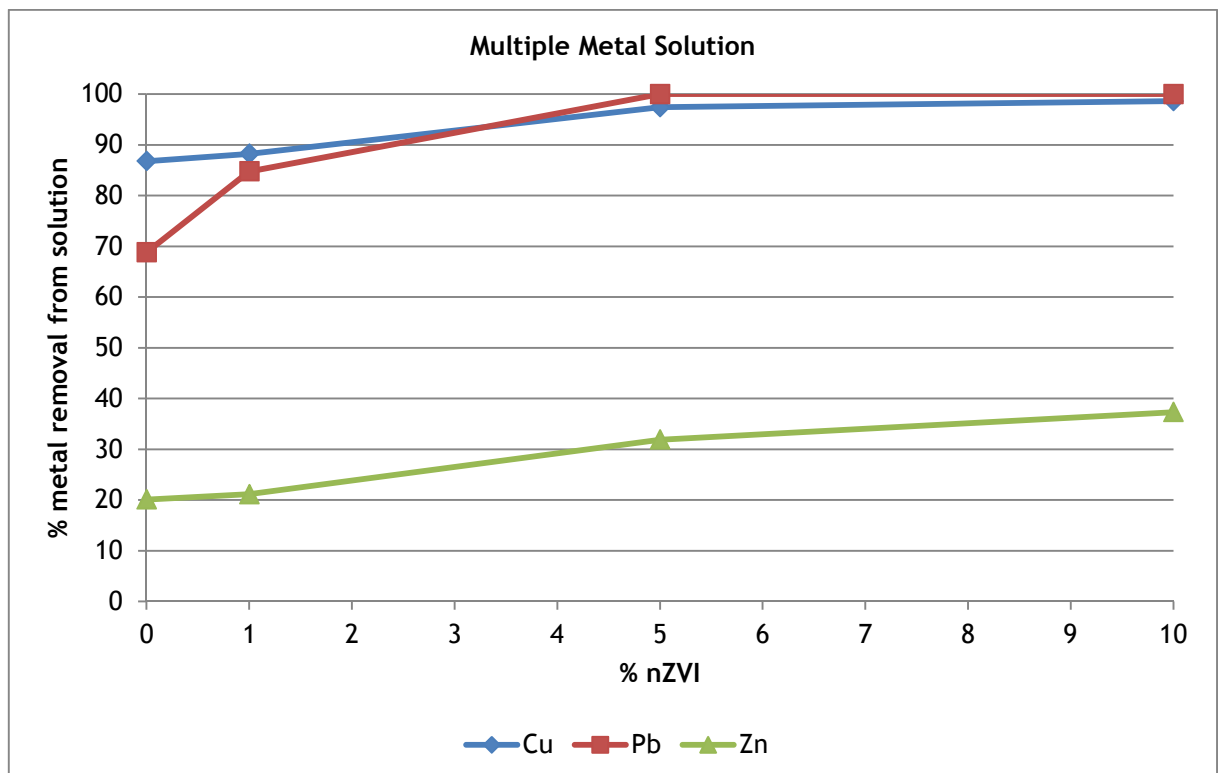


**Figure 5.12.** Summary of percentage of Cu, Pb and Zn removed within the unamended sand, 1%, 5% and 10% nZVI enhanced sand columns for mixed systems

10nZVI demonstrates ~100% removal of Cu and Pb, in both mixed and single element systems (Fig 5.11-5.12). This indicates amendment of sand by 10% nZVI

should be recommended in SUDS design guidelines for systems which experience high Cu and Pb loads. In contrast, 10% nZVI amended sand was much less efficient at removing Zn. Indeed, extrapolation of the data shown in figure 5.11 and 5.12 suggests as much as 20% nZVI (for single metal) and 40% nZVI (for multiple metal) would be needed to remove 100% Zn within the current experimental setup. Increasing the nZVI content in this way would significantly increase the cost of the SuDS system if efficient zinc removal was required. However, it should be noted that environmental regulations for Zn can be less stringent than for Cu and Pb. For example, groundwater threshold values are 3.75 ppm for Zn, 1.5 ppm for Cu and 0.018 ppm for Pb ((Water Framework Directive) (England and Wales) Directions 2009). Therefore, less efficient removal of Zn may be an acceptable deficiency of nZVI amended SUDS.

It is also worth noting is that nZVI enhanced sand increased the time to breakthrough of heavy metals as well as reducing the peak heavy metal concentration (Figures 5.13 for single metal and 5.14 for multiple metal), both of which further advantage nZVI amended SuDS over sand alone systems. Further, Figures 5.15 and 5.16 illustrates the enhancement of metal removal by nZVI compared to unamended sand (enhancement = metal removal by amended sand minus metal removal by unamended sand). Enhancement due to nZVI is broadly similar for all three metals in single metal systems (Figure 5.15) and similar for Zn and Cu in multimetal systems (Figure 5.16). Though, it can be noted that enhancement of Pb due to nZVI is between 10-20% stronger in the multiple metal solution in comparison to Cu and Zn.

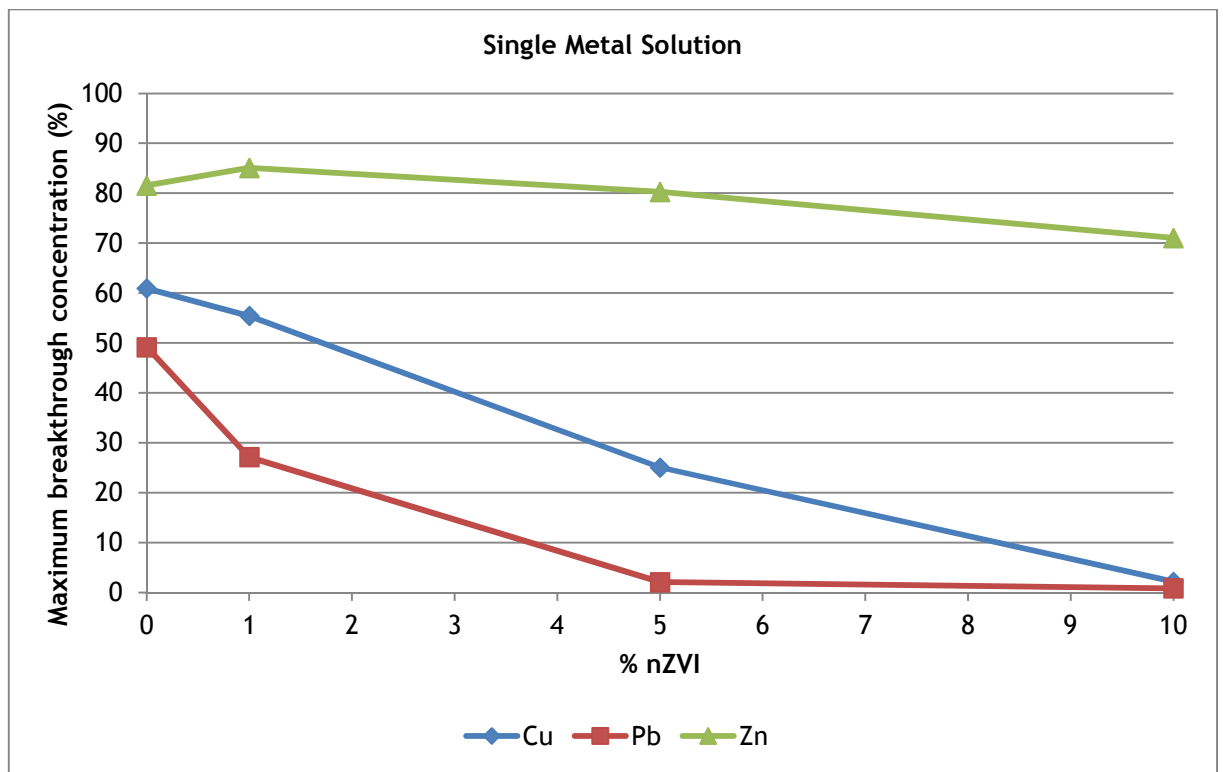


**Figure 5.13.** Maximum breakthrough concentration of Cu, Pb and Zn in single metal solutions for unamended sand and 1%, 5% and 10% nZVI enhanced sand columns

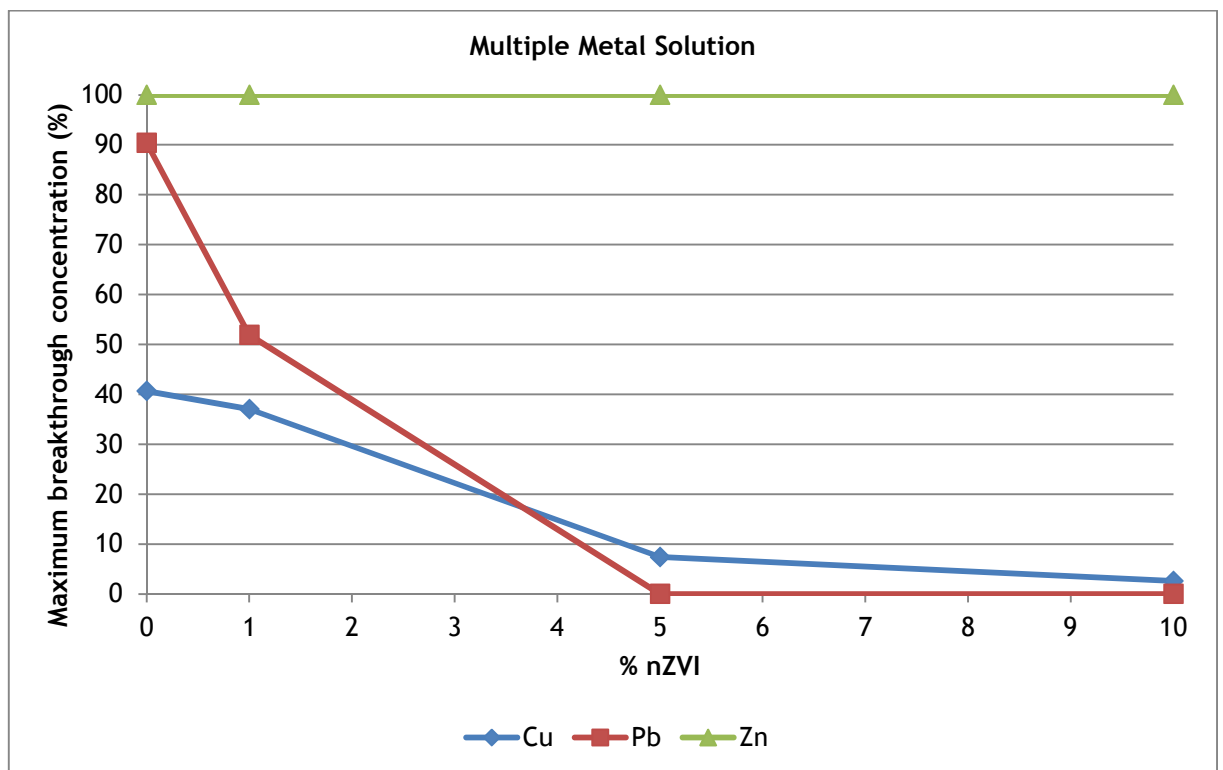


**Figure 5.14.** Maximum breakthrough concentration of Cu, Pb and Zn in multi-metal solutions for unamended sand and 1%, 5% and 10% nZVI enhanced sand columns

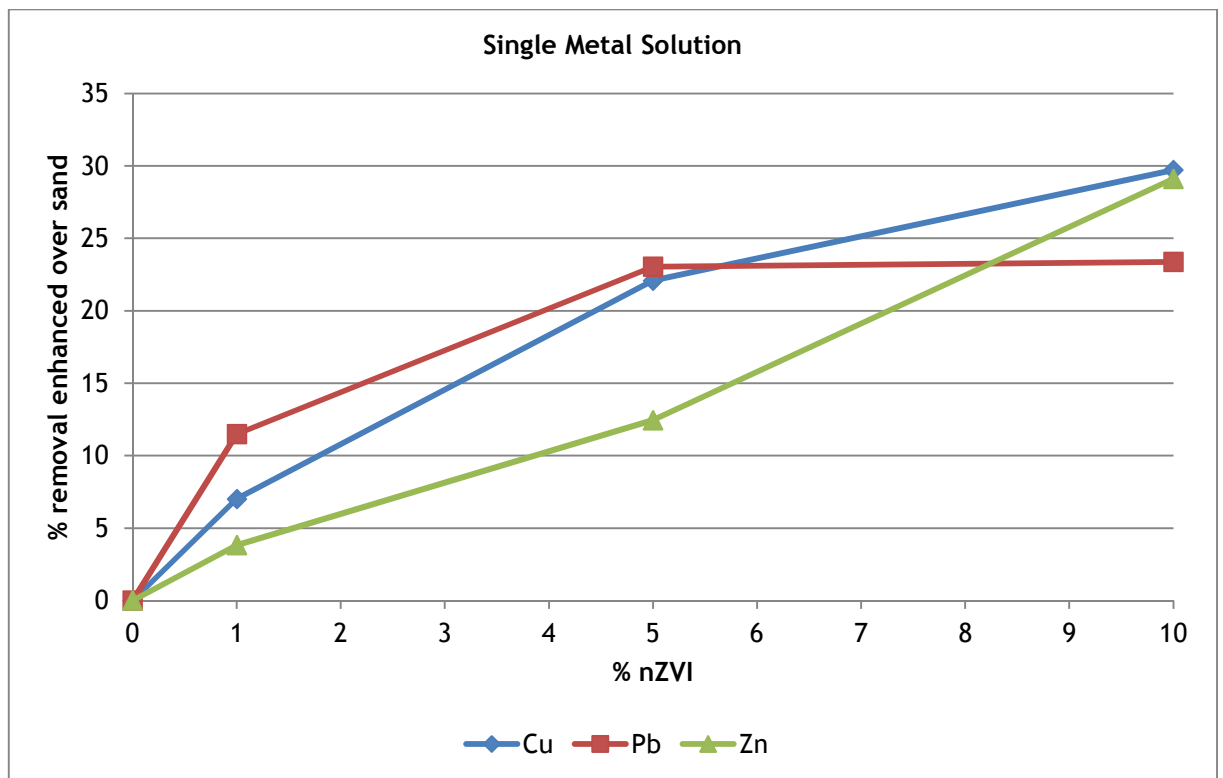


**Figure 5.15.** Percentage of enhanced Cu, Pb and Zn removal as compared to unamended sand for 1%, 5% and 10% nZVI sand columns

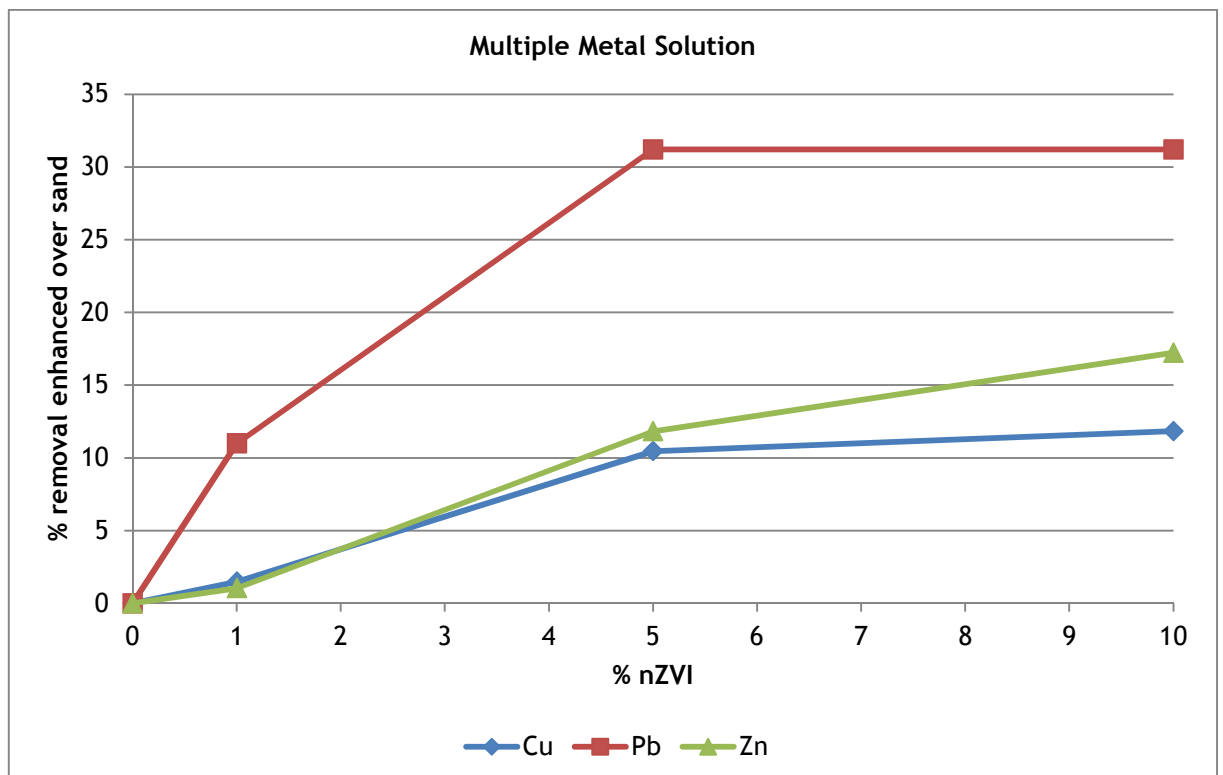


**Figure 5.16.** Percentage of enhanced Cu, Pb and Zn removal as compared to unamended sand for 1%, 5% and 10% nZVI sand columns

While nZVI columns did enhance heavy metal removal, nanoclay cannot be recommended for use in sand filtration techniques for several reasons. First, the

nanoclay columns results typically demonstrated reduced heavy metal removal when compared to unmodified sand. It is thought that this could be due to the loss of nanoclay from the columns, transporting absorbed metals with the eluent. Alternatively, it may be due to the reduced porosity exhibited by the nanoclay enhanced sand and thus, reduced removal capacity within the column (i.e. the residence time of the column is reduced and thus the metals have less time to be immobilized). Although nanoclay was mobile and a proportion exited the column, many nanoparticles are immobile, and this study was able to take advantage of this by simply mixing nZVI powder into the sand matrix without subsequent migration from the filter. In contrast, many studies have modified nanoparticles surfaces to enhance mobility to facilitate injection into groundwater and soils for in-situ remediation. For example, Kanel et al. (2007) modified nZVI with the surfactant Tween, while Parham et al. (2012) coated iron oxide nanoparticles with 2-mercaptobenzothiazole. Because we required immobile nZVI's, complex chemical surface stabilizing methods required for injection applications are not required and hence nanoparticles are immobilized and maintained within the filter to treat the contaminated water feed.

Due to the current trend in nanoparticle research for remediation strategies, Li et al. (2006) reports that prices for nZVI are decreasing with breakthroughs in synthesizing nZVI for mass production and use in environmental applications. The commercially produced nZVI, Nanofer, utilized in the current research is between £35-50/kg for small quantities, though would be further reduced for quantities needed for industrial scale applications.

#### 5.4.1 PHREEQC analysis

Saturation indices for the dominant hydroxide phases of Cu, Pb and Zn for each column for both the initial influent concentration and final metal concentrations at the outlet at the end of the experiment prior to injection with unamended river water were calculated using the PHREEQC geochemical modelling package. Input conditions to PHREEQC used the concentrations of  $\text{Cu}^{2+}$ ,  $\text{Pb}^{2+}$ ,  $\text{Zn}^{2+}$  and  $\text{NO}_3^-$ , while pH measurements recorded at the inlet and outlet were used. pH differences were observed between the influent solution and the outlet solution at the end of the experiment (Table 5.4) indicating solution pH was altered during passage through the column. The impact of this pH shift on dissolved

metal speciation for Cu, Pb and Zn was again determined using PHREEQC. For dissolved metal speciation the metal concentration in PHREEQC was set constant at 5 ppm to isolate the impact of pH. The minimal shifts in pH in the sand and nZVI systems are thought to be due to the buffering capacity of sand. Note that only known geochemical parameters were input to the modelling program (pH, temperature, metal and nitrate concentrations) and thus, the modelling results reported may differ from modelling results had the complete water chemistry profile been established. Sample PHREEQC input can be found in Appendix C. The pe indicates the redox potential of the solution and a pe of 4 was used as the PHREEQC default that is typical of oxic surface water. PHREEQC results for SI can be seen in Table 5.4 while Figures 5.17 (Cu), 5.18 (Pb) and 5.19 (Zn) illustrate the dominant speciation at specific pH's and slight changes of speciation between the single metal solution and multiple metal solution.

PHREEQC RESULTS												
Single Element	Cu				Pb				Zn			
Column	Initial RW + Cu pH	Initial SI Cu(OH) <sub>2</sub>	Final pH	Final SI Cu(OH) <sub>2</sub>	Initial RW + Pb pH	Initial SI Pb(OH) <sub>2</sub>	Final pH	Final SI Pb(OH) <sub>2</sub>	Initial RW + Zn pH	Initial SI Zn(OH) <sub>2</sub>	Final pH	Final SI Zn(OH) <sub>2</sub>
Sand	7.23	0.79	6.78	0.19	7.39	1.16	6.94	0.05	7.1	-1.51	6.65	-2.48
1nC	7.23	0.79	8.38	0.60	7.39	1.16	8.54	2.52	7.1	-1.51	8.23	0.40
1nZM	7.23	0.79	6.63	-0.55	7.39	1.16	6.79	-0.49	7.1	-1.51	6.50	-2.77
5nZM	7.23	0.79	6.91	-0.25	7.39	1.16	7.07	-0.71	7.1	-1.51	6.73	-2.33
10nZM	7.23	0.79	7.08	-0.82	7.39	1.16	7.24	-1.17	7.1	-1.51	6.95	-1.94
Multiple Element	Cu				Pb				Zn			
Column	Initial RW + Mix pH	Initial SI Cu(OH) <sub>2</sub>	Final pH	Final SI Cu(OH) <sub>2</sub>	Initial RW + Mix pH	Initial SI Pb(OH) <sub>2</sub>	Final pH	Final SI Pb(OH) <sub>2</sub>	Initial RW + Mix pH	Initial SI Zn(OH) <sub>2</sub>	Final pH	Final SI Zn(OH) <sub>2</sub>
Sand	6.98	0.62	6.53	-0.40	6.98	0.71	6.53	-0.46	6.98	-1.73	6.53	-2.61
1nC	6.98	0.62	8.13	0.31	6.98	0.71	8.13	2.00	6.98	-1.73	8.13	0.36
1nZM	6.98	0.62	6.38	-0.70	6.98	0.71	6.38	-0.99	6.98	-1.73	6.38	-2.92
5nZM	6.98	0.62	6.66	-0.84	6.98	0.71	6.66	*	6.98	-1.73	6.66	-2.34
10nZM	6.98	0.62	6.83	-1.10	6.98	0.71	6.83	*	6.98	-1.73	6.83	-2.00

**Table 5.4.** PHREEQC results for single and multi-elemental solutions for five experimental columns. “Initial” conditions are those in the metal amended river water prior to injection into the column. “Final” conditions are for the solution eluting the column at the end of the experiment, prior to injection with unamended river water. \* indicates final concentration was zero so SI could not be calculated

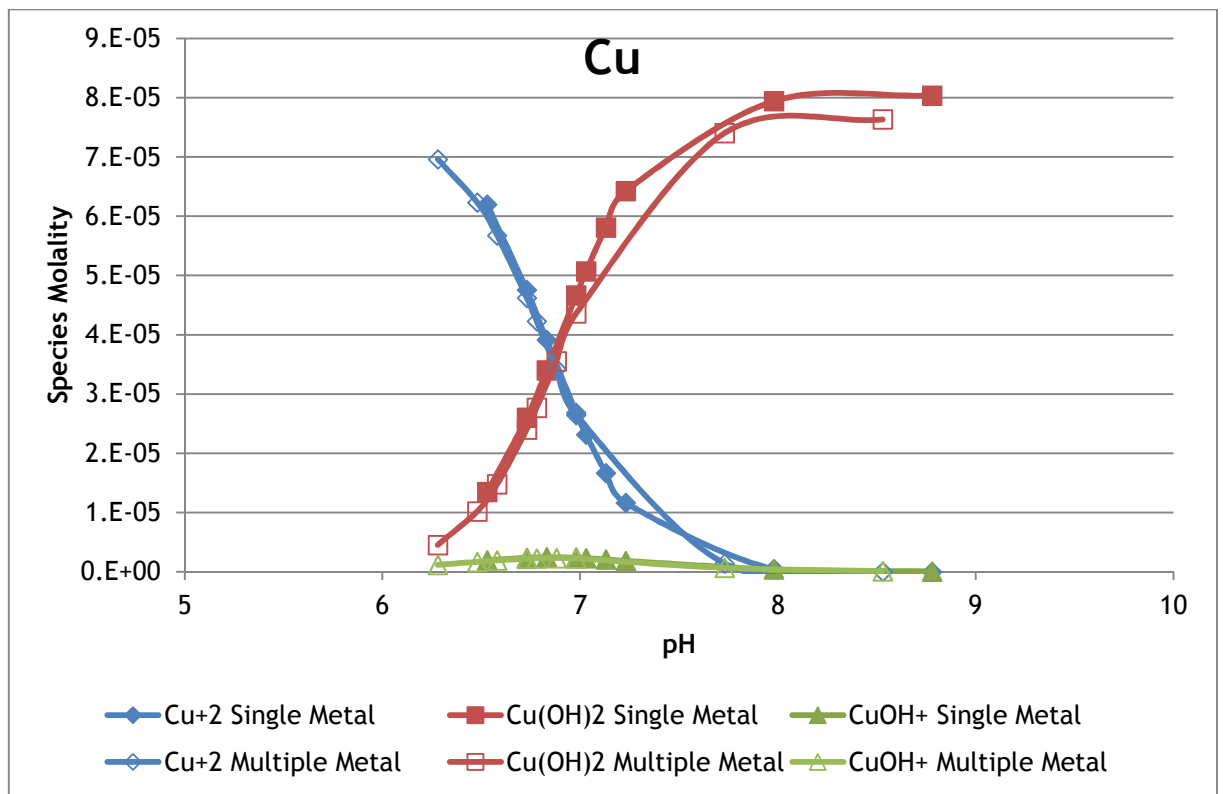


Figure 5.17. Impact of pH on dissolved copper speciation

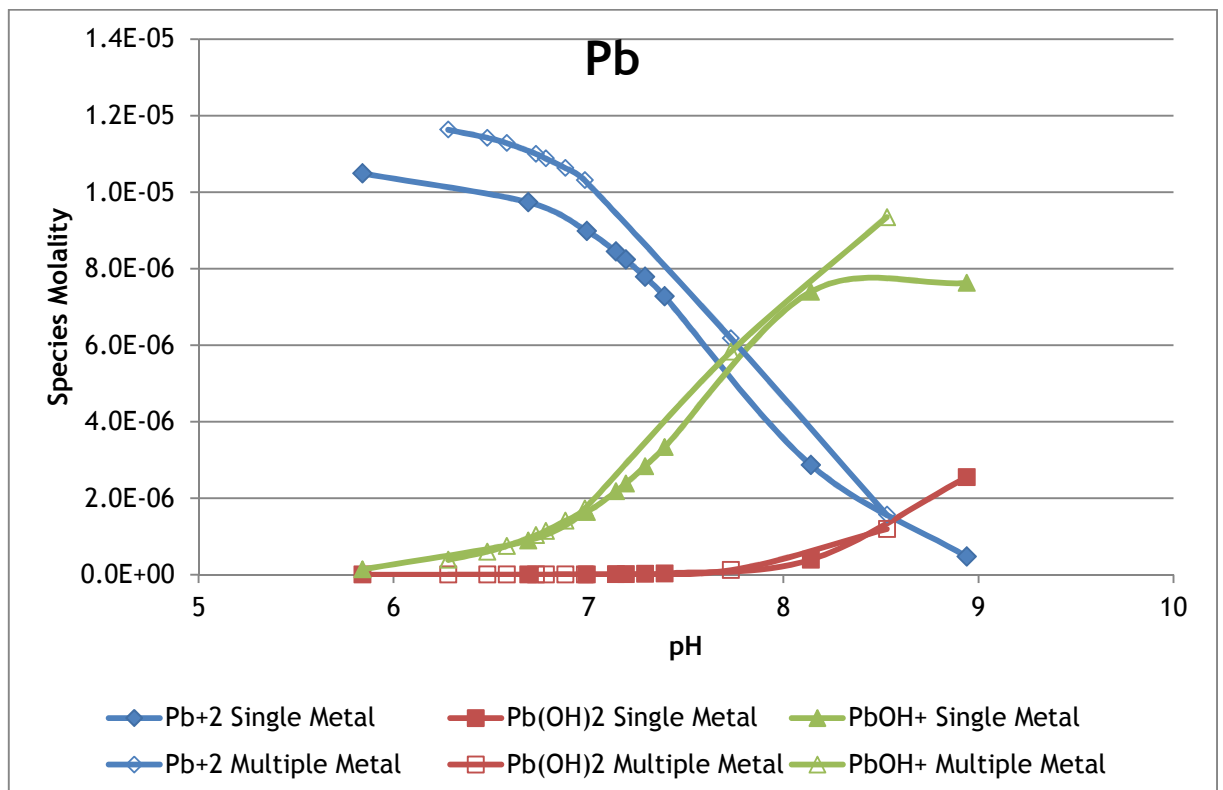
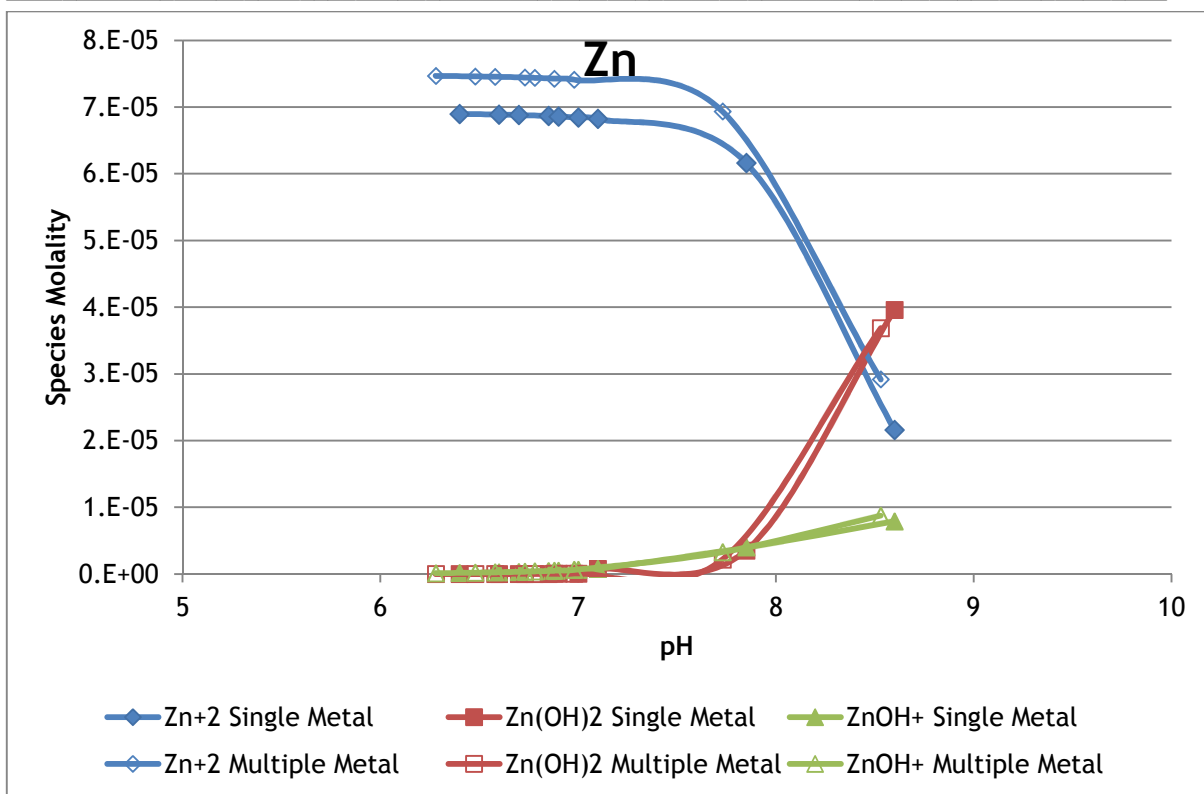


Figure 5.18. Impact of pH on dissolved lead speciation



**Figure 5.19.** Impact of pH on dissolved zinc speciation

As previously discussed in Section 2.4.2, saturation indices (SI) are an important geochemical parameter that can help determine mechanisms of metal removal in solutions, with  $SI > 0$  indicating precipitation as the dominant removal process due to supersaturation and  $SI < 0$  indicating adsorption as the dominant removal process due to undersaturation. In single metal experiments, saturation indices for copper and lead were supersaturated with respect to  $\text{Cu}(\text{OH})_2$  at 0.79 and  $\text{Pb}(\text{OH})_2$  at 1.16 (Table 5.4). Clearly for the Cu and Pb experiments saturation driven precipitation of metal phases likely play a role in the removal of these metals within the column. Moreover, this could explain the higher removal rates of both of these metals in the individual element experiments compared to Zn which has a saturation index for  $\text{Zn}(\text{OH})_2$  of  $-1.51$  at the beginning of the experiment and thus unlikely to experience any precipitation driven removal overall (i.e., it would have to rely only on adsorption as a removal mechanism). Similarly, in multi element systems, the initial saturation indices were supersaturated with respect to  $\text{Cu}(\text{OH})_2$  and  $\text{Pb}(\text{OH})_2$  at 0.62 and 0.71 respectively, while Zn remained undersaturated at  $-1.73$ , indicating that again precipitation was likely a significant mechanism for Cu and Pb removal, while Zn removal would again require adsorption. Note that in both single and mixed systems, the supersaturation of Cu and Pb phases does not preclude the

possibility of adsorption of Cu and Pb (in addition to precipitation) as will be discussed later.

Saturation indices were also calculated for the maximum breakthrough concentration of each metal at the end of each column experiment, thus displaying the maximum SI reached at the outlet (Table 5.4). For the Cu experiments, both unamended sand and sand amended with nZVI experience a drop in SI due to the removal of copper from solution and the drop in pH as it passes through the column. Notably, however, unamended sand remains supersaturated, while nZVI amended sand becomes undersaturated. Pb shows a similar trend to those for Cu in which all nZVI columns saturation indices are reduced to below zero while sand remains close to zero. This suggests that adsorption is occurring to a larger extent in the nZVI columns for both Cu and Pb systems, enabling SI to drop below zero. Overall, Zn saturation indices all stay undersaturated throughout the experiment suggesting that any removal of Zn must be via adsorption alone. Multi-element system saturation indices all decrease below zero (unamended and nZVI amended sand) but with nZVI systems showing more negative SI compared to unamended sand, again suggesting enhanced removal by adsorption in nZVI amended systems. Despite the elevated SI of the final solution in the nanoclay experiments (likely due to elevated pH) greater metal removal was not observed. The increased pH in the nanoclay columns increases the likelihood that precipitation of metals from solution takes place, although experimental results indicates otherwise, with an overall worse removal rate of metals compared to sand and nZVI columns. This is thought to be due to the observed migration of nanoclay from the columns, and thus the effects of increased pH and supersaturation are masked since some clays exit the column and thus transport metals with them.

The speciation of dissolved metals may also impact removal mechanisms. Speciation for dissolved metals over typical pHs observed are shown in Figures 5.17-19. Because the pH drops between influent and effluent in sand and nZVI systems, but increases in nanoclay systems (Table 5.4), there is significant potential for differences in dissolved metal species between influent and effluent and between nZVI and nanoclay systems. For Cu, the dominant species changes from  $\text{Cu}^{2+}$  to  $\text{Cu}(\text{OH})_2$  at around pH 6.85 (Figure 5.17). At the influent pH,  $\text{Cu}(\text{OH})_2$  is the slightly more dominant species over  $\text{Cu}^{2+}$ . The increase in pH

between influent and effluent in the 1nC columns, indicates the effluent solution should have a higher ratio of  $\text{Cu(OH)}_2/\text{Cu}^{2+}$  compared to the influent. In contrast, the decrease in pH between influent and effluent in the sand and 1nZVI columns indicates the effluent solution should have a lower ratio of  $\text{Cu(OH)}_2/\text{Cu}^{2+}$  compared to the influent. Consequently, the increase in relative abundance of  $\text{Cu}^{2+}$  ions in sand and nZVI systems may encourage further metal removal by adsorption. In contrast, the decrease in  $\text{Cu}^{2+}$  in the nanoclay systems may reduce adsorption. Overall, the relative electronegativity of the different metal species present and that form will affect the adsorption within the systems (Li et al. 2012).

Since sand has a negative charge, the fact that abundant species of metals are in the form of  $\text{Cu}^{2+}$ ,  $\text{Pb}^{2+}$  and  $\text{Zn}^{2+}$  at the pH's within the sand columns can help to explain why unamended sand retained higher levels of heavy metals than expected due to an electrostatic attraction between the metal species and sand surface. The negative surface charge of sand (Awan et al. 2003) and clay minerals (Bailey et al. 1999) will thus lead these materials to preferentially adsorb and form surface complexes with metal cations over metal hydroxide species. Note that while clay has a negative surface charge permanently (Sposito et al. 1999), silica and quartz minerals in sand have the potential to vary with differing pH's, though typically have a negative surface charge at relevant environmental pH's (Karlsson et al. 2001). nZVI also has strong propensity to adsorb metal cations as discussed in Section 5.4.2. For Pb, the dominant species in the effluent for all nZVI and sand columns is  $\text{Pb}^{2+}$  while for 1nC, the dominant species in the effluent is  $\text{PbOH}^+$ ; the more positive charge of the divalent ion potentially facilitating adsorption in sand and nZVI systems. As for Zn,  $\text{Zn}^{2+}$  is highly dominant at any pH's present in the sand, nZVI and nanoclay columns as  $\text{Zn}^{2+}$  dominates systems up until a pH of 8.4. Although the PHREEQC results give insight into the geochemical mechanisms of the current research, the complete water chemistry of solutions needed to fully understand the water-mineral interactions was not known.

### 5.4.2 Standard electron potential analysis

In order to further understand the removal mechanisms involved with nZVI and different metals, the standard electrode potentials ( $E^0$ ) were investigated for

Cu, Pb and Zn as discussed in Li and Zhang (2007). The  $E^0$  can be used as an indication of the standard oxidation-reduction potentials and thus the potential ability of a species to gain electrons and be reduced. This is important in explaining why different metals react differently with different materials, in this case nZVI. As discussed in Section 5.1.1, the ability of nZVI to react with metal species so efficiently is its ability to donate electrons to the surface and thus, offer reduction potential to metals as well as offering surface complexation to its metal hydroxide surface in the form of adsorption (Figure 5.20). Different metals standard reduction potentials will determine which metals are able to accept electrons and be reduced and which metals have a lower reduction potential and thus are more typically adsorbed to nZVI. As reported in Stumm and Morgan (1996) and Li and Zhang (2007), the  $E^0$  for Cu is 0.34, Pb is -0.13 and Zn is -0.76 while Fe is -0.41. When  $E^0$  of the metal species involved is close to or more negative than Fe, which is the case for Zn, then reduction is not possible and adsorption is the dominant removal mechanism (Li and Zhang 2007). When  $E^0$  of the metal species is significantly more positive than that of nZVI, in the case of Cu, then the high potential to receive electrons makes reduction the key removal mechanism (Li and Zhang 2007). Finally, when the  $E^0$  is only slightly more positive than nZVI, such as in the case of Pb, then both mechanisms of reduction and adsorption have the potential to remove the metal species (Li and Zhang 2007). This can be visualized in Figure 5.20.

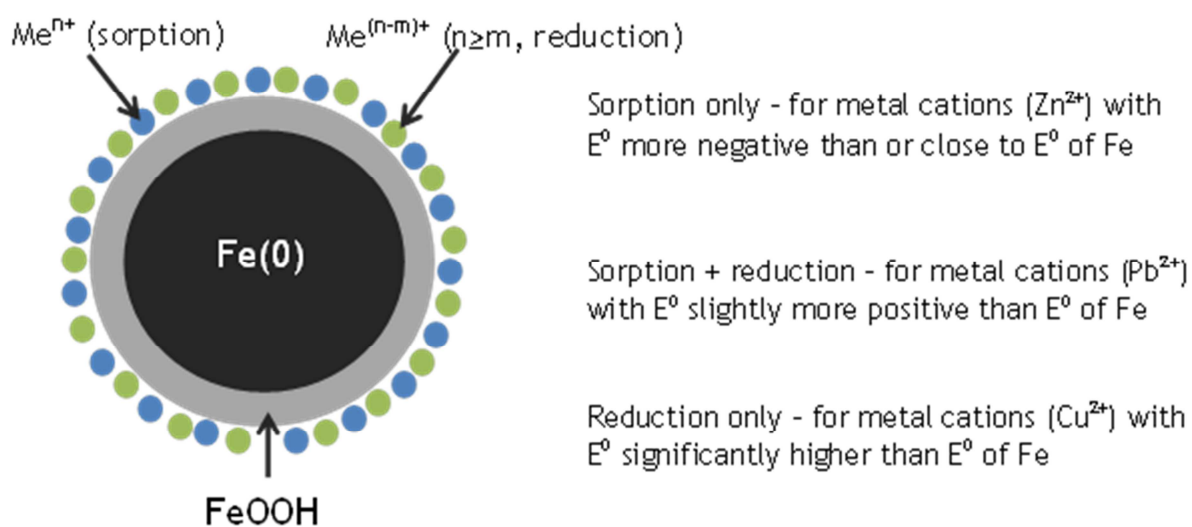


**Figure 5.20.** Schematic explaining different removal mechanisms involved between nZVI and different metal species. Adapted from Li, 2007.

Once the  $E^0$  are taken into consideration, the expected and observed effective removal of Pb within the nZVI columns can be explained by the combination of both reduction and adsorption of Pb onto nZVI. Along with precipitation due to supersaturation in the solution and adsorption onto sand, this can therefore explain the better removal of Pb over Cu or Zn. On the contrary, the lack in variety of mechanisms available for Zn immobilization may explain the reduced removal rates observed. Considering  $E^0$  of Zn allowing for adsorption onto nZVI only, as well as the undersaturated SI not allowing for Zn removal due to precipitation in the system, the removal mechanisms available for Zn removal are adsorption onto nZVI or sand only. Since adsorption is the dominant removal mechanism in the Zn columns that demonstrated the worst removal of metals, it is believed that sorption based mechanisms are less effective at removal of metals than reduction based mechanisms for nZVI. Finally, in addition to saturation driven precipitation and possible adsorption onto sand the  $E^0$  for Cu would follow removal by nZVI due to reduction. The possible mechanisms involved for heavy metal immobilization in the sand and nZVI systems is summarized in Table 5.5 following from a combination of PHREEQC analysis and  $E^0$  analysis.

	Possible Removal Mechanisms	Cu	Pb	Zn
PHREEQC	Adsorption onto sand	✓	✓	✓
PHREEQC	Saturation driven precipitation	✓	✓	
$E^0$	Adsorption onto nZVI		✓	✓
$E^0$	Reduction due to nZVI	✓	✓	

**Table 5.5.** Possible removal mechanisms for Cu, Pb and Zn according to PHREEQC and standard electrode potentials ( $E^0$ )

It is not known why exactly Cu retention would improve in a multi-element solution, though specifics of solution chemistry and geochemical parameters must have altered the solutions towards an ideal environment for Cu complexation. While Cu removal is increased in the multi-element solution and Zn removal is decreased in the multi-element solution, an explanation could be that the competition between the two mechanisms clearly favors reduction over adsorption. Thus, it is hypothesized that when competition between metals in the multi-element solution occurs, reduction is the prominent mechanism while the adsorption capacity seems to be diminished. This explanation is also supplemented in that Pb removal (in which both adsorption and reduction

contribute) was able to maintain similar retention rates between the multiple and single metal experiments even though different shape breakthrough curves were seen. It is possible that the different shape curves between the single and multi-elemental solution could be an indication of competition between removal mechanisms.

## 5.5 CONCLUSION

A simple system utilizing powdered commercially available nZVI to enhance a sand matrix for filter applications was constructed and showed improved heavy metal removal in all nZVI columns. Overall metal removal was proportional to the percentage of nZVI with higher percentages removing more metals and demonstrating enhancement over sand alone as well as reducing peak concentration and increasing time to breakthrough. The highest level of nanoparticle enhancement of 10% volume per weight demonstrated the most promise by removing > 98% Cu, > 99% Pb and 37-68% Zn (an enhancement over sand between 17-30%) over a one week pulse of 5ppm metals. 1% nZVI and 5% nZVI did show improved metal removal to a lesser degree in Cu and Zn systems but sufficient (100%) Pb removal at 5% nZVI. PHREEQC modelling of geochemical parameters suggests that supersaturation conditions may be present in the Cu and Pb systems, driving precipitation, while undersaturated conditions in the Zn systems may be a contributing factor to the lower metal removal observed within these systems. Adsorption onto sand may occur in all three metal systems. In addition to PHREEQC modelling, removal mechanisms are further evidenced by considering the standard electrode potentials of all three metals. This suggests removal mechanisms are reduction for Cu and reduction and sorption onto nZVI for Pb, with sorption onto sand or nZVI the only mechanisms for Zn. While nZVI enhanced sand columns can be recommended for further research for use in an industrial setting to improve heavy metal removal in areas prone to high heavy metal loads, nanoclay is not recommended for further research as reduced metal removal, high alkalinity, migration from the sand matrix as well as clogging was demonstrated.

## 5.6 REFERENCES

- Nanolron - Nanofer STAR. Retrieved 2013, from <http://www.nanoiron.cz/en/nanofer-star>.
- Awan, M. A., et al. (2003). "Removal of heavy metals through adsorption using sand." Journal of Environmental Sciences-China **15**(3): 413-416.
- Bailey, S. E., et al. (1999). "A review of potentially low-cost sorbents for heavy metals." Water Research **33**(11): 2469-2479.
- Chang, N. B., et al. (2008). "Integrating nanoscale zero-valent iron and titanium dioxide for nutrient removal in stormwater systems." Nano **3**(4): 297-300.
- Cole, R. H., et al. (1984). "Preliminary findings of the priority pollutant monitoring project of the nationwide-urban-runoff-program." Journal Water Pollution Control Federation **56**(7): 898-908.
- Comba, S., et al. (2011). "A Comparison Between Field Applications of Nano-, Micro-, and Millimetric Zero-Valent Iron for the Remediation of Contaminated Aquifers." Water Air and Soil Pollution **215**(1-4): 595-607.
- Crane, R. A., et al. (2011). "Magnetite and zero-valent iron nanoparticles for the remediation of uranium contaminated environmental water." Water Research **45**(9): 2931-2942.
- Crane, R. A. and T. B. Scott (2012). "Nanoscale zero-valent iron: Future prospects for an emerging water treatment technology." Journal of Hazardous Materials **211**: 112-125.
- Dickinson, M. and T. B. Scott (2010). "The application of zero-valent iron nanoparticles for the remediation of a uranium-contaminated waste effluent." Journal of Hazardous Materials **178**(1-3): 171-179.
- Engates, K. E. and H. J. Shipley (2011). "Adsorption of Pb, Cd, Cu, Zn, and Ni to titanium dioxide nanoparticles: effect of particle size, solid concentration, and exhaustion." Environmental Science and Pollution Research **18**(3): 386-395.
- USEPA. Stormwater Technology Fact Sheet - Sand Filters. (1999)
- Hua, M., et al. (2012). "Heavy metal removal from water/wastewater by nanosized metal oxides: A review." Journal of Hazardous Materials **211-212**(0): 317-331.
- Huang, Y., et al. (2011). "As(III) Adsorption from Drinking Water on Nanoscale Zero-Valent Iron: Kinetics and Isotherm Studies." Integrated Ferroelectrics **127**: 39-47.
- Huisman, L. and W. E. Wood (1974). Slow Sand Filtration. Geneva, Switzerland, WHO.
- Kanel, S. R., et al. (2006). "Arsenic(V) removal from groundwater using nanoscale zero-valent iron as a colloidal reactive barrier material." Environmental Science & Technology **40**(6): 2045-2050.
- Kanel, S. R., et al. (2005). "Removal of arsenic(III) from groundwater by nanoscale zero-valent iron." Environmental Science & Technology **39**(5): 1291-1298.

- Kanel, S. R., et al. (2007). "Transport of surface-modified iron nanoparticle in porous media and application to arsenic(III) remediation." Journal of Nanoparticle Research **9**(5): 725-735.
- Karabelli, D., et al. (2008). "Batch removal of aqueous Cu<sup>2+</sup> ions using nanoparticles of zero-valent iron: A study of the capacity and mechanism of uptake." Industrial & Engineering Chemistry Research **47**(14): 4758-4764.
- Karlsson, M., et al. (2001). "Surface charge concentrations on silica in different 1.0 m metal-chloride background electrolytes and implications for dissolution rates." Aquatic Geochemistry **7**(1): 13-32.
- Khin, M. M., et al. (2012). "A review on nanomaterials for environmental remediation." Energy & Environmental Science **5**(8): 8075-8109.
- Klimkova, S., et al. (2011). "Zero-valent iron nanoparticles in treatment of acid mine water from in situ uranium leaching." Chemosphere **82**(8): 1178-1184.
- Li, K., et al. (2012). "Solution-Phase Electronegativity Scale: Insight into the Chemical Behaviors of Metal Ions in Solution." Journal of Physical Chemistry A **116**(16): 4192-4198.
- Li, X.-q., et al. (2006). "Zero-valent iron nanoparticles for abatement of environmental pollutants: Materials and engineering aspects." Critical Reviews in Solid State and Materials Sciences **31**(4): 111-122.
- Li, X. Q. and W. X. Zhang (2006). "Iron nanoparticles: the core-shell structure and unique properties for Ni(II) sequestration." Langmuir **22**(10): 4638-4642.
- Li, X. Q. and W. X. Zhang (2007). "Sequestration of metal cations with zerovalent iron nanoparticles - A study with high resolution X-ray photoelectron spectroscopy (HR-XPS)." Journal of Physical Chemistry C **111**(19): 6939-6946.
- Mahlangu, T. O., et al. (2011). "A simplified cost-effective biosand filter (BSFZ) for removal of chemical contaminants from water." Journal of Chemical Engineering and Materials Science **2**(10): 156-167.
- Majdan, M., et al. (2010). "Uranium sorption on bentonite modified by octadecyltrimethylammonium bromide." Journal of Hazardous Materials **184**(1-3): 662-670.
- Masciangioli, T. and W. X. Zhang (2003). "Environmental technologies at the nanoscale." Environmental Science & Technology **37**(5): 102A-108A.
- Mpenyana-Monyatsi, L., et al. (2012). "Cost-Effective Filter Materials Coated with Silver Nanoparticles for the Removal of Pathogenic Bacteria in Groundwater." International Journal of Environmental Research and Public Health **9**(1): 244-271.
- Nabi, D., et al. (2009). "Evaluation of the adsorption potential of titanium dioxide nanoparticles for arsenic removal." Journal of Environmental Sciences-China **21**(3): 402-408.
- Noubactep, C., et al. (2012). "Nanoscale Metallic Iron for Environmental Remediation: Prospects and Limitations." Water Air and Soil Pollution **223**(3): 1363-1382.
- Parham, H., et al. (2012). "Fast and efficient removal of mercury from water samples using magnetic iron oxide nanoparticles modified with 2-mercaptobenzothiazole." Journal of Hazardous Materials **205**: 94-100.

- Ponder, S. M., et al. (2001). "Surface chemistry and electrochemistry of supported zerovalent iron nanoparticles in the remediation of aqueous metal contaminants." Chemistry of Materials **13**(2): 479-486.
- Ponder, S. M., et al. (2000). "Remediation of Cr(VI) and Pb(II) aqueous solutions using supported, nanoscale zero-valent iron." Environmental Science & Technology **34**(12): 2564-2569.
- Scott, T. B., et al. (2011). "Nano-scale metallic iron for the treatment of solutions containing multiple inorganic contaminants." Journal of Hazardous Materials **186**(1): 280-287.
- Shelp, G. S., et al. (1995). "The amelioration of acid mine drainage by an in situ electrochemical method .1. Employing scrap iron as the sacrificial anode." Applied Geochemistry **10**(6): 705-&.
- Shiple, H. J., et al. (2011). "Study of iron oxide nanoparticles in soil for remediation of arsenic." Journal of Nanoparticle Research **13**(6): 2387-2397.
- Sposito, G., et al. (1999). "Surface geochemistry of the clay minerals." Proceedings of the National Academy of Sciences of the United States of America **96**(7): 3358-3364.
- Stumm, W. and J. J. Morgan (1996). Aquatic Chemistry. New York, John Wiley & Sons, Inc.
- Wang, C. B. and W. Zhang (1997). "Rapid and complete dechlorination of TCE and PCBS by nanoscale Fe and Pd/Fe particles." Abstracts of Papers American Chemical Society **213**(1-3): 2-ENVR 2.
- Woods-Ballard, B., et al. (2007). The SuDS Manual. London, England, CIRIA: 606.
- Zaspalis, V., et al. (2007). "Arsenic removal from contaminated water by iron oxide sorbents and porous ceramic membranes." Desalination **217**(1-3): 167-180.
- Zhu, H., et al. (2009). "Removal of arsenic from water by supported nano zero-valent iron on activated carbon." Journal of Hazardous Materials **172**(2-3): 1591-1596.

# 6

## Conclusions and Future Recommendations

### 6.1 Summary of conclusions

Determining (bio)geochemical mechanisms responsible for heavy metal removal in Sustainable urban Drainage Systems (SuDS) that are susceptible to road runoff high in contaminant loads is imperative for better SuDS design and efficiency. Thus, the current research was undertaken to assess (bio)geochemical aspects of filtration based SuDS not necessarily acknowledged in the design guidelines. This was done in order to highlight and suggest important areas where mechanisms can enhance the pollutant removal of SuDS. The following summarizes the specific conclusions obtained within each chapter.

#### Chapter 2

- Due to their high surface area and ability to sequester heavy metals (Benjamin et al. 1996), an iron oxide coating was applied to gravel filter material in order to enhance metal immobilization. Though, within the current study, batch experiments demonstrated that while removal appeared to be more immediate in the iron oxide coated gravel (IOCG), after 48 hours removal rates were within 5% for Cu, the same for Pb and less by 4% for Zn when compared to un-amended rinsed microgabbro (RMG) gravel. Flow-through column experiments demonstrated that RMG consistently removed ~ 10% more Zn than IOCG. BET analysis revealed IOCG exhibited a 6x higher surface area compared to RMG; this enhanced surface area clearly did not significantly enhance heavy metal removal. Due to 1) the similar metal removal rates, 2) the difficulty in generating a coating with an environmentally suitable pH and 3) the added cost, an iron oxide coating for use in SuDS is not recommended.
- Since the un-amended RMG demonstrated excellent removal of metals and a highly weathered surface, further SEM analysis of a cross-section of

the surface of the gravel and subsequent EDS analysis revealed weathered particulates consistent with aluminosilicate clay minerals. As microgabbro is composed of pyroxenes and plagioclase feldspars that are known to chemically weather to smectite clay minerals (Banfield and Eggleton 1990), which are also known to sequester heavy metals readily (Odom 1984), it was determined that the naturally occurring minerals on the surface of the microgabbro are highly effective at removal of Cu, Pb and Zn.

- Further batch experiments confirmed that higher levels of weathered particulate matter on the surface of the microgabbro led to higher metal immobilization (up to 20% better than when the weathered surface has been removed). It was also established that microgabbro gravel consistently removed higher levels (between 3-80%) of metals than five other experimental lithologies of gravel. For this reason, it is suggested that the type of gravel utilized in filter drains is an important component to the system and that microgabbro gravel is an ideal filter material for use in SuDS in which heavy metal pollutants from road runoff is a concern.
- PHREEQC geochemical modelling revealed that all batch systems were supersaturated with regards to metal phases (saturation indices  $SI > 1$ ) and precipitation is a possible removal mechanism. Though, it is also believed that adsorption is a key mechanism in the gravel batch experiments as higher initial SI values do not necessarily lead to increased removal capacities. Thus the differences in surface reactivity of different gravel are responsible for the differences in heavy metal removal (this is consistent with the observation that gravel lithology and surface weathering influence metal removal).

### Chapter 3

- Since filter drains inevitably experience some extent of moisture from influent surface water, they are therefore capable of supporting biological growth. Thus quantifying the biological aspect of metal removal in such systems is imperative. A biofilm grown from collected filter drain gravel was investigated for its effect on contaminant transport in experimental gravel flow columns which demonstrated a 8-29% enhancement of total Cu, Pb or Zn retained within the column when compared to columns without biological growth. A non-conservative

tracer of DI (with a high Na background concentration) demonstrated 100% breakthrough.

- An advection diffusion model that describes any assortment of permanent removal mechanisms was successfully fit to breakthrough curves of biofilm growth columns and non-biofilm growth columns for both a conservative tracer and non-conservative tracer of Cu, Pb and Zn metals. With root mean squared error (RMSE) values ranging between 0.17-0.61 the model fit the curves well and slightly better in the biofilm columns. The model also determined permanent loss terms ( $k$ ) of 0.01 - 1.05 that correlated with observed percentages of metals retained within the columns (8-65%). Thus, an advection diffusion equation can be utilized to describe metal transport within a gravel filter column and possible further SuDS applications.
- Clone library analysis was undertaken to determine microbial community composition of the initial biofilm collected from filter drain gravel (after 10 months of growth on gravel in recirculated pond water) followed by biofilm grown in microgabbro columns and dolomite columns (after 8 months growth in recirculating pond water). Results indicate the initial filter drain gravel biofilm was composed of over 70% *cyanobacteria* followed by a combination of other phyla between 1-9% total makeup. Once the initial biofilm was inoculated into the microgabbro column, the dominant phyla became 54% *proteobacteria* followed by 25% *cyanobacteria* and 20% *bacteriodetes* while the dolomite column biofilm remains dominated by *cyanobacteria* at 47% followed by 25% *proteobacteria* and 22% *bacteriodetes*. This change in bacterial community suggests that the lithology of gravel influences bacterial communities, presumably due to the differences in lithology which better suits different types of microorganisms.
- Specific mechanisms responsible for permanent removal within the experimental columns are difficult to decipher from the model and are inherently complex for microorganisms, relying on numerous biogeochemical factors. Though, the enhanced metal removal observed in the biofilm growth columns is believed to be due to a combination of permanent removal mechanisms of biosorption to bacterial surface functional groups and the negatively charged EPS, bioaccumulation and

precipitation accelerated by photosynthetic activity increasing the pH and thus supersaturation. Removal in the non-biofilm columns is thought to be due to adsorption to the gravel and precipitation due to supersaturated conditions present for Cu and Pb.

#### Chapter 4

- While the first two chapters give insight into (bio)geochemical mechanisms responsible for heavy metal immobilization in gravel filter systems, Chapter 4 was undertaken to visualize contaminant transport and bio-physical processes inside a gravel filter column through non-invasive magnetic resonance imaging (MRI). High resolution 3D images obtained of an experimental gravel filter determined that average porosity ranged between 32-34% after post-processing thresholding methods, which corroborates with typical porosity values found in the literature (Morris and Johnson 1967) for dolomite and coarse gravel. Further analysis of before (Clean) and after (Bio) images obtained from columns where biofilms were allowed to colonize for up to 6 months indicated that biofilm growth was being segmented as the solid fraction during post-processing. This upholds observations from the literature that biofilms reduce the  $T_2$  relaxation time of water molecules.
- Biofilm growth was visually seen to grow mostly in the columns that had a light source and were allowed to grow for longer. Total biofouling for the column grown in light conditions for 6 months was calculated to be around 1.6% while localized analysis of biofouling indicates that higher concentrations of biofilm grew near the inlet of the water source with biofilm reducing the cross-sectional average porosity by 8.8% (compared to 3.3% in the middle of the column) and up to 49% in local regions of interest near the top of the column. It was also apparent from processing that all columns exhibited rearrangement and settling of particles due to movement between scans and pore pressure, thus, it is believed that the total percentage of biofilm calculated may be an underestimate.
- Copper tracer experiments indicated that flow within a horizontal gravel filter does not necessarily follow a plug flow regime but rather a more random flow from the top, circling around to the bottom and finally to the middle of the column.

---

## Chapter 5

- In order to enhance a second form of filter material that could be utilized in SuDS for increased heavy metal removal, sand was dry mixed with stable nano zero-valent iron (nZVI) in varying percentages. The nZVI amended sand columns demonstrated overall improved metal removal proportional to the percentage of nZVI used. The highest percentage of 10% nZVI immobilized > 98% Cu, > 99% Pb and 37-68% Zn. While Zn removal was the least efficient in all systems, nZVI did enhance Zn removal over unamended sand by 17-30%. Though, Zn tends to have less stringent environmental limits compared to other metals, so less efficient immobilization of Zn may be an acceptable deficiency of the system. Overall, 10% nZVI showed the most promise towards enhanced metal removal with 12-31% better removal over unamended sand, followed by 5% nZVI enhancing metal removal by 11-31% and finally 1% nZVI enhancing metal removal by 1-11%.
- PHREEQC modelling of geochemical parameters along with standard electron potentials ( $E^0$ ) were analyzed for insight into possible removal mechanisms present in the nZVI systems. PHREEQC indicates that supersaturated conditions exist in the Cu and Pb systems, and thus, precipitation may contribute to the overall removal, along with adsorption on to sand, while the undersaturated conditions in the Zn system indicates that precipitation is not likely but that adsorption onto sand is the key removal mechanism.  $E^0$  analysis indicates that in addition to adsorption to sand and saturation driven precipitation for Cu and Pb, immobilization due to reduction by nZVI is present in Cu systems, reduction and adsorption to nZVI is present in Pb systems and only adsorption to nZVI is present in Zn systems. The extra mechanisms due to the surface of the nZVI helps to explain metal enhancement over unamended sand. Overall, the multitude of possible mechanisms responsible for metal immobilization in the Cu and Pb systems helps to explain the excellent removal in these systems, while the limited mechanisms possible in the Zn systems explains the reduced removal observed in these systems. Clay enhanced sand was also investigated for increased heavy metal removal in sand systems, though, reduced metal

removal, high alkalinity, migration from the sand and clogging all were demonstrated and thus, not suggested for future research or use in SuDS.

#### **Overall important findings:**

- Lithology of gravel, and the presence of a weathered surface, considerably influences its ability to immobilize heavy metals with weathered microgabbro suggested to be an ideal lithology for use in SuDS where treatment of heavy metals in road runoff is important.
- Naturally occurring biofilm growth within a SuDS filter drain system has the possibility to enhance heavy metal removal from road runoff.
- Biofilm allowed to colonize in an experimental gravel column appeared to have reduced the MR signal through bacterial cell structure restricting the movement of the  $^1\text{H}$  atoms of the water molecules and subsequently segmented in post-processing as the solid fraction. This can be used to assess the local pore blockages in systems such as filter drains and is an important consideration in efficiency and design of such systems.
- nZVI enhanced sand, specifically 10% nZVI, demonstrated excellent enhancement of heavy metal removal when compared to unamended sand and can be suggested for further research in SuDS or industrial settings prone to high heavy metal loads.

## **6.2 Future recommendations**

The current research is an important first step in determining (bio)geochemical mechanisms responsible for heavy metal removal in filtration based SuDS with the overall goal of providing scientific evidence for better informed SuDS design and efficiency. With the current multidisciplinary approach, certain aspects of SuDS design have been highlighted which have previously been overlooked in design manuals including heavy metal removal capacity of different gravel filter media, effect on heavy metal removal and biofouling of biological growth in filter drains, simple enhancement of sand filter media with nZVI and the overall specific geochemical mechanisms responsible for metal immobilization. While the current study provided promising insight into (bio)geochemical mechanisms in a filter drain, as with any research, limitations have been realized and are acknowledged in the following paragraphs.

Batch and column experiments are conventionally used to determine contaminant transport and removal parameters in aquatic systems. However, each method is not necessarily representative of the systems they are meant to characterize, specifically a field infiltration system. As for column experiments, it is not typical for filter drains in the field to experience constant delivery and flow of water through the system, specifically as an upflow system needed for breakthrough curves in the current study. Even so, laboratory column experiments help to characterize and understand hydraulic processes and water quality parameters that would be difficult to ascertain from field studies alone (Hatt et al. 2007). That being said, it is also important to determine how infiltration systems respond to a more respective regime of sporadic influent surface water delivery and differing flow. Thus, it is suggested that in order to determine how gravel and biofilm treat pollutants in a typical SuDS filter drain, field monitoring and scaling up to an experimental filter drain is needed. In this respect, filter media can be exposed to contaminated runoff in a more intermittent fashion, as would be representative in an actual filter drain. It is also important to research and determine the lifespan of gravel filter media and when replacement and subsequent disposal of spent media would be needed.

Another limitation of the current research was that the concentrations of metals utilized were not necessarily representative of concentrations typical in road runoff. However, the higher concentrations were needed for determining and comparing rates and mechanisms of removal over the time scales of the experiment. Moreover, lower concentrations would be subject to greater error from AAS analysis. Also, metal solutions were spiked into SuDS pond water or River Kelvin water in order to represent a diverse water chemistry that a SuDS would experience, though other pollutants may typically be present in the SuDS influent, and effect the geochemical removal mechanisms. Further, complete water chemistry analysis is needed for comprehensive understanding of geochemical water-mineral and biogeochemical interactions that includes ionic strength and presence of anions, cations, trace elements, chemical compounds and specific speciation within the water utilized that was not determined within the current study. Therefore, it is advised that further research with representative metal concentrations and comprehensive water chemistry

---

analysis typical of road runoff be undertaken in order to verify metal removal efficiency holds true for influent concentrations to filter drains.

While iron oxides have been described and researched extensively in the literature for the ability to sequester heavy metals, the current research has determined that applying an engineered coating to gravel filter media is all together difficult, costly and lacking in any beneficial enhancement over natural gravel, especially gravel with a weathered surface. Even though the research set out to enhance metal removal of gravel material, it was determined natural gravel could sufficiently remove heavy metals without amendments, thus keeping in line with the sustainable aspect of SuDS. For that reason, it is recommended that the simplicity and cost-effectiveness that is inherent to gravel filtration of contaminated runoff be kept intact and that any future research focus on further types of natural unamended gravel contaminant removal rather than coating and amendments to gravel. It is suggested that engineered coatings are not appropriate for large scale environmental applications such as SuDS which corroborates with Scholz and Xu (2002), which found that there was no additional benefit of using expensive filtration media in a vertical flow filter SuDS system that was in combination with constructed reed beds.

In comparison to studies that have shown biofilm to hinder metal immobilization (by smothering mineral reactive sites (Kulczycki et al. 2005)), the current study demonstrated that biofilms enhanced heavy metal removal in experimental gravel columns and is an important aspect to consider in SuDS filter drain design. While the growth in the experimental columns was allowed to grow naturally from collected filter drain gravel and is believed to be representative of the microbial communities possible in a filter drain, many factors may have contributed to microbial communities differing in makeup and concentration from what might be found in a field filter drain. First of all, biofilm was grown in experimental columns with a constant flow of recirculated pond water which is not reflective of a field filter drain which will more likely experience irregular influent flow governed by the precipitation experienced where a filter drain is located. Therefore, even though a slimy biofilm was present on the filter drain gravel collected in Scotland, other locations may experience much drier climates, hence, long periods without a fresh water supply or nutrients or flow

to wash harmful byproducts away and thus microbial growth would be relegated to areas where moisture has been trapped between grains (Safferman et al. 1999). Second, the experimental biofilms were grown in the laboratory which allowed for sunlight to infiltrate into the columns, and while the top layer of a field filter drain would also be subjected to sunlight, there is a much larger area of a filter drain that would not experience any light, and thus would colonize a much different community of microorganisms. As such, the thick phototrophic biofilm grown in the experimental columns may not be experienced in all field scale filter drains, though, it was important to determine potential growth and possible subsequent effects on pollutant removal in a constantly submerged gravel filter as some systems may experience this phenomenon during high rainfall and flooding events that can then contribute to clogging and biofouling. It is suggested that further research with conditions typical in a filter drain such as intermittent flow and limited sunlight could offer results of how biofilm grows and effects contaminant transport in times and areas where drier conditions exist. Further, while column transport studies fit a permanent removal model well, more robust modelling could offer a more in depth look at specific mechanisms involved in gravel filters with and without biofilm growth.

While similar limitations for biofilm growth conditions also apply to the MRI analysis, the possible effects of biofouling were being sought, as well as growth of a biofilm that was distinguishable in the MRI being needed. Since the MRI research was carried out with a proof of concept notion for imaging biofilm growth and contaminant transport in an experimental gravel flow cell, results indicate that the binary processing of before (Clean) and after (Bio) biofilm 3D high resolution scans can be utilized for assessment of biofilm growth. While results for total biofouling corroborate with visual growth in the column allowed to grow for 6 months in light conditions, it is thought that total pore space lost to biofilm was underestimated due to all columns experiencing rearrangement and settling of particles between scans. Further, percentages of biofouling were based on regions of interest (ROI) that needed to be circular, further underestimating pore space fouling by including the gravel fraction when calculating percentages. A more rigorous process for post-processing of binary images is needed for further validation of biofouling results as uncertainty and

errors in processing are likely due to movement of the column, image resolution and the segmentation process.

Also, the experimental setup is highly limited by the MRI instrument. Movement of the columns between experiments is necessary, which made it difficult to perfectly match before and after scans after movement of gravel. This lead to errors in segmentation and estimating pore space lost to biofilm growth. The size of the column and imageable area is limited by the bore, hence, why it was only possible to construct and utilize a horizontal flow cell, not necessarily representative of a filter drain. Only certain materials can be used within the MRI so as to reduce interference by magnetic susceptibility of metals (Farahani et al. 1990) found in natural gravel media such as microgabbro, hence only dolomite was utilized. However, interference is still possible as seen with the intensity inhomogeneity and non-linearity of the images. While there are no studies to compare how biological growth in a gravel filter does image through MRI, this study is a first step towards developing an experimental method and post-processing to determine biofilm growth and biofouling possible in a filter drain. At this point, further tweaking to reduce movement of grains, post-processing methods and validation are required and suggested for a more robust assessment of biofilm growth in gravel filters through MR imaging.

Column breakthrough experiments for nano zero-valent iron (nZVI) enhanced sand demonstrated improved heavy metal removal for all metals investigated and particularly for 10% nZVI enhanced sand. Again, column experiments are an important aspect towards determining contaminant transport parameters, but further research is needed to explore how nZVI particles react and behave in a scaled up sand filter or as a sand base layer in SuDS systems susceptible to heavy metal pollution. Small scale column experiments indicate that no migration from the sand occurred, but it is not known for sure how the nanoparticles would behave on a larger scale and particularly in an environmental application. While nZVI enhanced sand demonstrated promising results, further verification, longevity analysis, scaling up to lab-scale filters and field filters, disposal considerations and cost-benefit analysis is needed and suggested for future research.

---

## 6.3 References

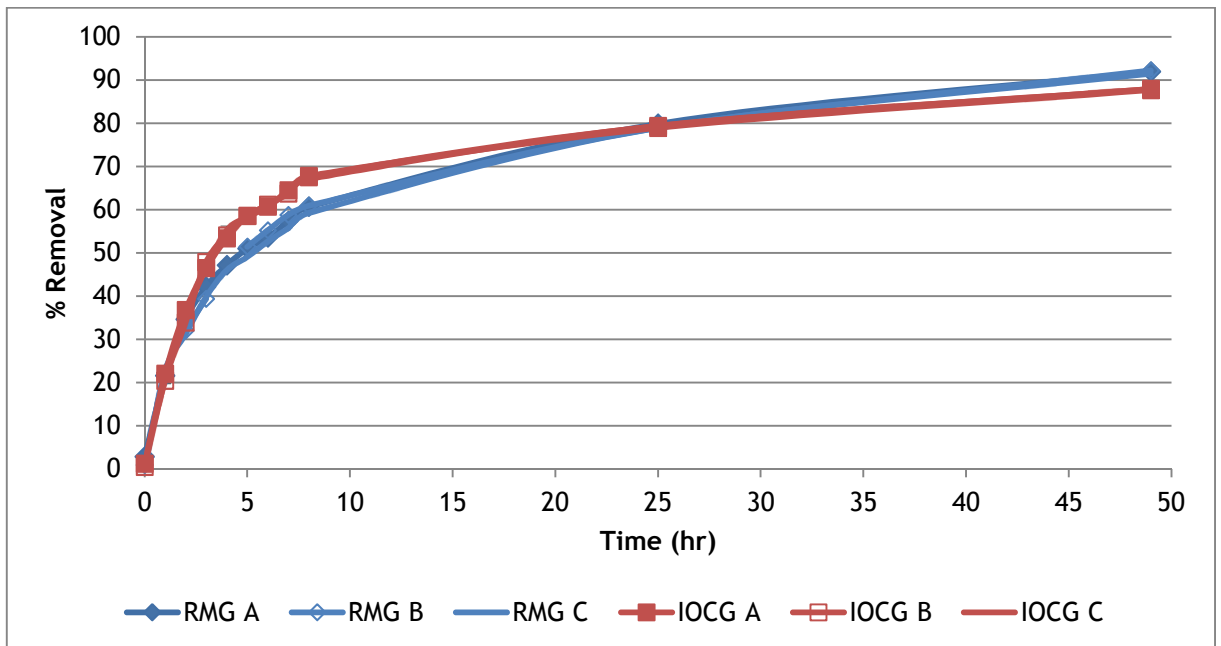
- Banfield, J. F. and R. A. Eggleton (1990). "Analytical transmission electron-microscope studies of plagioclase, muscovite, and K-feldspar weathering." Clays and Clay Minerals **38**(1): 77-89.
- Benjamin, M. M., et al. (1996). "Sorpton and filtration of metals using iron-oxide-coated sand." Water Research **30**(11): 2609-2620.
- Farahani, K., et al. (1990). "Effect of field-strength on susceptibility artifacts in magnetic-resonance imaging." Computerized Medical Imaging and Graphics **14**(6): 409-413.
- Hatt, B. E., et al. (2007). "Treatment performance of gravel filter media: Implications for design and application of stormwater infiltration systems." Water Research **41**(12): 2513-2524.
- Kulczycki, E., et al. (2005). "Sorpton of cadmium and lead by bacteria-ferrihydrite composites." Geomicrobiology Journal **22**(6): 299-310.
- U. S. G. Survey. Summary of hydrologic and physical properties of rock and soil materials, as analyzed by the hydrologic laboratory of the U.S. Geological Survey, 1948-60. Water Supply Paper (1967)
- Odom, I. E. (1984). "Smectite clay minerals - properties and uses." Philosophical Transactions of the Royal Society a-Mathematical Physical and Engineering Sciences **311**(1517): 391-+.
- Safferman, S. I., et al. (1999). "Providing moisture passively to enhance start up and maintain biofilm activity in an intermittently loaded reactor." Journal of Environmental Science and Health Part a-Toxic/Hazardous Substances & Environmental Engineering **34**(8): 1591-1605.
- Scholz, M. and J. Xu (2002). "Comparison of constructed reed beds with different filter media and macrophytes treating urban stream water contaminated with lead and copper." Ecological Engineering **18**(3): 385-390.

## Appendix A - Literature review of metal concentrations found in runoff studies and used in experimentation

Metals in Experimental and Runoff Studies													
Author	Year	Type of Study	Al (µg/L)	As (µg/L)	B (µg/L)	Ba (µg/L)	Br (µg/L)	Cd (µg/L)	Ce (µg/L)	Co (µg/L)	Cr (µg/L)	Cu (µg/L)	Fe (µg/L)
Asaf	2004	Runoff Study (Max-Min (Mean))	0-5569 (1054)		0-680 (57)	7-144 (29)					1-13 (4)	1-79 (4)	12-1427 (111)
Barrett	93/95	Runoff Study (total reported)										22-7033	
Drapper	2000	Runoff Study (total reported)										30-340	
Driscoll	1990	Runoff Study (total reported)										50.00	
Kayhanian	2007	Runoff Study (dissolved & (total))		0.5-20 (1), 0.5-70 (2.7)				0.2-8.4 (0.24), 0.2-30 (0.7)			1-23 (3.3), 1- 97 (8.6)	1.1-130 (14.9), 1.2-270 (33.5)	32-3310 (378), 1400- 104,000 (18500)
Makepeace	1995	Runoff Study (total reported)		1-210				0.3-11			10-230	6.5-150	
Sansalone	1997	Runoff Study (dissolved & (total))						2-9 (3) 5-32 (8)				13-279 (44) 43-325 (88)	
Walker	1999	Runoff Study (reported range)		1-21				0.05-13730				0.06-1410	
Ward	1990	Runoff Study (surface dust & (background))					45-190 (20), 132-265 (148)	2-10.7 (0.4), 4-15.4 (6.8)	47-136 (38.5), 114-149 (142)	18-31.9 (16.3), 19.3-41.7 (18.1)	130-290 (69), 260-536 (140)	22-54 (14), 256-429 (45)	2.4-3.1 (2.8), 2.9-4.1 (2.8)
Genç-Fuhrman	2007	Experimentation (concentration used)		<1-1000				0.1-2670			<0.5-2830	2.6-1820	
Liu	2004	Experimentation (concentration used)						5mg/L				5mg/L	
Liu	2005	Experimentation (concentration used)						50-5000				50-5000	
Pitcher	2004	Experimentation (concentration used)						25µg/L				250µg/L	
Scholz	2002	Experimentation (experimental & (background))										1280 (70)	
Seelsaen	2006	Experimentation (conc. = 50x runoff conc.)										5mg/L	
Vijayaraghavan	2009	Experimentation (10mg/L used in experiments)										14-134	

Metals in Experimental and Runoff Studies													
Author	Year	Type of Study	Mn (µg/L)	Mo (µg/L)	Ni (µg/L)	P (µg/L)	Pb (µg/L)	Rb (µg/L)	Si (µg/L)	Sr (µg/L)	Ti (µg/L)	V (µg/L)	Zn (µg/L)
Asaf	2004	Runoff Study (Max-Min (Mean))	1-516 (40)	2-74 (10)	2-44 (9)	63-4410 (592)	3-10 (6)		296-7800 (1748)	24-831 (131)	1-27 (4)	2-59 (14)	8-720 (81)
Barrett	93/95	Runoff Study (total reported)					7-1780						22-929
Drapper	2000	Runoff Study (total reported)					80-620						150-1850
Driscoll	1990	Runoff Study (total reported)					400.00						330.00
Kayhanian	2007	Runoff Study (dissolved & (total))			1.1-40 (4.9), 1.1-130 (11.2)		1-480 (7.6), 1-2600 (47.8)						3-1017 (68.8), 5.5-1680 (187.1)
Makepeace	1995	Runoff Study (total reported)			6-150								16.6-580
Sansalone	1997	Runoff Study (dissolved & (total))					13-21 (16) 31-1457 (88)						209-14786 (1322) 336-15244 (628)
Walker	1999	Runoff Study (reported range)			1-49,000		0.57-26,000						0.7-22,000
Ward	1990	Runoff Study (surface dust & (background))	2714-4172 (1650), 2975-5097 (1790)	4.2-7.1 (1.8), 5.5-11.6 (6.5)	161-314 (28), 256-429 (45)			104-120 (78), 147-175 (270)				180-618 (62), 320-820 (80)	320-940 (68), 860-1472 (152)
Genç-Fuhrman	2007	Experimentation (concentration used)			0.6-8640								22.5-52300
Liu	2004	Experimentation (concentration used)					5mg/L						5mg/L
Liu	2005	Experimentation (concentration used)					50-5000						500-5000
Pitcher	2004	Experimentation (concentration used)					50µg/L						500µg/L
Scholz	2002	Experimentation (experimental & (background))					990 (20)						
Seelsaen	2006	Experimentation (conc. = 50x runoff conc.)					5mg/L						27mg/L
Vijayaraghavan	2009	Experimentation (10mg/L used in experiments)	128-155				56-76						143-181

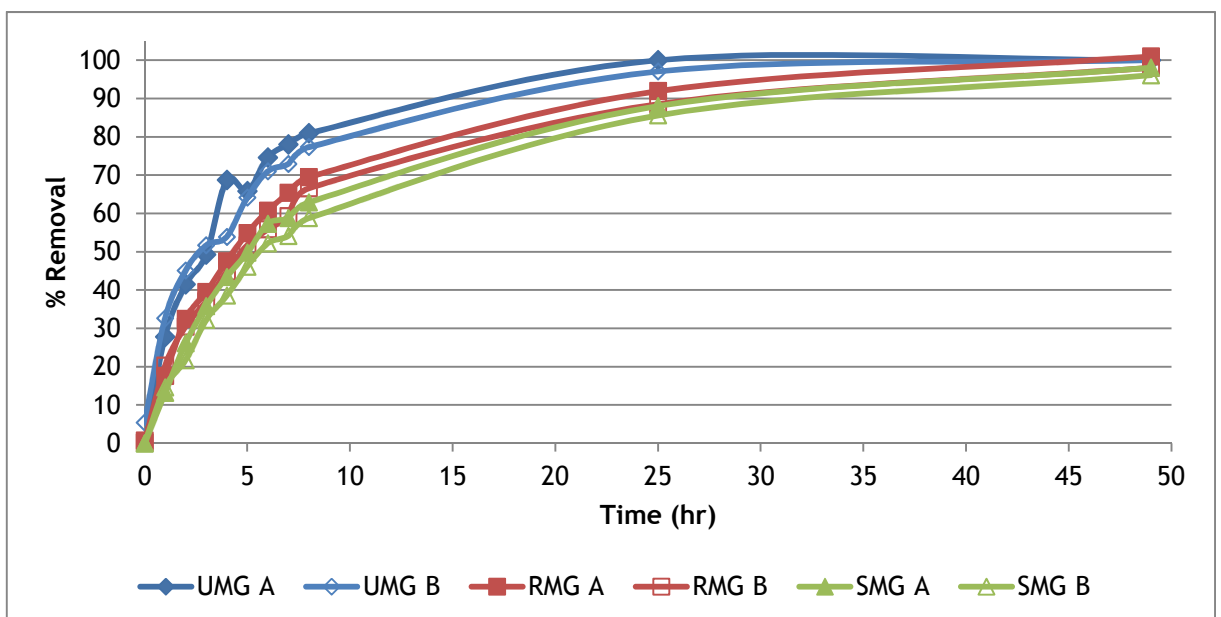
## Appendix B - Chapter 2 Analytical and Experimental Error Analysis



**Analytical error:** Triplicate aliquot samples taken during batch experiment for rinsed microgabbro (RMG) versus iron oxide coated gravel (IOCG) zinc removal

Standard Deviation (ppm)	0 h	1 h	2 h	3 h	4 h	5 h	6 h	7 h	8 h	24 h	48 h	Min	Max
RMG Triplicate Aliquot	0.07	0.03	0.07	0.06	0.04	0.05	0.06	0.07	0.04	0.02	0.02	0.02	0.07
IOCG Triplicate Aliquot	0.02	0.04	0.06	0.03	0.04	0.01	0.01	0.02	0.02	0.01	0.01	0.01	0.06

**Standard Deviation:** Standard deviation of triplicate aliquot zinc samples.



**Experimental verification:** Duplicate batch experiments run for unrinsed microgabbro (UMG), rinsed microgabbro (RMG) and scrubbed microgabbro (SMG) zinc removal

# Appendix C - Example of PHREEQC Input and Output

**INPUT:**

```
SOLUTION 1
  temp      23.5
  pH        7.03
  pe        4
  redox     pe
  units     ppm
  density   1
  Cu(2)     4.96
  N(5)      9.21
  -water    1 # kg
```

**OUTPUT:**

-----Solution composition-----  
-----

Elements	Molality	Moles
Cu(2)	7.805e-005	7.805e-005
N(5)	6.576e-004	6.576e-004

-----Description of solution-----  
-----

```

                                pH = 7.030
                                pe = 4.000
                                Activity of water = 1.000
                                Ionic strength = 3.789e-004
                                Mass of water (kg) = 1.000e+000
                                Total alkalinity (eq/kg) = 1.049e-004
                                Total carbon (mol/kg) = 0.000e+000
                                Total CO2 (mol/kg) = 0.000e+000
                                Temperature (deg C) = 23.500
                                Electrical balance (eq) = -6.064e-004
Percent error, 100*(Cat-|An|)/(Cat+|An|) = -85.53
                                Iterations = 3
                                Total H = 1.110125e+002
                                Total O = 5.550829e+001
```

-----Distribution of species-----  
-----

Log Species	Molality	Activity	Log	Log	
			Molality	Activity	
Gamma					
OH-	9.782e-008	9.568e-008	-7.010	-7.019	-
0.010					
H+	9.536e-008	9.333e-008	-7.021	-7.030	-
0.009					
H2O	5.551e+001	1.000e+000	1.744	-0.000	
0.000					
Cu(2)	7.805e-005				
Cu(OH)2	4.933e-005	4.933e-005	-4.307	-4.307	
0.000					
Cu+2	2.248e-005	2.057e-005	-4.648	-4.687	-
0.039					
CuOH+	2.253e-006	2.204e-006	-5.647	-5.657	-
0.010					

Cu <sub>2</sub> (OH) <sub>2</sub> +2 0.039	1.999e-006	1.829e-006	-5.699	-5.738	-
Cu(OH) <sub>3</sub> - 0.010	3.257e-011	3.185e-011	-10.487	-10.497	-
Cu(OH) <sub>4</sub> -2 0.039	7.442e-017	6.810e-017	-16.128	-16.167	-
H(0)	1.252e-025				
H <sub>2</sub> 0.000	6.259e-026	6.259e-026	-25.204	-25.203	
N(5)	6.576e-004				
NO <sub>3</sub> - 0.010	6.576e-004	6.431e-004	-3.182	-3.192	-
O(0)	0.000e+000				
O <sub>2</sub> 0.000	0.000e+000	0.000e+000	-42.460	-42.460	

-----Saturation indices-----  
-----

Phase	SI	log IAP	log KT	
Cu(OH) <sub>2</sub>	0.68	9.37	8.70	Cu(OH) <sub>2</sub>
Cu <sub>2</sub> (OH) <sub>3</sub> NO <sub>3</sub>	-0.78	8.52	9.30	Cu <sub>2</sub> (OH) <sub>3</sub> NO <sub>3</sub>
H <sub>2</sub> (g)	-22.06	-25.20	-3.14	H <sub>2</sub>
H <sub>2</sub> O(g)	-1.55	-0.00	1.55	H <sub>2</sub> O
O <sub>2</sub> (g)	-39.58	-42.46	-2.88	O <sub>2</sub>
Tenorite	1.70	9.37	7.68	CuO

-----  
End of simulation.  
-----

## Appendix D - Advection Diffusion Matlab Code

```

function adv_diff_calibrate_k0
% Calibrate an advection diffusion equation with permananet adsorption
% Make the paramater values global so that they can be seen anywhere in
the
% program
% global D
% global U
% global k
% Initial guess at dispersal coeff m^2/s
D = 3e-6;
% Initial guess at velocity coeff m/s
U = .01/3600;
% Initial guess at loss term k (mg/l)/s
k = 0.00000;
pulse_length = 3*60*60;
input_conc = 1.4;

%Times in seconds that you have data points
tspan = [0.000 300.000 600.000 900.000 1200.000 1500.000 1800.000
2100.000 2400.000 2700.000 3000.000 3300.000 3600.000
3900.000 4200.000 4500.000 4800.000 5100.000 5400.000
5700.000 6000.000 6300.000 6600.000 6900.000 7200.000
7500.000 7800.000 8100.000 8400.000 8700.000 9000.000
9300.000 9600.000 9900.000 10200.000 10500.000 10800.000
11100.000 11400.000 11700 12000 12300 12600 12900 13200
13500 13800 14100 14400 14700 15000 15300 15600 15900
16200];

xmesh = linspace(0, .150,100);

%Observed concentration
obs = [0.018 0 0.042 0.263 0.533 0.661 0.902 1.171 1.313
1.389 1.382 1.425 1.496 1.464 1.084 1.062 1.161 1.182
1.304 1.333 1.333 1.356 1.342 1.328 1.325 1.33 1.324
1.335 1.385 1.337 1.373 1.402 1.408 1.424 1.408 1.409
1.442 1.371 1.373 1.358 1.355 1.243 1.152 1.006 0.876
0.691 0.553 0.474 0.458 0.461 0.441 0.436 0.429 0.424
0.416];

x0 = D
x = fminsearch(@objective,x0,[],k,pulse_length,input_conc, tspan, xmesh,
obs, U);
D = x(1);

% set up the functional coeffieicients in pdefun and bounday conditions in
% bcfun and initial conditions in icfun for a generc diffusion equation (
See
% the form under matlab help for pdepe function;
m =0;
sol =
pdepe(m,@pdefun,@icfun,@bcfun,xmesh,tspan,[],D,U,k,pulse_length,input_con
c);

figure(1)
u = sol(:,:,1);
surf(xmesh,tspan,u)
figure(2)

```

---

```

for i = 1:length(obs)
    plot(xmesh,u(i,:))
    hold on
end

% plot break through
figure(3)
D

plot(tspan,u(:,100))
hold on
plot(tspan, obs)

end

function object = objective(x,k,pulse_length,input_conc, tspan, xmesh,
obs, U);
D = x(1);

m = 0;
sol =
pdepe(m,@pdefun,@icfun,@bcfun,xmesh,tspan,[],D,U,k,pulse_length,input_conc);
u = sol(:,100,1);
sum = 0;
for i = 1:length(obs)
    sum = sum + (u(i) - obs(i))^2;
end
object = sum
end

function uu = icfun(x,D,U,k,pulse_length,input_conc)
% global D
% global U
% global k

uu = 0*x;

end

function [pl,ql,pr,qr] =
bcfun(xl,ul,xr,ur,t,D,U,k,pulse_length,input_conc)
% global D
% global U
% global k

% flow left to right

pr = U*ur;
qr = 1;

delta = 60;

```

```
if t > pulse_length+ delta;
    pl = ul;
    ql = 0;
elseif t < pulse_length;
    pl = ul-input_conc;
    ql = 0;
else
    pl = ul-input_conc + input_conc*(t-pulse_length)/delta;
    ql = 0;
end

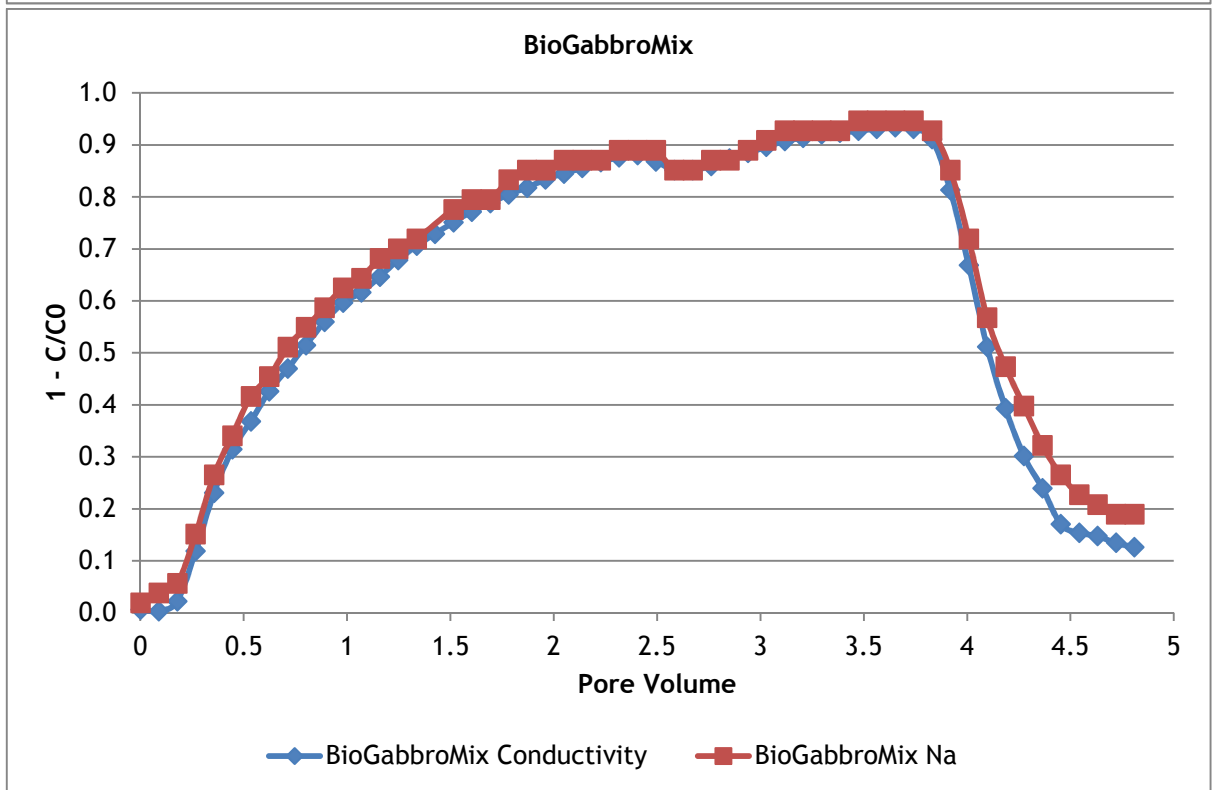
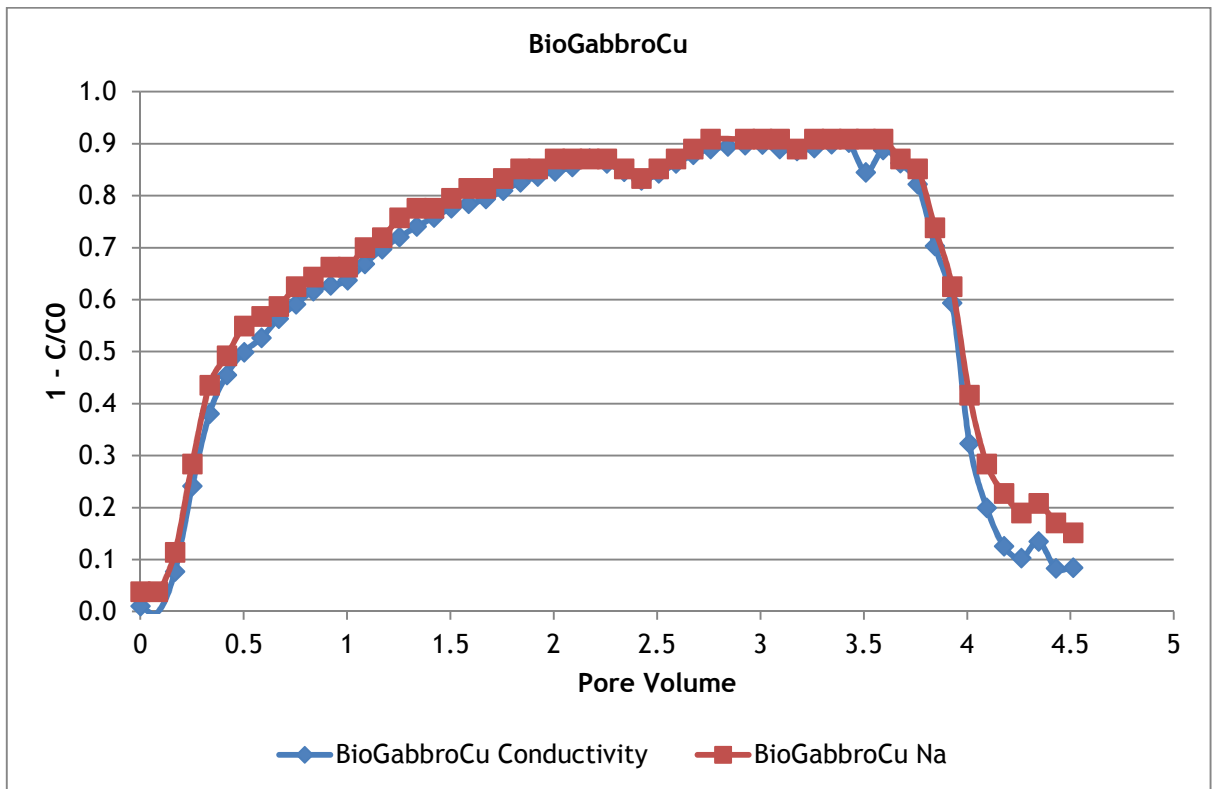
end

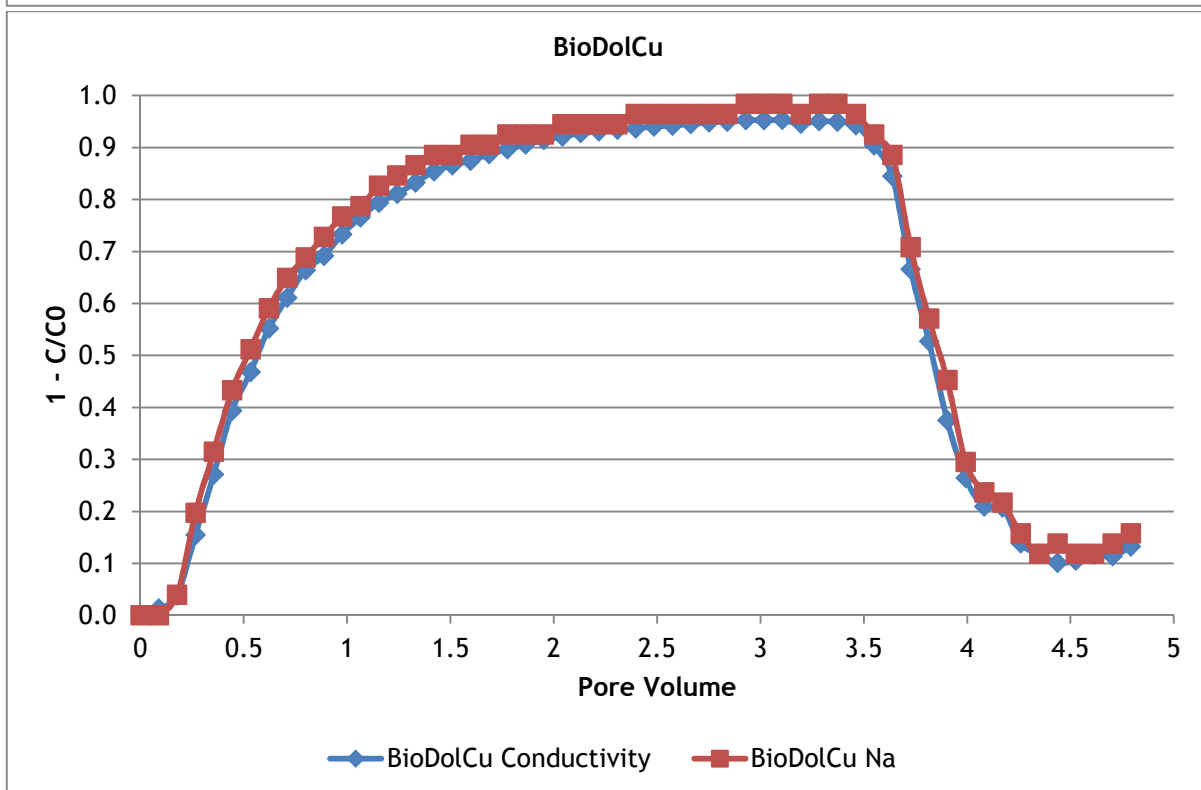
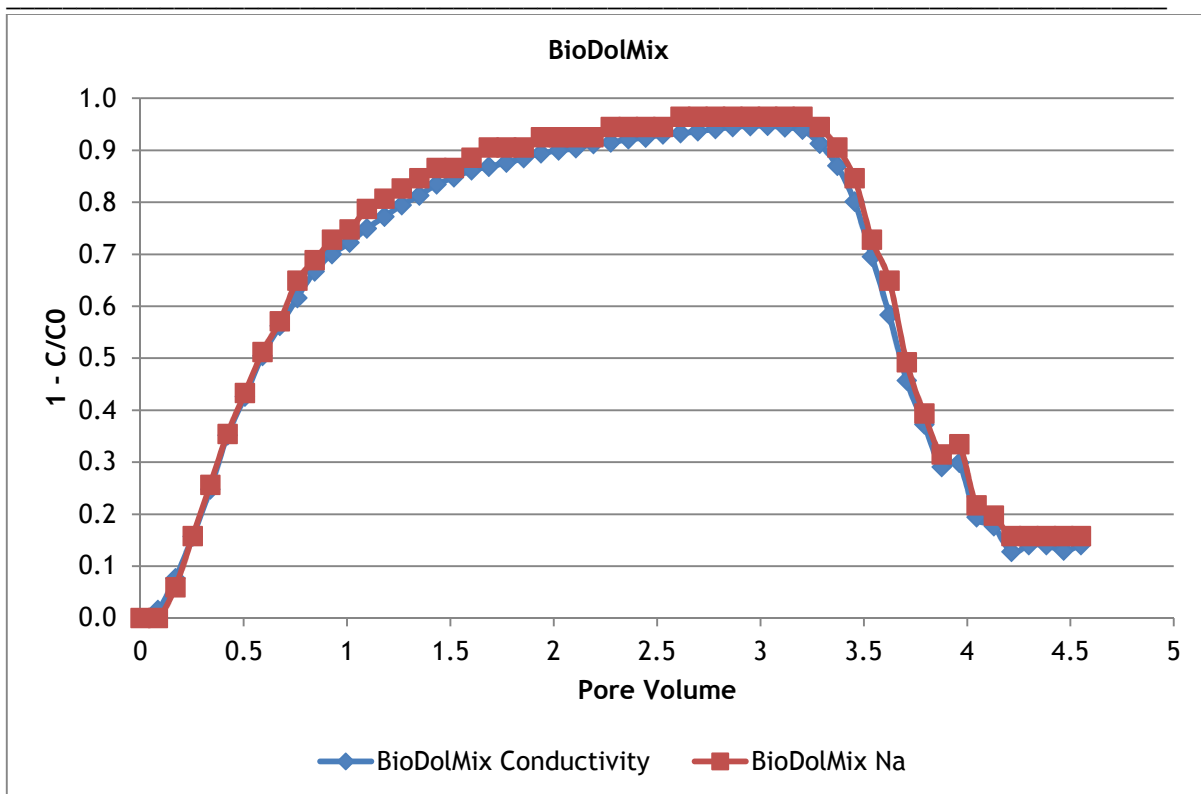
function [c,f,s] = pdefun(x,t,u,dudx,D,U,k,pulse_length,input_conc)
% global D
% global U
% global k

c = 1;
f = D*dudx -U*u;
s = -k*u;

end
```

## Appendix E - Comparison of conductivity measurements to Na flame photometer analysis





## Appendix F - Clone library breakdown, sequencing and classification

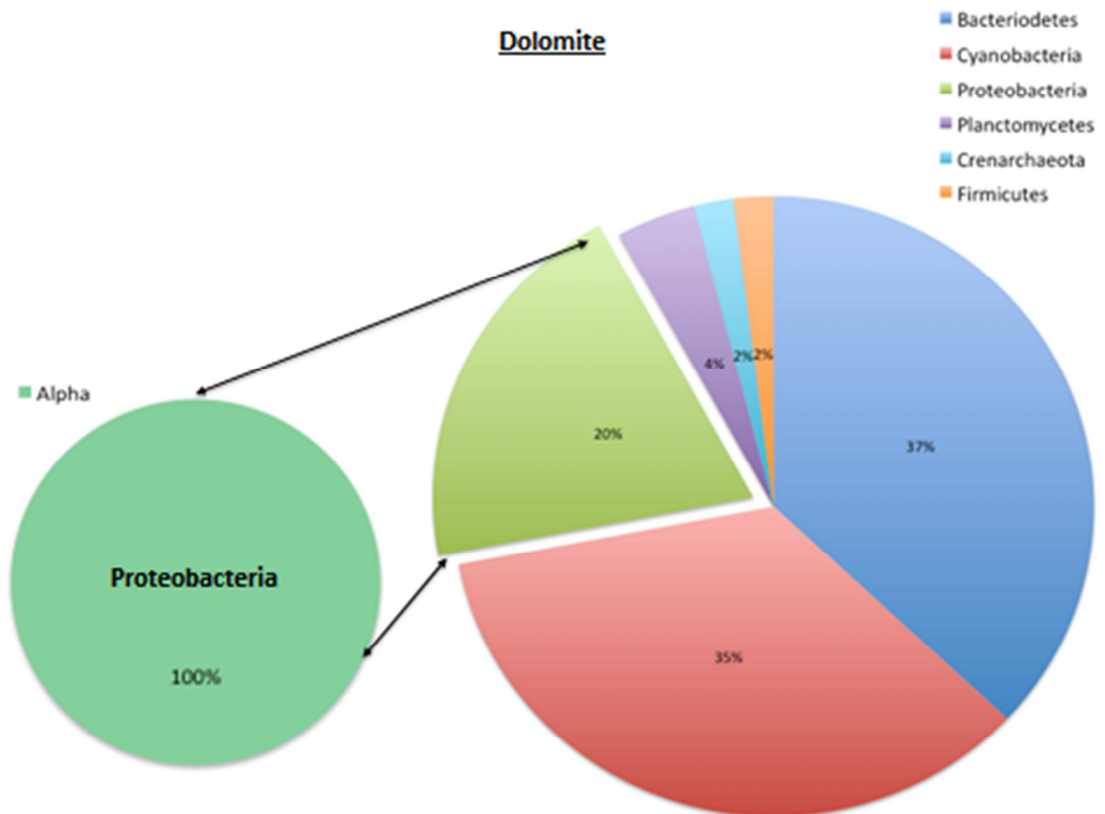
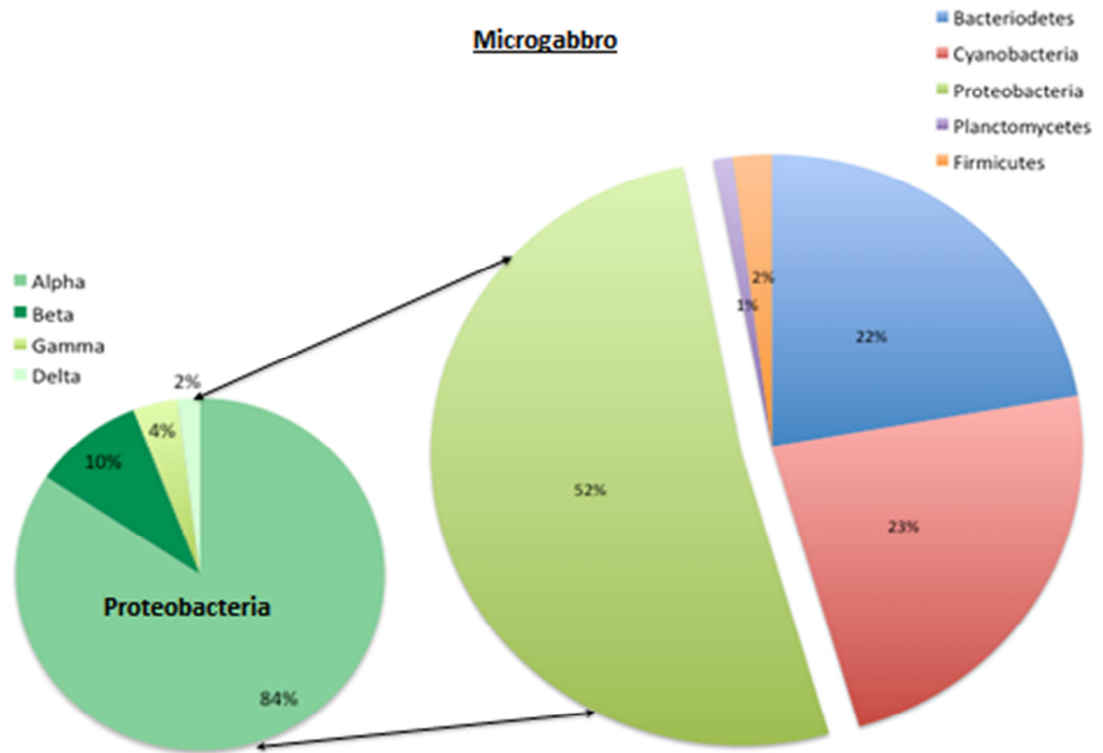
Clone Library Breakdown			
Microgabbro		Dolomite	
O.T.U.	% OF LIBRARY	O.T.U.	% OF LIBRARY
1	2	1	2
2	1	2	1
3	1	3	1
9	1	4	1
13	15	5	15
20	1	6	1
22	8	7	8
23	5	8	5
24	6	9	6
25	2	10	2
26	2	11	2
27	2	12	2
28	10	13	10
29	20	14	20
30	2	15	2
31	2	16	2
32	2	17	2
33	1	18	1
34	1	19	1
35	2	20	2
36	3	21	3
37	8	29	8
38	1	39	1
40	1	42	1
41	1	43	1
		44	1

Blue bold = O.T.U. shared by both libraries

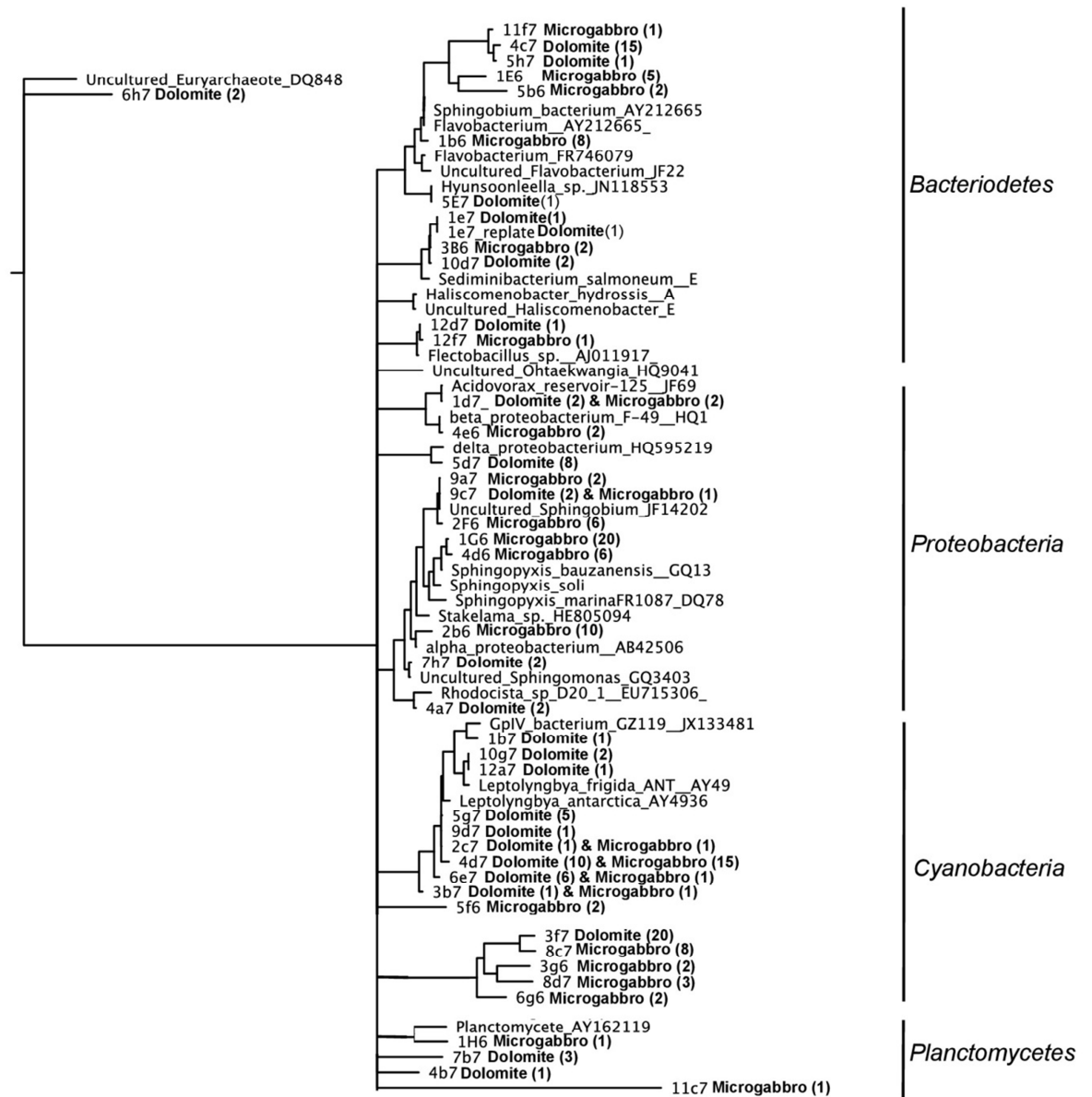
Clone Library Sequencing							
Clone	OTU	Frequency	RDP Phylum (% match)	RDP Class (% match)	RDP Order (% match)	RDP Family (% match)	RDP Genus (% match)
1A5	1	2.6	Cyanobacteria (100)	Cyanobacteria (100)		Family IV (100)	GpIV (51)
1A6	2	1.3	Firmicutes (90)	Bacilli (90)	Bacillales (90)	Pasteuriaceae (90)	Pasteuria (90)
1A7	3	1.3	Cyanobacteria (100)	Cyanobacteria (100)		Family IV (56)	GpIV (56)
1A10	4	1.3	Proteobacteria (100)	Betaproteobacteria (100)	Methylophilales (99)	Methylophilaceae (99)	Methylobacillus (44)
1B4	5	4	Cyanobacteria (91)	Cyanobacteria (91)		Family X (21)	GpX (21)
1B6	6	8	Firmicutes (95)	Clostridia (45)	Clostridiales (36)	Peptococcaceae 2 (26)	Desulfurispora (26)
1B8	7	5.3	Cyanobacteria (100)	Cyanobacteria (100)		Family IV (56)	GpIV (56)
1C1	8	1.3	Lentisphaerae (89)	Lentisphaeria (8)	Lentisphaerales (8)	Lentisphaeraceae (8)	Lentisphaera (8)
1C3	9	13.3	Cyanobacteria (100)	Cyanobacteria (100)		Family IV (82)	GpIV (82)
1C5	10	4	Cyanobacteria (100)	Cyanobacteria (100)		Family IV (80)	GpIV (80)
1C6	11	1.3	Planctomycetes (98)	Phycisphaerae (92)	Phycisphaerales (92)	Phycisphaeraceae (92)	Phycisphaera (92)
1C7	12	2.6	Bacteroidetes (64)	Sphingobacteria (11)	Sphingobacteriales ( )	Sphingobacteriaceae (7)	Pseudosphingobacterium (5)
1C8	13	2.6	Aquificae (76)	Aquificae (11)	Aquificales (11)	Aquificaceae (5)	Aquifex (4)
1E4	14	1.3	Euryarchaeota (39)	Halobacteria (32)	Halobacteriales (19)	Halobacteriaceae (19)	Halonotius (6)
1E7	15	1.3	Euryarchaeota (36)	Halobacteria (29)	Halobacteriales (19)	Halobacteriaceae (19)	Halonotius (6)
1F1	16	1.3	Euryarchaeota (39)	Halobacteria (25)	Halobacteriales (14)	Halobacteriaceae (14)	Salarchaeum (7)
1F10	17	5.3	Cyanobacteria (100)	Cyanobacteria (100)		Family IV (70)	GpIV (70)
1G1	18	12	Cyanobacteria (100)	Cyanobacteria (100)		Family IV (92)	GpIV (92)
1G3	19	2.6	Cyanobacteria (100)	Cyanobacteria (99)		Family IV (80)	GpIV (80)
1G6	20	18.6	Cyanobacteria (100)	Cyanobacteria (99)		Family IV (76)	GpIV (76)
1G7	21	1.3	Cyanobacteria (100)	Cyanobacteria (99)		Family IV (76)	GpIV (76)
1H1	22	2.6	Proteobacteria (100)	Deltaproteobacteria (94)	Bdellovibrionales (92)	Bdellovibrionaceae (92)	Vampirovibrio (92)
1H8	23	1.3	Fusobacteria (86)	Fusobacteria (3)	Fusobacteriales (3)	Leptotrichiaceae (3)	Streptobacillus (3)
2D3	24	1.3	Fusobacteria (92)	Fusobacteria (3)	Fusobacteriales (3)	Leptotrichiaceae (3)	Streptobacillus (2)
2E2	25	1.3	Proteobacteria (100)	Alphaproteobacteria (100)	Rhizobiales (100)	Bradyrhizobiaceae (55)	Agromonas (22)
2F2	26	1.3	Cyanobacteria (100)	Cyanobacteria (100)		Family IV (71)	GpIV (71)

Classification of Clones									
Clone	OTU	% in microgabbro	% in dolomite	Phylum	Class	Order	Family	Genus	NCBI hit
10d7	17	0	2	"Bacteroidetes" (100%)	"Sphingobacteria" (100%)	Sphingobacteriales" (100%)	Chitinophagaceae (100%)	Sediminibacterium (100%)	HM066523.1
10g7	15	0	2	Cyanobacteria (100%)	Cyanobacteria (100%)		Family IV (66%)	GplV (66%)	AY493575.1
11c7	41	1	0	"Proteobacteria" (97%)	Deltaproteobacteria (34%)	Bdellovibrionales (13%)	Bdellovibrionaceae (11%)	Vampirovibrio (11%)	
11f7	40	1	0	"Bacteroidetes" (100%)	Flavobacteria (100%)	"Flavobacteriales" (100%)	Flavobacteriaceae (100%)	Flavobacterium (100%)	JN397751.1
12a7	44	0	1	Cyanobacteria (100%)	Cyanobacteria (100%)		Family IV (76%)	GplV (76%)	AY493575.1
12d7	18	0	1	"Bacteroidetes" (100%)	"Sphingobacteria" (100%)	Sphingobacteriales" (100%)	Cytophagaceae (100%)	Flectobacillus (100%)	AJ011917.1
12f7	38	1	0	"Bacteroidetes" (100%)	"Sphingobacteria" (100%)	Sphingobacteriales" (100%)	Cytophagaceae (100%)	Flectobacillus (100%)	AJ011917.1
1E6	23	5	0	"Bacteroidetes" (100%)	"Sphingobacteria" (100%)	Sphingobacteriales" (100%)	"Saprosiraceae" (100%)	Haliscomenobacter (100%)	JN391741.1
1G6	29	20	8	"Proteobacteria" (100%)	Alphaproteobacteria (100%)	Sphingomonadales (100%)	Sphingomonadaceae (100%)	Sphingopyxis (100%)	GQ131578.1
1H6	34	1	0	"Planctomycetes" (99%)	Phycisphaerae (88%)	Phycisphaerales (88%)	Phycisphaeraceae (88%)	Phycisphaera (88%)	
1b6	22	8	0	"Bacteroidetes" (100%)	Flavobacteria (100%)	"Flavobacteriales" (100%)	Flavobacteriaceae (100%)	Flavobacterium (100%)	AY212665.1
1b7	39	0	1	Cyanobacteria (100%)	Cyanobacteria (100%)		Family IV (88%)	GplV (88%)	JX133481.1
1e7	10	0	1	"Bacteroidetes" (100%)	"Sphingobacteria" (100%)	Sphingobacteriales" (100%)	Chitinophagaceae (100%)	Sediminibacterium (98%)	JQ684454.1
1e7replate	42	0	1	"Bacteroidetes" (100%)	"Sphingobacteria" (100%)	Sphingobacteriales" (100%)	Chitinophagaceae (100%)	Sediminibacterium (100%)	
2b6	28	10	0	"Proteobacteria" (100%)	Alphaproteobacteria (100%)	Sphingomonadales (98%)	Sphingomonadaceae (98%)	Sphingosinicella (46%)	AB425062.1
2F6	24	6	0	"Proteobacteria" (100%)	Alphaproteobacteria (100%)	Sphingomonadales (100%)	Sphingomonadaceae (100%)	Sphingobium (100%)	
3B6	33	1	0	"Bacteroidetes" (100%)	"Sphingobacteria" (100%)	Sphingobacteriales" (100%)	Chitinophagaceae (100%)	Sediminibacterium (100%)	JQ684454.1
3f7	14	0	20	Cyanobacteria (100%)	Cyanobacteria (100%)		Family IV (93%)	GplV (93%)	JX133481.1
3g6	25	2	0	"Proteobacteria" (100%)	Gammaproteobacteria (100%)	Chromatiales (100%)	Chromatiaceae (100%)	Rheinheimera (100%)	JN868893.1
4d6	26	2	0	"Proteobacteria" (100%)	Alphaproteobacteria (100%)	Sphingomonadales (100%)	Sphingomonadaceae (100%)	Sphingopyxis (99%)	GQ131578.1
4d7	13	15	10	Cyanobacteria (100%)	Cyanobacteria (100%)		Family IV (95%)	GplV (95%)	
4e6	27	2	0	"Proteobacteria" (100%)	Betaproteobacteria (100%)	Burkholderiales (100%)	Burkholderiales-incertae-sedis (100%)	Aquabacterium (100%)	HQ132426.1
5b6	32	2	0	"Bacteroidetes" (100%)	Bacteroidetes"-incertae-sedis (100%)			Ohtaekwangia (100%)	JQ958624.1
5e7	6	0	1	"Bacteroidetes" (100%)	Flavobacteria (100%)	"Flavobacteriales" (100%)	Flavobacteriaceae (100%)	Hyunsoonleella (80%)	
5f6	31	2	0	"Bacteroidetes" (100%)	Flavobacteria (100%)	"Flavobacteriales" (100%)	Flavobacteriaceae (100%)	Flaviramulus (39%)	
5h7	43	0	1	"Bacteroidetes" (100%)	Flavobacteria (100%)	"Flavobacteriales" (100%)	Flavobacteriaceae (100%)	Flavobacterium (100%)	EU057851.1
6g6	30	2	0	"Proteobacteria" (100%)	Alphaproteobacteria (100%)	Sphingomonadales (100%)	Sphingomonadaceae (100%)	Sphingopyxis (100%)	GQ131578.1
6h7	11	0	2	"Crenarchaeota" (94%)	Thermoprotei (64%)	Thermoproteales (28%)	Thermoproteaceae (18%)	Thermocladium (13%)	
7b7	21	0	3	"Planctomycetes" (100%)	"Planctomycetacia" (100%)	Planctomycetales (100%)	Planctomycetaceae (100%)	Gemmata (62%)	GQ500794.1
7h7	16	0	2	"Proteobacteria" (100%)	Alphaproteobacteria (100%)	Sphingomonadales (100%)	Sphingomonadaceae (100%)	Sphingomonas (100%)	GQ340337.1
8c7	37	8	0	Cyanobacteria (100%)	Cyanobacteria (100%)		Family IV (73%)	GplV (73%)	EU022730.1
8d7	36	3	0	"Proteobacteria" (100%)	Betaproteobacteria (100%)	Burkholderiales (100%)	Comamonadaceae (100%)	Acidovorax (100%)	
9a7	35	2	0	"Proteobacteria" (100%)	Alphaproteobacteria (100%)	Sphingomonadales (100%)	Sphingomonadaceae (100%)	Sphingobium (100%)	
9c7	20	1	2	"Proteobacteria" (100%)	Alphaproteobacteria (100%)	Sphingomonadales (100%)	Sphingomonadaceae (100%)	Sphingobium (100%)	JN628333.1
9d7	19	0	1	Cyanobacteria (100%)	Cyanobacteria (100%)		Family IV (89%)	GplV (89%)	
2C7	2	1	1	Cyanobacteria (100%)	Cyanobacteria (100%)		Family IV (88%)	GplV (88%)	
3b7	3	1	1	"Proteobacteria" (100%)	Alphaproteobacteria (88%)	Sphingomonadales (88%)	Sphingomonadaceae (86%)	Stakelama (60%)	AF076164.1
4b7	4	0	1	Planctomycetes (100%)	Planctomycetacia (87%)	Planctomycetales (86%)	Planctomycetaceae (86%)	Rhodopirellula (52%)	JN869038.1
4c7	5	0	15	Bacteroidetes (100%)	Flavobacteria (100%)	Flavobacteriales (100%)	Flavobacteriaceae (100%)	Flavobacterium (100%)	HM807713.1
5d7	7	0	8	Proteobacteria (100%)	Deltaproteobacteria (100%)	Myxococcales (100%)	Cystobacterineae (100%)	Anaeromyxobacter (40%)	HQ595219.1
1d7	1	2	2	Proteobacteria (100%)	Betaproteobacteria (100%)	Burkholderiales (100%)	Comamonadaceae (100%)	Acidovorax (100%)	JF697506.1
4a7	12	0	2	"Proteobacteria" (100%)	Alphaproteobacteria (100%)	Rhodospirillales (100%)	Rhodospirillaceae (100%)	Rhodocista (100%)	EU715306.1
5g7	8	0	5	Cyanobacteria (100%)	Cyanobacteria (100%)		Family IV (100%)	GplV (83%)	AB630390.1
6e7	9	1	6	Cyanobacteria (100%)	Cyanobacteria (100%)		Family IV (90%)	GplV (70%)	HQ188984.1

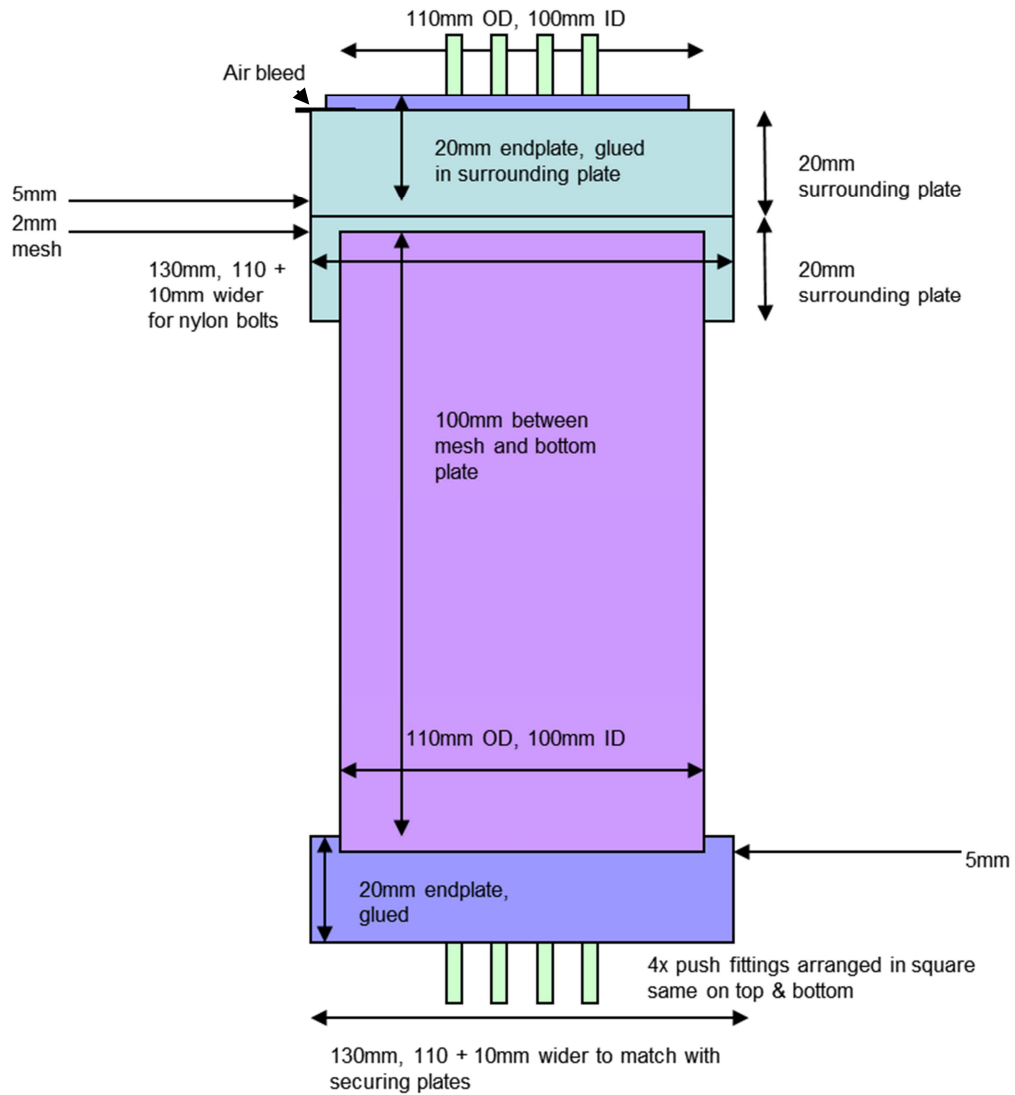
## Appendix G - Class breakdown of *Proteobacteria*



# Appendix H - Phylogenetic tree of bacteria identified in gravel growth columns

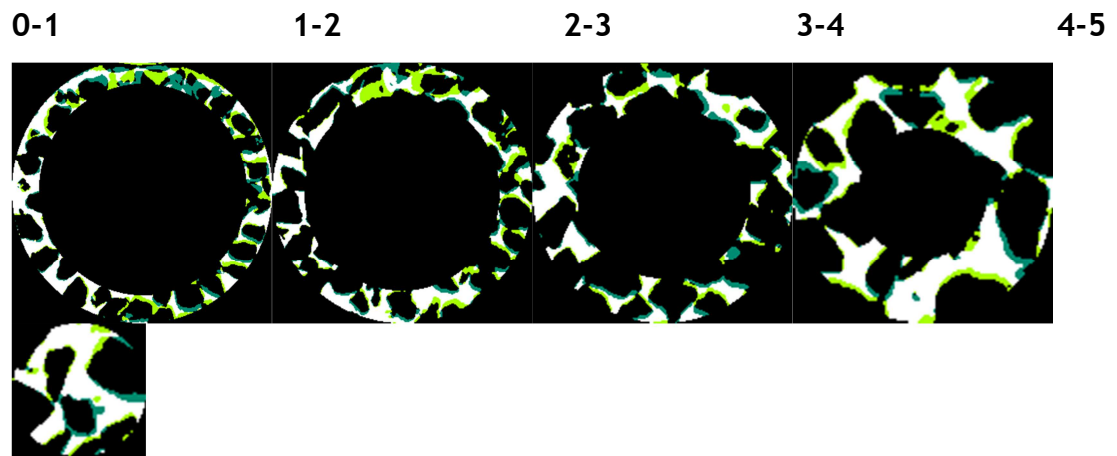


# Appendix I - Specifications of experimental gravel filter

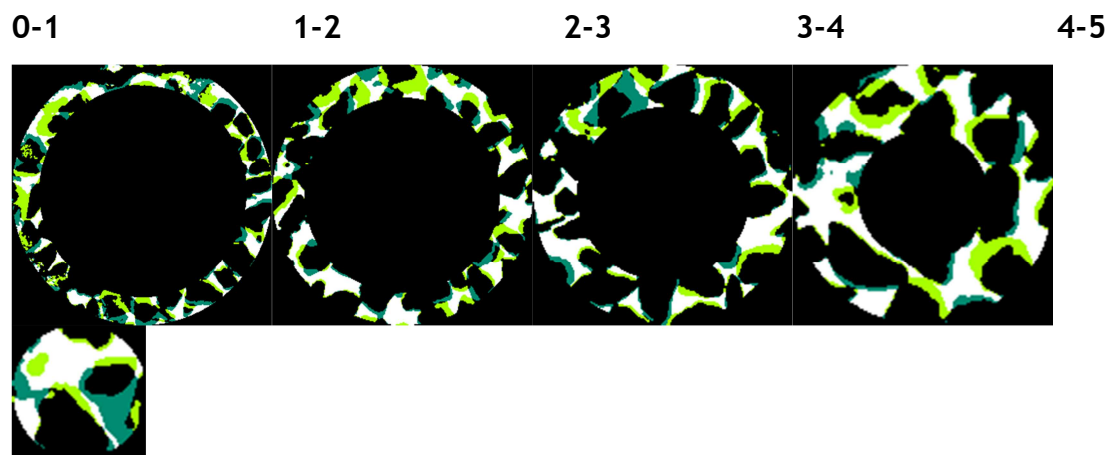


## Appendix J - MRI Concentric ROI for BLL, BDL, BLS & BDS

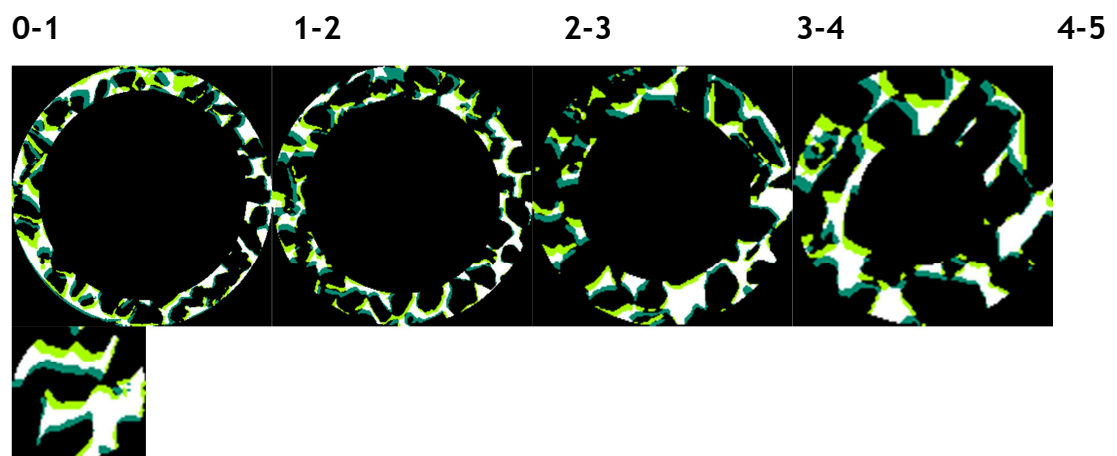
BLL 76



BLL 135

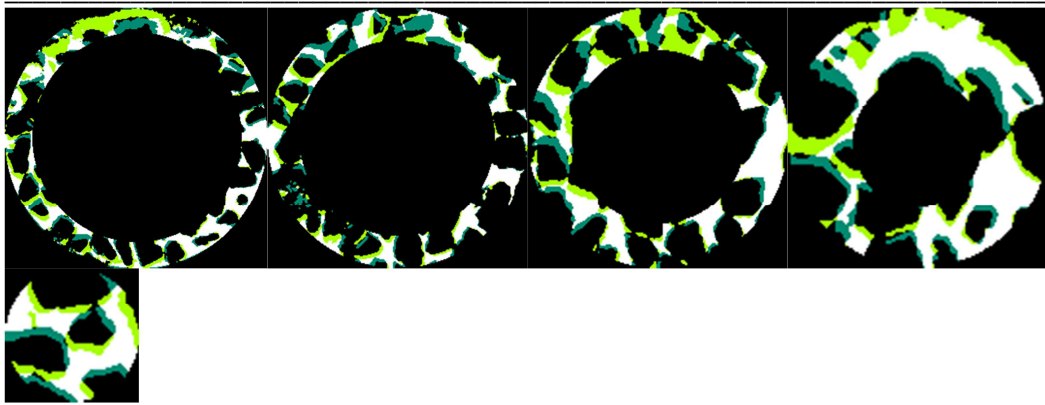


BDL 76



BDL 135





**BLS 76**

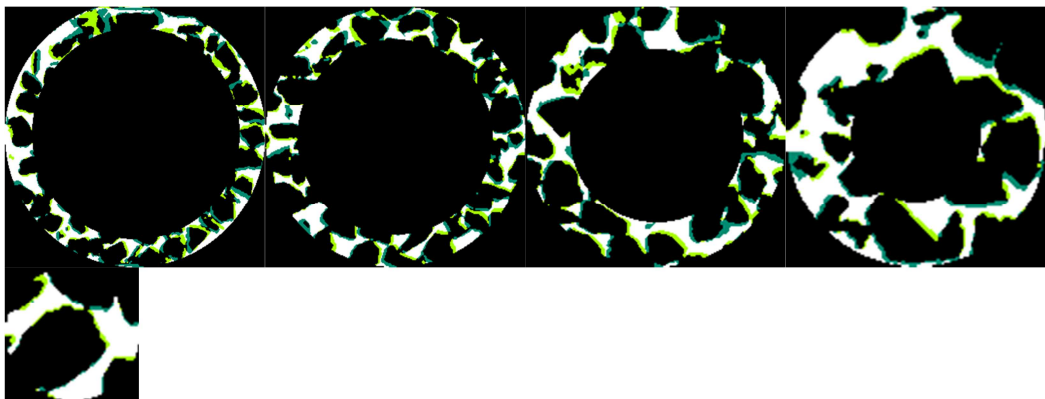
0-1

1-2

2-3

3-4

4-5



**BLS 135**

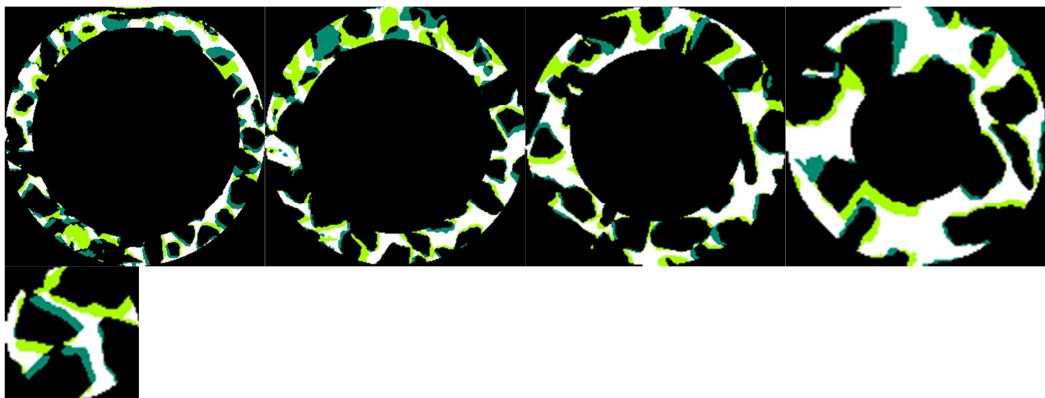
0-1

1-2

2-3

3-4

4-5



**BDS 76**

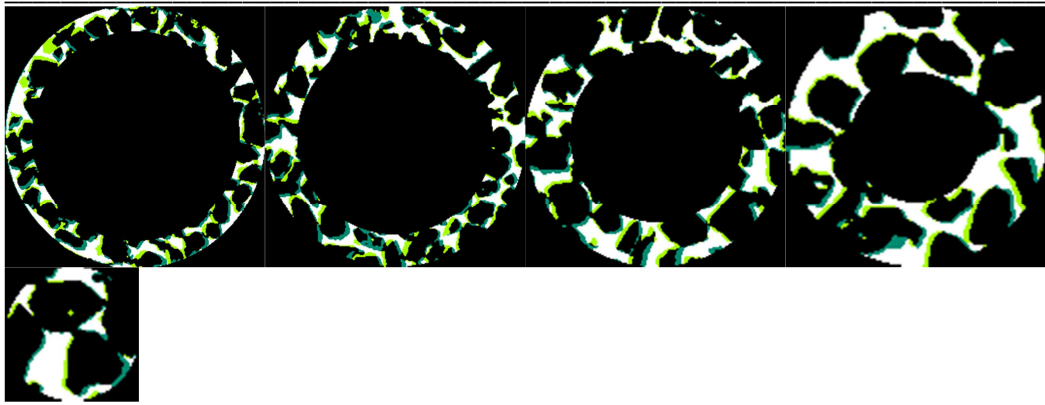
0-1

1-2

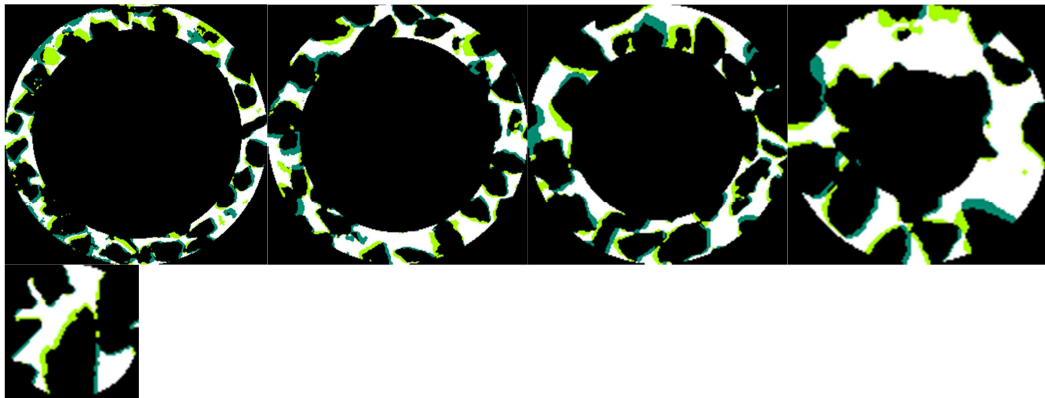
2-3

3-4

4-5



**BDS 135**



---

## Papers

Norris, M. J., et al. (2013). "Treatment of heavy metals by iron oxide coated and natural gravel media in Sustainable urban Drainage Systems." Water Science and Technology 68(3): 674-680.